Max-Planck-Institut
für Meteorologie

MAX-PLANCK-GESELLSCHAFT

International Max Planck Research School
on Earth System Modelling

Can convective precipitation variability be deduced from the variability in CAPE and CIN?

An analysis of global CAPE and CIN variability in present and future climates

Kathrin Riemann-Campe

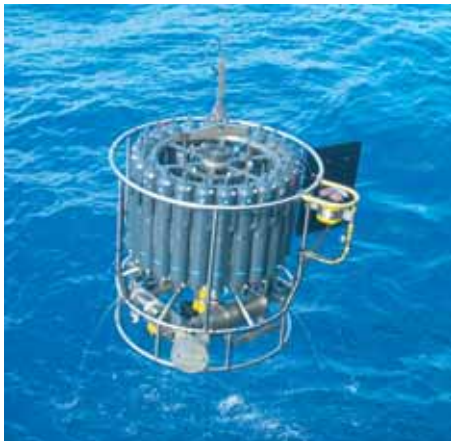

Berichte zur Erdsystemforschung 87/2011

Reports on Earth System Science

Hinweis

Die Berichte zur Erdsystemforschung werden vom Max-Planck-Institut für Meteorologie in Hamburg in unregelmäßiger Abfolge herausgegeben.

Sie enthalten wissenschaftliche und technische Beiträge, inklusive Dissertationen.

Die Beiträge geben nicht notwendigerweise die Auffassung des Instituts wieder.

Die "Berichte zur Erdsystemforschung" führen die vorherigen Reihen "Reports" und "Examensarbeiten" weiter.

Notice

The Reports on Earth System Science are published by the Max Planck Institute for Meteorology in Hamburg. They appear in irregular intervals.

They contain scientific and technical contributions, including Ph. D. theses.

The Reports do not necessarily reflect the opinion of the Institute.

The "Reports on Earth System Science" continue the former "Reports" and "Examensarbeiten" of the Max Planck Institute.

Anschrift / Address

Max-Planck-Institut für Meteorologie
Bundesstrasse 53
20146 Hamburg
Deutschland

Tel.: +49-(0)40-4 11 73-0
Fax: +49-(0)40-4 11 73-298
Web: www.mpimet.mpg.de

Layout:

Bettina Diallo, PR & Grafik

Titelfotos:
vorne:
Christian Klepp - Jochem Marotzke - Christian Klepp
hinten:
Clotilde Dubois - Christian Klepp - Katsumasa Tanaka

Berichte zur Erdsystemforschung 87/2011

Can convective precipitation variability be deduced from the variability in CAPE and CIN?

An analysis of global CAPE and CIN variability in present and future climates

Kathrin Riemann-Campe

aus Bremerhaven

Hamburg 2010

Reports on Earth System Science 87/2011

ISSN 1614-1199

Kathrin Riemann-Campe
Max-Planck-Institut für Meteorologie
Bundesstrasse 53
20146 Hamburg
Germany

Als Dissertation angenommen
vom Department Geowissenschaften der Universität Hamburg

auf Grund der Gutachten von
Prof. Dr. Klaus Fraedrich
und
Prof. Dr. Hartmut Graßl

Hamburg, den 19. Oktober 2010
Prof. Dr. Jürgen Oßenbrügge
Leiter des Departments für Geowissenschaften

ISSN 1614-1199

Can convective precipitation variability be deduced from the variability in CAPE and CIN?

An analysis of global CAPE and CIN variability in present and future climates

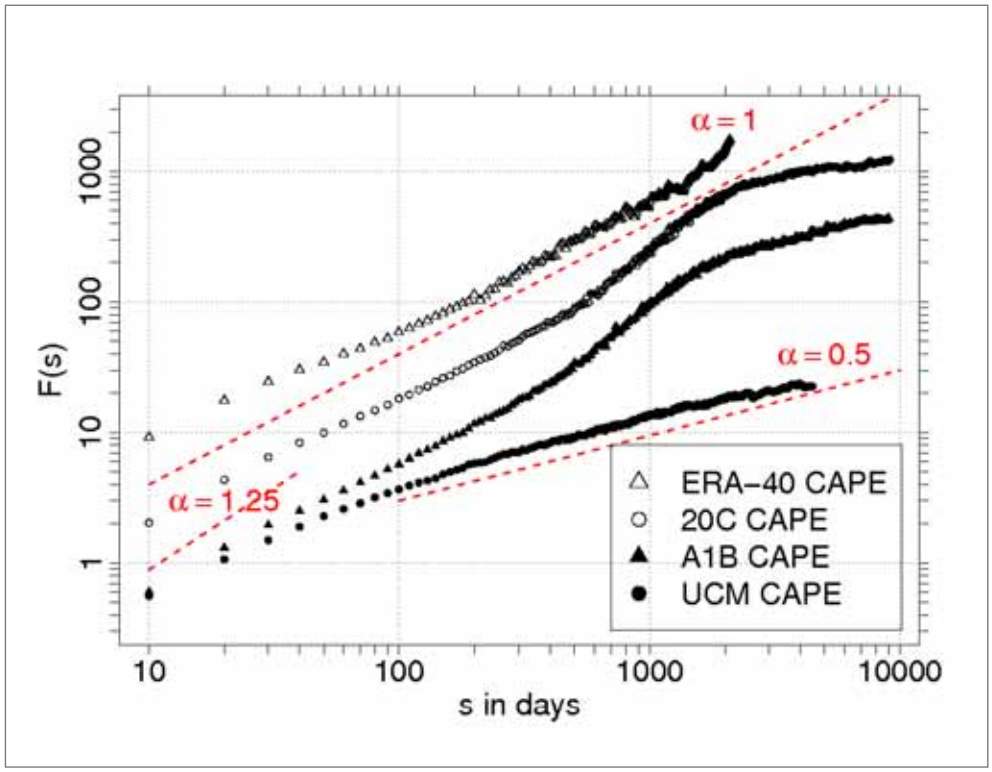

Kathrin Riemann-Campe

Hamburg 2010

Contents

’Sind denn nicht die Naturgesetze als die Ergebnisse der Forschung objektive Wahrheit, allenfalls noch behaftet mit Unvollkommenem, Korrigierbarem, aber in ihrem Wesen nach das wirkliche? Strenge Prüfung zeigt, daß dem nicht so ist. Die Ergebnisse der Naturforschung, die Gesetze und auch die sogenannten Tatsachen, sind nicht etwas Objektives. Sie sind die Natur, wie der Mensch sie sieht und erkennt, nicht wie sie an sich ist.’

Albert Wigand, Vom Wesen meteorologischer Arbeit.
Meteorologische Zeitschrift, März 1932

Acknowledgements

To give everybody credit who supported me on my way to this thesis, I need to start early. In 2004, I visited the School of Meteorology at the University of Oklahoma during an exchange semester. There I wrote an essay, which was about convective parameters. Harold Brooks from the National Severe Storm Laboratory in Norman was my advisor and introduced me to the general topic of CAPE and alike in convective severe weather research. Back at Hamburg University, Klaus Fraedrich, head of the Theoretical Meteorology department, gave me the opportunity of extending the essay into my Bachelor thesis. Furthermore, he and his group gave me the opportunity to write my Diploma thesis in the Theoretical Meteorology department, which was about a global CAPE climatology. Thus, I want to thank Harold Brooks for introducing the topic of CAPE to me and Klaus Fraedrich for letting me further work with it in his group.

I am very grateful for the support my advisory panel gave me during my time as a PhD:
My supervisor Klaus Fraedrich gave me again the opportunity to work on the topic of CAPE and always finds time for my work when matters are urgent.
I also want to thank my panel chair Hartmut Graßl who kept the calm during our panel meetings.
Richard Blender and Frank Lunkeit were my co-advisors from Hamburg and always had an open ear for my questions.
I would like to give my special thanks to Nikolai Dotzek who helped me as an external co-advisor from the Deutsches Zentrum für Luft- und Raumfahrt in Oberpfaffenhofen (DLR). Rest in peace. You were the best! You also introduced me to Julia Sander at the DLR. First, I would like to thank you and Julia to make me feel welcome during my several visits of the DLR. Also, I want to acknowledge the many discussions with Julia about CAPE, CIN and their computation.
In addition, I want to acknowledge the support from the IMPRS in general and specifically from Antje Weitz and Cornelia Kampmann.

During my third year, I visited the group of Robert J. Trapp, head of the Severe Weather Research Group at Purdue University in Indiana for several weeks. I want to give many thanks to Jeff and Sonia Trapp, Mallie Toth, Eric Robinson, Nathan Hitchens, Erin Jones and Jacob Carley for making my stay not only very informative but to make me feel very welcome.

Further, I acknowledge Frank Sielmann and Edilbert Kirk who always helped me, when my computer was on strike. Also, I want to give my thanks to Axel Andersson for providing the HOAPS/GPCC data, to Daniel Klocke for providing the ECHAM5 run with climatological SST and especially to DKRZ, DWD, and ECMWF for providing the other data sets.

My special thanks are given to Andrea Schneidereit, Kerstin Haberkorn, Eileen Dahms, Xiuhua Zhu and Dan Zhang for making life in and outside the office so much more enjoyable. Furthermore, I would like to mention the motivation skills of my lovely neighbours Kati Vorbeck, Frank Schlüter and Hendrik as well as Franziska Hoppe, Henry Ober-Blöbaum, Mia and Kim.

Last but not least, I want to give my very special thanks to my family and Pascal.

Abstract

The variability of convective precipitation is relevant for its prediction on short and long time scales. On short time scales severe weather events are vital for weather forecasting, on long time scales convection anomalies affect wetness and droughts. Since convective precipitation requires parameterisation in numerical models, CAPE (convective available potential energy) and CIN (convective inhibition) are applied to estimate trends and long-term memory. Their variability is determined in present-day climate (ECMWF reanalysis: 6 hourly during 1979-2001 in T106 truncation; ECHAM5/MPI-OM, 20C simulation: 6 hourly during 1902-2001 in T63 truncation) and a possible warmer future scenario (ECHAM5/MPI-OM, A1B scenario: 6 hourly during 2002-2101 in T63 truncation).

Future changes in CAPE and CIN reveal similar changes for small, mean and large values. A global pattern is found of increasing values in CAPE and CIN over most regions of the continents and northern hemispheric ocean basins, while decreasing values are found over the Southern Ocean. This pattern changes towards mostly positive trends if CAPE is analysed for large CIN occurring simultaneously. In contrast, the original pattern remains similar if CAPE is investigated for small CIN.

Temperature and humidity, which form the basis of CAPE and CIN, show almost entirely higher values in the future. Decreasing values in CAPE and CIN correlate with large scale patterns like the North Atlantic Oscillation (NAO), El Niño/Southern Oscillation (ENSO) and the Southern Annular Mode (SAM). Furthermore, a southward shift of the descending branch of the southern hemisphere Hadley Cell in a warmer climate decreases CAPE further.

The correlations of CAPE with the above named teleconnections influence the distribution of global memory on long time scales. The influence of ENSO on the memory in CAPE and CIN intensifies in a warmer climate with regards to spread and frequency. Furthermore, the impact of the NAO on CAPE also spreads in terms of location, while the frequency remains similar in a warmer climate. In contrast, the regions where SAM influences CAPE decrease due to declining values of the SAM index. Additional analyses with an ECHAM5 simulation and climatological sea surface temperature reveal that the variability of the ocean has a stronger influence on CAPE than on CIN.

Chapter 1

Introduction

The variability of convective precipitation is relevant for its prediction on short and long time scales. On long time scales convection anomalies affect wetness and droughts, on short time scales severe weather events are relevant for forecasting. Therefore, a realistic simulation of convective precipitation (CP) is vital for determining its variability and thus for underpinning the predictability of CP in future climate scenarios. This thesis addresses the question whether convective available potential energy (CAPE) and convective inhibition (CIN) combined are able to reflect the variability in CP.
The detour via CAPE and CIN is needed due to the fact that CP cannot be measured independently from large scale precipitation (LSP). Moreover, CP in general circulation models is parameterised. The coupled atmosphere-ocean global circulation model developed at the Max-Planck Institute for Meteorology ECHAM5/MPI-OM is known to have problems in simulating CP with regard to magnitude and location (e.g. Arpe et al., 2005 and Hagemann et al., 2006). In addition, reanalysis data sets like the one of the European Centre for Medium-Range Weather Forecasts (ECMWF) also determine CP from forecasts and convective parameterisation schemes (Uppala et al., 2005). The advantages of CAPE and CIN are their direct dependences on temperature and humidity, which are known to be less problematic in measurements and simulations.
CAPE determines the energy available to develop convection, while CIN describes the stability of the lower atmosphere and thus determines whether convection is likely to be initiated. Many parametrisation schemes of CP depend on CAPE, including those in ECHAM5 (Hagemann et al., 2006) and the ECMWF reanalysis (ERA-40) (Gregory et al., 2000). However, it is debated whether CIN is sufficient in estimating the initiation of convection. The studies of e.g. Emori et al. (2001) and Emori et al. (2005) investigate modelled mean precipitation distributions on a global scale and their dependencies on the cumulus parameterisation scheme. They report an overestimation of precipitation frequency, if no further cumulus suppression treatment is present, which they add with a critical value of cloud-mean ambient relative humidity (RH). In contrast, Market et al. (2003) and Kuang and Bretherton (2006) recommend a combination of CAPE and CIN for their regional analyses in the United States of America without additional criteria. Furthermore, Wang and Schlesinger (1999), Zhang (2002) and Khodayar et al. (2010) support the combination of CAPE and CIN in synoptic situations with weak large scale forcing. They argue that, if strong large scale forcing is present, it is probably sufficient to overcome the stability of the lower atmosphere expressed by CIN. Therefore, Wang and Schlesinger (1999) suggest to include

a RH threshold into the parameterisation scheme for the tropics. Although Khodayar et al. (2010) agree on the CAPE-CIN combination they propose the additional use of a critical temperature T_c, which they determine for a region in England. The above mentioned studies are mostly restricted on either a regional or a temporal scale. Global data sets of CAPE and CIN or a combination of both over a time period longer than a decade have not yet been analysed.
In this thesis, the variability in CAPE and CIN is determined on a global scale from observations, which are represented by the ERA-40 data (1979-2001), from a simulated present-day climate (ECHAM5/MPI-OM, 20C simulation, 1902-2001) and in a warmer future climate (ECHAM5/MPI-OM, A1B scenario, 2002-2101). In addition, the impact of the variability of the ocean on the variability in CAPE and CIN is estimated by analysing an ECHAM5 simulation with climatological sea surface temperature (SST) distribution. The variability in atmospheric temperatures, which is expressed by memory on long time scales, is caused by internal ocean dynamics (Fraedrich and Blender, 2003). As CAPE and CIN are directly linked to temperature, it is expected to find an impact of the ocean on the distributions of CAPE and CIN.
The global variabilities in CAPE and CIN are determined in terms of trends and memory on short and long time scales. To identify the sources of their variability additional analyses of temperature and humidity in the mixed layer (ML, the lowest 100 hPa of the atmosphere) and above of the free troposphere are conducted. Furthermore, correlations between CAPE, CIN and temperature and humidity at several altitudes are investigated. Several studies debate whether temperature or humidity have a stronger influence on the development on CAPE. For example, Ye et al. (1998) report that CAPE variations in space and time are dominated by regional changes in boundary layer temperature and humidity. Zhang (2002) confirms the findings of Ye et al. (1998) for the midlatitudes. In contrast, Holloway and Neelin (2009) find that the moisture in the free troposphere has the strongest impact on the development of CAPE in the tropics.
Further sources of the variability in CAPE and CIN are expected to lie in teleconnections. Norris (2005) reports about the relation between deep convection and El Niño over the Indian Ocean and the tropical Pacific. In addition, Mo (2010) finds that the El Niño/Southern Oscillation (ENSO) influences the precipitation over the United States, while Cai et al. (2010) detect an asymmetry in ENSO related with regional rainfall in Australia. Andersson et al. (2010) report about a link between observed precipitation and the North Atlantic Oscillation (NAO). In addition, Watterson (2009) investigates correlations between the Southern Annular Mode (SAM) and precipitation. Furthermore, Claud et al. (2007) report a relation between the NAO and polar low development which occurs simultaneously with CAPE development. Thus, CAPE is expected to be related to the variability in the NAO. Furthermore, on the Southern Hemisphere, similar relationships between CAPE, polar lows and large scale patterns are expected to be found. In addition to large scale features like teleconnections, the Mean Meridional Circulation also interacts with the distribution of CAPE and thus CP (e.g. Dudhia and Moncrieff, 1987; Dima and Wallace, 2003 and Allan and Soden, 2007). Moreover, Ye et al. (1998) report about how a changing Hadley Cell due to climate change causes changes in CAPE.
The regional and global memory in CAPE and CIN are analysed via autocorrelation functions and decay time scales on short time scales, while the low frequency variability is determined by power density spectra and detrended fluctuation analyses. Several studies analyse memory on various time scales in temperature and moisture variables revealing memory patterns over oceans and continents on almost all latitudes (e.g. Fraedrich and Larnder, 1993; Blender and Fraedrich, 2003;

Fraedrich and Blender, 2003; Fraedrich et al., 2004). Only a few studies focus on the memory in CAPE and CIN. Zawadski et al. (1994) analyse the persistence in CAPE and helicity on time scales of hours to improve the predictability of precipitation in storms. Yano et al. (2001) investigate the memory in CAPE reporting 1/f scaling over the tropical western Pacific for 30 days. The only known global memory analysis in CAPE and CIN computed from present-day climate is investigated by Riemann-Campe et al. (2010), which is discussed in this thesis in chapter 5.
The analysis of energy available for convection reaches back to Margules (1905). However, the name CAPE was first mentioned in a publication by Moncrieff and Miller (1976). CAPE and some times CIN are also used for severe weather analysis and forecasting (e.g. Colby Jr., 1984; Rasmussen and Blanchard, 1998; Craven et al., 2002; Markowski et al., 2002; Brooks et al., 2003; Brooks et al., 2007; Doswell III and Evans, 2003). The analysis of trends in CAPE has been subject of several regional studies: e.g. Gettelmann et al. (2002) and DeMott and Randall (2004) detect CAPE trends computed from observations in the tropics. Outside the tropics, trends in CAPE are found by e.g. Trapp et al. (2007) and Trapp et al. (2009), who compare reference scenarios to several possible future scenarios (A1B and A2) in the USA. The only known global trend estimation of CAPE and CIN computed from the ERA-40 data is investigated by Riemann-Campe et al. (2009), which is discussed in this thesis in chapter 3.

The outline of this thesis is as follows: The data sets and variables used in this thesis are introduced in chapter 2. The global distributions of the first moments of CAPE and CIN and their correlations with temperature and humidity are described in chapter 3. Chapters 4 and 5 report about CAPE and CIN in terms of trends and memory respectively. The following chapter 6 discusses the interactions of teleconnections and the mean meridional circulation (MMC) with CAPE and CIN as possible sources of the their variability. The here gained results are compared to observed precipitation and its variability in chapter 7. A final discussion and conclusion are given in chapter 8, which is followed by an outlook in chapter 9.

Chapter 2

Data and variables

For an analysis of convective precipitation variability the ideal data set would consist of observational data covering the whole globe with a high spatial and temporal resolution. However, such a data set does not exist. Data closest to matching these ideal criteria are reanalysis data, which are based on observations. However, precipitation in reanalysis data is parameterised instead of being measured. Moreover, convective precipitation is not directly measurable, as measurement systems cannot distinguish between convective and large scale precipitation (often called stratiform precipitation). However, the reanalysis data from the European Centre for Medium-Range Weather Forecasts ECMWF (ERA-40) discriminate between convective and large scale precipitation as these are not based on observations but on forecasts and convective parameterisation schemes (Uppala et al., 2005). The global distributions of precipitation in the ERA-40 data as well as those in complex atmosphere-ocean global circulation models, e.g. ECHAM5/MPI-OM are known to be problematic in terms of magnitudes and location (e.g. Arpe et al., 2005; Hagemann et al., 2005; Uppala et al.,2005; Jungclaus et al., 2006). Therefore, the variability of convective precipitation is not determined directly here but via the variability in CAPE and CIN, which are computed from temperature and humidity.
CAPE determines the potential energy available for convection and is included in the convection parameterisation schemes of the ERA-40 and the ECHAM5 data. Were the scheme based on CAPE alone, convection would be overestimated. Therefore, additional variables as e.g. CIN or relative humidity (RH) are combined with CAPE. Several studies address the question of which variable combination works best. Emori et al. (2001) and Emori et al. (2005) investigate modelled mean precipitation distributions on a global scale and their dependencies on the cumulus parameterisation scheme. They emphasise a realistic accumulation of CAPE as a key factor for precipitation intensity. Furthermore, they point out the overestimation of precipitation frequency without a cumulus suppression treatment, which they applied via a critical value of cloud-mean ambient relative humidity. Other research groups focus on a regional approach of the parameterisation scheme. Market et al. (2003) and Kuang and Bretherton (2006) recommend a combination of CAPE and CIN for the United States of America. Wang and Schlesinger (1999), Zhang (2002) and Khodayar et al. (2010) support the combination of CAPE and CIN in synoptic situations with weak large scale forcing. They argue that strong large scale forcing is enough to overcome the stability of the lower atmosphere expressed by CIN. Therefore, Wang and Schlesinger (1999) suggest to include a RH threshold into the parameterisation scheme for the tropics, while Khodayar

et al. (2010) propose the usage of a critical temperature T_c for a region in England. The above mentioned studies are mostly restricted on either a regional or a temporal scale. Global data sets of CAPE and CIN or a combination of both over a time period longer than a decade have not yet been analysed with the exception of Riemann-Campe et al. (2009) and Riemann-Campe et al. (2010) (Chapter 5 contains parts of the published results).
CAPE and CIN are computed from the ERA-40 data set, which covers the years 1958-2001 (Uppala et al., 2005). Bengtsson et al. (2004) and Simmons et al. (2004) find artificial 'jumps' within the data during the transition of the years 1978 and 1979 due to changing measurement systems. These 'jumps' create false signals in trend detection (Riemann-Campe et al., 2009) and memory analysis (Vyushin and Kushner, 2009). Thus, only the years 1979 until 2001 are analysed in this study.
The investigation of variability, especially long term memory, is based upon long time series, which preferably cover also a possible future climate. Hence, simulated data supplement this study. The present-day climate is simulated by the coupled atmosphere-ocean global circulation model developed at the Max-Planck Institute of Meteorology ECHAM5/MPI-OM. The 20th century (20C) simulation covers the years 1902 until 2001. To compare the variability in the simulated data with those within the observed data, the 20C simulation is also analysed for a shorter time period covering 1979 until 2001. A possible future climate is simulated by the model ECHAM5/MPI-OM for scenario A1B and covers the years 2002 until 2101. Furthermore, the influence of the variability of the ocean is determined by comparison with results from an ECHAM5 simulation with climatological sea surface temperature (SST).
The technical details of the different data sets analysed in this thesis are described in Section 2.1. The impact of resolution on the distributions of CAPE and CIN is analysed in Section 2.1.1. The definition of CAPE, CIN and additional analysed variables are found in Section 2.2.

2.1 Data

ERA-40 data: The reanalysis data set of the ECMWF (ERA-40) (Uppala et al., 2005) serves as observations, which are compared to the simulated present-day climate used in this study. Here, data is analysed at four times a day (00, 06, 12, 18 UTC) between 1979 and 2001. The original convection parameterisation scheme in ERA-40 was based on Tiedtke (1989). This scheme was revised and includes now CAPE in its closure assumption (Gregory et al., 2000). CAPE and CIN are computed diagnostically from temperature and humidity values, which are available on 13 pressure levels between 1000 and 100 hPa. The question whether 13 vertical levels are enough to compute CAPE and CIN for this study is addressed in subsection 2.1.1. The horizontal resolution is available in the spectral truncation of T159 ($\sim$1.125°).

20C simulation: The 20th century (20C) climate is simulated by the coupled atmosphere ocean general circulation model ECHAM5/MPI-OM (Roeckner et al., 2003). This simulation includes observed anthropogenic forcings such as $CO_2, CH_4, N_2O, CFCs, O_3$, and sulfate. The convective parameterisation scheme in ECHAM5 is based on Tiedtke (1989) and Nordeng (1994) and includes CAPE in its closure assumption for deep convection (Hagemann et al., 2006). To compare the simulations with the ERA-40 data, CAPE and CIN are computed diagnostically from

temperature and humidity on the same 13 pressure levels as available by the ERA-40 data also at four times a day (00, 06, 12, 18 UTC) between 1979 and 2001. This time span is extended to 1902-2001 in order to analyse variability, especially memory, on long time scales. The 20C simulation consists of a spectral truncation of T63, equivalent to a horizontal resolution of $\sim$1.875°.

A1B scenario: A possible future scenario of a warmer climate is investigated by using temperature and humidity from the A1B scenario of the ECHAM5/MPI-OM model. This scenario is one of those used for the IPCC (Intergovernmental Panel on Climate Change) fourth assessment report (AR4). The anthropogenic forcings ($CO_2, CH_4, N_2O, CFCs, O_3$ and sulfate) change according to the special report on emission scenarios (SRES) (Nakicenovic et al., 2000). The spatial resolution is the same as in the 20C simulation. CAPE and CIN are analysed at four times a day (00, 06, 12, 18 UTC) between 2002 and 2101.

ECHAM5 and climatological SST: The influence of the ocean on the variability in CAPE and CIN is investigated by a simulation with the atmosphere model ECHAM5 uncoupled from a complex ocean model (UCM). The ocean is represented by observed climatological sea surface temperature (SST) distributions from the Atmospheric Model Intercomparison Project 2 (AMIP2, Gates et al. (1999)). The variability in the atmosphere is directly linked to SST distributions via e.g. El Niño. Furthermore, the memory in atmospheric temperatures on long time scales is caused by internal ocean dynamics (Fraedrich and Blender, 2003). CAPE and CIN depend on temperature and its variability. Thus, it is expected to find an impact of the ocean on CAPE and CIN and their variability. The uncoupled simulation has a coarse spatial resolution of T31 ($\sim$3.75°). Temperature and humidity are available four times a day between 1979 and 2027 with fixed CO_2 concentration levels of 348 ppm. The lower spatial resolution of the UCM in comparison with the 20C simulation leads to a colder troposphere in the midlatitudes (Roeckner et al., 2006). Therefore, differences in distributions of CAPE and CIN computed from the 20C and the UCM simulation are not entirely caused by the differences in SST. However, differences caused by a somewhat colder troposphere are much smaller than those caused by missing ocean variability.

2.1.1 Vertical resolution and its effect on the variability

The above mentioned data sets differ in their vertical resolution. Although these GCMs and the reanalysis model run with up to 60 vertical levels, their output on pressure levels is stored on much fewer. CAPE and CIN are computed diagnostically by vertical integration of virtual temperature between 1000 and 100 hPa (Sec. 2.2). The ERA-40 and ECHAM data sets provide their output on 13 pressure levels within the range of interest (Tab. 2.1). For the reason of comparison, the vertical distribution of nine levels as is it used in the PLASIM (Planet Simulator, GCM developed by the University of Hamburg, see for further details at $www.mi.uni - hamburg.de/plasim$) is analysed additionally. The general vertical profile of atmospheric temperature and humidity comprises many details (Fig. 2.1). It is a difficult task to represent these details well by a limited amount of vertical levels. Fewer levels are bound to underestimate gradients resulting in different vertical profiles and thus in different amounts of CAPE and CIN.

Table 2.1— Location of vertical levels in hPa in ERA-40 data and ECHAM simulations (upper line) and PLASIM (lower line).

Level No.	1	2	3	4	5	6	7	8	9	10	11	12	13
Pressure	1000	925	850	775	700	600	500	400	300	250	200	150	100
in hPa	982	924	823	699	567	437	317	211	119				

This subsection addresses the question how the vertical resolution affects the computation of CAPE and CIN. Regional observed sounding data, which are available on a high vertical resolution, and the software tool GEMPAK are used to compute reversible mixed layer CAPE and CIN, where the term mixed layer refers to the lowest 100 hPa of the atmosphere. The GEMPAK tool is able to compute CAPE and CIN from subsamples of the original data set for a given vertical resolution. Therefore, it is possible to compare the magnitudes of CAPE and CIN from all vertical levels with those computed from fewer vertical levels. The observed data is provided by the National Severe Storms Laboratory Historical Weather Data Archives (HWDA) in Norman, Oklahoma ($http://data.nssl.noaa.gov/$). The HWDA provides upper-air data from approximately 65 stations non-uniformly distributed within the USA. The number of stations as well as the vertical resolution of the data varies on a day to day basis. In general, HWDA data is available on 30 to 50 levels. Upper-air data of the month May 1999 on a 12 hourly basis is chosen for the comparison. The data of all stations is transformed onto an equidistant grid with a 2 degree spacing. Their means and standard deviation over time are analysed as well as time series at single stations. In addition to the comparison of magnitudes from different number of levels, CAPE and CIN computed from 13 level ERA-40 data is compared to the 13 level HWDA data to verify the quality of the algorithm computing CAPE and CIN, which is used here.

Time series at 96°W, 40°N: Data from two single stations are used for the analyses. These stations are chosen from the most southern and northern latitudes available to investigate magnitudes depending on latitude. Both stations reveal similar results, therefore results from only one station are presented (Fig. 2.2). It is assumed that the values of CAPE and CIN computed from all available levels are closest to the real ones. Therefore, the results computed from all levels are presented in combination with the difference to the results computed from fewer levels.
CAPE and CIN computed from fewer levels agree reasonably well with those of all levels in general. However, high values of CAPE, which exceed approximately 1000 Jkg^{-1} are overestimated by up to 500 Jkg^{-1} if computed from fewer levels. There does not seem to be a clear pattern of over- or underestimations with regard to CIN. Fig. 2.1 reveals that the temperature and humidity profiles of lower resolution are not able to capture strong vertical gradients, which leads to an underestimation of gradients on multiple levels. The height of a gradient determines whether the underestimation of the gradient results in an under- or overestimation of CAPE and CIN. An underestimated temperature gradient within the mixed layer (lowest 100 hPa of the atmosphere) leads to a lower height of the lifting condensation level (LCL) as well as to a colder parcel in general. The colder parcel results in a higher altitude of the level of free convection (LFC) and a lower level of neutral buoyancy (LNB, see subsection 2.2.1 for definition of levels). In contrast, an underestimated humidity gradient within the mixed layer (ML) leads to a higher altitude of the LCL as well as to a drier parcel. The humidity of the parcel is expressed in terms of virtual

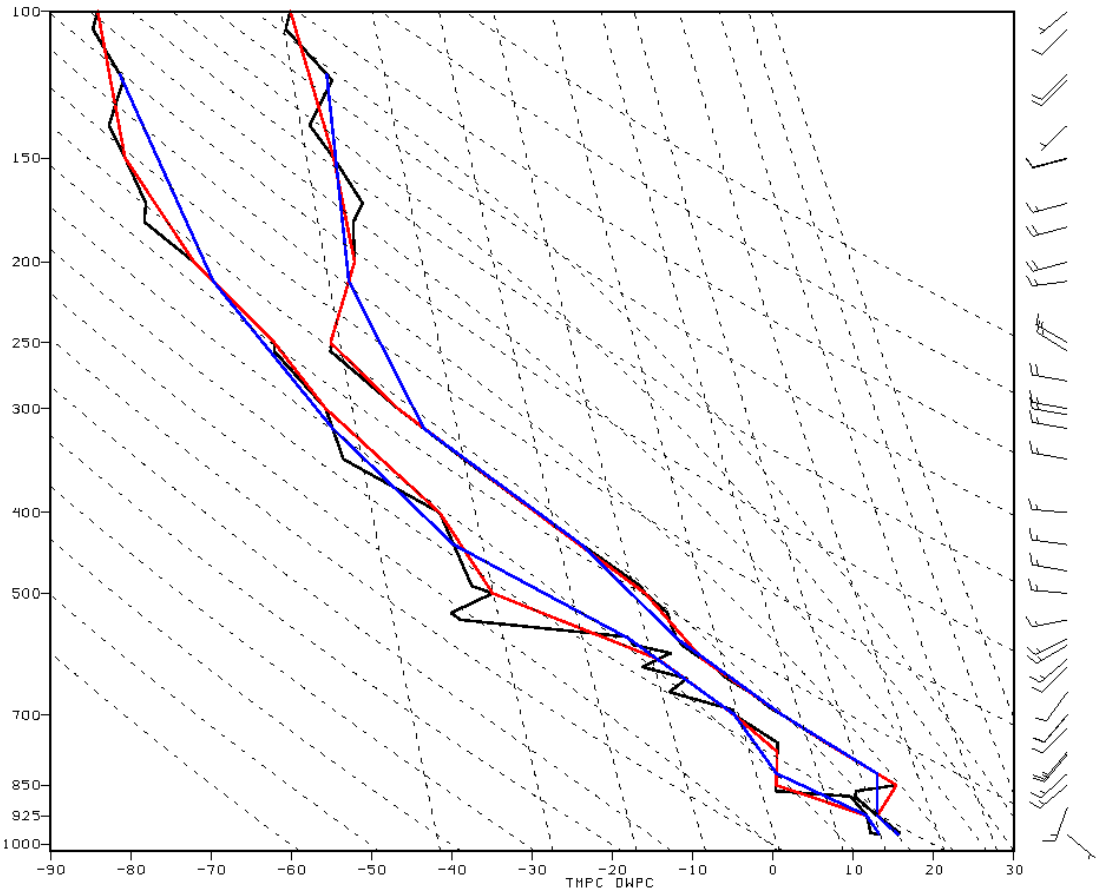

Figure 2.1— Skew-T/Log-P diagram at the station Topeka (TOP), at 96°W; 39°N, on 3rd May 1999, 12 UTC. The vertical profiles of temperature and dew point temperature in °C are displayed as solid curves for different number of pressure levels: (black) all available levels, (red) 13 levels, (blue) 9 levels.

temperature T_v. A drier parcel has lower values of T_v which again lead to a higher altitude of the LFC and a lower LNB. Lower (higher) LCL and LFC altitudes can lead to higher CAPE (lower CIN) due to a higher (lower) number of integrated levels (Eqn. 2.3). If a gradient of temperature or humidity is underestimated above the ML, the virtual temperature of the atmosphere decreases. Note, that the vertical distribution of the virtual temperature of the parcel is determined from the temperature and humidity profiles within the ML only. Therefore, a lower virtual temperature of the atmosphere above the ML leads to a stronger difference to a rising parcel and therefore to higher CAPE and lower CIN. Note, that the differences caused by underestimated gradients above the ML are more strongly pronounced in CAPE as in CIN. For the calculation of CAPE, more levels are affected by underestimated gradients above the ML than for CIN.
The comparison of CAPE and CIN computed from ERA-40 with those computed from HWDA reveals a general underestimation of CAPE and a general overestimation of CIN with varying offset in the ERA-40 data. These under- and overestimations in CAPE and CIN computed from the ERA-40 data are also caused by the fact that temperature and humidity values in ERA-40 data

represent mean values within a 1.125° wide grid box. However, the day to day variability as well as the trends within the time series of CAPE and CIN are captured reasonably well.

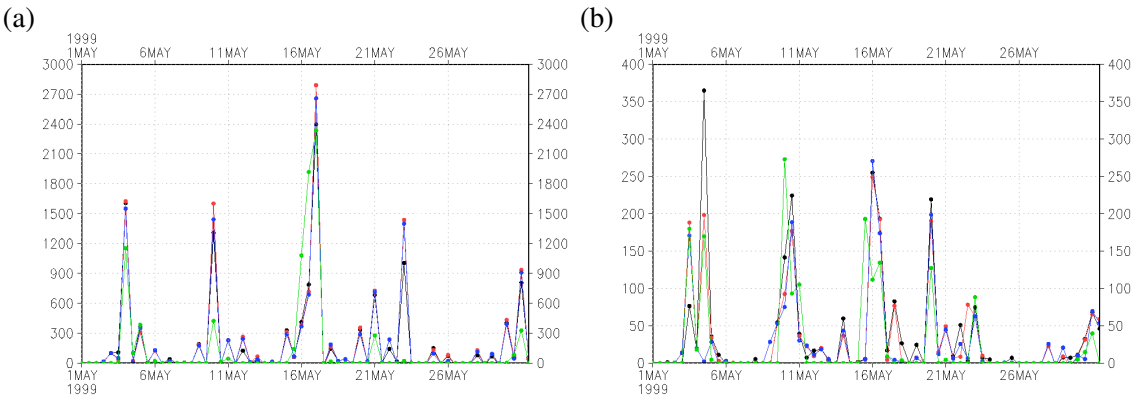

Figure 2.2— Time series of reversible mixed layer (a) CAPE and (b) CIN in Jkg^{-1} at 96°W; 40°N computed from the HWDA data with different number of levels: (black) all levels available, (blue) 13 levels, (red) 9 levels. CAPE and CIN computed from 13 level ERA-40 data is added in green for comparison.

Mean and standard deviation at all stations: The data from all stations is transferred onto an equidistant grid with a 2 degree spacing (Fig. 2.3). The mean and standard deviation during May 1999 computed from all levels available show a maximum over Texas. The decrease of the values around this maximum follows an almost elliptical shape, which results from general favourable large scale conditions for convection over the so called Tornado Alley during spring. The ratio of the differences in % between the mean values computed from the data with all levels and those with the lower resolutions (Fig. 2.3) reveal that the maximum in the mean and also standard deviation is well captured. The differences of CAPE computed from all levels in comparison with those of 13 levels are smaller than 5 % in the southern USA, and range between 5 and 20 % in the northern parts of the USA. Moreover, some grid points adjacent to the west coast reveal negative differences up to 20 %. Two grid points show very high differences between 80 and 100 %. The mean magnitude of CAPE (all levels) at these grid points are below 50 Jkg^{-1}. Therefore, the differences are probably caused by different number of events with CAPE > 0 Jkg^{-1}. The differences of CAPE computed from all levels with those of 9 levels show a different pattern. CAPE from 9 levels is generally underestimated between 5 and 20 % over the central and southern USA and overestimated between 5 and 20 % in the northern parts of the USA. Stronger differences also occur in the vicinity of the west coast where mean CAPE is low.
The mean pattern of CIN computed from all levels available is not concurrent with its pattern of the standard deviation. Local effects within the boundary layer play a more pronounced role than the large scale synoptic conditions in the formation of CIN (Fig. 2.4). Therefore, the general pattern, which is visible in CAPE, is not necessarily seen in CIN.

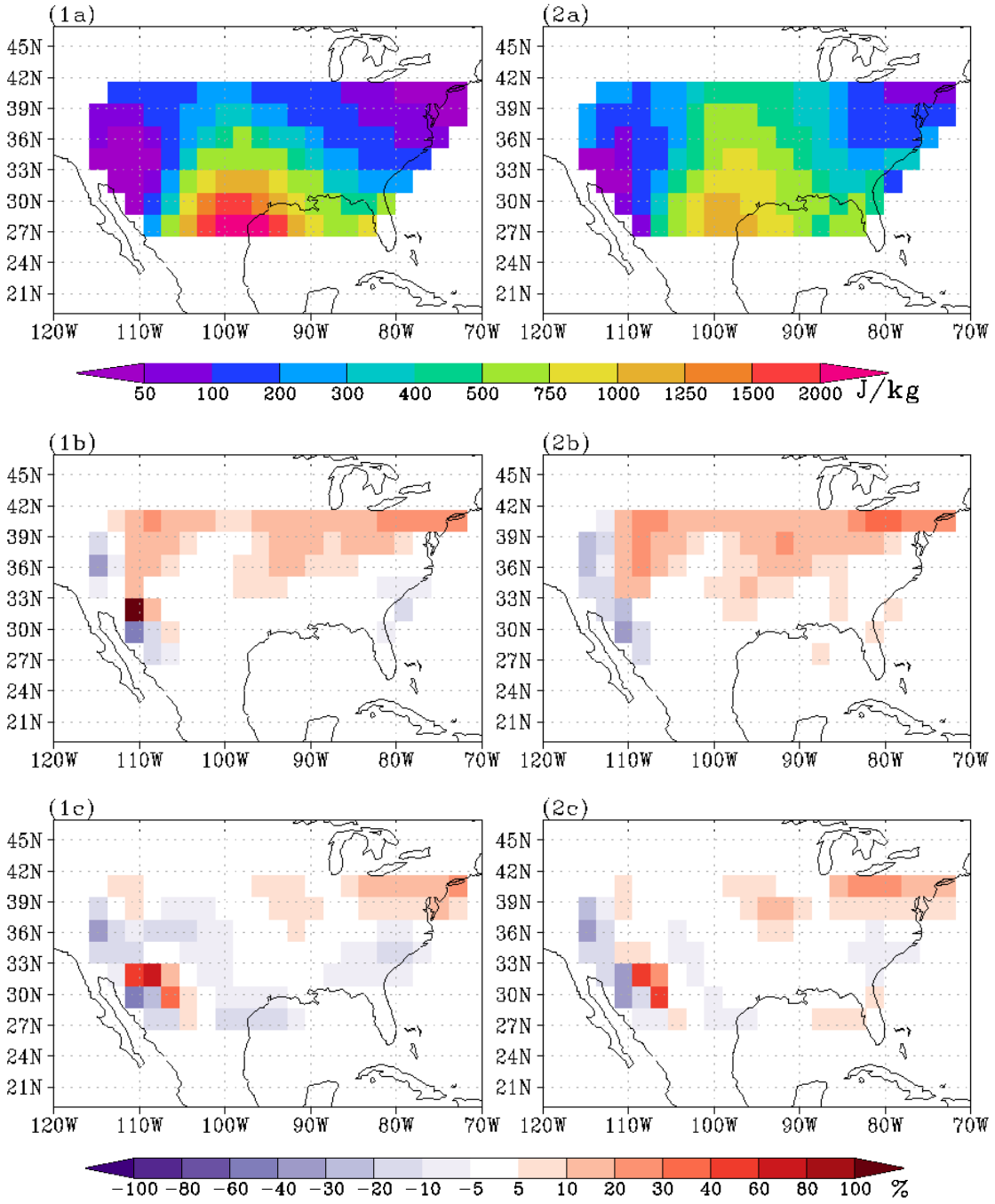

Figure 2.3— (1) Mean and (2) standard deviation of CAPE in Jkg^{-1} computed from HWDA from all levels available (a). The ratio of difference in % between 13 and all levels (b) and the ratio of difference in % between 9 and all levels (c) are displayed. Blue (red) colours show an under- (over-) estimation of CAPE computed from fewer levels.

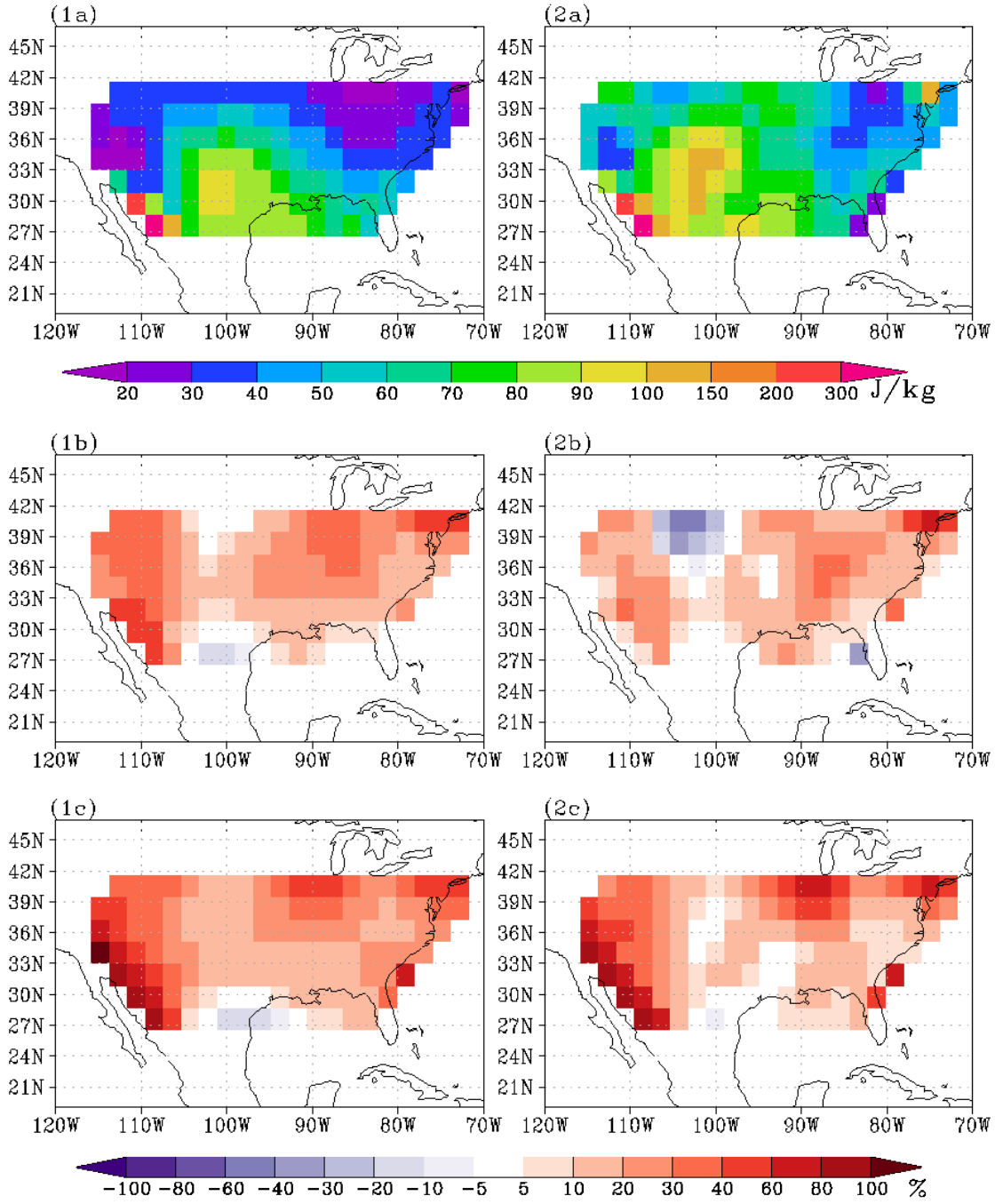

Figure 2.4— (1) Mean and (2) standard deviation of CIN in Jkg^{-1} computed from HWDA from all levels available (a). The ratio of difference in % between 13 and all levels (b) and the ratio of difference in % between 9 and all levels (c) are displayed. Blue (red) colours show an under- (over-) estimation of CIN computed from fewer levels.

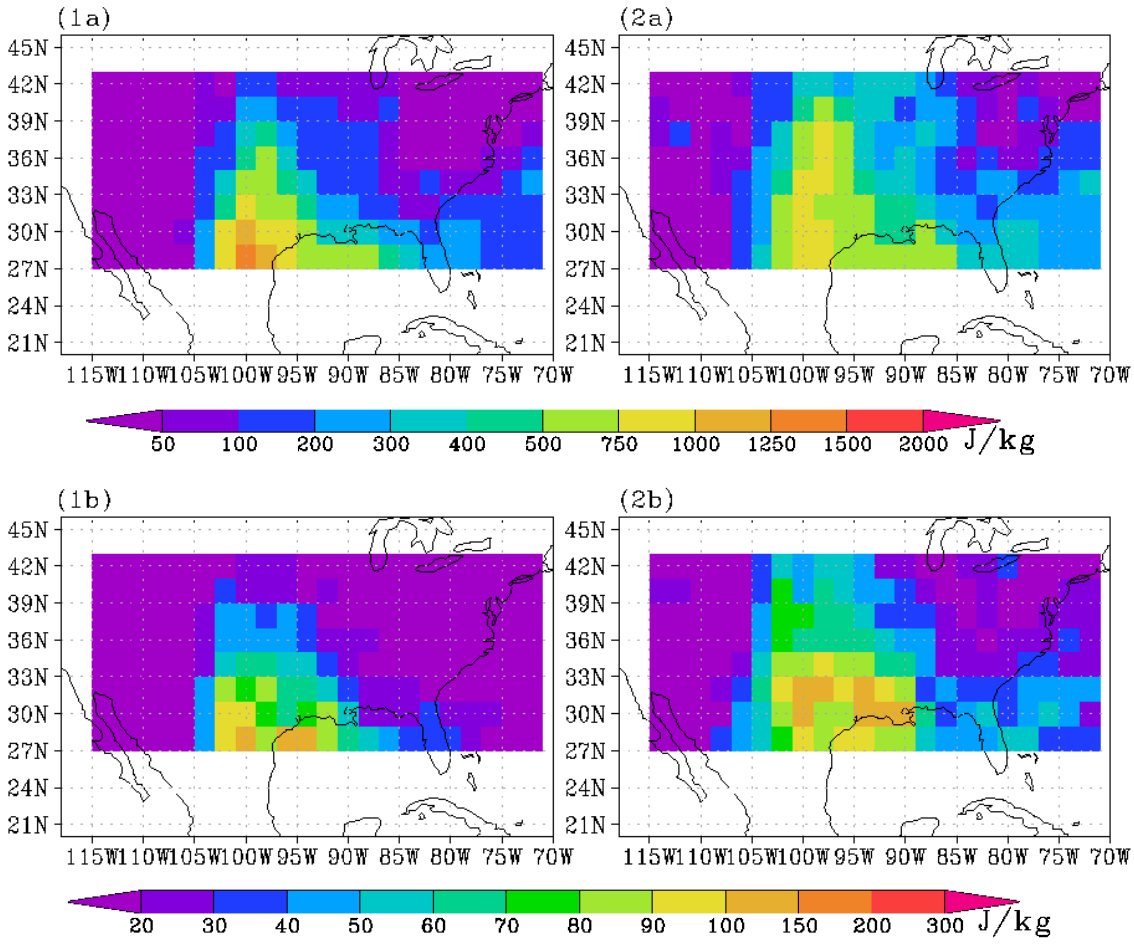

Figure 2.5— (1) Mean and (2) standard deviation of (a) CAPE and (b) CIN in Jkg^{-1} computed from ERA-40 data.

The ratio of the differences of the magnitudes from fewer levels relative to all levels (Fig. 2.4) reveals a general overestimation of the mean of about 5-30 %. Grid points with stronger overestimations occur also in the vicinity of the west coast but independent of the mean magnitude of CIN of all levels. There is also a general overestimation of the standard deviation visible. However, the magnitudes computed from 13 levels show also a local underestimation up to 60 % over Montana, which does not occur if the magnitudes are computed from 9 levels. Therefore, the number of levels is not only crucial but their distribution.

The mean and standard deviation from May 1999 are also computed for CAPE (Fig. 2.5) and CIN (Fig. 2.5) from 13 level ERA-40 data, also transferred onto a 2 degree equidistant grid. Although, the spacing and resolution of the ERA-40 data agrees with those of the HWDA data, the grids are shifted to each other by 0.5 degrees. Therefore, it is not possible to subtract one grid from the other. The distribution of the mean in CAPE in the ERA-40 data is narrower than in the HWDA data. In addition, the values computed from the ERA-40 data are generally lower than those computed from the 13 level HWDA data. The distributions of the mean and standard deviation of CIN computed from the ERA-40 data show a closer analogy to the distribution of ERA-40 CAPE than those of the HWDA data. In general, CAPE and CIN computed from the ERA-40 data reflect the distributions of mean and standard deviation computed from the 13 level HWDA data. Although regional discrepancies can be relatively strong, the general performance is good.
The results show that not only the number of vertical levels is crucial but also their vertical distribution. An underestimated temperature (humidity) gradient leads to higher (lower) values of CAPE and lower (higher) CIN respectively if it occurs within the ML. In contrast, an underestimated gradient above the ML leads to lower virtual temperatures of the atmosphere and therefore to higher (lower) values of CAPE (CIN). Hence, a lower vertical resolution can bias the true values of CAPE and CIN in both directions. From the analysed time series, it seems that the underestimation of humidity gradients within the ML, which leads to smaller CAPE, either occur more often or are stronger than the underestimation of temperature within the ML as well as the underestimation of humidity and temperature above the ML, which all lead to an overestimation of CAPE.
The comparison between CAPE and CIN computed from 13 level ERA-40 data with 13 level HWDA data shows a general under- (over-) estimation of CAPE (CIN) in ERA-40. However, time series analyses at single stations shows that the general variability, which is represented by the diurnal cycle and trends, is reflected.

2.1.2 Horizontal resolution and its effect on the variability

The horizontal resolution of any data set affects the values of its variables, which reflect the mean values over the whole grid box. The larger the area covered by one grid box the weaker reflected are strong horizontal gradients. This effect is also visible in the global distributions of CAPE and CIN in the above mentioned data sets. With decreasing grid resolution, the values of CAPE decrease as well independent of the model. CAPE is computed from the ERA-40 data, which is interpolated from T106 to T63, T42 and T21 resolution (not shown). Although the mean values of CAPE decrease with decreasing resolution, the global pattern of memory derived from detrended fluctuation analysis remains similar. According to Roeckner et al. (2006), the troposphere simulated by the ECHAM5 model warms with increasing resolution, while an increase of vertical resolution has the opposite effect. These differences occur if the resolution varies between T21L19

and T195L31. However, the differences caused by the horizontal resolution is assumed to be small in comparison to the differences caused by the complex ocean and the climatological SST.

2.2 Variables

2.2.1 Convective Available Potential Energy, CAPE

Convective available potential energy (CAPE) determines the potential energy available to be transformed into kinetic energy to cause cumulus convection. These energies are assessed by applying parcel theory (Emanuel, 1994). An assumed air parcel rises adiabatically from the surface towards the tropopause. The temperature and humidity within the parcel reflect the current condition of its surrounding environment of its starting position. Its ascent follows along a dry adiabat until the moisture within the parcel condensates at the lifting condensation level (LCL). The temperature at the LCL (T_{LCL}) is determined after Bolton (1980):

$$T_{LCL} = \frac{2840}{3.5 \cdot \ln T - \ln e - 4.805} + 55 \tag{2.1}$$

The temperature T in K and vapour pressure e in hPa reflect the atmospheric conditions at the starting position of the parcel. The pressure at the LCL (p_{LCL}) can be derived by integrating the first law of thermodynamics:

$$p_{LCL} = p \cdot \exp\left[\frac{c_{pd} + r c_{pv}}{R_d\left(1 + \frac{1}{\epsilon}\right) \cdot \ln\left(\frac{T_{LCL}}{T}\right)}\right] \tag{2.2}$$

with pressure p in hPa, mixing ratio r and temperature T in K at the starting position of the parcel. R_d denotes the gas constant of dry air and of water vapour (R_v) respectively in $Jkg^{-1}K^{-1}$. c_p is heat capacity at constant pressure for dry air (c_{pd}) and of water vapour (c_{pv}) respectively in $Jkg^{-1}K^{-1}$. ϵ denotes the division of R_d by R_v.
Several types of CAPE can be defined which are based on the starting position of the parcel. Surface based (SB) CAPE is computed with temperature and humidity values from the surface resulting in very high CAPE values. Most unstable (MU) CAPE refers to the most unstable parcel within the lowest 300 hPa. In this study mixed layer (ML) CAPE is analysed. The lowest 100 hPa of the atmosphere are assumed to be well mixed. The parcel starts from the ML with mean ML temperature and humidity values. MLCAPE is often used if the boundary layer is represented by few vertical levels. In addition, the CAPE computation differs with regard to the humidity within the parcel after condensation. If the water vapour rises further within the parcel, the ascent follows a reversible moist adiabat. In contrast, if the water vapour forms droplets and falls out as rain, latent heat is released which warms the parcel. The parcel will follow then an irreversible or pseudo-adiabat. The true magnitude of CAPE ranges between the reversible (lower bound) and the pseudo-adiabatic (upper bound). For this study, pseudo-adiabatic MLCAPE is used with the exception in Section 2.1.1. The GEMPAK software computes reversible CAPE only (GEMPAK manual available at

$http://www.unidata.ucar.edu/software/gempak/help\_and\_documentation/manual/$).

CAPE is defined between the level of free convection (LFC) and the level of neutral buoyancy (LNB). If the air parcel rises above the LCL, it reaches the LFC when the virtual temperature T_v within the parcel (T_{vp}) exceeds that of its immediate environment (T_{ve}). The density of the parcel becomes lower than that of the surrounding air and it rises freely. Below the LFC a lifting mechanism is needed to rise the parcel. Above the LFC the parcel rises until its density is at equilibrium with the surrounding air which happens at the LNB, which is also expressed by ceasing differences of T_{vp} and T_{ve}. CAPE is expressed by differences of T_v:

$$CAPE = R_d \int_{LFC}^{LNB} (T_{vp} - T_{ve})\, d\ln p \tag{2.3}$$

where R_d denotes the gas constant of dry air in $Jkg^{-1}K^{-1}$ and p is pressure in hPa (Emanuel, 1994). If the parcel converts all potential energy into kinetic energy, and if the upward velocity w in ms^{-1} is not influenced by horizontal wind, then:

$$w_{max} = \sqrt{2CAPE} \tag{2.4}$$

Usually, perturbations of the upward motion lead to considerably smaller values of w_{max} by mixing with environmental air (Emanuel, 1994).

2.2.2 Convective Inhibition, CIN

CAPE describes the energy available for cumulus convection. However, large values of CAPE do not necessarily lead to convection and precipitation. The parcel needs a lifting mechanism to reach the LFC (e.g. orographically induced, overlapping air masses along fronts). Convective inhibition (CIN) denotes the energy needed by the parcel to arrive at the LFC. CIN is defined between the ML and the LFC and is also expressed by T_v:

$$CIN = R_d \int_{ML}^{LFC} (T_{ve} - T_{vp})\, d\ln p \tag{2.5}$$

CIN and CAPE are specific energies with the unit Jkg^{-1}. The presence of high CIN prevents ascending parcels to reach the CAPE layer. Thus, CIN can lead to an accumulation of high CAPE magnitudes, which might develop into convection eventually (Parker, 2002). The stability of the lower atmosphere can be expressed in terms of velocity:

$$-w_{max} = \sqrt{2CIN} \tag{2.6}$$

Note that $-w_{max}$ also refers to a parcel undisturbed by the ambient atmosphere.

2.2.3 Temperature and humidity related variables

CAPE and CIN depend directly on temperature and humidity. The question arises which variable at which height has the stronger influence on the variability of CAPE and CIN. Therefore, mean

values of temperature and specific humidity within the ML (T_{ML}, q_{ML}) and also between the ML and the 100 hPa level are analysed. For a consistent comparison, temperature and specific humidity above the ML are converted to energies. The temperature is multiplied by the heat capacity of dry air at constant pressure c_{pd} with individual values at each pressure level, yielding enthalpy H with the same units as CAPE and CIN, [H] = Jkg^{-1}:

$$H = \frac{1}{n_L} \sum_{k=ML}^{100hPa} (c_p T)_k \tag{2.7}$$

where n_L denotes the number of vertical levels between the ML and 100 hPa.
For the same reason, specific humidity between the ML and 100 hPa is multiplied by the latent heat of evaporation L (also varying with height). The resulting vertical mean of latent heat equivalent of precipitable water LPW is also counted in units of energy per mass, [LPW] = Jkg^{-1}:

$$LPW = \frac{1}{n_L} \sum_{k=ML}^{100hPa} (Lq)_k \tag{2.8}$$

According to Holloway and Neelin (2009) the free tropospheric humidity plays the most important role in developing CAPE in the tropics. Furthermore, Zhang (2002) reports that the contribution of humidity in the free troposphere is negligible in the midlatitudes in comparison with the thermodynamic changes in the boundary layer. The global analyses of temperature and humidity within the ML and above in this thesis contribute to this discussion.

Chapter 3

First moments and correlations of CAPE and CIN

This chapter focuses on the global distributions of mean and standard deviation of CAPE and CIN computed from the ERA-40 data set as well as the different ECHAM5 simulations. The results from the 20C simulations are compared to the ERA-40 data serving as a simple form of verification of the simulated present-day climate. The distributions from the A1B scenario are then compared to the 20C simulation to reveal the impact of a warmer climate. The differences between the 20C simulation and a simulation where the complex ocean is represented by climatological SST reveal the impact of the ocean.
A global climatology of surface based CAPE and CIN distributions of the present-day climate is reported by Riemann-Campe et al. (2009). The higher values of surface based CAPE and CIN in comparison with the mixed layer variables (the mixed layer covers the lowest 100 hPa of the atmosphere), which are investigated here, are clearly visible. These differences are caused by the parcel conditions at its starting point (more details in Subsec. 2.2.1). The closer the parcel is located to the surface, usually the warmer and more humid the parcel is. In addition, the mean and standard deviation of temperature and humidity in and above the mixed layer (ML) are analysed in order to find first indications of relations between T_{ML}, q_{ML}, H, LPW and CAPE and CIN. The question of possible relations between the variables is further investigated in section 3.2 via correlation analyses. Holloway and Neelin (2009) find via correlation analyses that the free tropospheric moisture has the strongest impact on the development of CAPE in the tropics. Zhang (2002) investigates also the impact of the troposphere on the development of CAPE and CIN for the mid-latitudes and reports that the boundary layer has a stronger influence. The conclusion drawn from the different sections of this chapter are summarised in section 3.3.

3.1 Global distributions of mean and standard deviation

The global distributions show the mean values of CAPE and CIN and their residual standard deviation, meaning that the mean annual cycle was subtracted before computing the standard deviation (Fig. 3.1 - 3.2). The mean and standard deviation are computed from all years available (Subsec. 2.1). In addition to analysing the mean over the full years, the mean and standard deviation

are analysed for each season separately. However, due to the high number of additional plots, these are placed in the appendix. The differences between the mean and standard deviation from the 20C simulation over the shorter time period (1979-2001) are negligible compared to those from the longer time period (1902-2001). Therefore, only the results from the longer time period are shown and discussed here.
The general distribution of mean CAPE values is similar in all datasets. Highest values occur over the continental tropical regions. Also very high values are found over the tropical ocean basins. The magnitudes of CAPE decrease with increasing latitude. Regions with mean CAPE values smaller than 10 Jkg^{-1} occur along the west coasts of the American, African and Australian continents where cold water currents are upwelling which lead to a colder and dryer atmosphere above. Further regions with minima in mean CAPE occur over either very dry regions like the Sahara or very cold regions like Antarctica and Greenland.
The comparison between CAPE computed from ERA-40 with the ECHAM5 simulations reveals that the regions with minima are less pronounced with regard to space in the ECHAM5 simulations. In contrast, the mean magnitude of CAPE is less than 10 Jkg^{-1} in Eurasia in the ERA-40 data, while the magnitudes vary between 10 and 400 Jkg^{-1} in the 20C simulation. Further differences occur along the equator. CAPE ranges between 1250 and 1500 Jkg^{-1} in a region over the western equatorial Pacific which expands towards the eastern Pacific south of the equator in the ERA-40 data, whereas CAPE varies between 1000 and 1250 Jkg^{-1} north and south of the equator emphasising a double ITCZ in the Pacific in the 20C simulation. These differences become more evident in the zonal mean distributions which has a bimodal shape in the 20C simulation due to the double ITCZ. The differences in mean CAPE in the ERA-40 data and the 20C simulation are also visible in the mean distributions of q_{ML} (Fig. 3.4) and even more pronounced in LPW (Fig. 3.6). However, the differences in humidity distributions in the 20C simulation and the ERA-40 data does not account for the differences in CAPE distribution over Eurasia. Both data sets have similar distributions of temperature and humidity over Eurasia. Therefore, it remains unclear what causes the differences over Eurasia.
The distributions of mean and standard deviation of CAPE obtained from each season separately pronounce the dependence of CAPE on temperature (Fig. A.1-A.4). The magnitudes in CAPE are generally higher during the warm summer months than during winter. However, without the availability of humidity, CAPE would not develop at all. The differences in CAPE magnitudes and distributions between the 20C simulation and the ERA-40 data are far less pronounced if the seasons are analysed separately. The differences over Eurasia are negligibly small whereas the differences over the tropical Pacific vary with the seasons. The magnitudes of CAPE computed from the ERA-40 data exceed those from the 20C simulation by several hundred Jkg^{-1} throughout the whole year. However, the differences with regard to the double ITCZ pattern in the Pacific are stronger pronounced during the hemispheric summer (Northern hemispheric summer: June, July, August (JJA); Southern hemispheric summer: December, January, February (DJF)) and autumn than during the other seasons.
While mean CAPE values are considerably higher in the ERA-40 data than in the 20C simulations, the magnitudes of the residual standard deviation range in both data sets within the same boundaries from less than 10 Jkg^{-1} up to 1000 Jkg^{-1}. However, regions with standard deviation up to 400 Jkg^{-1} reach further north over Eurasia and North America in the 20C simulation than in the ERA-40 data. Values even exceed 1000 Jkg^{-1} over central North America. Similar to the dif-

ferences in mean values between the 20C simulation and the ERA-40 data, the standard deviation computed from the ERA-40 data consists of higher values in the tropics. These differences also decrease when the seasons are analysed separately including those over Eurasia and North America. The standard deviation of temperature and humidity confirm the findings when analysing the mean distributions. Higher temperatures favour the development of CAPE. However, the large scale distributions of CAPE resemble those of humidity. The question of what causes the differences over Eurasia is still unanswered.
The distribution of CIN shows much smaller mean values than CAPE due to the general smaller depth between ML and LFC in comparison to the depth between LFC and LNB (Subsec. 2.2.1). Nevertheless, these small values indicate relatively stable boundary conditions. According to Eqn. 2.6, an upward velocity of 8.9 m/s is needed to overcome CIN = 40 Jkg^{-1} which is the mean value in the tropical regions. High values of mean CIN occur over the central Pacific along the equator. In contrast to the distribution of mean CAPE, larger values of mean CIN are shifted to approximately 10-30° latitude. Highest values up to 250 Jkg^{-1} occur in the ERA-40 data and up to 175 Jkg^{-1} in the 20C simulation over the Red Sea and the Arabian Sea. Over the mid-latitudes, CIN forms a region exceeding 60 Jkg^{-1} over the Central USA, the region also known as 'Tornado Alley'. Differences in the mean distributions between the ERA-40 data and the 20C simulation are expressed in higher values along equatorial Pacific and Atlantic in the 20C simulation, which also decrease during the individual seasons.
The comparison with the mean distributions of T_{ML} and q_{ML} reveals that the distribution of CIN resembles those of q_{ML} more than that of T_{ML}. The zonal means in CIN are multi modal, with peaks at the equator (more pronounced in the 20C simulation), at around 15°N and an indication of peak at 15°S. The peak at 15°S becomes stronger during the Southern Hemispheric summer months. An additional peak occurs around 40°N during the Northern Hemispheric summer with high values of CIN over the Mediterranean Sea, which is probably caused by dry air masses coming from the Sahara. The standard deviation of CIN show similar or even higher values than in the mean distribution indicating its high variability. Higher magnitudes occur for example over the tropical Atlantic and the Mediterranean Sea during the summer months. The regions in the CIN standard deviation are similar to those in CAPE which reach further to the North in the 20C simulation. The distributions of temperature (T_{ML} and H) and humidity (q_{ML} and LPW) show highest mean values in the tropics, whereas the standard deviation display their maxima in the mid-latitudes.
The high mean values which do not change much in the tropics are caused by the large scale circulation and the absence of an annual cycle. In contrast, the smaller mean values with their high variability are due to synoptic disturbances. The movements of highs and lows bring a regular change in the temperature and humidity distributions and thus in the distributions of CAPE and CIN. The distributions of CAPE and CIN resemble the upward and downward branches of the Hadley Cell, with the exception of the high mean CIN values over the equatorial Pacific. The large magnitudes of CAPE occur in the regions of the ascending branches, whereas the high magnitudes of CIN happen in the regions of the descending branches of the Hadley Cell. These findings are more pronounced in surface based CIN (Riemann-Campe et al., 2009). The impact of the mean meridional circulation is also visible in the trends discussed in chapter 4.

3.1.1 Mean and standard deviation in a warmer climate

One possible future climate scenario is implemented by the A1B simulation. The general pattern of mean and standard deviation of CAPE computed from the A1B data remains similar to those from the 20C simulation. However, regions with CAPE $> 10\ Jkg^{-1}$ expand further to the north and cover now wide parts of Siberia. CAPE also increases over continental Europe, the so called 'Tornado Alley' in the south central USA and over regions in the tropics. There, the double ITCZ is stronger pronounced in this warmer climate. The regions with a standard deviation of CAPE $\leq 100\ Jkg^{-1}$ remain similar to those in 20C, with the exception of an expansion over Europe and the tropics. This feature is more pronounced during the individual seasons.
The mean CIN increases over the equatorial Atlantic and the Arabic Sea. The expansion of the regions with high values is more pronounced in the standard deviation of CIN than they appear in the mean, especially during the summer months. A general increase is also visible in the temperature related variables T_{ML} and H, and the humidity related variables q_{ML} and LPW in the tropics. While the increase in temperature occurs homogeneously in a belt like pattern in the tropics, the increase in humidity resembles the pattern of the double ITCZ, which is also visible in the warmer CAPE magnitudes. Whereas, the pattern of the increase in CIN over the Mediterranean reflects those of temperature. The increase of humidity over the Mediterranean is only weakly distinct. The increase in T_{ML} in combination with a weak change in q_{ML} leads to a higher LCL altitude and thus to a deeper layer of CIN. In general it can be said that CIN increases in regions with an increase of temperature and a lesser pronounced increase in humidity, whereas CAPE increases in regions with an increase in temperature as well as in humidity. Therefore, no strong differences are apparent over the Mediterranean Sea. A more detailed investigation of changes in CAPE and CIN between the 20C simulation and the A1B scenario is described in chapter 4.

3.1.2 The impact of SST on CAPE and CIN

Although the general distribution of CAPE remains, the magnitudes are much smaller with maximum values between 400 and 600 Jkg^{-1} over the tropical ocean basins and values up to 1250 Jkg^{-1} over tropical Africa. In addition, the ITCZ is not as clearly visible in the UCM. The mean values of CAPE are generally smaller by about 500 Jkg^{-1} if the ocean is represented by climatological SST. In contrast, the magnitudes of CIN increase, especially over the ocean basins where the magnitudes more than double. Moreover, the very high values over the Red Sea occur only in the seasonal mean distributions. These differences in CAPE and CIN distributions do not seem to be caused by similar changes in temperature and humidity like in the previous subsection. The mean distribution of temperature and humidity do not reveal strong differences in comparison with the 20C simulation, with the exception of the ITCZ pattern. However, their standard deviations show much less variability in the tropics in the UCM. Due to the climatological SST distribution, no long memory is present in the SST which can be passed on to the atmosphere. In addition, the ENSO cycle is also not present in the UCM. The following chapters present how the memory and the ENSO cycle influence magnitudes and thus the variability in CAPE and CIN.

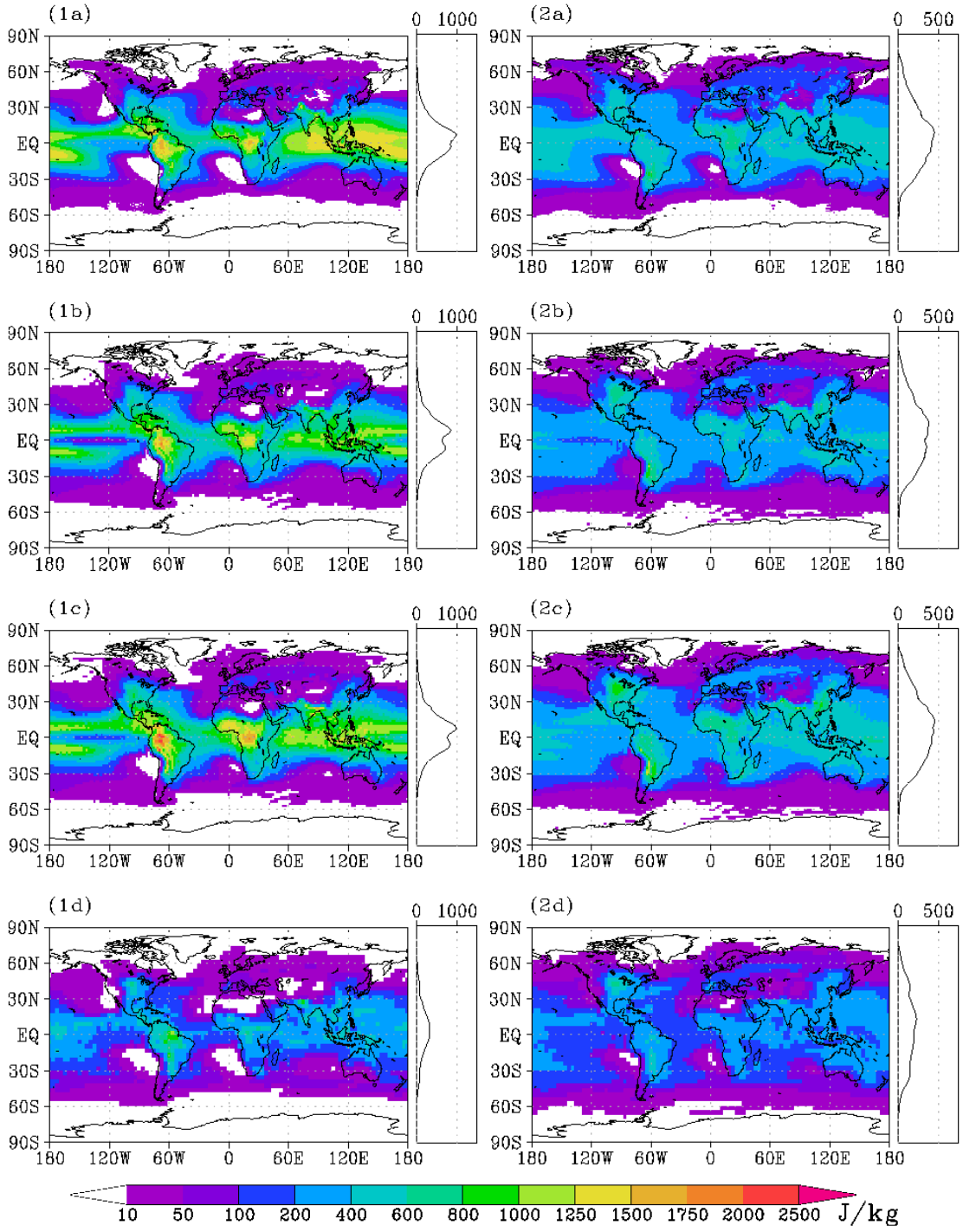

Figure 3.1— (1) Mean and (2) residual standard deviation of CAPE in Jkg^{-1} computed from (a) ERA-40 data, (b) 20C simulation, (c) A1B scenario, and (d) UCM.

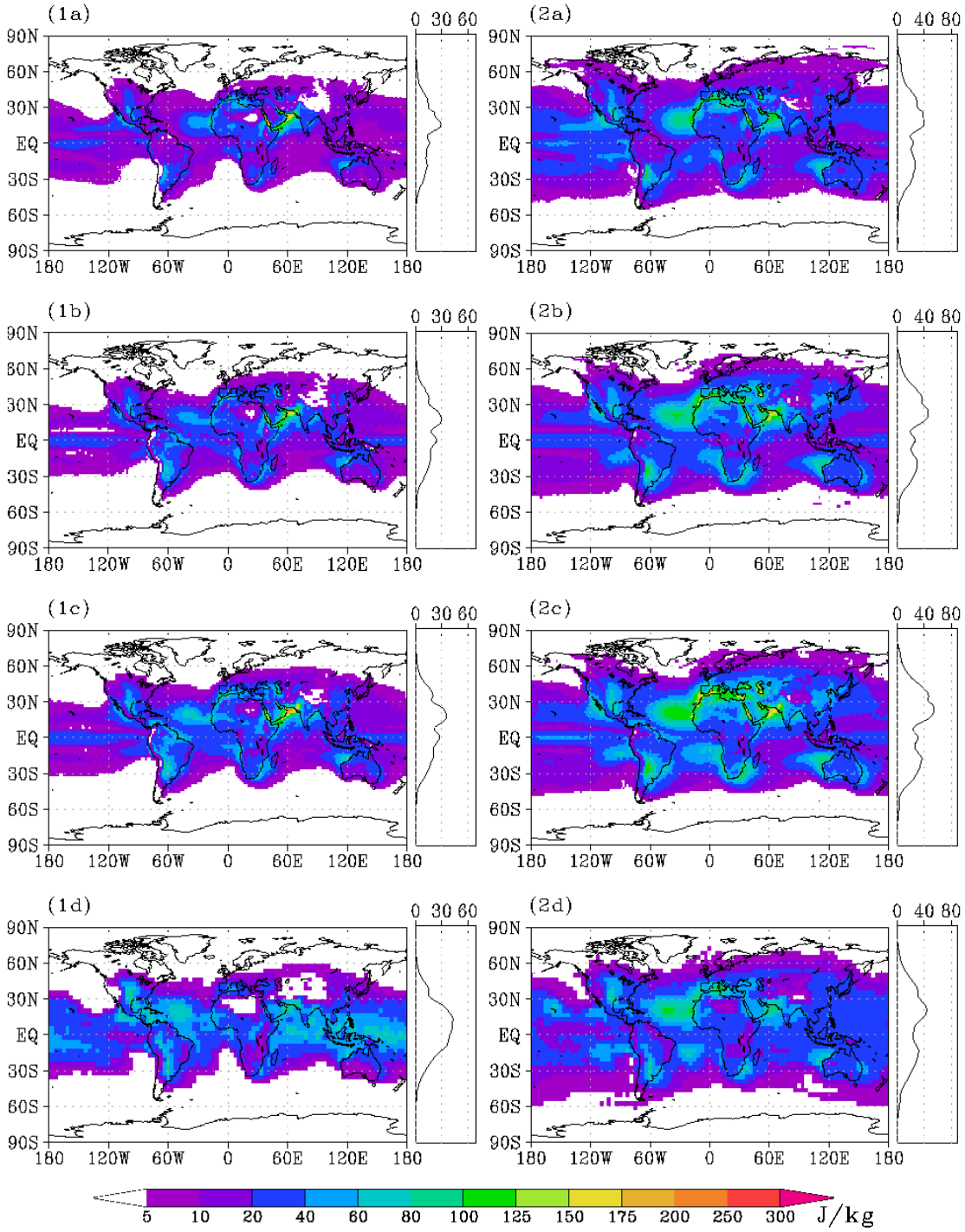

Figure 3.2— (1) Mean and (2) residual standard deviation of CIN in Jkg^{-1} computed from (a) ERA-40 data, (b) 20C simulation, (c) A1B scenario, and (d) UCM.

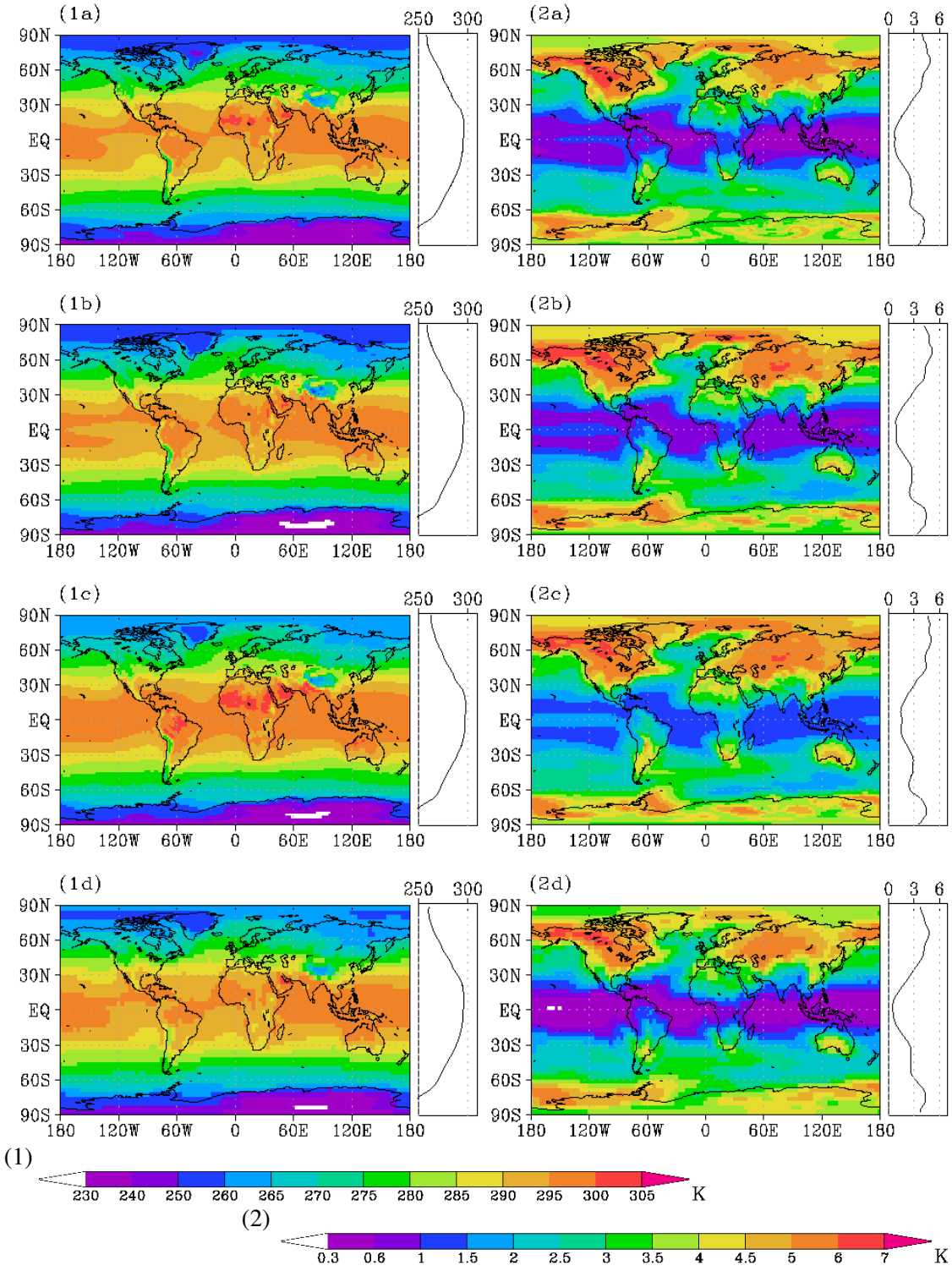

Figure 3.3— (1) Mean and (2) residual standard deviation of T_{ML} in K computed from (a) ERA-40 data, (b) 20C simulation, (c) A1B scenario, and (d) UCM.

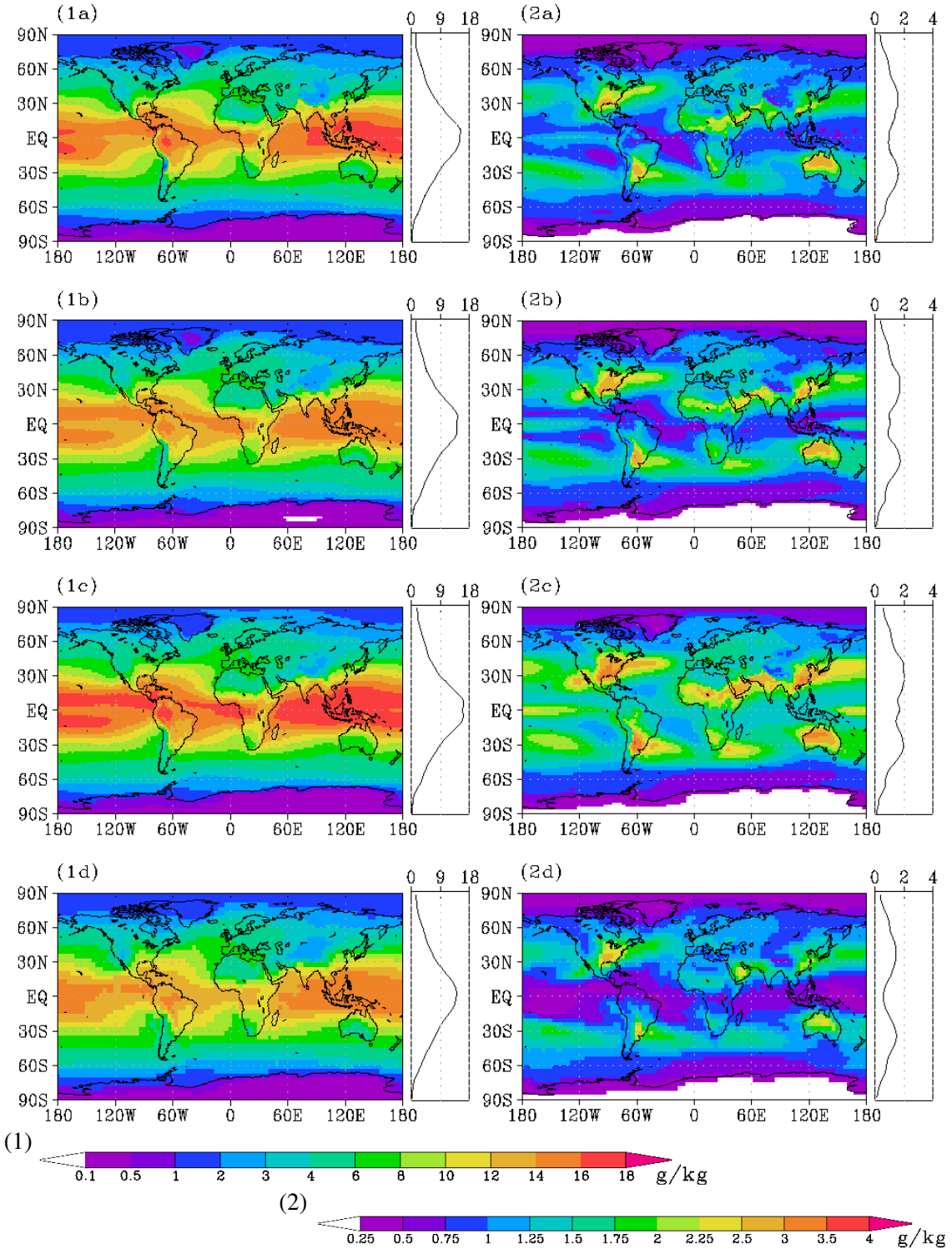

Figure 3.4— (1) Mean and (2) residual standard deviation of q_{ML} in gkg^{-1} computed from (a) ERA-40 data, (b) 20C simulation, (c) A1B scenario, and (d) UCM.

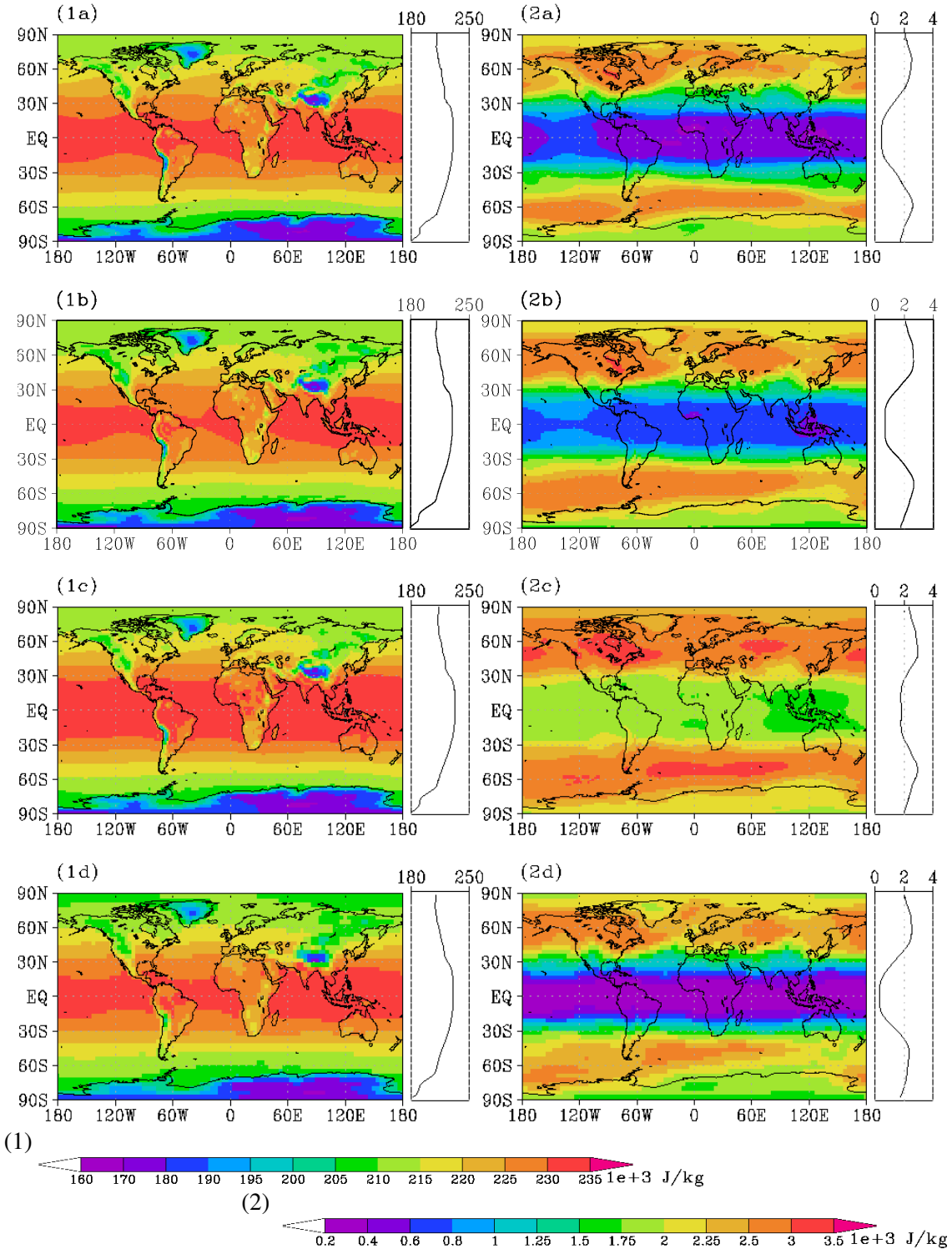

Figure 3.5— (1) Mean and (2) residual standard deviation of H in $10^{+3}\ Jkg^{-1}$ computed from (a) ERA-40 data, (b) 20C simulation, (c) A1B scenario, and (d) UCM.

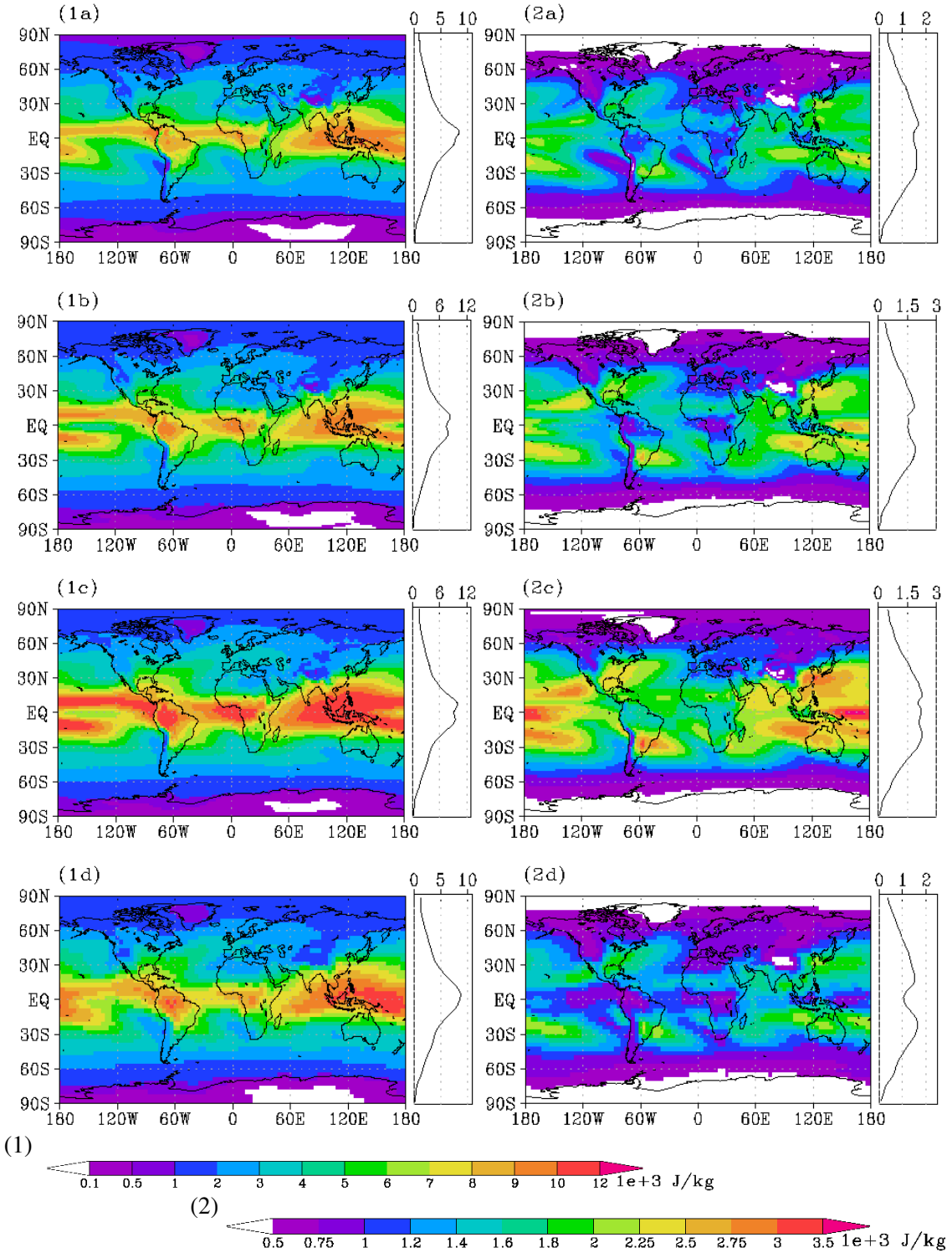

Figure 3.6— (1) Mean and (2) residual standard deviation of LPW in 10^{+3} Jkg^{-1} computed from (a) ERA-40 data, (b) 20C simulation, (c) A1B scenario, and (d) UCM.

3.2 Correlations

The analyses of variability in CAPE and CIN and their origin lead automatically to the question whether temperature and humidity in the mixed layer respectively boundary layer or in the free troposphere have a stronger influence on the development of CAPE and CIN. The strength of impact of the boundary layer or the free troposphere depends on the latitude. Holloway and Neelin (2009) report that buoyancy is correlated to the free tropospheric humidity in the tropics. Khodayar et al. (2010) and Zhang (2002) identify the boundary layer as the main contributor in developing CAPE and CIN in the Northern hemispheric mid-latitudes. In this section, global distributions of CAPE and CIN respectively are correlated with those of T_{ML}, q_{ML}, H, and LPW to further investigate the question of the influence. An additional correlation between CAPE and CIN respectively with surface pressure is determined.
Spearman rank correlations are applied to all data sets, due to the non-stationarity of CAPE and CIN (Riemann-Campe et al., 2009; Riemann-Campe et al., 2010). Before ranking the data, a trend is subtracted which is assumed to be linear in a first approximation. The correlation is applied to yearly and seasonal mean values. The different lengths of the data sets lead to different absolute values of where the correlation coefficient ρ is significant at the 95 % level. For the ERA-40 data, the correlation coefficient $\rho \geq 0.4$, for the UCM $\rho \geq 0.3$ and for the 20C and the A1B simulation $\rho \geq 0.2$ are significant. Correlations in CAPE and CIN are discussed only in those regions where CAPE $> 0\ Jkg^{-1}$ occurs at least ten times within an average year (For each grid point the total number of days with CAPE $> 0\ Jkg^{-1}$ is determined and divided by the number of years.). All other regions, which are mostly located in the polar regions, are left out and marked by black shadings in the figures.

Surface pressure: The global distribution of yearly surface pressure correlated with yearly CAPE shows mostly negative correlation coefficients (Fig. 3.7). CAPE develops preferentially in low pressure regions. Positive correlation coefficients occur over the coastline of Antarctica, over Northern parts of the Indian Ocean and over regions of the midlatitudinal Atlantic. Most of the previously mentioned regions consist of positive correlation coefficients only in the ERA-40 data and not in the 20C simulation. However, regions with positive correlations increase in the A1B scenario and occur in areas similar to those from the ERA-40 analysis, e.g. the Northern Indian Ocean. In contrast, the analyses reveal continental regions with positive correlations in the ERA-40 analysis which are neither reproduced in the 20C simulation nor in the A1B scenario, e.g. over Australia.
In general, the pattern changes only slightly in the warmer scenario. However, the pattern differs strongly in comparison with those from the UCM, where the regions with the positive correlation coefficients are even less pronounced. Highest negative correlations occur in the UCM over the midlatitudinal ocean basins which are concurrent with the trajectories of synoptic disturbances. In contrast, largest magnitudes of ρ occur along the ITCZ in the 20C and A1B simulations. The distribution of the correlation coefficients between yearly surface pressure and yearly CIN (Fig. 3.7 (2)) shows a similar spread of positive and negative correlation coefficients in the ERA-40 data. In contrast, the regions with negative correlations outbalance those with positive correlations in the ECHAM5 simulations. All data sets agree on mostly positive coefficients over the tropical Atlantic and the Indian Ocean. Largest values of positive ρ occur in the tropical Pacific along two

thin lines over the double ITCZ pattern in the tropical Pacific in the 20C and the A1B simulations. Note the high values of negative correlations in between.

Mixed layer temperature: The distribution of the correlation between yearly T_{ML} and yearly CAPE and CIN respectively (Fig. 3.8) reveals mostly positive correlation coefficients. The correlation with CAPE shows regions with negative correlations south of Greenland and over the Southern Ocean where polar lows develop (Blechschmidt et al., 2009 and Carleton and Carpenter, 1990). Polar lows are relatively cold and develop high magnitudes of CAPE relative to their environment. These regions are far less pronounced in the 20C and the A1B simulations. However, they occur in the UCM run. In contrast to the ERA-40 data set, the 20C and the A1B simulations reveal positive correlation coefficients along the coast of Antarctica, which resemble the correlation pattern of CAPE and SAM (Southern Annular Mode, chapter 6). Strongest values of positive correlations occur along the equator and the ITCZ and also over the midlatitudinal Atlantic. The correlation pattern of T_{ML} and CIN do not reveal the negative correlation coefficients in the polar low regions due to the effect, that CIN is generally low in polar lows. Nevertheless, some regions over the Southern Ocean reveal a negative correlation. More prominent are the negative coefficients along the equator and over the Pacific double ITCZ pattern.

Mixed layer specific humidity: The correlation pattern of q_{ML} and CAPE and CIN respectively resemble those of T_{ML} roughly (Fig. 3.9). The regions with positive correlations are stronger pronounced in terms of spread and magnitude. Almost every region shows a positive correlation. The few exceptions with negative correlations are located in regions where polar lows occur. The pattern of q_{ML} and CIN reveals mostly negative coefficients in the tropical regions especially along the equator. Small values of humidity lead to high LCL heights and thus to a deep layer of CIN.

Enthalpy: The correlation pattern of yearly H and CAPE and CIN respectively resemble those pattern discussed in the teleconnection chapter (Chapter 6). Large values of positive correlations occur along the equator adjacent to regions with large values of negative correlations. This pattern resembles the correlation pattern between CAPE and ENSO, respectively CAPE and CIN (compare Fig. 3.10 with Fig. 6.2). Moreover, this pattern is not present in the UCM run, which does not consist of an ENSO cycle. However, the sign of the correlation coefficients over the Southern Ocean are directly opposed to those from the correlation of CAPE and SAM (Fig. 6.6). The fact that the negative correlation coefficients are also present in the UCM run which does not include cycles such as SAM contradict the influence of SAM.

Latent heat equivalent precipitable water: The pattern of yearly LPW and CAPE, and CIN respectively is very similar to the correlation pattern of q_{ML} and CAPE, and CIN respectively (Fig. 3.11). One difference is the stronger pronounced negative correlation in the Southern Ocean and south of Greenland in the 20C and the A1B simulations.

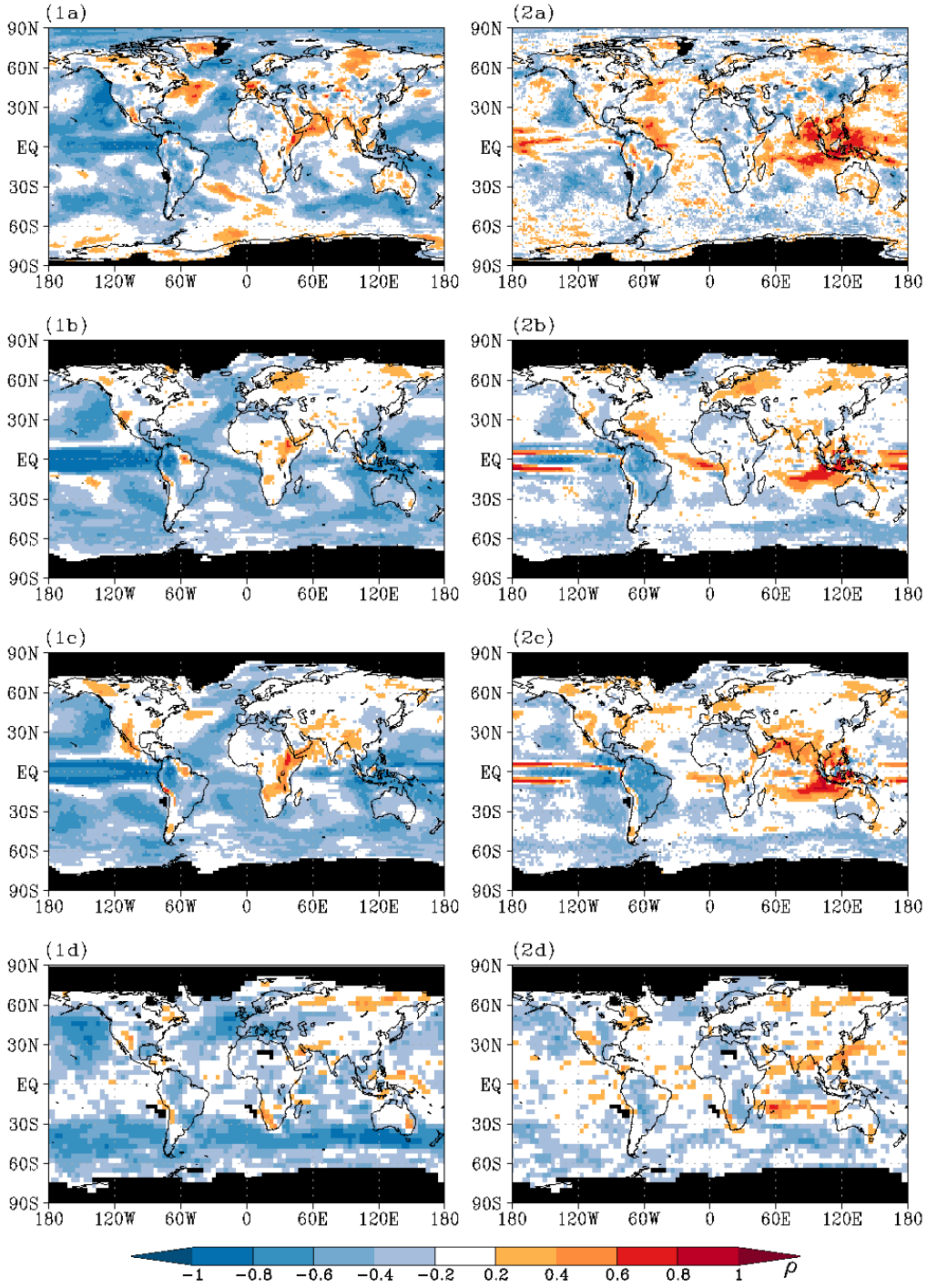

Figure 3.7— Correlation coefficient ρ of surface pressure and (1) CAPE, and (2) CIN respectively computed from yearly means of the (a) ERA-40 data, (b) the 20C simulation, (c) the A1B scenario and (d) the UCM run. The different lengths of the data sets lead to different absolute values of where the correlation coefficient ρ is significant at the 95 % level. For the ERA-40 data $\rho \geq 0.4$, for the UCM $\rho \geq 0.3$ and for the 20C and the A1B simulation $\rho \geq 0.2$ to be significant. The black shading marks those regions with CAPE $>$ 0 Jkg^{-1} occurring less than 10 times during an average year.

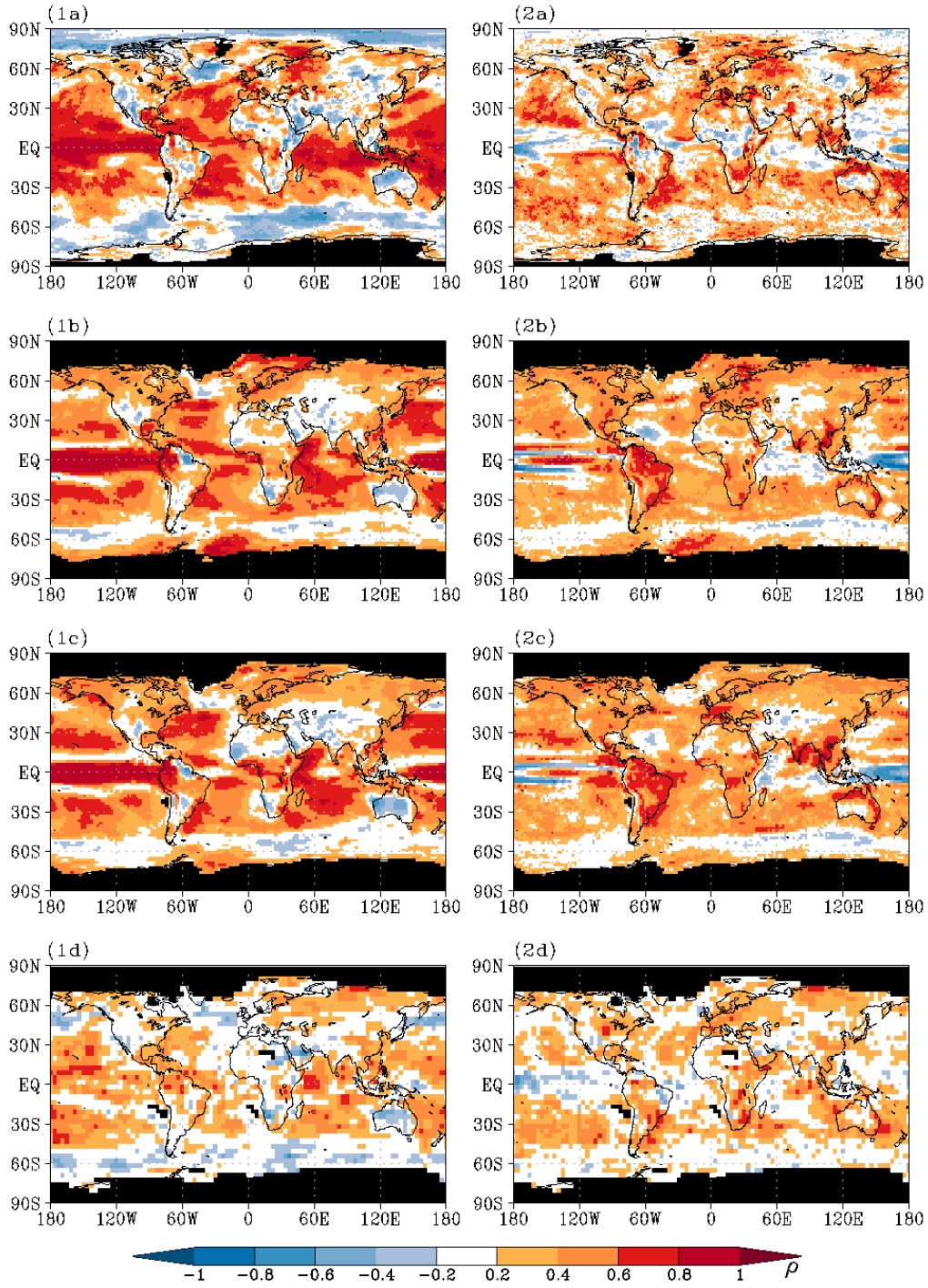

Figure 3.8— Correlation coefficient ρ of T_{ML} and (1) CAPE, and (2) CIN respectively computed from yearly means of the (a) ERA-40 data, (b) the 20C simulation, (c) the A1B scenario and (d) the UCM run. The different lengths of the data sets lead to different absolute values of where the correlation coefficient ρ is significant at the 95 % level. For the ERA-40 data $\rho \geq 0.4$, for the UCM $\rho \geq 0.3$ and for the 20C and the A1B simulation $\rho \geq 0.2$ to be significant. The black shading marks those regions with CAPE > 0 Jkg^{-1} occurring less than 10 times during an average year.

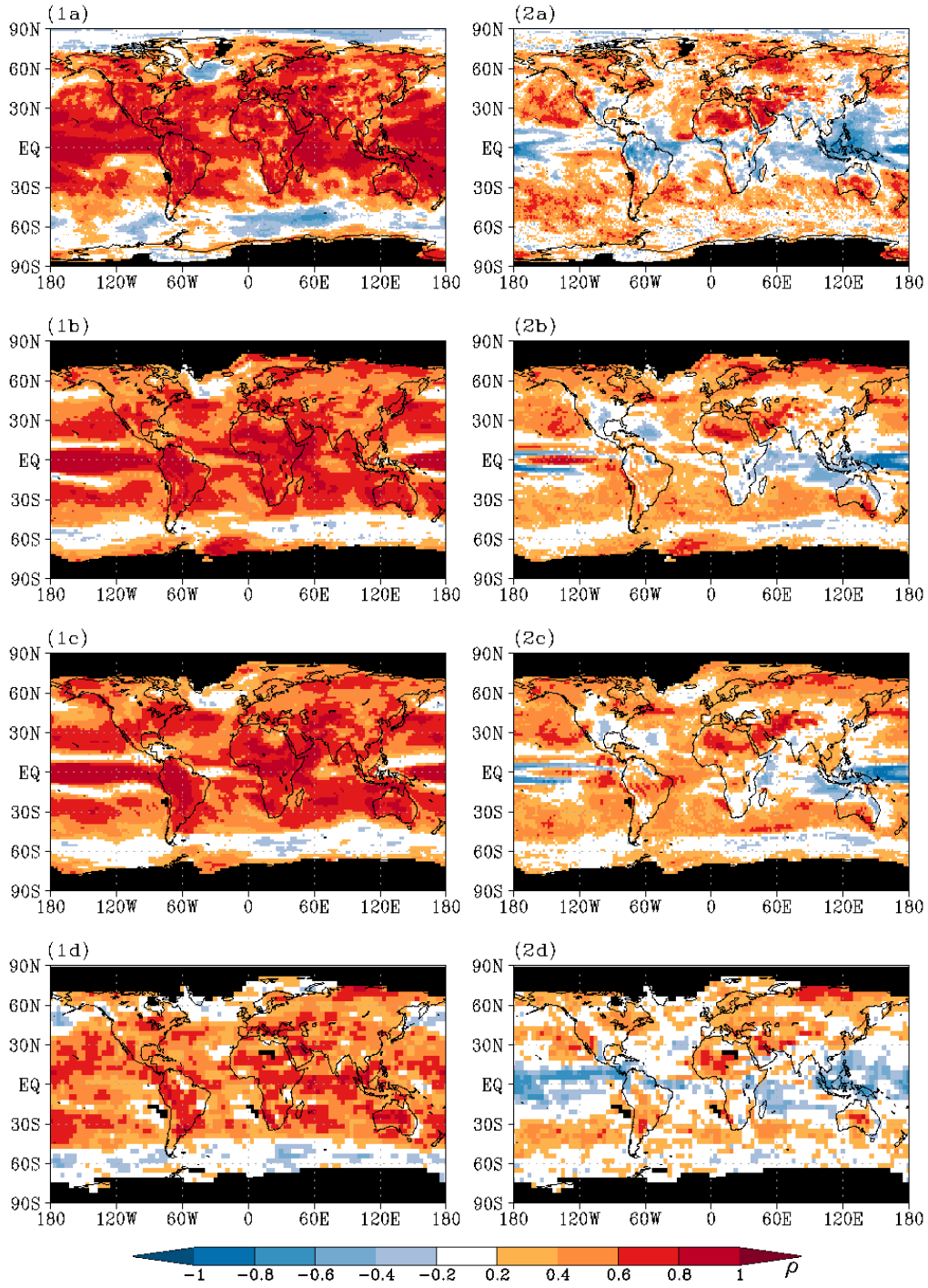

Figure 3.9— Correlation coefficient ρ of q_{ML} and (1) CAPE, and (2) CIN respectively computed from yearly means of the (a) ERA-40 data, (b) the 20C simulation, (c) the A1B scenario and (d) the UCM run. The different lengths of the data sets lead to different absolute values of where the correlation coefficient ρ is significant at the 95 % level. For the ERA-40 data $\rho \geq 0.4$, for the UCM $\rho \geq 0.3$ and for the 20C and the A1B simulation $\rho \geq 0.2$ to be significant. The black shading marks those regions with CAPE > 0 Jkg^{-1} occurring less than 10 times during an average year.

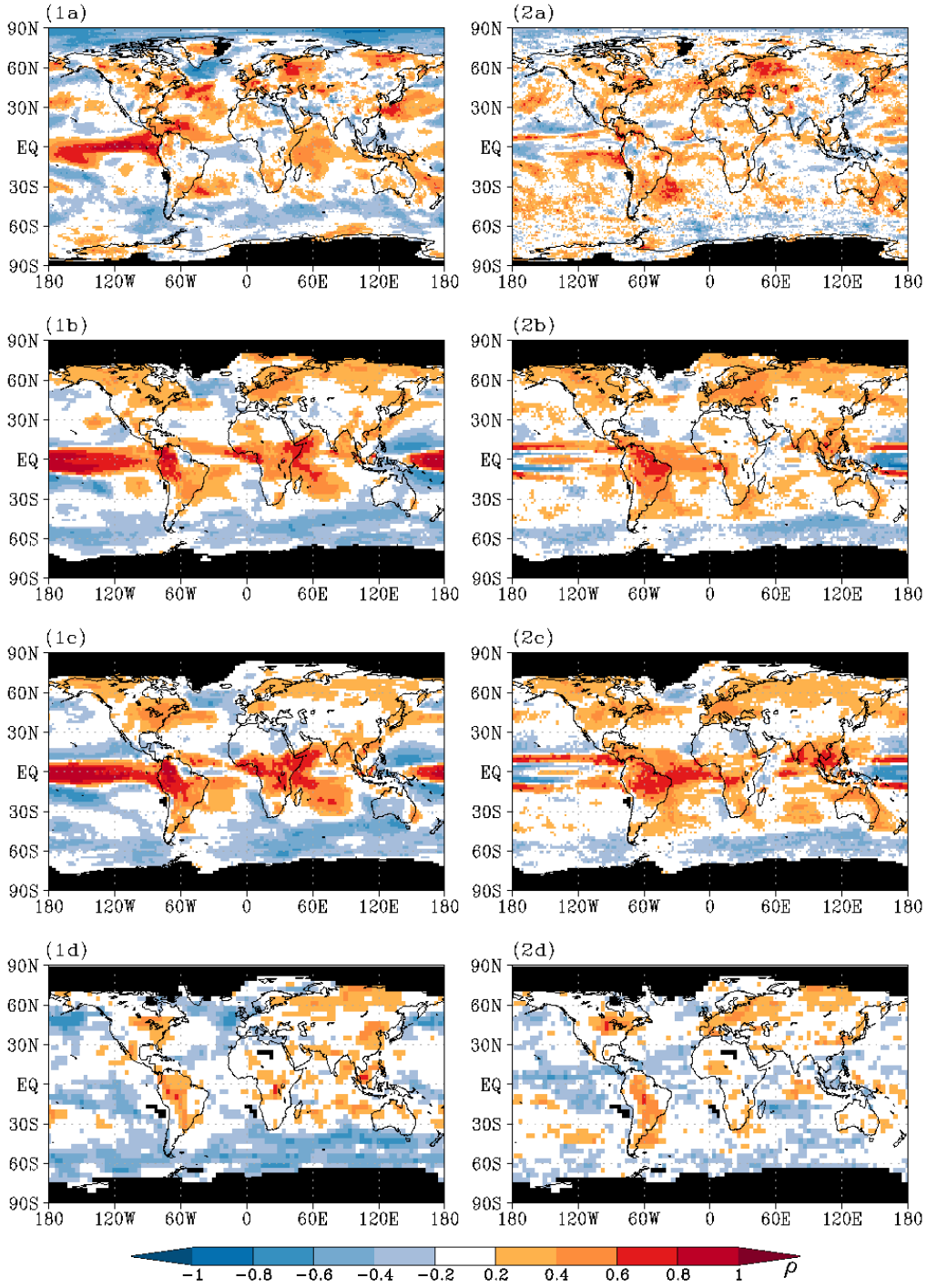

Figure 3.10— Correlation coefficient ρ of H and (1) CAPE, and (2) CIN respectively computed from yearly means of the (a) ERA-40 data, (b) the 20C simulation, (c) the A1B scenario and (d) the UCM run. The different lengths of the data sets lead to different absolute values of where the correlation coefficient ρ is significant at the 95 % level. For the ERA-40 data $\rho \geq 0.4$, for the UCM $\rho \geq 0.3$ and for the 20C and the A1B simulation $\rho \geq 0.2$ to be significant. The black shading marks those regions with CAPE > 0 Jkg^{-1} occurring less than 10 times during an average year.

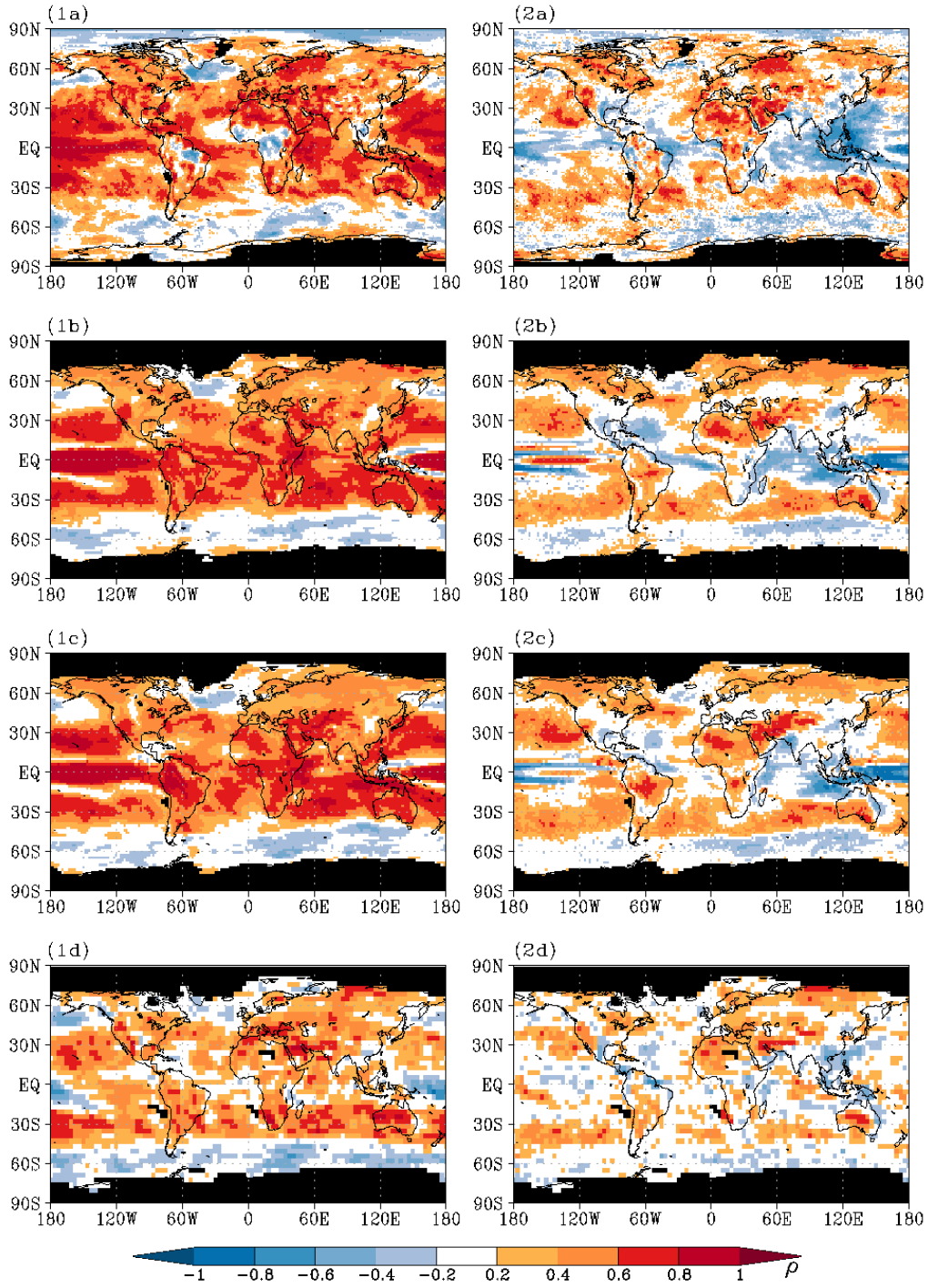

Figure 3.11— Correlation coefficient ρ of LPW and (1) CAPE, and (2) CIN respectively computed from yearly means of the (a) ERA-40 data, (b) the 20C simulation, (c) the A1B scenario and (d) the UCM run. The different lengths of the data sets lead to different absolute values of where the correlation coefficient ρ is significant at the 95 % level. For the ERA-40 data $\rho \geq 0.4$, for the UCM $\rho \geq 0.3$ and for the 20C and the A1B simulation $\rho \geq 0.2$ to be significant. The black shading marks those regions with CAPE > 0 Jkg^{-1} occurring less than 10 times during an average year.

3.3 Summary and conclusions

In this chapter, the global mean distributions of CAPE, CIN, temperature and humidity within the ML and above are shown in an observed and simulated present-day climates, a possible future climate and a simulation with climatological SST. The main findings in this chapter are:

- The strongest differences between the observed and simulated present-day climates lie in the tropical humidity distributions, which lead to the differences in CAPE and in CIN from observed and simulated data.
- The mean distributions of CAPE and CIN reveal the interaction with the Hadley Cell. The ascending branch of the Hadley Cell is visible in the tropical maxima of CAPE along the ITCZ, whereas the descending branch of the Hadley cell is expressed by the maxima in mean CIN around 30° latitude.
- The residual standard deviation of CIN reveals that in some regions its variability is higher than its mean value.
- The distributions of the mean and residual standard deviation show increasing magnitudes in the warmer climate, which are strongest pronounced in the tropical regions.
- The magnitudes of mean and standard deviation CAPE are considerably smaller in the UCM than in the other data sets. However, the mean and standard deviation of CIN remain similar in all data sets. Therefore, the ocean has a much stronger influence on the magnitudes of CAPE than on CIN.
- In the polar regions, the influence of polar low activity causes the negative correlations between temperature and CAPE, respectively humidity and CAPE. The pattern of humidity distributions resemble those patterns visible in CAPE. These similarities are more pronounced than between temperature and CAPE.
- Furthermore, the correlation analyses reveal higher correlation coefficients over a wider area when CAPE is correlated with humidity than when it is correlated with temperature.
- The coefficients seem similarly with regard to magnitude and spread in humidity within the ML and above. Therefore, the findings of Zhang (2002) and Khodayar et al. (2010) can only be partially confirmed. The strong influence of the lower atmosphere is clearly visible. However, the contribution of the free troposphere is not much smaller. The comparison of the findings of Holloway and Neelin (2009) with those from this chapter leads to the same conclusion. The strong influence of the free tropospheric humidity on CAPE is distinctive. However, it is not distinguishable from the ML humidity or temperature. Note that the findings of the previously mentioned publications are mostly based on observational data covering a small region. Thus, small regional features influencing the distributions of temperature and humidity may not be resolved in a global GCM output.

Chapter 4

Trends in CAPE and CIN in a warmer climate

This chapter focuses on the change of the global distributions of CAPE and CIN in a possible future climate scenario. The future is simulated by the ECHAM5/MPI-OM applying the A1B scenario, which is one of several scenarios developed and analysed for the IPCC fourth assessment report AR4 (Bernstein et al., 2007). The changes in the warmer climate are examined relative to the distributions in the 20C simulation. The mean of a time slice from the 20C simulation is subtracted from the mean of a time slice of the A1B scenario. For the reason of comparison, the time slices are chosen according to those for the estimation of changes in a warmer climate in the AR4. The A1B time slice covers the time period 2090-2099 and is compared to the 20C time slice which covers the period 1980-1999. The ratio of change relative to the mean of the 20C time slice is determined by dividing the difference of the time slices by the mean of the 20C time slice. The result is multiplied by 100 to receive the unit percent.

$$\text{ratio of change} = \frac{\overline{(2090-2099)} - \overline{(1980-1999)}}{\overline{(1980-1999)}} \cdot 100 \tag{4.1}$$

The overline indicates the mean taken over the according time slice.
The ratio of change is computed from different percentiles (5th, 20th, 40th, 60th, 80th, 95th) of the variables to investigate whether the changes occur similarly for large (80th and 95th percentile), intermediate (40th and 60th percentile) and small values (5th and 20th percentile). In addition, changes in CAPE are computed on those time steps when CIN is large (CIN $\geq$ 100 Jkg^{-1}). Thus, the stability in the lower atmosphere would probably prevent the CAPE to develop convection. Furthermore, changes in CAPE are investigated when CIN is small (CIN $<$ 20 Jkg^{-1}) and convection is very likely to happen. Changes in CAPE and CIN are discussed only in those regions where CAPE > 0 Jkg^{-1} occurs at least ten times within an average year. All other regions, which are mostly located in the polar regions, are left out and marked by black shadings in the figures.

The analysis of trends in CAPE has been subject to several regional studies: e.g. Gettelmann et al. (2002) and DeMott and Randall (2004) investigate CAPE computed from observations in

the tropics. While Gettelmann et al. (2002) report about mostly positive trends which are caused by increasing near surface temperature and humidity, DeMott and Randall (2004) find positive as well as negative trends in CAPE which are primarily driven by low-level humidity. In addition, Ye et al. (1998) compare observed with simulated CAPE in the tropics and report that CAPE depends mostly on surface wet bulb potential temperature. Outside the tropics, trends in CAPE are investigated by e.g. Trapp et al. (2007) and Trapp et al. (2009) who compare reference scenarios to several possible future scenarios (A1B and A2) in the USA. According to Trapp et al. (2007) and Trapp et al. (2009) the increase in CAPE is caused by increasing water vapour in the boundary layer. The only known global trend estimation of CAPE and CIN computed from the ERA-40 data is investigated by Riemann-Campe et al. (2009).

4.1 Changes in mean CAPE and CIN

Changes in CAPE and CIN are caused by either changes in temperature and humidity within the parcel, which are determined by the mixed layer (ML, the lowest 100 hPa of the atmosphere) conditions, or by changes of the ambient air properties which also determine the altitude of the LFC and LNB and thus the depth of the CAPE layer. An increase of the depth of the CAPE layer due a lower LCL altitude can be caused by an increase in q_{ML} or a decrease in T_{ML} if the other one remains similar. This lower LCL altitude decreases the depth of the CIN layer. The opposite effect of an higher LCL altitude is caused by a decreasing q_{ML} or an increasing T_{ML} if the other variable does not change simultaneously.
The ratio of change varies in sign and strength with the percentiles, which are roughly grouped in low, intermediate and high percentiles. All percentiles describing the ratio of change in CAPE (Fig. 4.1) have in common that positive trends occur in regions with high Northern latitude and along the equatorial and Northern Pacific and over most continental regions. Negative trends in CAPE occur in all percentiles southeast of Greenland and over most regions of the Southern Hemisphere ocean basins. In contrast, regions with a change of sign in different percentiles are visible over the Northern Atlantic, where the region with the negative trend southeast of Greenland spreads southwards with high percentiles. The tropical ocean basins reveal several regions with negative trends in the low and intermediate percentiles which transform into positive trends in the high percentiles. In the high percentiles, CAPE consists of mostly positive trends over the continents and the Northern hemispheric ocean basins with the exception of the Northern Atlantic, whereas the Southern hemispheric ocean basins are mostly covered by negative trends.
The trend estimation in CIN (Fig. 4.1) shows that the positive trends have not so strong values as seen in CAPE. The strongest values occur in the high percentiles over the ocean basins and Siberia. The magnitudes of the negative trends do not vary much in general. Another feature distinguishing the distributions of trends in CAPE and CIN is the regional discontinuity between regional CIN trends. Very small regions show for instance a strong positive trends which are enclosed by small regions with negative trends which are discontinuous by small regions without a trend larger than 10 %. However, positive trends in CIN occur generally in regions with positive trend in CAPE e.g. the equatorial Pacific, most continental regions and most of the Northern hemispheric ocean basins. Similarly, negative trends in CIN happen mostly in regions where CAPE also consists of negative trends e.g. Southern Hemispheric ocean basins. However, in some regions trends in

CIN and CAPE have opposite signs. Southeast of Greenland occur positive trends in CIN in all percentiles but the 95th, while the trend in CAPE is negative in all percentiles. The opposite effect is visible over the eastern Indian Ocean where low percentiles of CAPE decrease, whereas CIN increases in all percentiles.
The trends estimated in temperature and humidity reveal a different pattern of positive trends than those in CAPE and CIN. Positive trends in temperature in the ML (Fig. 4.1) and above (Fig. 4.1) cover the every region with values an order of magnitude smaller than the trends in CAPE, CIN and humidity. Largest changes in T_{ML} occur in the lower percentiles of the Northern hemispheric polar regions. In general, T_{ML} changes occur more pronounced in the Northern hemisphere than in the Southern Hemisphere. In contrast, largest changes in H occur over the tropics. However, changes are also more pronounced over the Northern hemisphere. Trends in humidity within the ML (Fig. 4.1) and above (Fig. 4.1) show positive trends in most regions. Several regions in the Southern Ocean consist of trends weaker than 10 % and are therefore not shown. Largest trends in q_{ML} and LPW occur over the Northern high latitudes in the lower percentiles. In addition, q_{ML} reveals positive trends with similar strength along the coast of Antarctica in the lower percentiles, while strong trends in LPW also occur over the equatorial Pacific. The comparison of the pattern of the positive trends leads to the conclusion that the pattern of humidity, especially of LPW reflect best those of the increase in CAPE and CIN. The increase in temperature has certainly also an effect on the trends in CAPE and CIN. Nevertheless, those seem less pronounced than the impact of humidity.
However, the question arises what causes the decreases in CAPE and CIN. Some regions over the Southern Ocean reveal an increase in T_{ML} while q remains similar, which leads to a decrease in LCL height. The change of the LCL height is one explanation of the decrease in CIN in this region. However, this explanation holds not true for the decrease in CAPE. Chapter 6 focus on the influence of teleconnections and the mean meridional circulation which are able to explain most of the negative trends in CAPE and CIN.

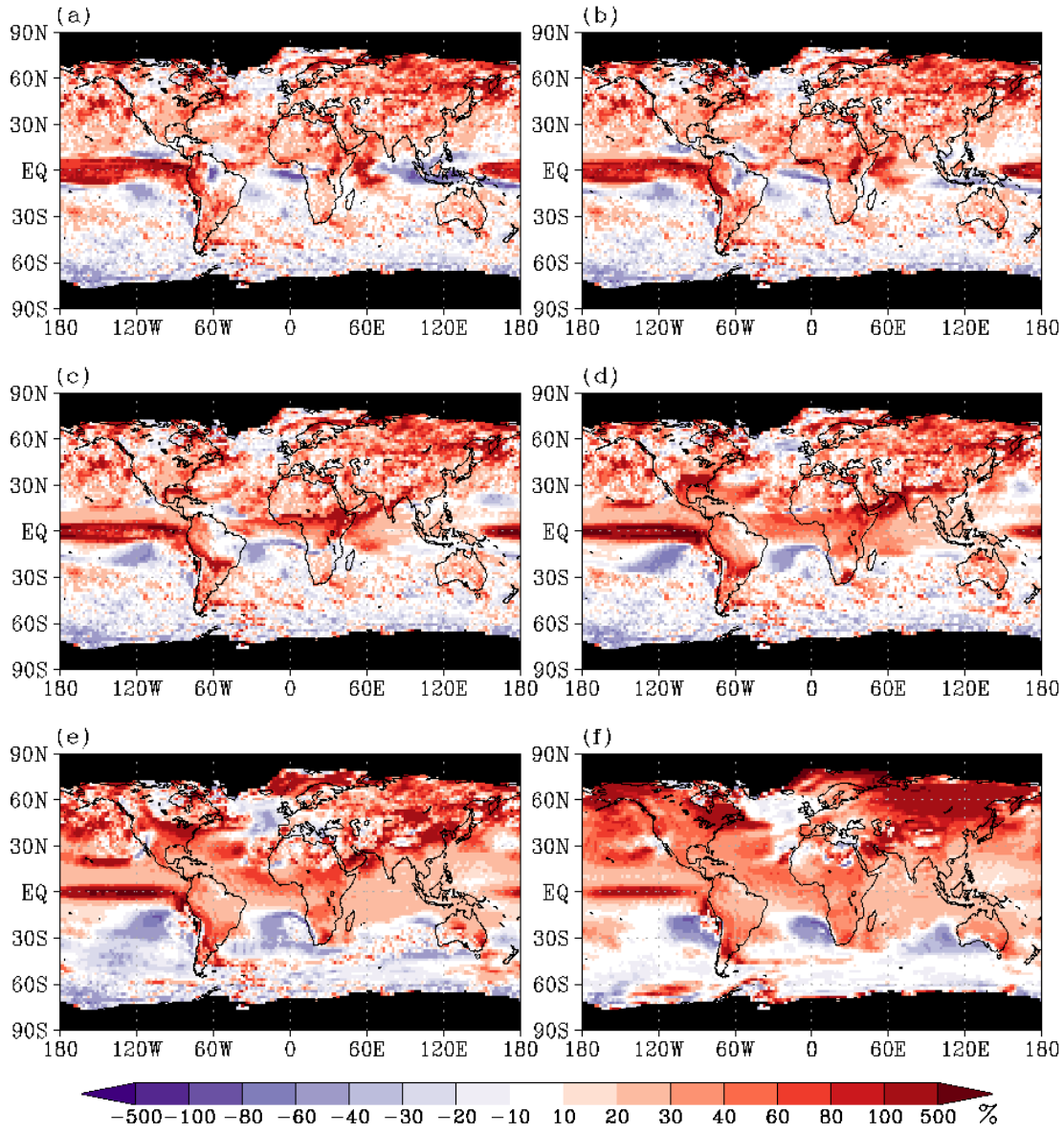

Figure 4.1— Ratio of change in % in CAPE between the A1B scenario (2090-2099) and the 20C simulation (1980-1999) for different percentiles: (a) 5th, (b) 20th, (c) 40th, (d) 60th, (e) 80th, (f) 95th. The black shading marks those regions with CAPE > 0 Jkg^{-1} occurring less than 10 times during an average year.

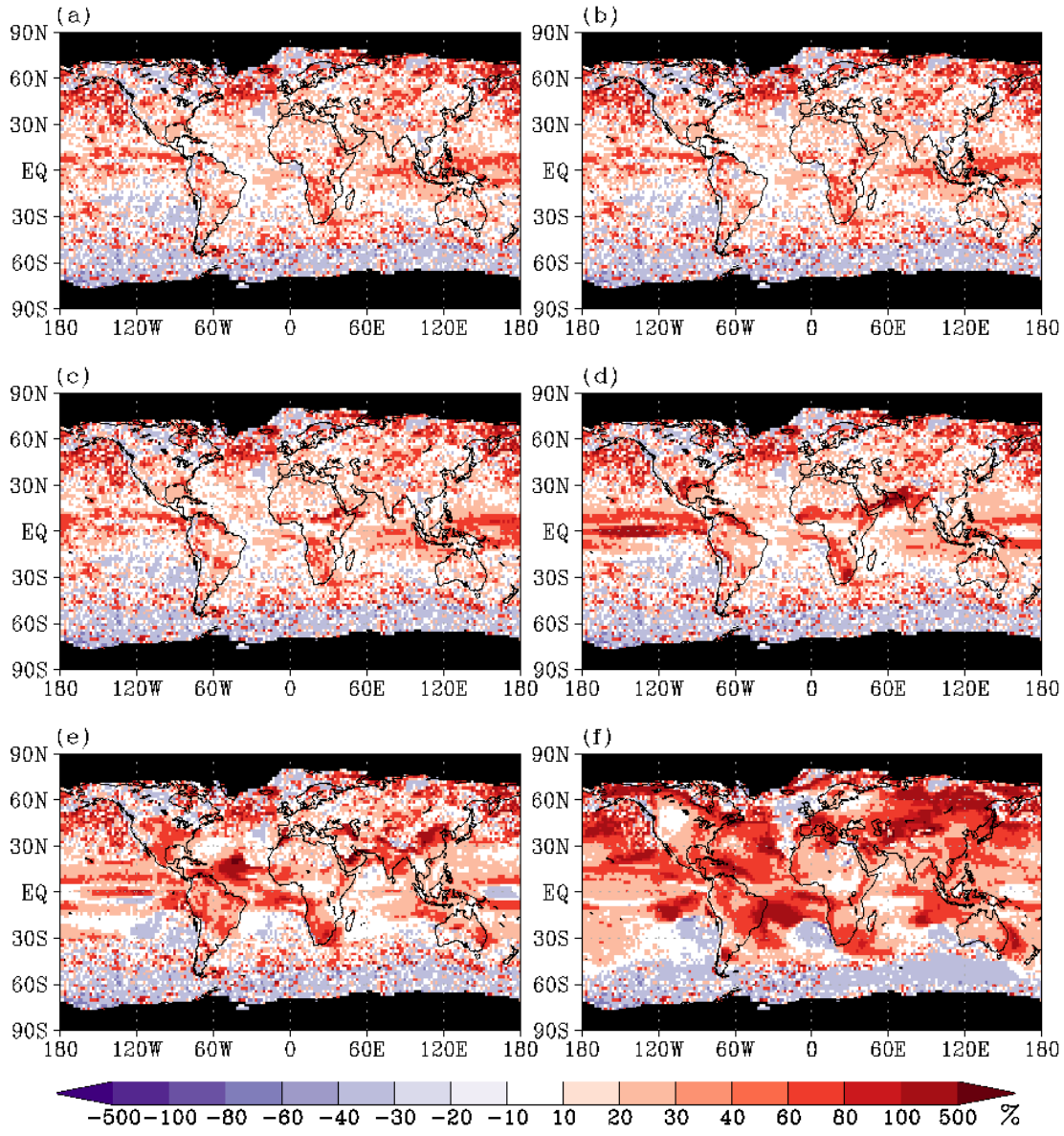

Figure 4.2— Ratio of change in % in CIN between the A1B scenario (2090-2099) and the 20C simulation (1980-1999) for different percentiles: (a) 5th, (b) 20th, (c) 40th, (d) 60th, (e) 80th, (f) 95th. The black shading marks those regions with CAPE > 0 Jkg^{-1} occurring less than 10 times during an average year.

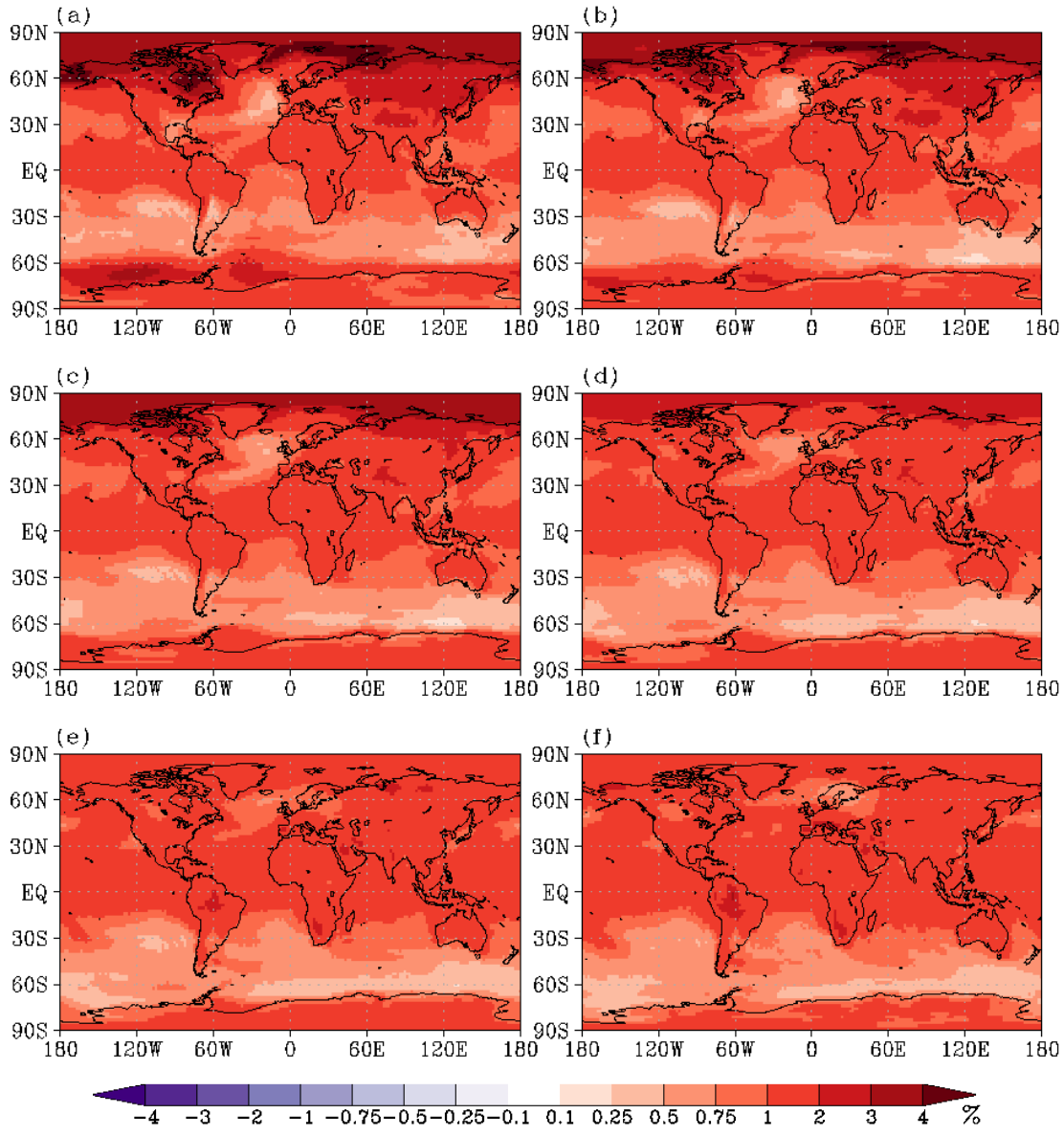

Figure 4.3— Ratio of change in % in T_{ML} between the A1B scenario (2090-2099) and the 20C simulation (1980-1999) for different percentiles: (a) 5th, (b) 20th, (c) 40th, (d) 60th, (e) 80th, (f) 95th. The black shading marks those regions with CAPE > 0 Jkg^{-1} occurring less than 10 times during an average year.

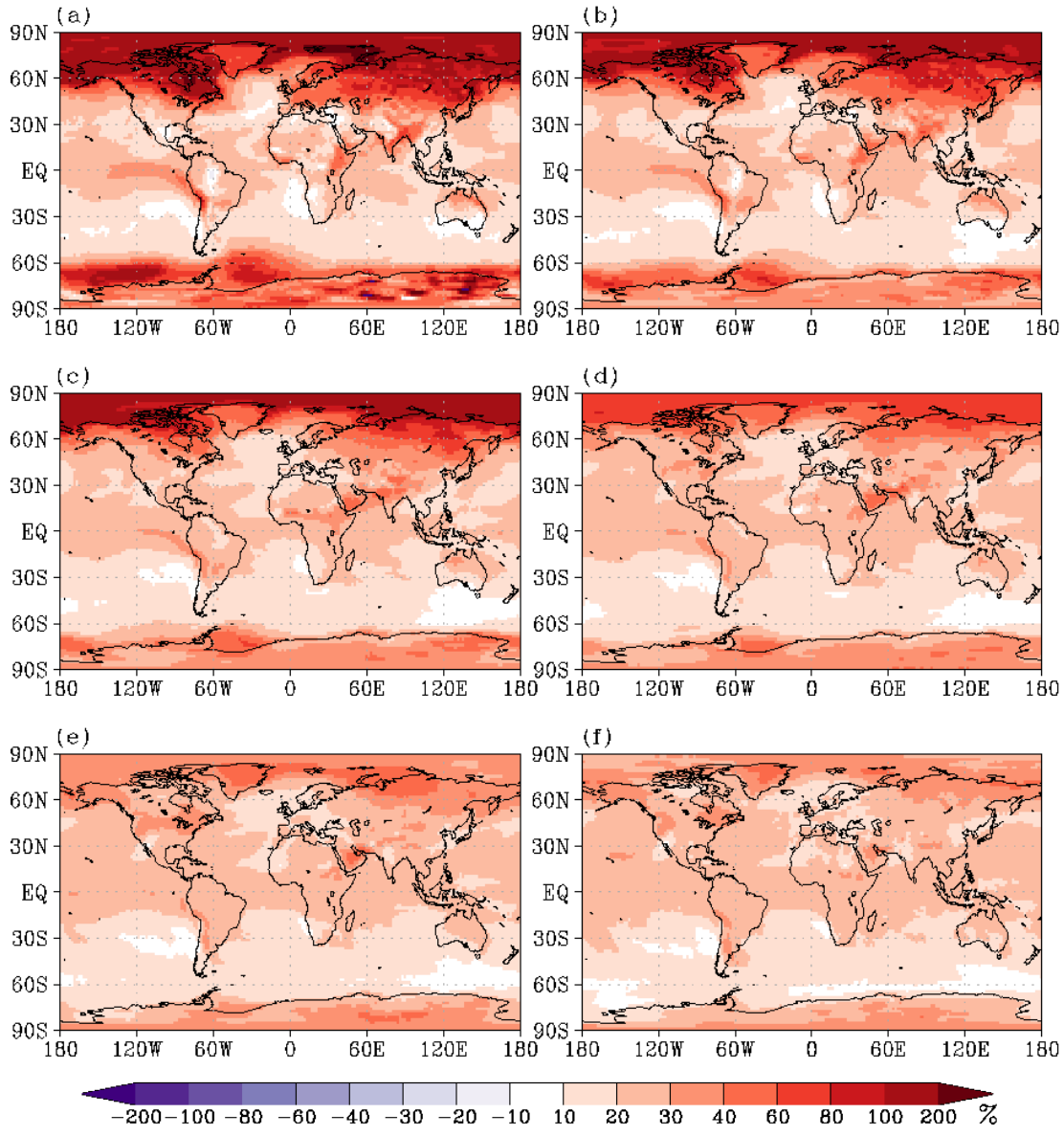

Figure 4.4— Ratio of change in % in q_{ML} between the A1B scenario (2090-2099) and the 20C simulation (1980-1999) for different percentiles: (a) 5th, (b) 20th, (c) 40th, (d) 60th, (e) 80th, (f) 95th. The black shading marks those regions with CAPE > 0 Jkg^{-1} occurring less than 10 times during an average year.

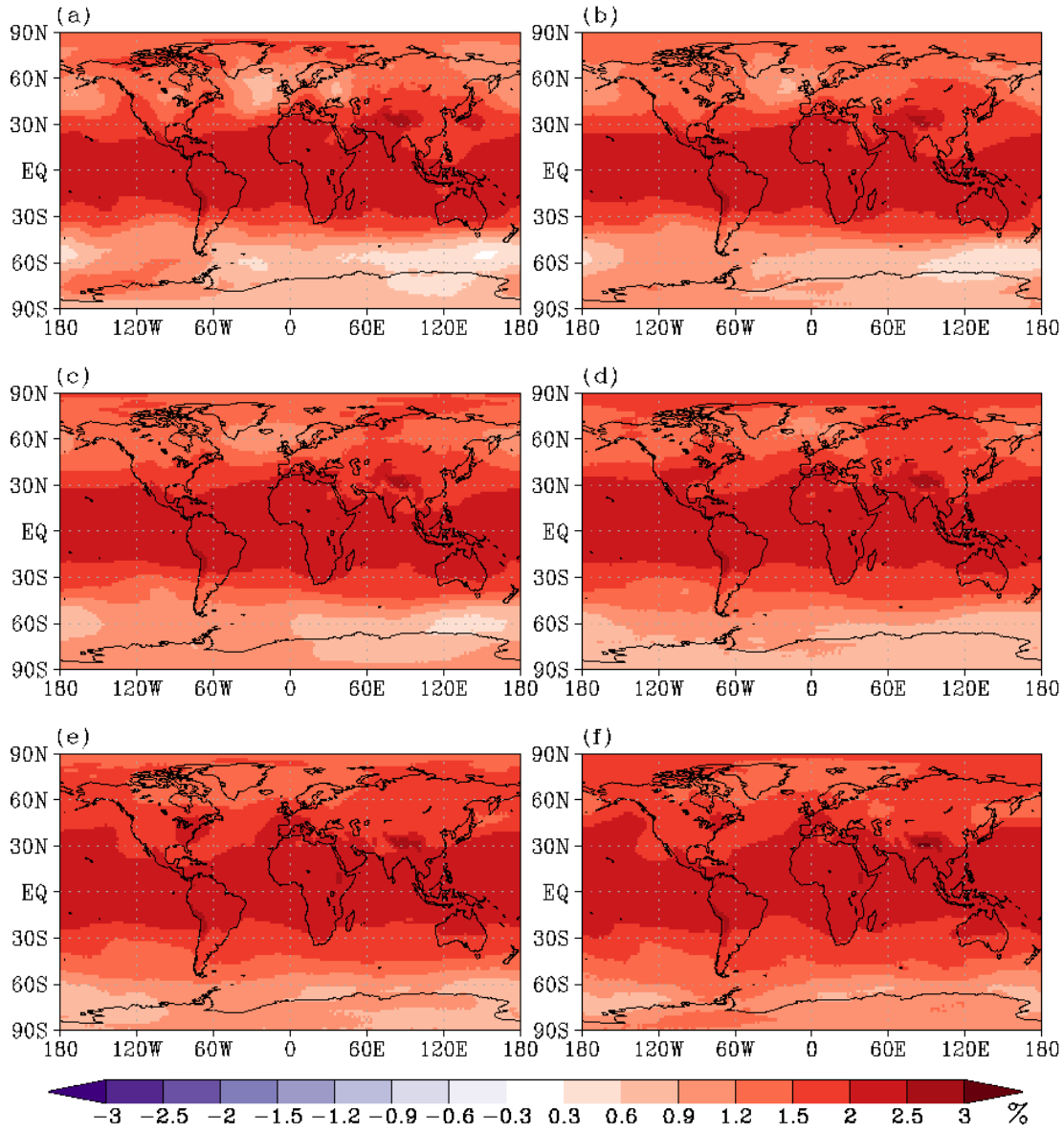

Figure 4.5— Ratio of change in % in H between the A1B scenario (2090-2099) and the 20C simulation (1980-1999) for different percentiles: (a) 5th, (b) 20th, (c) 40th, (d) 60th, (e) 80th, (f) 95th. The black shading marks those regions with CAPE > 0 Jkg^{-1} occurring less than 10 times during an average year.

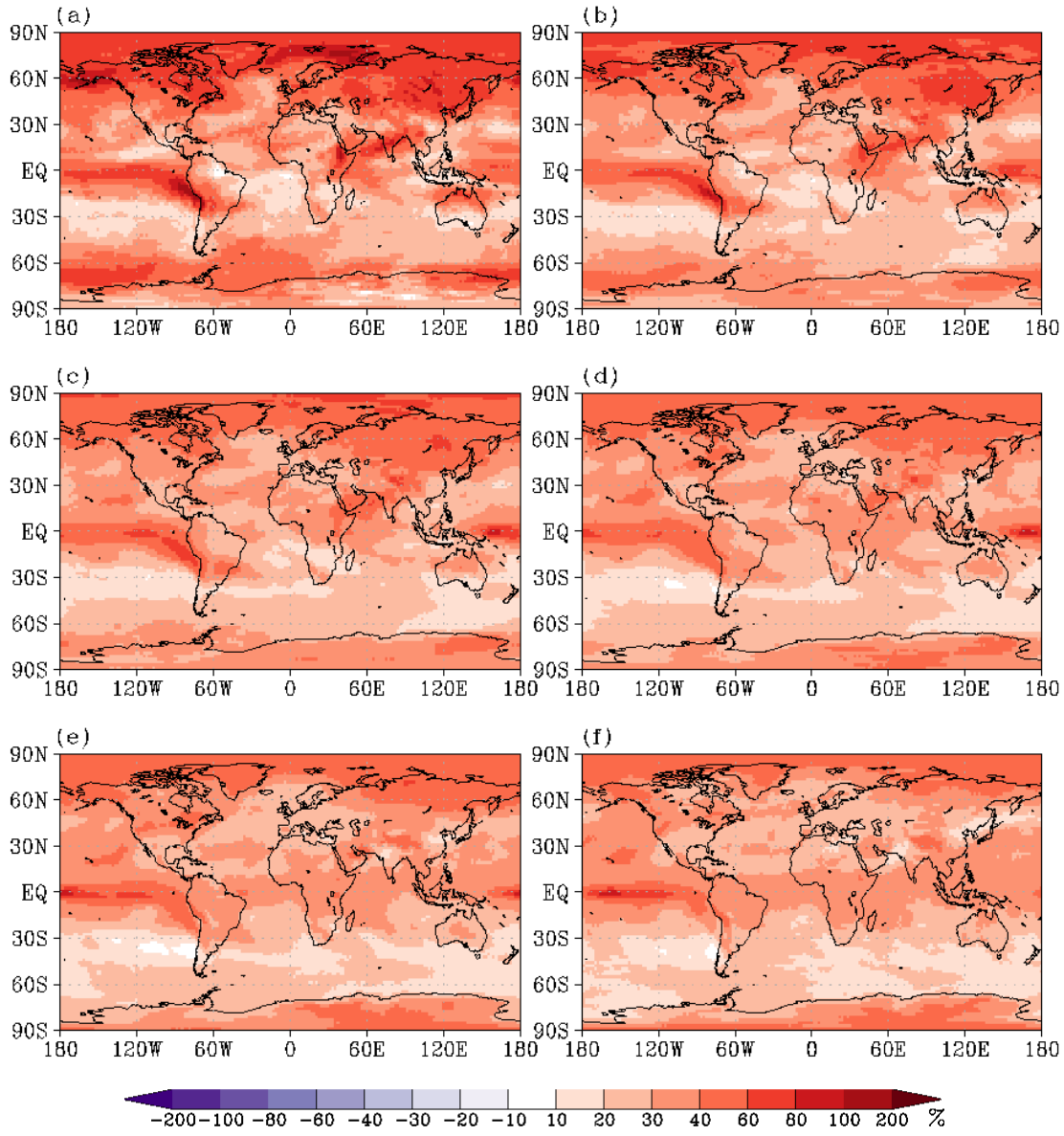

Figure 4.6— Ratio of change in $\%$ in LPW between the A1B scenario (2090-2099) and the 20C simulation (1980-1999) for different percentiles: (a) 5th, (b) 20th, (c) 40th, (d) 60th, (e) 80th, (f) 95th. The black shading marks those regions with CAPE > 0 Jkg^{-1} occurring less than 10 times during an average year.

4.2 Changes in CAPE if CIN is large

The results from the previous section lead to the conclusion that CAPE increases but the development of convection is prevented by increasing CIN. CAPE increases up to 100 % in equatorial regions and at high northern latitudes, especially the high percentiles of CAPE. At the same time the large percentiles of CIN increase in the same regions with a similar ratio. However, these results show that the mean change in CAPE is determined over a time period of several years. It is unclear whether the large magnitudes of CAPE in the warmer climate will happen at the same day or more specifically time of day when CIN is large. The large values of each variable might not happen simultaneously but shifted in time.
Therefore, the trend in CAPE is computed a second time and only those time steps are taken account of if CIN $\geq$ 100 Jkg^{-1}. An upward velocity of $-w \approx 14\ ms^{-1}$ (Eqn. 2.6) is needed to lift the parcel towards the LFC to initiate the development of convection. The trend estimation of CAPE if CIN is large reveals a different pattern compared to those of the previous trends (Fig. 4.3). Negative trends occur in a few regions e.g. west of central South America and west of Australia. Several regions over the Southern Ocean reveal no change larger than 10 %. Most regions show strong positive trends in all percentiles. Thus, the earlier conclusion is confirmed. The increase in CAPE occurs simultaneously with an increase in CIN. The development of convection leading to precipitation is prevented by large values of CIN. However, if convection is initiated, enough potential energy is available to develop severe precipitating storms.

4.3 Changes in CAPE if CIN is small

The boundary layer is generally well mixed, which is expressed by small magnitudes of CIN, especially during the afternoon when large CAPE are most likely. Therefore, the trend estimation of CAPE is determined a third time and only those time steps are considered if CIN $<$ 20 Jkg^{-1}. An upward velocity of $-w \approx 6\ ms^{-1}$ (Eqn. 2.6) is still needed to lift the parcel towards the LFC to initiate convection. The pattern of the trends in CAPE for small CIN resembles the pattern of CAPE if all time steps are considered (Fig. 4.3). Positive trends occur along the equator and above high Northern latitudes, which are visible under all conditions analysed. An increase in CAPE if CIN is small means that the frequency as well as the intensity of convection and thus precipitation in a warmer climate increases. This increase is also present in the so called 'Tornado Alley' in the Central USA, especially in the high percentiles. However, an increase in CAPE leads to more severe weather but not necessarily to a higher potential of tornadoes, which is influenced by other factors too. In contrast to the pattern of trends of CAPE if CIN is large, trends of CAPE at all time steps and if CIN is small show large regions with decreasing CAPE, which are most pronounced in the high percentiles. The negative trends occur over the Northern Atlantic, the Mediterranean Sea and most pronounced over large regions of the Southern hemispheric ocean basins.
Less CAPE leads to smaller potential of convection. However, it will be easier initiated. The frequency of convection probably increases while the amount of convection decreases. One example of a sign change in the percentiles of trends in CAPE if CIN is low occurs in the marine regions around Indonesia. Small magnitudes of CAPE decrease while those of intermediate and high percentiles increase. Thus, the frequency of strong convective events increases. A negative

trend throughout all percentiles is visible southeast of Greenland and over large regions of the Southern Ocean. The strength of Polar Lows decreases. The cause of these negative trends is still not explained by the trends visible in temperature and humidity. They result from the influence of teleconnections and the mean meridional circulation which are discussed in chapter 6.

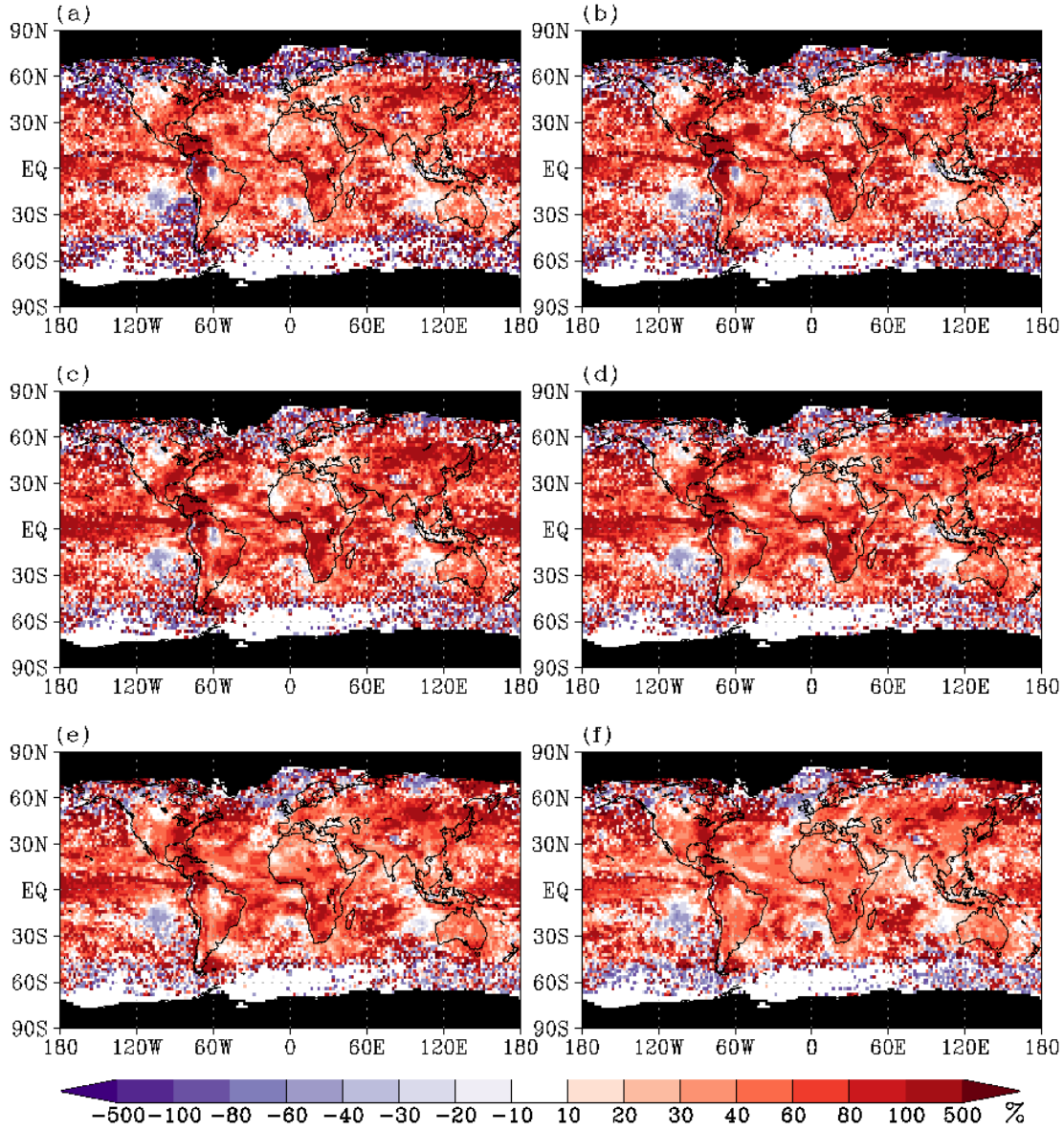

Figure 4.7— Ratio of change in % in CAPE if CIN $\geq$ 100 Jkg^{-1} between the A1B scenario (2090-2099) and the 20C simulation (1980-1999) for different percentiles: (a) 5th, (b) 20th, (c) 40th, (d) 60th, (e) 80th, (f) 95th. The black shading marks those regions with CAPE $>$ 0 Jkg^{-1} occurring less than 10 times during an average year.

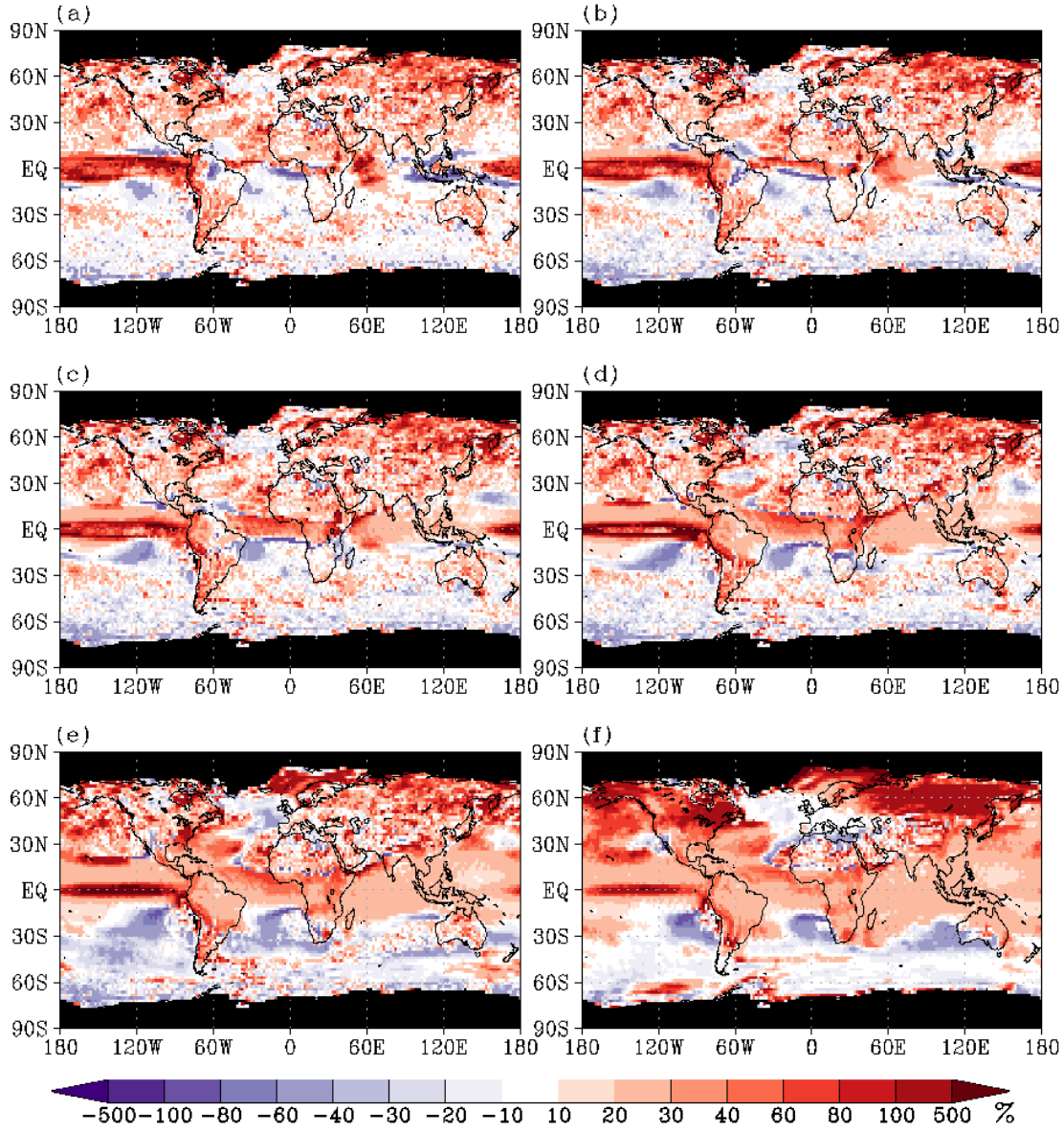

Figure 4.8— Ratio of change in % in CAPE if CIN $< 20\ Jkg^{-1}$ between the A1B scenario (2090-2099) and the 20C simulation (1980-1999) for different percentiles: (a) 5th, (b) 20th, (c) 40th, (d) 60th, (e) 80th, (f) 95th. The black shading marks those regions with CAPE $> 0\ Jkg^{-1}$ occurring less than 10 times during an average year.

4.4 Summary and conclusions

The ratio of change of CAPE and CIN in the A1B scenario relative to the 20C simulation reveals that most regions show an increase in CAPE as well as in CIN. These regions cover most of the continents as well as the northern hemispheric ocean basins. However, large regions over the North Atlantic and the southern hemispheric ocean basins also show negative trends.
Additional trend estimations of CAPE if CIN is large reveal that in most regions CAPE increases strongly if CIN is large, which leads to the conclusion that the frequency of convection probably decreases while the intensity of the convective event increases. More energy is needed to initiate convection. The negative trends in CAPE occur if CIN is small leading to more frequent smaller convective events. An additional study about the distribution of updrafts in a warmer climate would underpin the concluding remark about the frequency of convective events.
The positive trends in CAPE and CIN can be explained by increasing temperature and humidity in almost every region. Those regions which do not consist of a positive trend in temperature and humidity show no change e.g. over the Southern Ocean. The means of temperature and humidity do not decrease. The ratio of change ranges between 0.1 to 3 % for temperature in and above the ML, while those of humidity share the same order of magnitude as the changes in CAPE and CIN, between 10 and 500 %.
The correlation analyses in the previous chapter lead to the conclusion that humidity within and above the ML has a stronger impact on CAPE and CIN than temperature. The pattern of the positive trends analysed in this chapter confirms these findings. Moreover, the reported positive trends in Trapp et al. (2007) and Trapp et al. (2009) in CAPE and humidity in the US are also found here, which support the theory of humidity playing the more pronounced part in CAPE development, too. However, the negative trends in CAPE and CIN can neither be explained by temperature nor humidity. Those trends are the result of large scale impacts such as teleconnections and the mean meridional circulation discussed in chapter 6.

Chapter 5

Long and short term memory in CAPE and CIN

Memory is essential for prediction. It can be defined as the dependency of a time series value on previous values of the same times series. The memory of convective precipitation is relevant for short term and long range prediction. On long time scales convection anomalies affect wetness and droughts, on short time scales severe weather events are relevant for forecasting. In this chapter, the distributions of short term (STM) and long term memory (LTM) on regional and global scales are analysed in observed and simulated present-day climates as well as in a possible future climate. The impact of the ocean is shown by analysing a present-day climate simulation which is uncoupled from a complex ocean model. The ocean is represented by climatological sea surface temperature (SST) distribution (Subsec. 2.1).
CAPE and CIN are variables dependent on temperature and moisture. Therefore, the role of temperature and humidity within and above the mixed layer (ML, the lowest 100 hPa of the atmosphere) on the memory distributions of CAPE and CIN are investigated. Several studies have analysed memory on various time scales in temperature and moisture variables revealing memory pattern over oceans and continents on almost all latitudes (e.g. Fraedrich and Larnder, 1993; Blender and Fraedrich, 2003; Fraedrich and Blender, 2003; Fraedrich et al., 2004). Only a few studies focus on the memory in CAPE and CIN. Zawadski et al. (1994) analyse the persistency in CAPE and helicity on time scales of hours to improve the predictability of precipitation in storms. Yano et al. (2001) investigate the memory in CAPE reporting 1/f scaling over the tropical western Pacific for 30 days. Riemann-Campe et al. (2009) report indications of low frequency variability in CAPE and CIN over tropical and extra-tropical regions, which are confirmed by Riemann-Campe et al. (2010).
The description of the memory analysing methods as well as the results on present-day memory are published in Riemann-Campe et al. (2010). Since the publication of Riemann-Campe et al. (2010), additional data sets have been analysed (idealised model set up, possible future climate) which are discussed here and complement the earlier results.

5.1 Determining memory

In meteorological time series memory can roughly be divided into short-term memory (STM) and long-term memory (LTM) processes, with a threshold often given by the synoptic time scale. In many circumstances, STM processes are adequately simulated by autoregressive (AR) processes. For example, the memory of a first order process, AR(1), can be measured by the finite decay time scale of the exponentially decreasing autocorrelation function (ACF). On longer e.g. inter-annual time scales many climatological time series reveal LTM which is related to increasing variance for decreasing or low frequencies; the ACF does not decay exponentially, inhibits the definition of a decay time scale and the power spectrum increases typically according to a power law, $S(f) \sim f^{-\beta}$ with positive exponents $0 < \beta < 1$. The global distribution of memory on intra- and inter-annual frequency ranges are investigated of CAPE and CIN as well as in temperature and humidity within and above the ML. In addition to the global analysis, the focus is on two grid points in the western equatorial Pacific and the North Atlantic southeast of Greenland. These regions show long memory in previous studies in near surface temperature (e.g. Fraedrich and Blender (2003)). The memory on short time scales in these region is determined by autocorrelation functions, while the memory on longer time scales is investigated by power density spectra and detrended fluctuation analyses of daily values of CAPE, CIN temperature and humidity within and above the ML.

5.1.1 Short- and long-term memory

STM in climate time series is often analysed by AR(1) processes:

$$x_t = \varphi x_{t-\Delta t} + \epsilon_t \tag{5.1}$$

with autocorrelation coefficient (ACC) φ and white noise forcing ϵ_t. The decay time scale τ is given by $\tau = \frac{\Delta t}{(1-\varphi)}$ with the time step Δt. Trends and periodic components, e.g. diurnal and seasonal cycles need to be removed as previous studies have shown that CAPE and CIN are non-stationary (Riemann-Campe et al., 2009) with trends and annual cycles. The decay time scale is computed from daily and monthly mean values of CAPE, CIN, T_{ML}, q_{ML}, H and LPW.

The LTM is investigated by the detrended fluctuation analysis (DFA, Peng et al. (1995)) which provides a method to detect LTM in stationary time series which would not be accessible in an ACF or the power spectrum. To compute DFA the standardised anomalies of a time series $x = x(t)$ are computed by removing the mean annual cycle $\bar{x}$ and dividing by the standard deviation σ_x:

$$x_i = \frac{x - \bar{x}}{\sigma_x} \tag{5.2}$$

Then, the profile y_j of the standardised anomalies x_i, $i = 1, \ldots, N$, of total length N is computed by

$$y_j = \sum_{i=1}^{j} x_i \tag{5.3}$$

The profile is divided into segments of equal length s, which overlap for 50 %. In each segment a polynomial $y\prime_j$ with degree k is fitted to the profile. The degree of the polynomial used is denoted by the version of the DFA, e.g. DFA2 uses polynomials of the second order. The root mean square error is computed by the deviations in the segments resulting in the fluctuation function $F(s)$

$$F(s) = \sqrt{\frac{1}{N}\sum_{j}^{N}(y_j - y\prime_j)^2} \tag{5.4}$$

The fluctuation function is computed repeatedly for varying segment lengths s. For a scaling LTM the fluctuation function is $F(s) \sim s^{\alpha}$ with the Hurst exponent $\alpha \geq 0.5$, which is related to the power spectral exponent $\beta = 2\alpha - 1$. In the presence of linear trends, LTM is determined by DFA2 (Maraun et al., 2004) (note that DFA does not remove trends). If oscillations are superimposed on a LTM signal, the scaling of $F(s)$ is interrupted by an increase of variability on the time scale given by the oscillation. This is typically observed as a saddle point (Fraedrich, 2002). The uncertainty of the DFA exponent is $\alpha \approx 0.05$ and $\beta \approx 0.1$ (Fraedrich and Blender, 2003). Therefore, memory is recognised here if $\alpha \geq 0.55$.

5.2 Regional memory distributions

The focus is on two regions to investigate the memory in greater detail and to deduce its origins. ACF, power spectra, and DFA2 are applied to daily mean values of CAPE and CIN. In addition, daily values of T_{ML}, q_{ML}, H, and LPW are analysed to reveal their relations to CAPE and CIN. A first focus is on the western equatorial Pacific (at $\sim$ 161°E, 0.5°N). Yano et al. (2001) report 1/f scaling in CAPE in this region in a four months long observed data set. The ERA-40 data as well as the simulations reveal whether the 1/f scaling continues further. Furthermore the SST in the tropical Pacific is strongly influenced by ENSO (El Niño/Southern Oscillation) which is expected to affect the memory in CAPE and CIN.
A second region is chosen in the North Atlantic south-east of Greenland (at $\sim$ 41°W, 59°N) where LTM in sea surface temperature (SST) is found by Fraedrich and Blender (2003). Furthermore, Claud et al. (2007) report a relation between the North Atlantic Oscillation (NAO) and polar low development which occurs simultaneously with CAPE development. Thus, the NAO is expected to be related to the memory in CAPE.

5.2.1 Western equatorial Pacific

The ACF in Fig. 5.1 shows memory on short time scales, up to 50 days. The log-log diagram is chosen to reveal power-law like behaviour which shows as a straight line. The ACC is positive for CAPE, T_{ML}, q_{ML}, H and LPW from the ERA-40 data and the 20C simulation. In all variables but CIN the ACC follows almost a straight line with values mostly higher than 0.5 in the 20C simulation, which hints to long memory with power law like behaviour. In contrast, all variables but CIN have also positive ACCs after 50 days which also hints to long memory in the ERA-40 data. However, ACCs are generally lower in ERA-40 data than in the 20C simulation. In addition, the ACCs in the ERA-40 data are not as smooth and do not follow straight lines (Fig. 5.1) and thus

do not indicate power-law like behaviour. The general lower ACCs in the ERA-40 data apply also to CIN, which decrease below 0.1 after 10 days, while it lasts up to almost 50 days when computed from the 20C simulation. The ACF hints to memories on longer time scales in all variables but CIN hint, which cannot be analysed by ACF. Indeed, the power spectra (Fig. 5.2) and DFA2 (Fig. 5.3) reveal memory on longer time scales up to 500 days in the ERA-40 data and the 20C simulation. However, the long memory is visible in CAPE, CIN and the humidity related variables q_{ML} and LPW. The power density spectra are able to capture memory on long as well as on short time scales which is an advantage the DFA does not provide. The spectra reveal much steeper slopes in all variables during the first 10 to 20 days. The temperature related variables T_{ML} and H keep these steep slopes of $\beta \sim 2$ and $\alpha \sim 1.5$ up to 100 days where it decays. Thus, T_{ML} and H show red noise behaviour typical for atmospheric variables. In contrast, the slope in CIN follows a power law with $\beta \sim 1$ and $\alpha \sim 1$ between 10 and 500 days in the ERA-40 data and the 20C simulation.

All variables show a superimposed cycle in the 20C simulation in the fluctuation functions (Fig. 5.3) between 1000 and 2000 days which is also visible in the spectra (Fig. 5.2). In contrast, the superimposed cycle is not as distinctive in the spectra from the ERA-40 data. Although, the slope increases around 2000 days in the fluctuation functions from the ERA-40 data, it is not clear whether it indicates a cycle in the ERA-40 data. As the cycle is indicated by a saddle point, the slope increases and decreases, respectively, within the cycle and thus changes the value of α within the considered frequency range. The period of the cycle between 1000 and 2000 days as well as its location suggests ENSO to be the physical mechanism. van Oldenborgh et al. (2005) reported that ENSO is realistically represented in the 20C simulation. Moreover, the short time series of the analysed ERA-40 data is not an ideal source to analyse ENSO regarding its strength. The long memory in CAPE is caused by large-scale atmospheric flow conditions favouring CAPE development. CIN occurs as often as CAPE in this regions but with lower values.

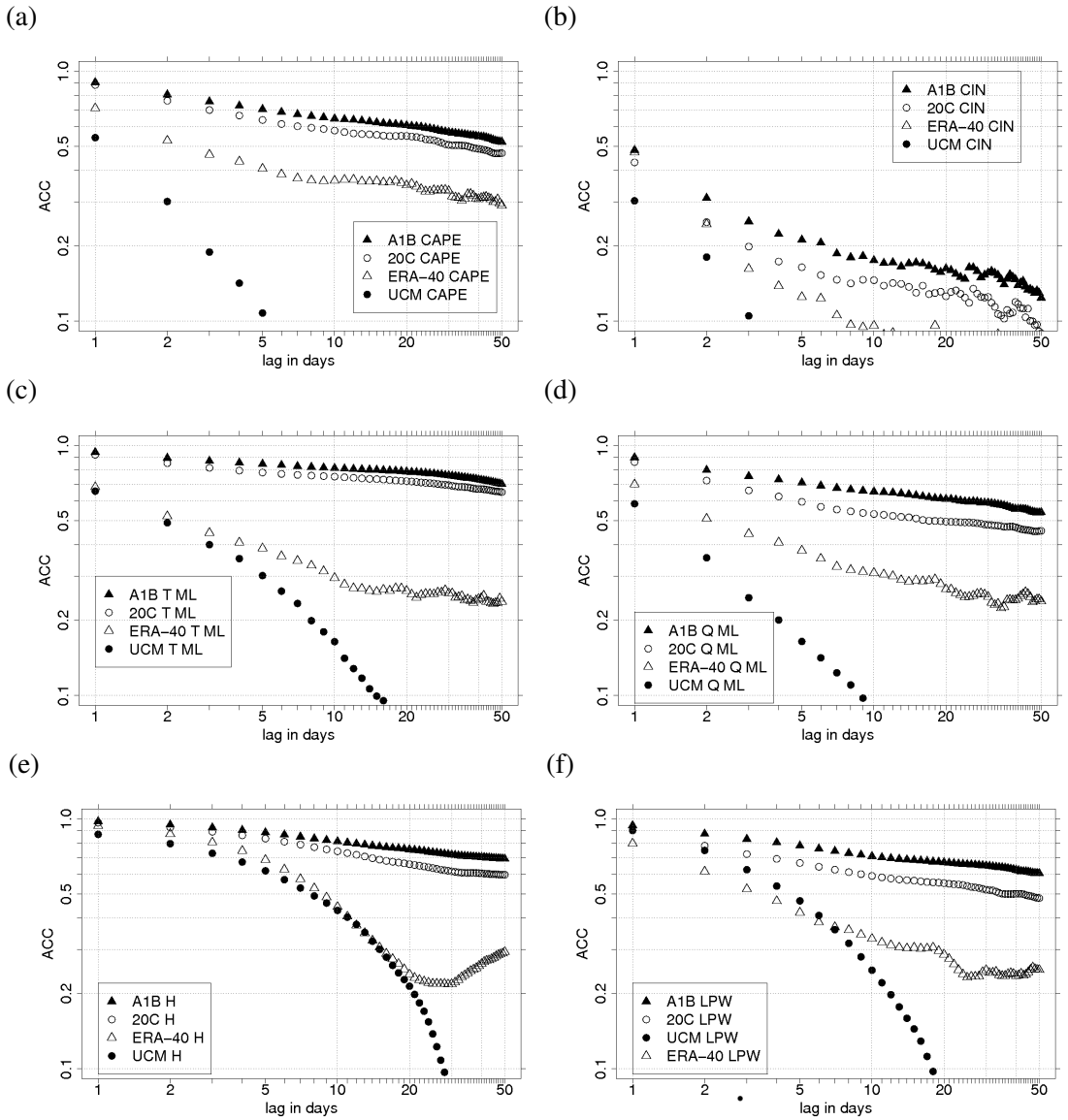

Figure 5.1— Auto correlation function at the equatorial Pacific of (a) CAPE, (b) CIN, (c) T_{ML}, (d) q_{ML}, (e) H, and (f) LPW computed from ERA-40 data (open triangle), the 20C simulation (open circle), the A1B scenario (filled triangle), and the uncoupled model (UCM) simulation (filled circle).

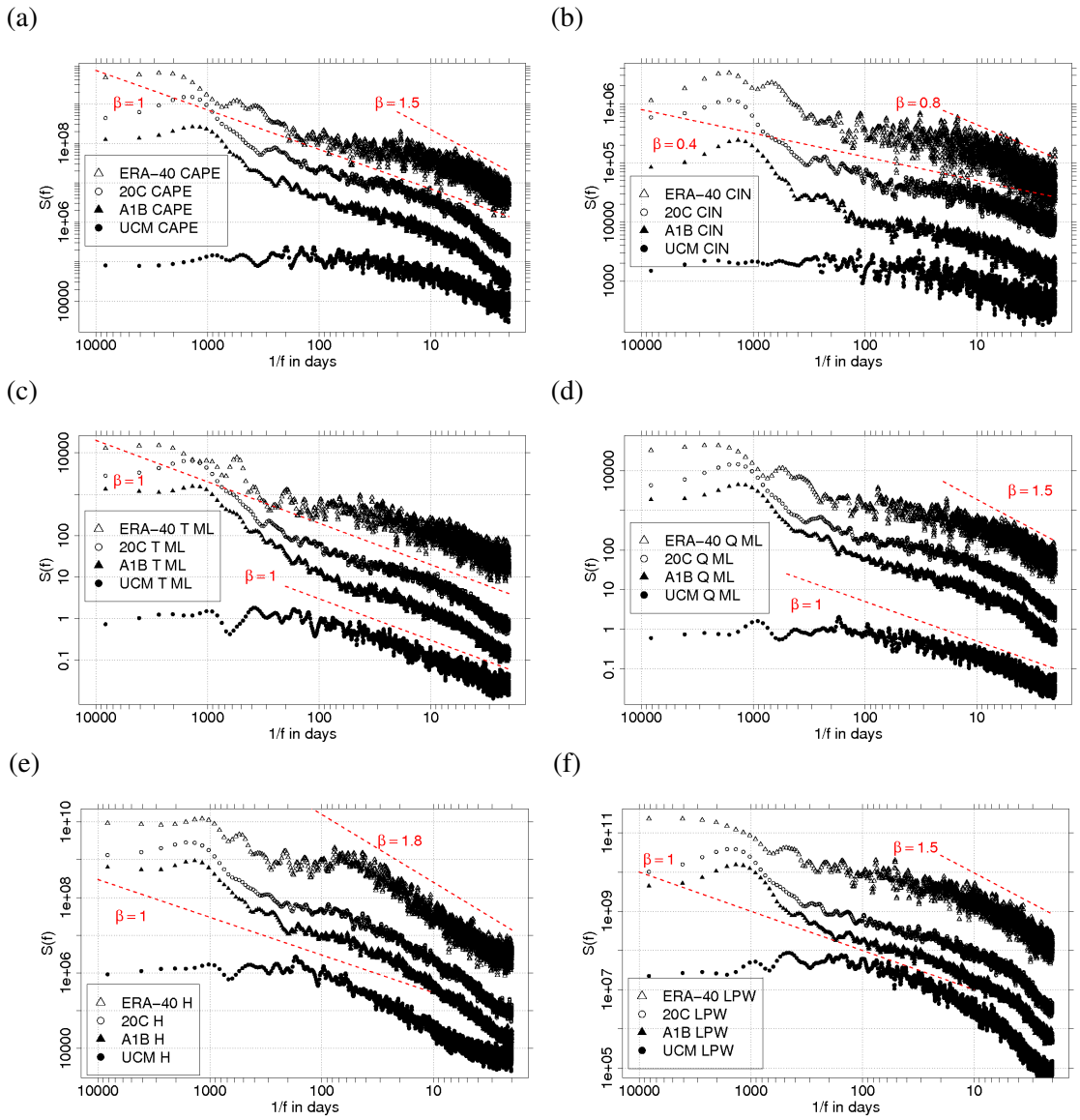

Figure 5.2— Power spectra at the equatorial Pacific of (a) CAPE, (b) CIN, (c) T_{ML}, (d) q_{ML}, (e) H, and (f) LPW computed from ERA-40 data (open triangle), the 20C simulation (open circle), the A1B scenario (filled triangle), and the uncoupled model (UCM) simulation (filled circle). Dashed lines indicate slope β. Spectra are shifted vertically to avoid overlap.

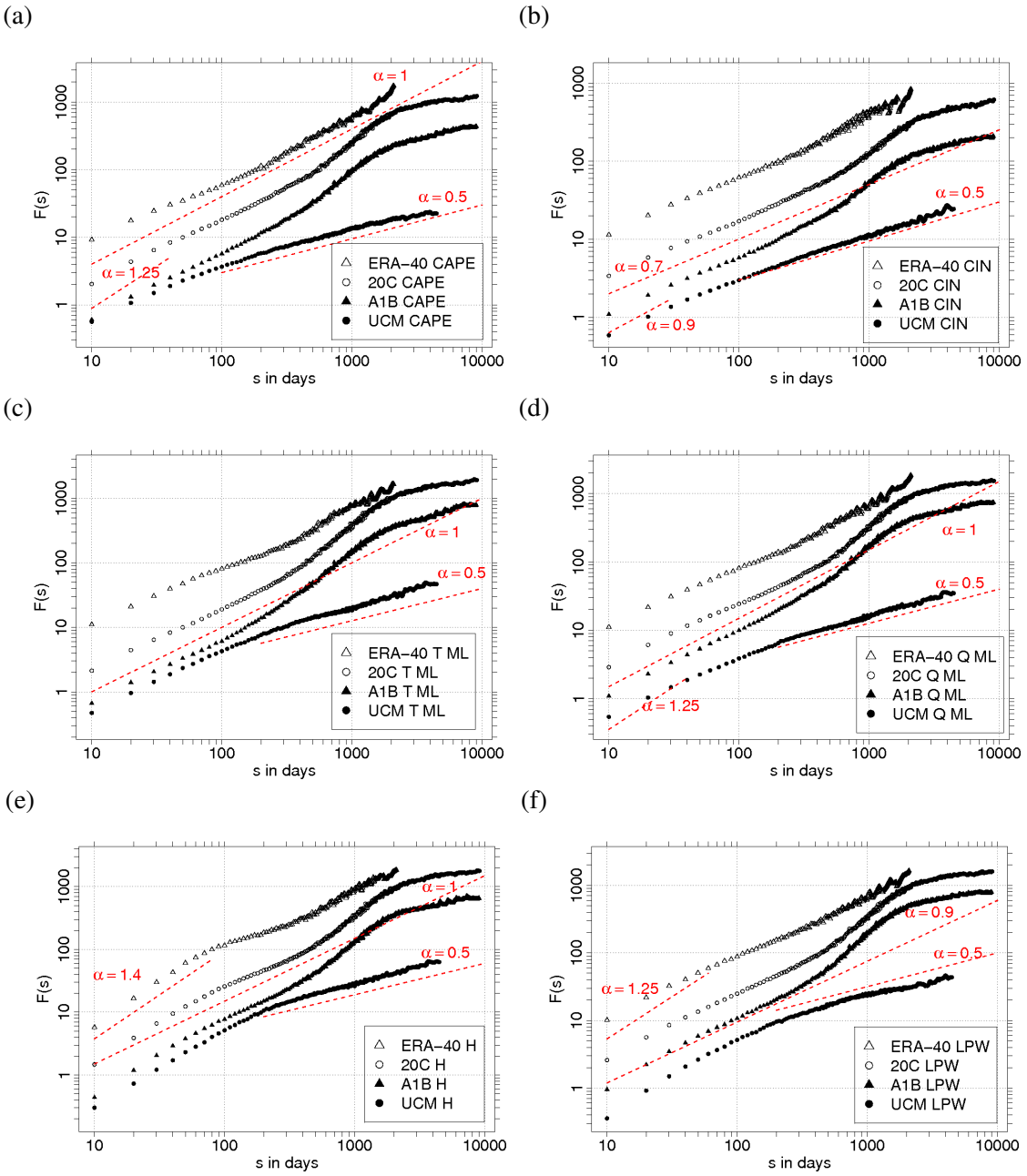

Figure 5.3— Fluctuation functions (DFA2) at the equatorial Pacific of (a) CAPE, (b) CIN, (c) T_{ML}, (d) q_{ML}, (e) H, and (f) LPW computed from ERA-40 data (open triangle), the 20C simulation (open circle), the A1B scenario (filled triangle), and the uncoupled model (UCM) simulation (filled circle). Dashed lines indicate slope α. Fluctuation functions are shifted vertically to avoid overlap.

5.2.2 South-East of Greenland

The ACF shows that the memory is considerably shorter above the North Atlantic than above the equatorial Pacific (Fig. 5.1). The memory in CAPE in ERA-40 lasts up to three days, whereas it lasts of one day in CAPE computed from the 20C simulation. The ACC in CIN is also only positive for one day. The duration of the memory corresponds to the life span of synoptic disturbances, e.g. polar lows which consist of high magnitudes of CAPE and low values of CIN. Polar lows are relatively small in terms of size, which might be the reason why the lower-resolution ECHAM5 data do not consist of memory in CAPE. In contrast, temperature and humidity in and above the mixed layer reveal memory between 5 and 10 days if computed from ERA-40 data or the 20C simulation (Fig. 5.1). The results from the ACF does not hint towards memory on longer time scales. However, the power spectra (Fig. 5.5) and fluctuation functions (Fig. 5.6) reveal LTM up to 9000 days in all variables computed from ERA-40 and in CAPE, CIN, T_{ML} and q_{ML} in the 20C simulation. The slopes from the fluctuation functions reveal a power law with $0.55 < \alpha < 0.65$. The corresponding slopes of $0.1 < \beta < 0.3$ are also visible in the power spectra but not as uniformly. These slopes are steeper during the first four to five days, especially in enthalpy H which shows red noise behaviour with $\beta \sim 2$ which decreases to $\beta = 0$ around 20 days in the 20C simulation. While the memory in CAPE, CIN, T_{ML} and q_{ML} are very similar in the ERA-40 data and the 20C simulation, those of H and LPW differ. The memory decays in both variables around 2000 days in the 20C simulation, whereas it shows LTM in the ERA-40 data. Thus, the question arises why H and LPW differ in ERA-40 and in the 20C simulation above the North Atlantic but not above the equatorial Pacific. The higher mean distributions of humidity in the tropics in the ERA-40 data in comparison with the 20C simulation have probably an impact (Fig. 3.4 and 3.6). The long memory visible in CAPE, CIN, T_{ML}, q_{ML}, H, and LPW is probably related to the NAO. A positive correlation between the NAO and CAPE is described in chapter 6.

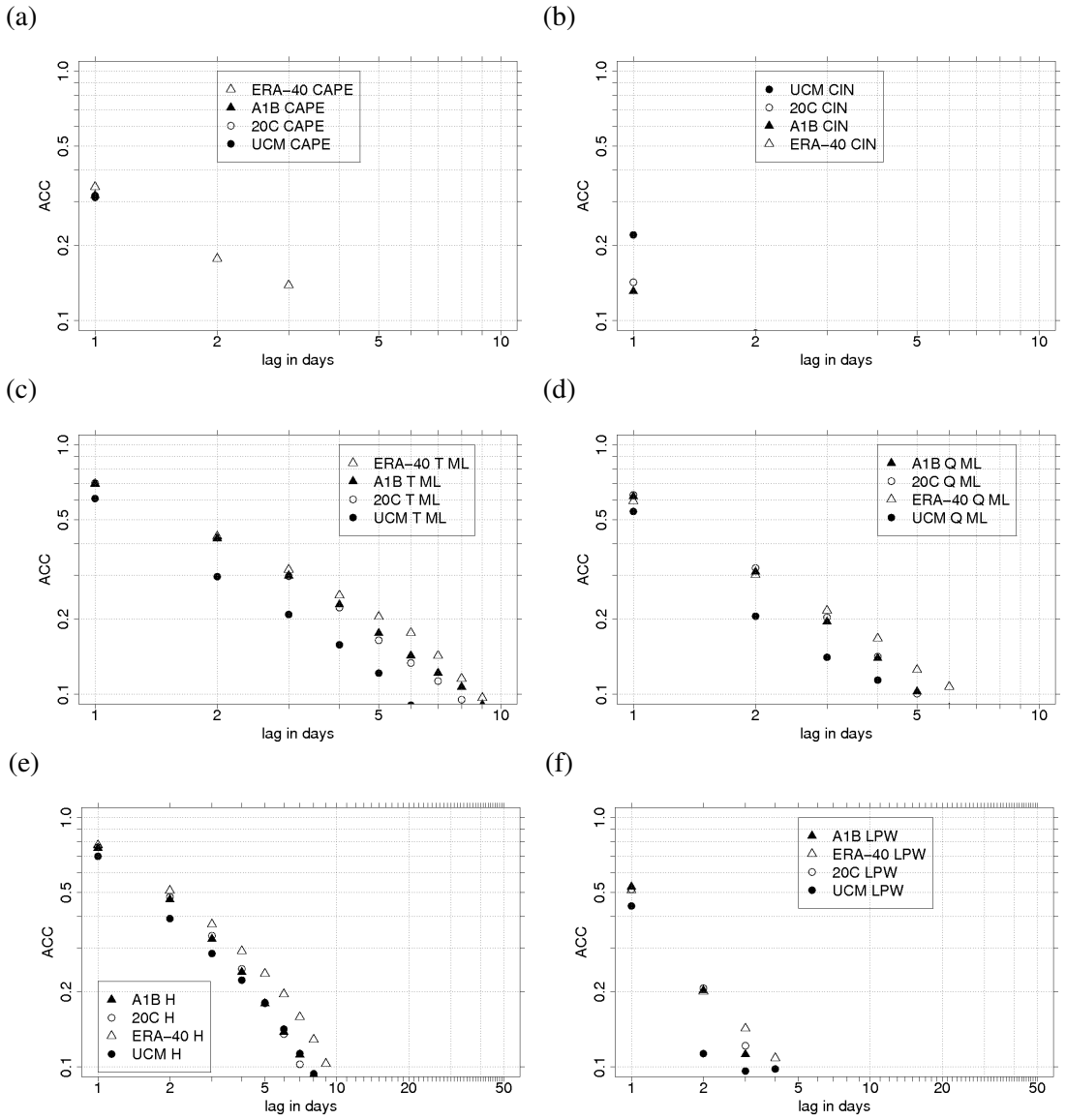

Figure 5.4— Auto correlation function south-east of Greenland of (a) CAPE, (b) CIN, (c) T_{ML}, (d) q_{ML}, (e) H, and (f) LPW computed from ERA-40 data (open triangle), the 20C simulation (open circle), the A1B scenario (filled triangle), and the uncoupled model (UCM) simulation (filled circle).

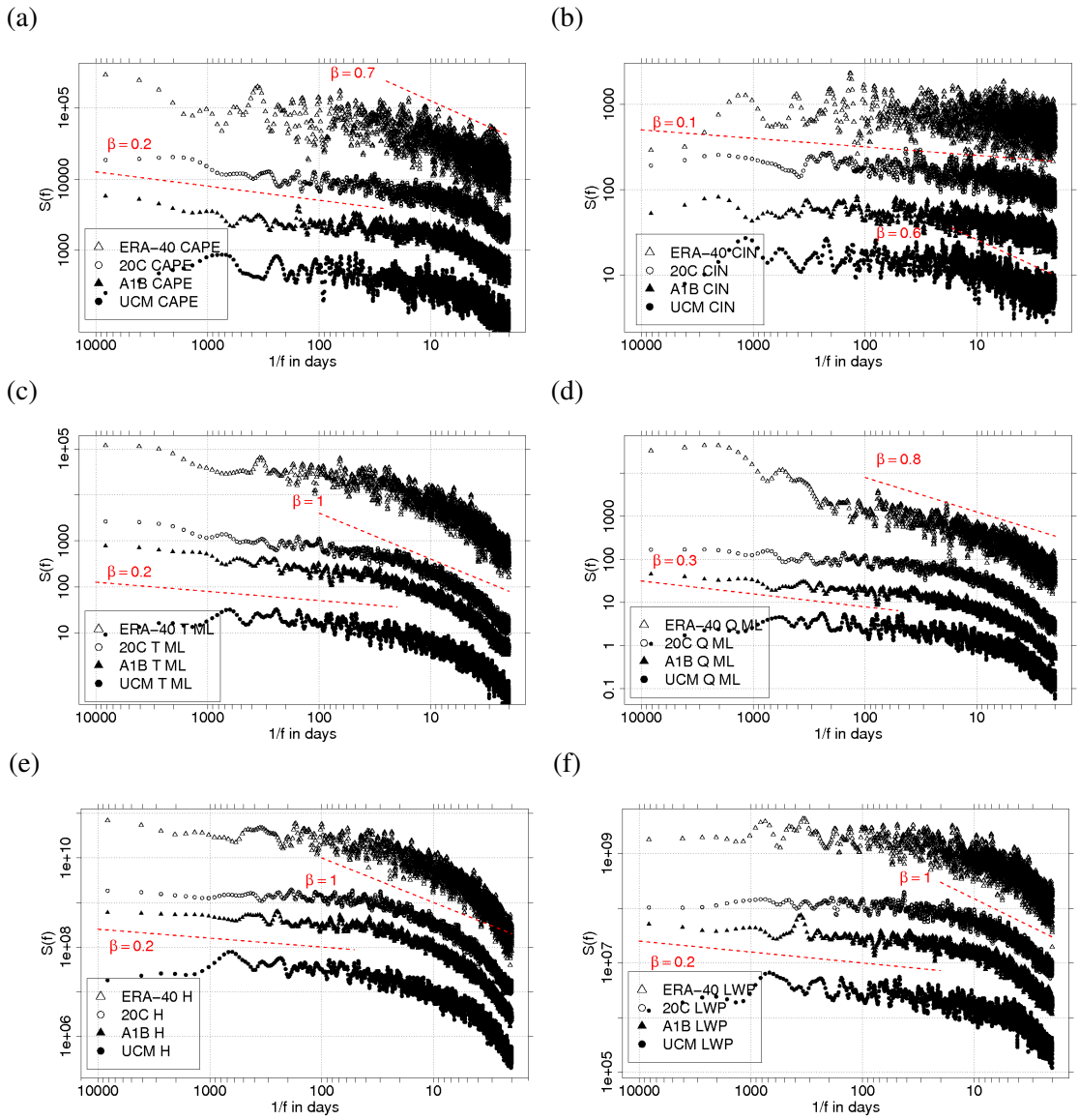

Figure 5.5— Power spectra south-east of Greenland of (a) CAPE, (b) CIN, (c) T_{ML} , (d) q_{ML}, (e) H, and (f) LPW computed from ERA-40 data (open triangle), the 20C simulation (open circle), the A1B scenario (filled triangle), and the uncoupled model (UCM) simulation (filled circle).Dashed lines indicate slope β. Spectra are shifted vertically to avoid overlap.

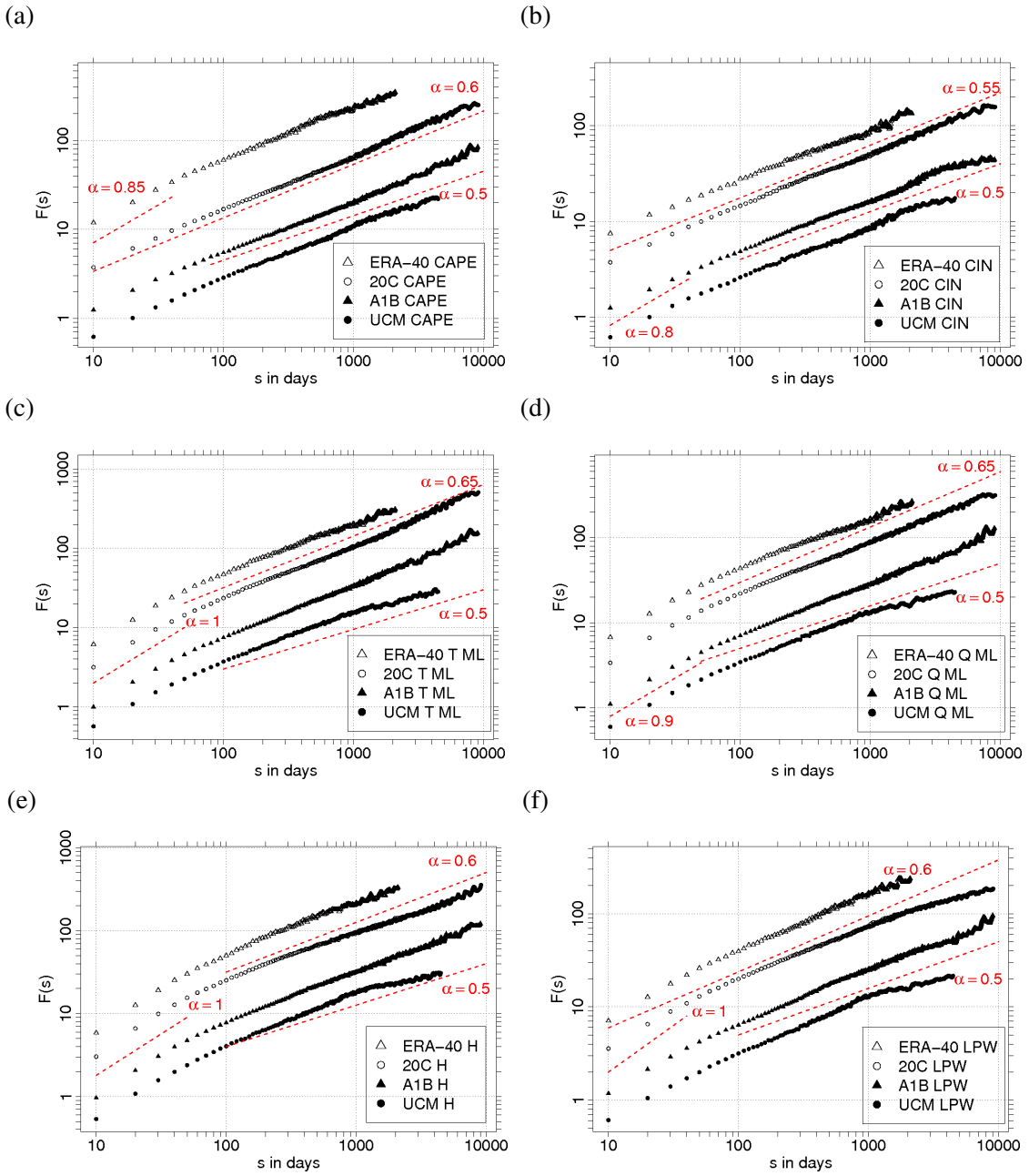

Figure 5.6— Fluctuation functions (DFA2) south-east of Greenland of (a) CAPE, (b) CIN, (c) T_{ML}, (d) q_{ML}, (e) H, and (f) LPW computed from ERA-40 data (open triangle), the 20C simulation (open circle), the A1B scenario (filled triangle), and the uncoupled model (UCM) simulation (filled circle). Dashed lines indicate slope α. Fluctuation functions are shifted vertically to avoid overlap.

5.2.3 Changes in a warmer climate

The comparison of the memory analysis between the ERA-40 data and the simulated 20C data shows a good agreement with the exception of the memory pattern in H and LPW above the North Atlantic. Given that the memory in CAPE and CIN is captured well in the simulated present-day climate, it is assumed that the memory is also well expressed in a simulated possible future climate. ACF, power density spectra as well as DFA2 are applied to all variables computed from the A1B scenario above the equatorial Pacific (Fig. 5.1, 5.2 and 5.3) and south-east of Greenland (Fig. 5.4, 5.5 and 5.6). While the ACCs above the equatorial Pacific exceed those of the 20C simulation, these remain similar above the North Atlantic with the exception of LPW. In the A1B scenario, LPW consists of positive ACCs for three days only which is less than half compared to the 20C simulation. However, the power spectra and fluctuation functions reveal almost parallel curves in comparison with those from the 20C simulation above the equatorial Pacific as well as above the North Atlantic. The main difference between the present-day and the warmer climate lies in a slightly shorter period of the superimposed cycle in the spectra in the A1B scenario.

5.2.4 The impact of the ocean

The ocean plays a major role in the development of atmospheric memory on long time scales, e.g. memory in SST, which affects the near surface air temperature above. To investigate the impact of the ocean on the memory of CAPE and CIN, all variables are computed from an ECHAM5 simulation which is uncoupled from an ocean model. Instead, the ocean is represented by a climatological SST distribution. ACF, power density spectra as well as DFA2 are applied to all variables computed from the uncoupled model (UCM) above the equatorial Pacific (Fig. 5.1, 5.2 and 5.3) and south-east of Greenland (Fig. 5.4, 5.5 and 5.6). The ACF reveals a relatively short memory in CAPE and CIN of up to 5 days over the equatorial Pacific, whereas the variables within the mixed layer consist of memory between 10 and 20 days. Temperature and humidity above the mixed layer exhibit positive ACCs between 20 and 30 days. Furthermore, CAPE and CIN do not consist of positive ACCs for more than a day above the North Atlantic, whereas temperature and humidity related values show positive ACCs up to 8 days. The power spectra and fluctuation analyses reveal that the memory within all variables consists of around 200 days above the equatorial Pacific. The absence of the super imposed cycle above the equatorial Pacific confirms the conclusion of ENSO being the cause of the cycle. The length of the memory in T_{ML} and q_{ML} above the North Atlantic also does not exceed 200 days. CIN does not reveal any memory at all. However, CAPE as well as H and LPW consist of memory up to 1000 days which is surprising as the analyses of memory in CAPE from the ERA-40 data and the 20C simulation lead to the conclusion that temperature and humidity within the mixed layer play a more dominant role in developing CAPE than those above the mixed layer in higher latitudes and vice versa in tropical regions. The question arises whether the impact of the NAO causes the longer memory in CAPE, H and LPW and why it is not affecting the mixed layer variables.

5.3 Global memory distributions

The global distributions of memory on short time scales are investigated via the decay time scale τ based on daily and monthly data. To analyse the global distributions of memory on longer time scales, the Hurst exponent is obtained in an intra-annual period of 30 days to 300 days, as well as in inter-annual periods of 400 days to 5 years, and 2 years to 20 years. Memory obtained from the ERA-40 data (1979-2001) is compared to the 20C simulation for the years 1979-2001 and 1902-2001 respectively. The differences between the shorter and the longer 20C simulations are negligible small, thus only the latter is shown and discussed here. How the distribution of memory changes in a possible future climate is obtained from the A1B scenario. In addition, the impact of the memory within the ocean, which is transmitted via the SST distribution, is identified from the uncoupled model (UCM) simulation. Antarctica is not considered in the analyses, because CAPE and CIN values are only computed for approximately 10 days during an average year in this region. The memory is obtained from CAPE and CIN. The distributions gained from the related variables T_{ML}, q_{ML}, H and LPW are discussed here, while their figures are found in the Appendix.

5.3.1 Intra-annual memory

The global pattern of intra-annual memory in CAPE in the present-day climate is described by the decay time scale of daily, τ_d (Fig. 5.7), and monthly values, τ_m (Fig. 5.8), and the Hurst exponent α in the time interval 30 to 300 days (Fig. 5.9). The analyses of τ_d and α, agree on the general memory distribution in CAPE, which consists of memory over all continents and ocean basins in ERA-40 data and the 20C simulation. However, τ_m reveals memory ≥ 2 months only over the tropical Pacific (in the ERA-40 data and the 20C simulation), the tropical Atlantic and Indian Ocean as well as over several small regions on all continents except Greenland and Australia (in ERA-40 data only). The global distribution of intra-annual memory in CIN in the present-day climate (Fig. 5.7-5.9) reveals also memory over all continents and ocean basins. However, the regions with memory are considerably smaller in CIN than in CAPE. While highest values of τ_d in CAPE occur along the equator in the Pacific and the Atlantic, the regions with $\tau_d \geq 2$ days in CIN are shifted to the North and South of the equator. This shift is not recognisable in τ_m and α. The Hurst exponent covers the largest regions in the 20C simulation. However, regions with $0.9 \leq \alpha \leq 1.1$ occur only along the equatorial ocean basins in the ERA-40 data. The zonal mean values of τ_d and τ_m in CAPE and CIN show highest values along the equator. In addition, the larger spread of α also reveals additional much less pronounced peaks around $60°$ latitude.
The memory distributions obtained from the decay time scale in T_{ML} and H show that regions with memory ≥ 4 days and months respectively are considerably larger than those in q_{ML} and LPW (Fig. A.25-A.28). Moreover, the distribution of τ_m in LPW agrees well with those found in CAPE which confirms the results of Holloway and Neelin (2009) who report a correlation between buoyancy and the humidity of the free atmosphere to be stronger than between buoyancy and temperature or humidity in the boundary layer. In addition, the distributions of $\alpha \geq 0.9$ in q_{ML} and LPW resemble those in CAPE better than T_{ML} and H in the ERA-40 data. In contrast, the regions with $\alpha \geq 0.9$ in T_{ML}, q_{ML}, H and LPW are larger in the 20C simulation also covering the equatorial Atlantic, the Indian Ocean and several continental tropical regions.

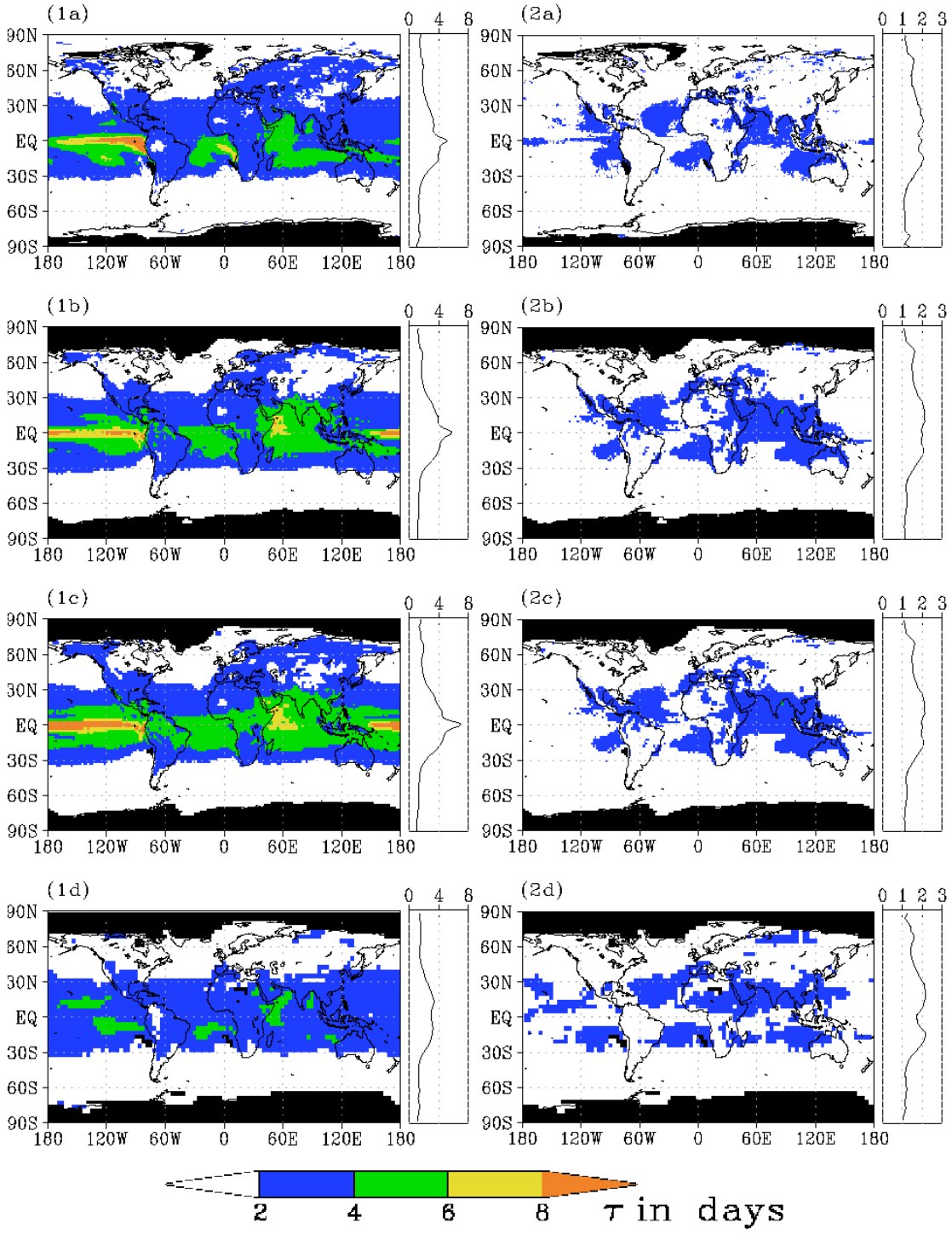

Figure 5.7— Decay time scale τ_d in days of (1) CAPE and (2) CIN computed from: (a) ERA-40 data, (b) 20C simulation, (c) A1B scenario, and (d) UCM. The black shading marks those regions with CAPE > 0 Jkg^{-1} occur in less than 10 times during an average year.

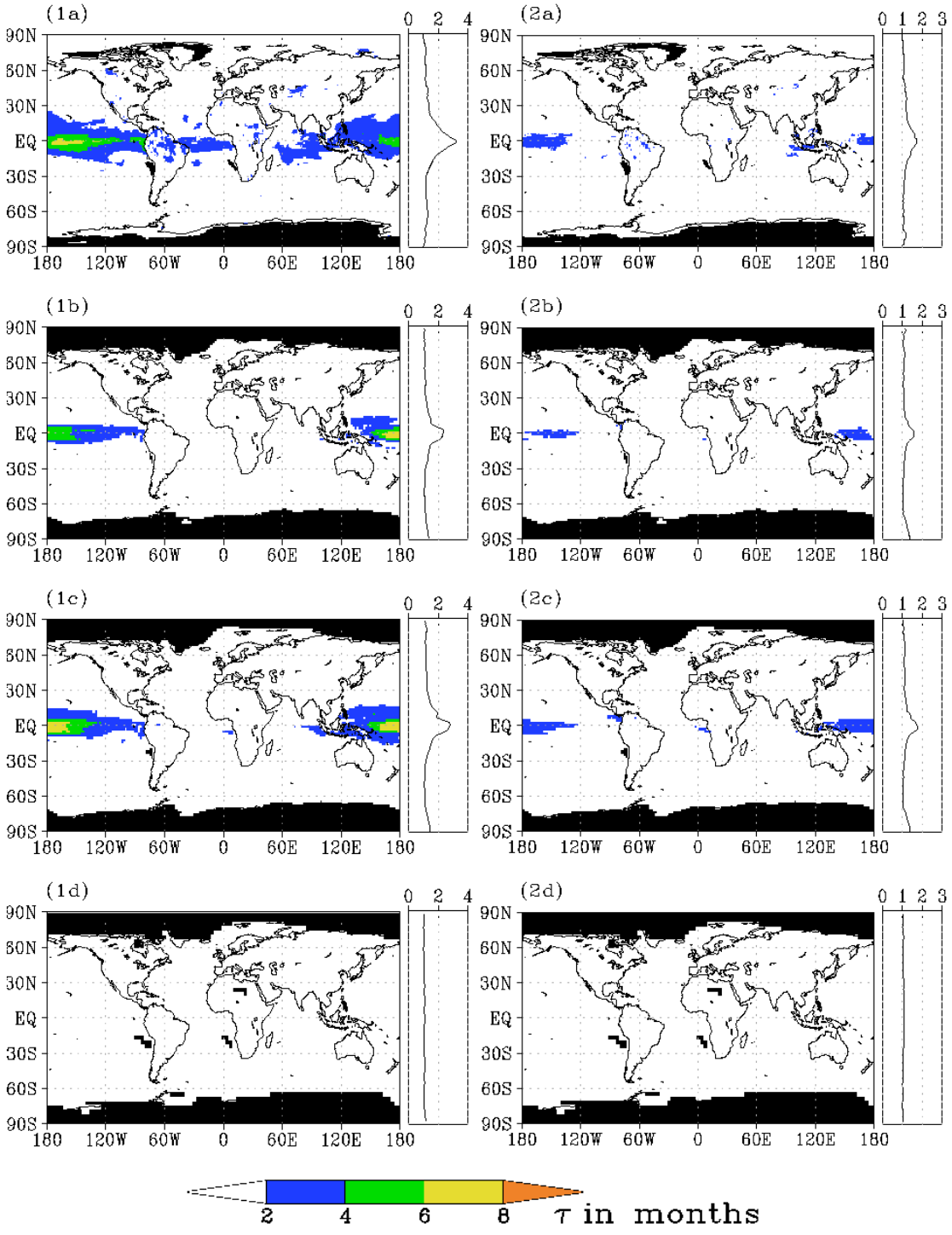

Figure 5.8— Decay time scale τ_m in months of (1) CAPE and (2) CIN computed from: (a) ERA-40 data, (b) 20C simulation, (c) A1B scenario, and (d) UCM. The black shading marks those regions with CAPE > 0 Jkg^{-1} occur in less than 10 times during an average year.

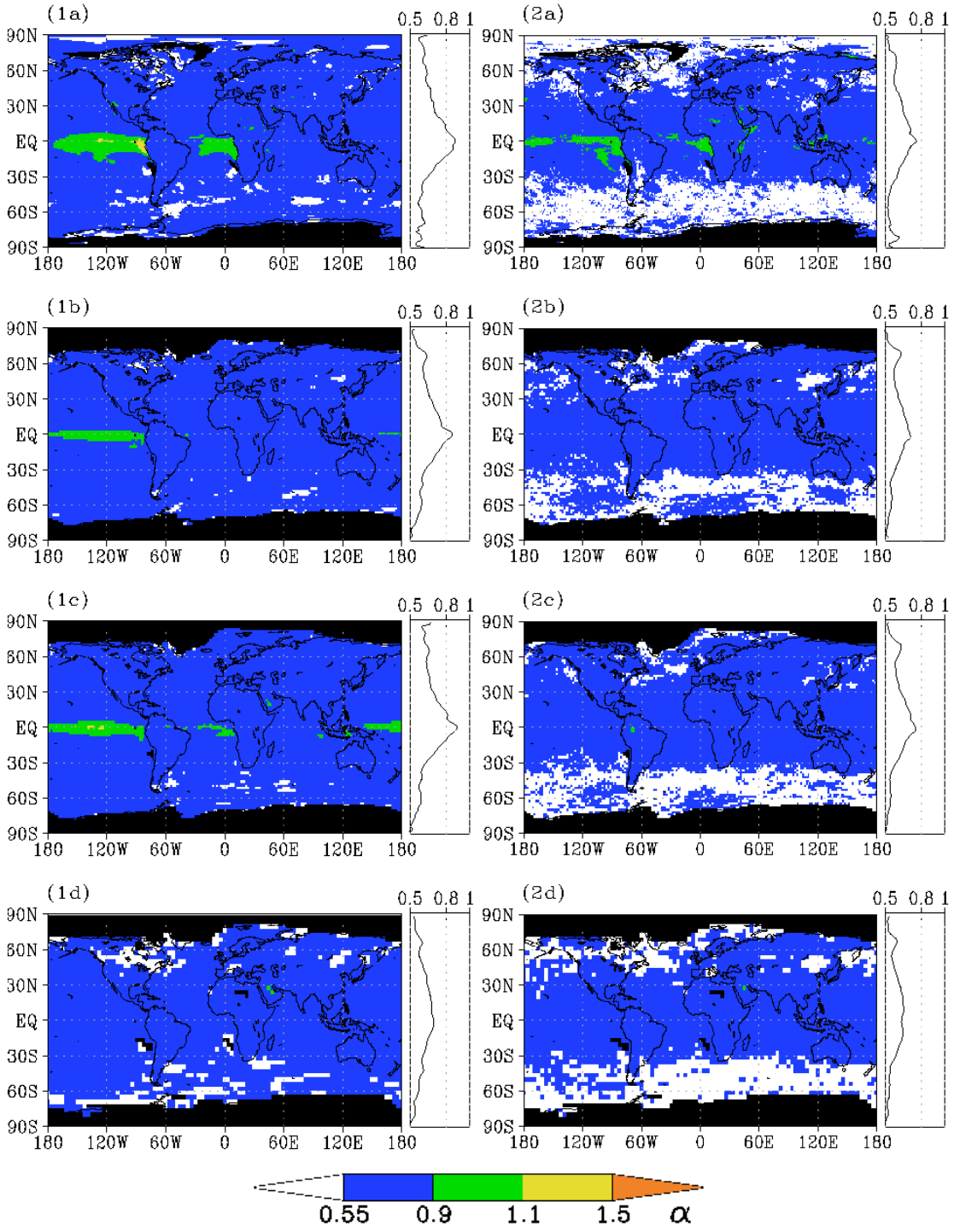

Figure 5.9— Hurst exponent α in 30 days to 300 days of (1) CAPE and (2) CIN computed from: (a) ERA-40 data, (b) 20C simulation, (c) A1B scenario, and (d) UCM. Hurst exponents exceeding 0.55 indicate memory. The black shading marks those regions with CAPE > 0 Jkg^{-1} occur in less than 10 times during an average year.

5.3.2 Inter-annual memory

The global distribution of inter-annual memory in CAPE in the present-day climate is determined by the Hurst exponent α in the time interval of 400 days to 5 years (Fig. 5.10). Additionally, α is also obtained in the time interval 2 years to 20 years in the 20C simulation to investigate the memory distribution up to decades (Fig. 5.11). The general pattern of the inter-annual memory distribution in CAPE resembles those of intra-annual memory with memory over all continents and ocean basins. Values of $\alpha \geq 0.9$ occur over the equatorial Pacific (in the ERA-40 data and the 20C simulation) and the Indian Ocean (in ERA-40 data only). The Hurst exponent reaches $1.1 < \alpha < 1.5$ over the equatorial Pacific. Such high values are caused by ENSO (Subsec. 5.2.1). The ENSO cycle, which superimposes the memory signal, enlarges the Hurst exponent in the periodicities affected (between 1000 and 2000 days). The zonal mean emphasises the ENSO cycle which leads to a strong gradient towards the equator.
The memory visible over the polar oceans is related to the variability in polar low occurrence. Claud et al. (2007) report associations between large-scale atmospheric circulations and polar low development over the North Atlantic including SST distribution, sea ice extent and the NAO. Carleton and Carpenter (1990) report similar relations for the Southern Hemisphere. According to their studies polar low occurrences and thus CAPE are related to sea ice extent and ENSO. The global distribution of α in CIN reveals similarities to that of CAPE (Fig. 5.10). Regions with $\alpha > 0.55$ indicating memory cover smaller regions. However, those regions are over all ocean basins and continents. The values of $0.9 < \alpha < 1.1$ in CIN occur along the equatorial Pacific (in the ERA-40 data and the 20C simulation) and over the Indian Ocean (in ERA-40 data only) but are less pronounced regarding spatial extent compared to CAPE. In addition, values of $0.9 < \alpha < 1.1$ occur also over small regions in the tropical Atlantic and North America in the ERA-40 data. Although, there are less regions with $0.9 < \alpha < 1.1$ in the 20C simulation, α exceeds 1.1 in the western equatorial Pacific. This suggests that ENSO also influences the memory in CIN. However, ENSO is only visible in the 20C simulation.
The memory distribution on longer time scales (2 years to 20 years) in CAPE and CIN in the 20C simulation reveals memory over every ocean basin and continent (Fig. 5.11). However, these regions are considerably smaller than in the time interval 400 days to 5 years. The Hurst exponent does not exceed $\alpha > 0.9$ with the exception of a small region in the equatorial central Pacific in CAPE. There is no apparent influence of ENSO. However, the memory in CAPE and CIN over the Southern and Northern Ocean indicate the impact of the NAO.
The global distribution of inter-annual memory in T_{ML}, q_{ML}, H and LPW in the present-day climate reveal that memory in LPW agrees well with that in CAPE (Fig. A.31-A.32). The distributions in T_{ML}, q_{ML} and H show $\alpha \geq 0.9$ also over larger regions in the Indian Ocean and the Atlantic as well as over tropical continental regions. However, α in the time interval 2 years to 20 years (Fig. A.33-A.34) in LPW covers larger regions than in CAPE, especially $\alpha \geq 0.9$ over the equatorial Pacific. In general, regions with $\alpha > 1.1$ show a larger spatial extent towards the Atlantic in the 20C simulation. According to van Oldenborgh et al. (2005) the ENSO cycle is represented realistically regarding its strength and location within the 20C simulation. Therefore, the smaller Hurst exponent indicates an underestimation of ENSO in the ERA-40 data which is probably related to the shorter length of data set.

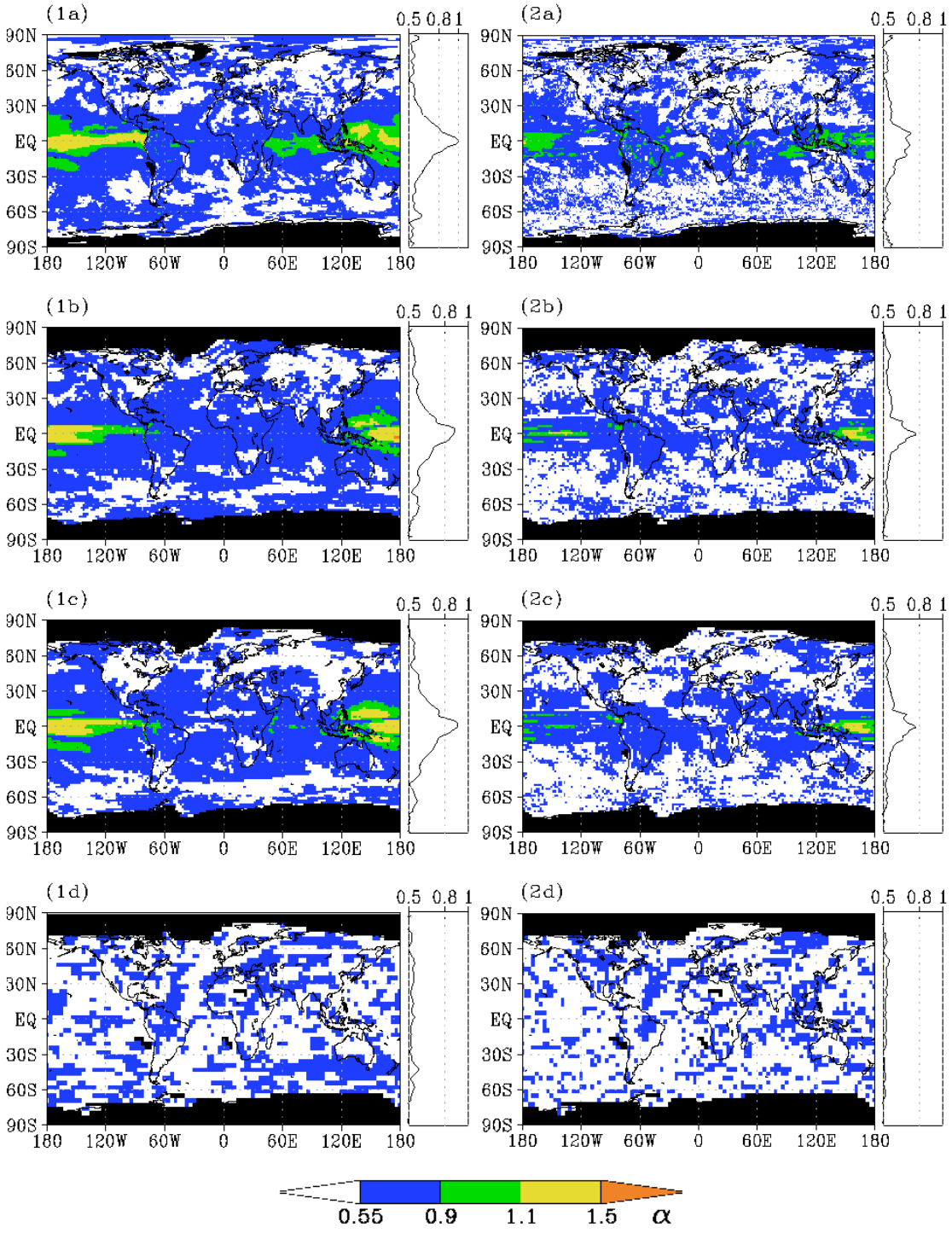

Figure 5.10— Hurst exponent α in 400 days to 5years of (1) CAPE and (2) CIN computed from: (a) ERA-40 data, (b) 20C simulation, (c) A1B scenario, and (d) UCM. Hurst exponents exceeding 0.55 indicate memory. The black shading marks those regions with CAPE > 0 Jkg^{-1} occur in less than 10 times during an average year.

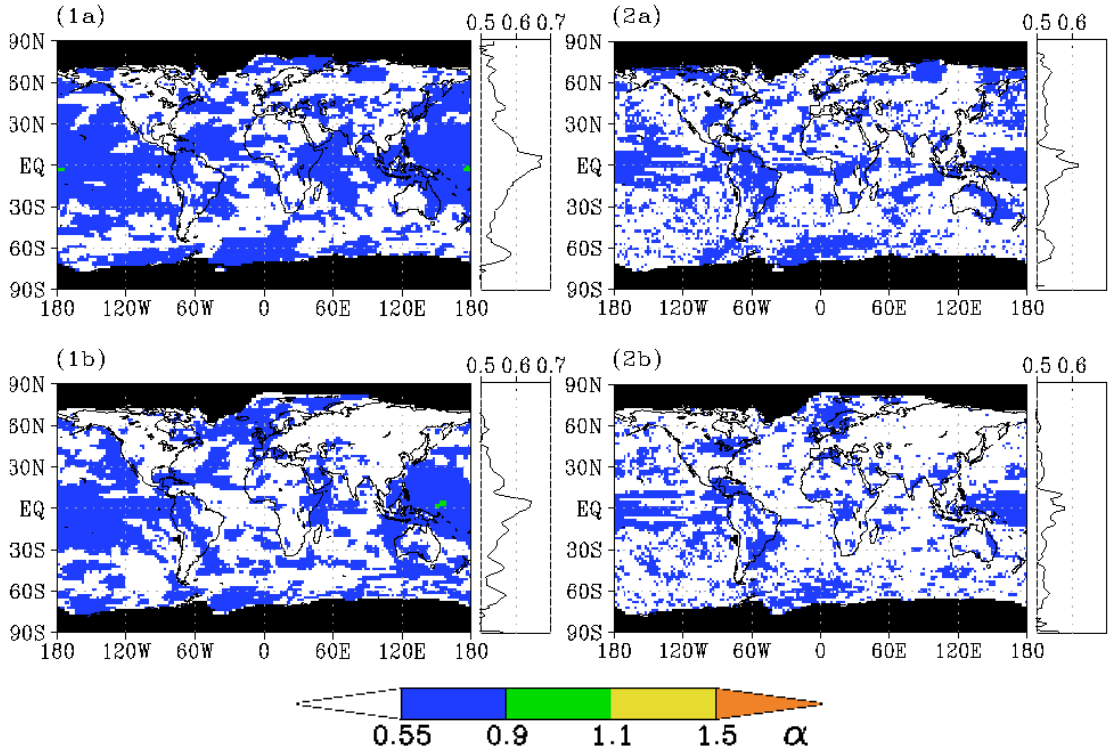

Figure 5.11— Hurst exponent α in 2 years to 20 years of (1) CAPE and (2) CIN computed from: (a) 20C simulation, (b) A1B scenario. Hurst exponents exceeding 0.55 indicate memory. The black shading marks those regions with CAPE > 0 Jkg^{-1} occur in less than 10 times during an average year.

5.3.3 Changes in a warmer climate

The comparison of the memory analyses between the ERA-40 data and the simulated 20C data reveals that the ECHAM5/MPI-OM model is capable of capturing the memory distributions in CAPE and CIN well. The regions influenced by ENSO are more pronounced in terms of spread in the mixed layer variables and H. Given that the memory in CAPE and CIN is captured well in the simulated present-day climate, it is assumed that the memory is also well expressed in a simulated possible future climate. The distributions of memory on shorter time scales in CAPE and CIN reveal a small change in τ_d and τ_m (Fig. 5.7-5.8). The region with $\tau \geq 4$ time steps expands in the tropical Pacific. A similar change in a warmer climate occurs in q_{ML} and LPW. Moreover, $\tau_m \geq 8$ months occurs almost everywhere between the 15° latitudes in H in a warmer climate.
The distribution of the Hurst exponent in the time interval 30 days to 300 days expands over the high latitudes in CAPE and CIN. Moreover, the region with $\alpha \geq 0.9$ spreads towards the western equatorial Pacific and the equatorial Atlantic in CAPE. Larger differences are visible in the mixed layer variables. While the region of $\alpha \geq 0.9$ increases in T_{ML}, it decreases in q_{ML}. A similar change occurs in H and LPW. While the distribution of α in the time interval 30 days to 300 days expands in CAPE and CIN, it reduces in the regions with memory in the high latitudes in the time interval 400 days to 5 years. In contrast, $\alpha \geq 0.9$ in CAPE occurs in a wider region in the central and western equatorial Pacific and spreads in the Indian Ocean. Larger regions of $\alpha \geq 1.1$ indicate a stronger influence of ENSO on CAPE but not on CIN. The stronger influence of ENSO is also visible in the spreading distribution of $\alpha \geq 1.1$ along the equator in T_{ML}, q_{ML}, H and LPW.
While the memory distributions in CAPE and CIN changed similarly in a warmer climate for intra-annual and inter-annual memory up to 5 years, the distribution of α in the time interval 2 years to 20 years reveals a decrease in distribution in CAPE and an increase in CIN (Fig. 5.11). The regions with memory in CAPE vanish especially over the tropical Atlantic and the Indian Ocean, whereas they increase over the North Atlantic. In contrast, $\alpha \geq 0.55$ occurs almost everywhere with the exception of Northern Asia. The memory distributions in the mixed layer variables both decrease in the time interval 2 years to 20 years. This change is even more pronounced in LPW while the regions with memory in H slightly decrease over the Southern Hemisphere but increase over the Northern Hemisphere, especially over the Pacific and Atlantic.

5.3.4 The impact of sea surface temperature

The memory in SST has a very strong influence on the memory within the atmosphere. Memory on shorter time scales like several days is still recognisable in CAPE and CIN in the UCM. However, its location has shifted (Fig. 5.7). The length of the memory decreases along the equator, especially in the Pacific in CAPE or vanishes in CIN. The reduction of the length of the memory along the equator is also visible in T_{ML}, q_{ML}, H and LPW (Fig. A.25-A.26). Moreover, the length of the memory increases around 20° latitude and over the northern high latitudes ≥ 60°N. The memory obtained by τ_m reveals that no variable analysed here exceeds $\tau_m > 1$ month. In contrast, the Hurst exponent in the time interval 30 days to 300 days reveals memory almost everywhere in CAPE and CIN, with $0.55 \leq \alpha \leq 0.9$. The distributions of α in T_{ML} and q_{ML} show also memory with $0.55 \leq \alpha \leq 0.9$ almost everywhere. However, a large region without memory occurs around 45°S in the Atlantic and the Indian Ocean, while $\alpha \geq 0.9$ forms over the Middle-East and Brazil

which has not formed in the ERA-40 data, the 20C simulation or the A1B scenario. A similar development happens for the memory distribution in H. The regions with $\alpha \geq 0.9$ decrease in the tropical Atlantic and Pacific but increases in the tropical Indian Ocean towards the Middle-East in comparison with the 20C simulation. The memory distribution in LPW does not show a decrease. However, the regions with $\alpha \geq 0.9$ also decrease in in the Pacific and the Atlantic and a gap without memory occurs along 45°S. The absent memory in SST has the largest impact on the memory on longer time scales. Therefore, α in the time range 400 days to 5 years reveals the strongest change in comparison with the ERA-40 data, the 20C simulation and the A1B scenario. Memory in all variables investigated here is still occurring over all continents and ocean basins. However, large regions without memory are visible also over all continents and ocean basins leading to a memory pattern which seems randomly distributed.

5.4 Summary and conclusions

The comparison of the memory in the ERA-40 data with those in the 20C simulation reveals a good agreement of the global patterns. The strongest memory signals in CAPE and CIN occur along the equatorial Pacific and are caused by the ENSO cycle. A general strong memory in CAPE is visible on inter-annual time scales in the tropics, extending to extra-tropical regions on all continents except Antarctica, and over all oceans including the polar oceans. The memory in CAPE and CIN lasts up to 9000 days south-east of Greenland. The memory analyses of related parameters (T_{ML}, q_{ML}, H, and LPW) reveal that their influence on memory in CAPE and CIN differs with location. In the tropics, the spatial pattern in LPW resembles that of CAPE suggesting that it plays the dominant role in CAPE memory. These findings are confirmed by the study of Holloway and Neelin (2009), who report a correlation between buoyancy and specific humidity in the free troposphere over the tropical Pacific. However, in this study, the extra-tropical T_{ML} and q_{ML} have a stronger influence on the memory of CAPE when comparing their spatial memory patterns.

Polar low occurrence yields an explanation on probable mechanisms of the STM and LTM for CAPE found in the Polar Regions, as considerable CAPE is accumulated in polar lows. On the one hand, STM up to three days represents the duration of a polar low life cycle. On the other hand, LTM may be caused by the correlation found between CAPE and the NAO. Similar relations are reported by Claud et al. (2007), substantiating the findings here concerning the NAO. Correlations between monthly means of CAPE and NAO, as well as ENSO, reveal global teleconnections. Consequently, ENSO is identified to influence strongly the variability in CAPE and CIN in the tropical Pacific. Almost all continents and ocean basins show memory in daily CAPE and CIN time series at long time scales.

The good agreement between the observed and the simulated present-day climate leads to the conclusion that the ECHAM5/MPI-OM is capable of simulating memory distributions in a warmer climate. The memory patterns in CAPE and CIN in a warmer climate resemble those in the 20C simulation generally. The regions with higher Hurst exponents expand slightly towards higher latitudes for intra- and inter-annual time ranges. The influence of ENSO is also expanding in the tropical Pacific. The regional analyses indicate that the peak of the ENSO cycle occurs earlier by several hundred days. In contrast to the expanding regions with memory up to 5 years, those

regions decrease which consist of memory up to 20 years over most continents and the tropical Atlantic. The distributions of temperature and humidity in a warmer climate change accordingly. The UCM simulation confirms the findings of Fraedrich and Blender (2003) who report of longer temperature memory if the ocean is represented more realistically. The regional memory does not exceed 200 days in variables investigated here in the UCM simulation. The Hurst exponents reveal memory up to 5 years in several continental and oceanic regions. However, no pattern is visible in these distributions which occurs in the other data sets.

Chapter 6

Large scale influences on global CAPE and CIN distributions

Previous chapters of this thesis report about relations between atmospheric temperature, sea surface temperature, atmospheric humidity and CAPE and CIN respectively. These relations occur on a regional and global scale as well as on short and long time scales. Temperature and humidity on various atmospheric levels are known to be influenced by large scale factors such as teleconnections or the mean meridional circulation (MMC) or both. These impacts in the present-day climate and their changes in a future warmer climate are the focus of many studies. Müller and Roeckner (2008) for example report about future changes in ENSO and a shift in the Hadley Cell. Moreover, Allan and Soden (2007) discuss how changes in the tropical circulation affect precipitation. The strong influence of ENSO on the memory in CAPE and CIN is revealed in chapter 5. The long memory in CAPE south-east of Greenland hints towards an impact of the NAO. Moreover, the pattern in the southern hemispheric trend distribution in CAPE and in CIN show regions with decreasing magnitudes which cannot be fully explained by trends in temperature and humidity. Therefore, the impacts of teleconnections and the MMC on CAPE and CIN are in the focus of this chapter.
In addition to the impacts of ENSO and the NAO, those of SAM (Southern Annular Mode) are investigated. Watterson (2009) reports about correlations between SAM and precipitation and an additional relation between SAM and ENSO. The largest magnitudes in CAPE occur in the ascending branches of the Hadley Cell, which are part of the MMC. The descending branch of the Hadley Cell is related to high magnitudes in CIN. Therefore, shifts in the MMC as described in future global warming scenarios occur simultaneously with shifts of regional maxima in CAPE and CIN and thus lead to the decreasing trends. Correlations with the three named teleconnections are described in the following three sections. The influence of the MMC is discussed in section 6.4. The correlation analyses of present-day simulated CAPE and ENSO and NAO respectively are published in Riemann-Campe et al. (2010).

6.1 El Niño/Southern Oscillation, ENSO

The El Niño/Southern Oscillation (ENSO) is based on the oceanic part El Niño, which denotes an anomalous warming of the tropical Pacific, and the Southern Oscillation describes the corresponding changes within the atmosphere (Trenberth, 1997). ENSO occurs irregularly about every 4 to 8 years (Müller and Roeckner, 2008). The changes in SST directly influence the near surface temperature and humidity and thus the development of convection. According to van Oldenborgh et al. (2005), the ECHAM5/MPI-OM model simulates ENSO realistically. Jungclaus et al. (2006) confirm this statement. However, they point out that the interannual variability in the tropical Pacific associated with ENSO is about 0.5 K higher than in observations. Moreover, Müller and Roeckner (2008) report an underestimation of the nonlinearity of ENSO in ECHAM5/MPI-OM.
A Spearman rank correlation is applied on CAPE and CIN respectively with ENSO. The ENSO time series is determined from the field mean of a 5-month running mean of SST anomalies within the Niño 3 region (150°W -90°W; 5°S - 5°N) (Trenberth, 1997) from the 20C and the A1B simulation. A linear trend is subtracted from the ENSO time series, CAPE and CIN before the correlation (Fig. 6.1). The correlation is applied between the ENSO time series and CAPE (CIN) at every grid point with CAPE $> 0\ Jkg^{-1}$ occurring at least at 10 days during an average year. Regions with less often positive CAPE events are neglected and marked in black in the figures (Fig. 6.2). Correlations are based on monthly mean values from the 20C simulation during 1902-2001 as well as from the A1B scenario during 2002-2101. The 95 % significance level is estimated by Fishers z-transformed inferences.
The ENSO time series (Fig. 6.1) reveal a clear trend in the A1B scenario. Hardly any differences are visible between the original and the detrended time series during the 20th century. Moreover, both show equal numbers of events with temperature anomalies exceeding 1 K and -1 K respectively between 1980 and 1999, which form the time slice used in the trend analyses. The impacts of ENSO on CAPE and CIN within the 20C time slice should approximately cancel each other out. In contrast, the original ENSO time series in the A1B scenario shows a clear increase of temperature anomalies over time. The first half of the 21st century consists of many large negative temperature anomalies. However, the second half of the 21st century, reveals a stronger development towards positive temperature anomalies, especially during the time slice taken for the trend estimation (2090-2099). Many years within the A1B time slice are influenced by a positive ENSO. The detrended time series is used for the correlation analysis. Therefore, the correlation in the 20C simulation and the A1B scenario are relatively similar (Fig. 6.2). The correlation with CAPE shows the typical pattern of a positive relation along the equatorial Pacific and a negative relationship along 20° North and South, respectively, in the eastern Pacific. Furthermore, a positive correlation exists above the eastern equatorial Atlantic. The correlation with CIN reveals several narrow bands of positive and negative correlations each covering about 5 latitudes over the tropical eastern Pacific. Negative correlations north and south of the equator frame positive correlations at the equator. Additional positive correlations occur adjacent to the narrow stripes of negative correlations. Those stripes resemble the pattern of a double ITCZ in the humidity distributions discussed in section 3.1. Differences between the 20C and the A1B simulation occur over the tropical regions of Africa, Asia and the Indian Ocean. There, regions with positive correlations are enhanced. In addition, positive correlations in CAPE and CIN occur at the west coast of North America in the A1B scenario.

The correlation pattern between 10° latitude in CAPE and CIN conform to the pattern in the trend distributions in the same region (Fig. 4.1 and 4.1). However, the negative correlations between 10 and 30° North and South respectively are not visible in the trend distributions. One reason for this discrepancy could be the magnitude of the correlation coefficient. The positive correlation coefficient has values up to 0.8, while the negative correlation coefficients are half as large. The correlations with ENSO are not restricted to the tropics. The Southern Hemisphere shows regions in the Southern Pacific with negative (around 60°S) and positive (between 30 and 60°S) correlation coefficients in CAPE and CIN, which also occurring in the trend pattern. In addition, a positive correlation is visible in the north Pacific west of North America only in the A1B scenario in CAPE and CIN which agree both with a positive trend.

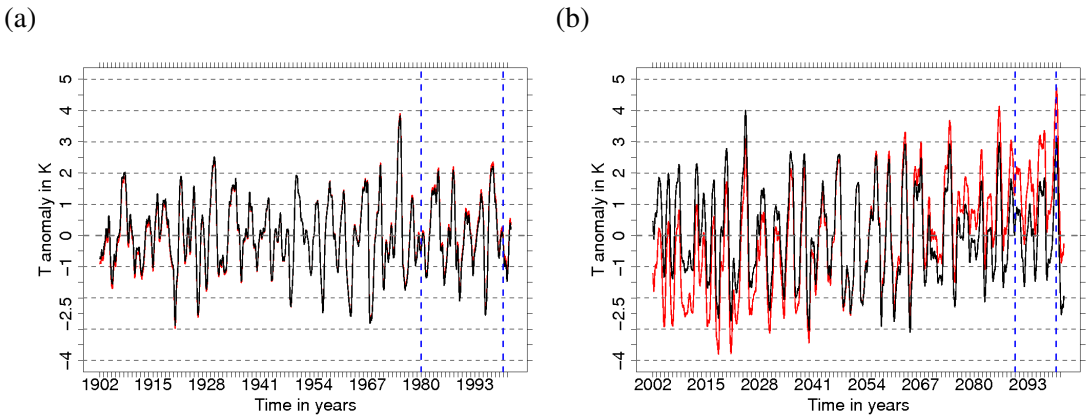

Figure 6.1— ENSO time series computed from monthly means of (a) the 20C simulation and (b) the A1B scenario. The red line shows the original time series, while a linear trend is subtracted in the black line. The blue dashed lines denote the first and last year of the time slice taken for the trend analysis in chapter 4.

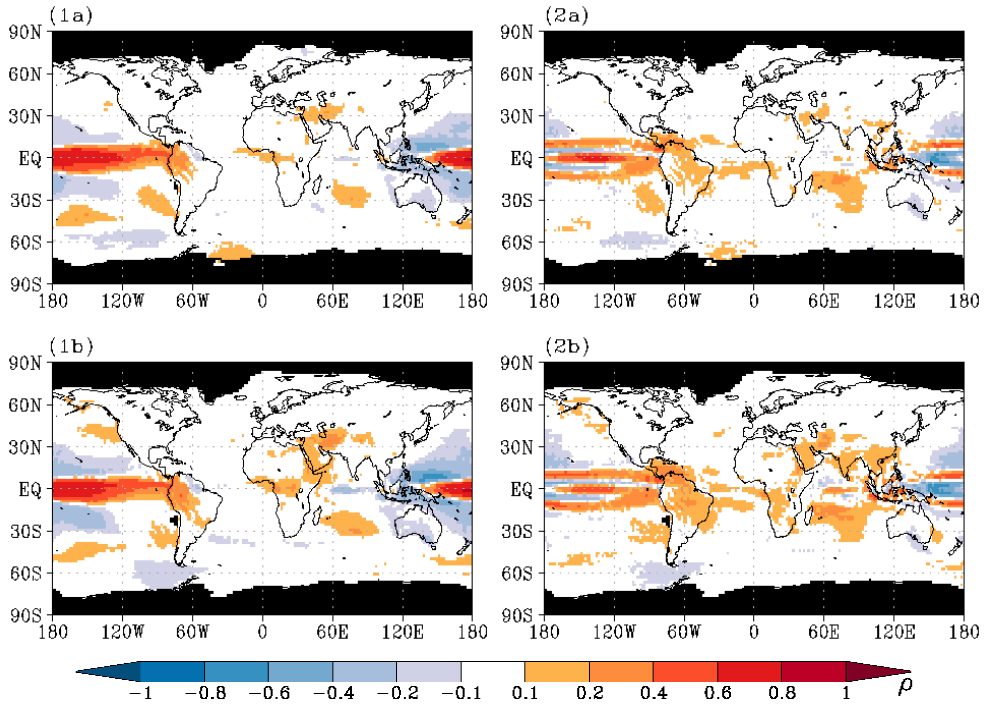

Figure 6.2— Correlations between ENSO and (1) CAPE and (2) CIN respectively. Correlation coefficients ρ computed from monthly means of (a) the 20C simulation and (b) the A1B scenario. Coloured shadings are significant at the 95 % level. The black shading marks those regions with CAPE > 0 Jkg^{-1} occurring less than 10 times during an average year.

6.2 North Atlantic Oscillation, NAO

The North Atlantic Oscillation (NAO) has strong impact on the Northern hemispheric weather and climate variability, especially during the winter months (DJF). The NAO is defined as a dipole of the mean sea level pressure (MSLP) over the North Atlantic. The surface pressure field directs the location of the stormtrack over the North Atlantic. The position of the stormtrack is directly linked to the position of CAPE and CIN occurring within lows and along their fronts.
The NAO-index time series is determined as the first principal component computed via Empirical Orthogonal Functions (EOF) applied to the anomalies of MSLP mean winter months in the North Atlantic sector (90°W - 40°E; 20°N - 70°N) (Hurrell and Deser, 2010). The time series of the NAO index in Fig. 6.3 is detrended and divided by its standard deviation. A Spearman rank correlation is applied on the detrended NAO index time series with detrended monthly mean values of CAPE and CIN respectively (Fig. 6.4).
The time series of the NAO index shows hat it is only marginally affected by a trend in the 20C simulation as well as in the A1B simulation. The time slice of the 20C simulation used for the trend estimation in chapter 4 is dominated by a positive index while in the time slice of the A1B scenario the negative index prevails.
The correlation coefficients in Fig. 6.4 show a similar pattern in CAPE and CIN. A dipole pattern is located over the North Atlantic and parts of Europe, with a positive correlation between Iceland and Svalbard ranging from Greenland to Scandinavia. Marsland et al. (2003) report that the NAO is represented well in the ECHAM5/MPI-OM model. However, additional regions with significant correlations occur over North America and the North Pacific. Furthermore, those additional regions with correlations expand in the A1B scenario revealing the ENSO pattern in the equatorial Pacific with reversed sign.
Although, the NAO is a teleconnection interacting in the Northern Hemisphere, smaller regions with correlations occur on the Southern Hemisphere. A similar effect is visible in the correlation pattern of the SAM (following section), which also expands towards the Northern Hemisphere, although it is a teleconnection of the Southern Hemisphere. The comparison of the NAO correlation pattern with those of the trends during winter (DJF, Fig. A.9 and A.13) shows agreement of the pattern in the equatorial regions. As the negative NAO index prevails the time slices applied for the trend estimation, the negative correlation coefficients along the equator lead to a positive trend in CAPE and CIN. However, the other regions showing correlations, especially the dipole over the North Atlantic are not clearly recognisable in the pattern of the trends, which is surprising as the correlation coefficients range between $0.6 < \rho < 0.8$ over the North Atlantic.

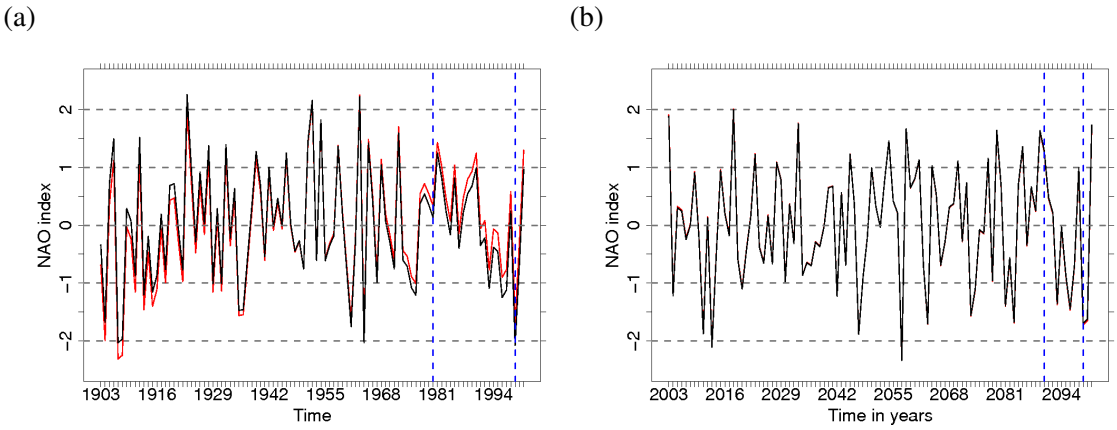

Figure 6.3— NAO time series computed from monthly means of (a) the 20C simulation and (b) the A1B scenario. The red line shows the original time series, while a linear trend is subtracted in the black line. The blue dashed lines denote the first and last year of the time slice taken for the trend analysis in chapter 4.

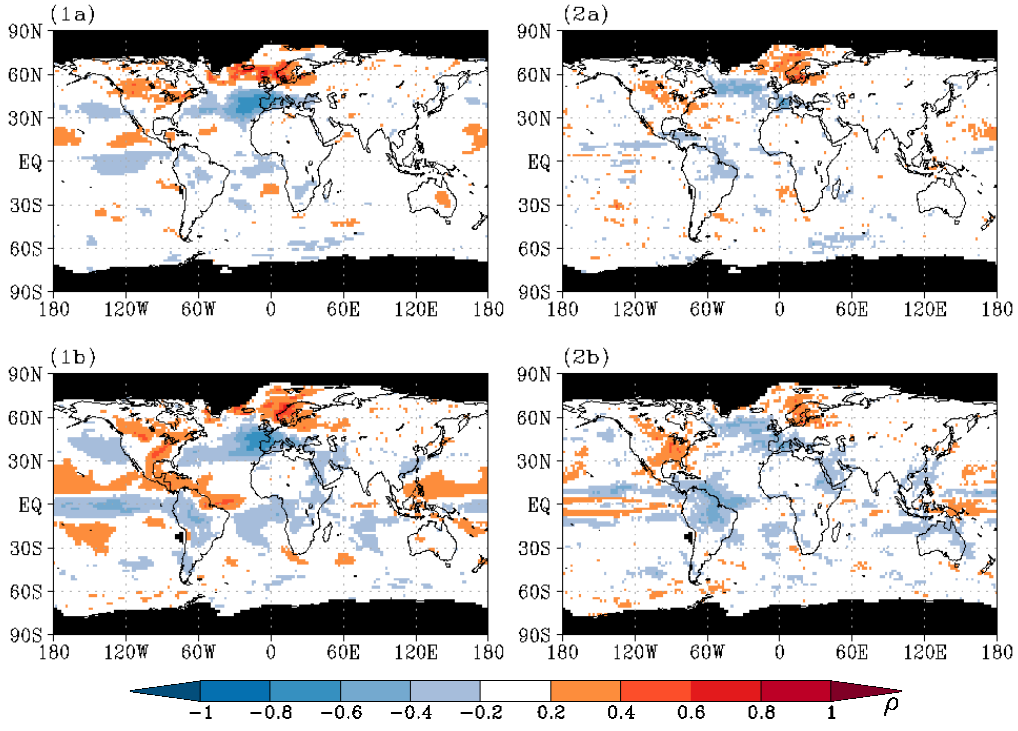

Figure 6.4— Correlations between NAO (1) and CAPE, and (2) CIN respectively. Correlation coefficients ρ computed from monthly means of (a) the 20C simulation and (b) the A1B scenario. Coloured shadings are significant at the 95 % level. The black shading marks those regions with CAPE > 0 Jkg^{-1} occurring less than 10 times during an average year.

6.3 Southern Annular Mode, SAM

The Southern Annular Mode (SAM) is the largest source of variability in the Southern Hemisphere. Similar to the NAO, SAM also has its strongest influence of the atmosphere during the winter months (JJA). The SAM index is determined from monthly mean values of the geopotential height at 700 hPa. First the annual mean is subtracted, then the mean is determined over the winter months. The first principal component is computed via EOF analysis of the region 0-360°E; 20-90°S. A linear trend is removed before the Spearman rank correlation is applied on CAPE and CIN respectively. The SAM index time series in Fig. 6.5 is divided by its standard deviation.
The original and detrended time series of the SAM index show hardly any differences. The time slice of the 20C simulation is dominated by a strong negative SAM event. The time slice of the A1B scenario also shows a prevailing negative index. However, the magnitude of the index is weak with $\text{SAM}_{index} < -1$. In general, the SAM index is weaker in the A1B scenario exceeding the absolute value of 1 less often than during the 20C simulation.
The correlation analysis reveals similar pattern for CAPE and CIN (Fig. 6.6). Although the SAM is defined by a pressure pattern in the Southern Hemisphere, significant correlation coefficients occur also in the Northern Hemisphere. The dominant pattern in the Southern hemisphere with regard to magnitude shows a band of positive correlation coefficients between approximately 50°S and Antarctica, interrupted by negative correlations over the Weddell Sea and the Ross Sea, which are less pronounced in the A1B scenario. Adjacent to the band of positive coefficients is a band of negative coefficients between approximately 30-50°S, which extend towards the tropical regions. Correlations are also visible along the equator and on the Northern Hemisphere. Similar to the correlation pattern of the NAO the pattern of the SAM resembles those of ENSO with reversed sign along the equator (occurs only in the 20C simulation). Claud et al. (2009) report about relations between the teleconnections of ENSO and SAM. However, the influence of ENSO on SAM is more pronounced in the 20C simulation than in the A1B scenario, which discriminates SAM from ENSO and NAO and their increasing correlation coefficients with a warmer climate.
The negative correlation coefficients over the Southern Hemisphere ocean basins might explain the negative trends in CAPE and CIN during JJA (Fig. A.11 and A.15). The negative SAM index during the 20C time slice enhances the magnitudes of CAPE and CIN in regions with a negative correlation. In contrast, the weak index during the A1B corresponding time slice leads to weaker magnitudes in CAPE and CIN and thus to their negative trends. However, the positive correlation along 60°S in turn should lead to positive trends in CAPE and CIN which is not the case. The correlation between SAM and CAPE and CIN explains the trend pattern only partially.

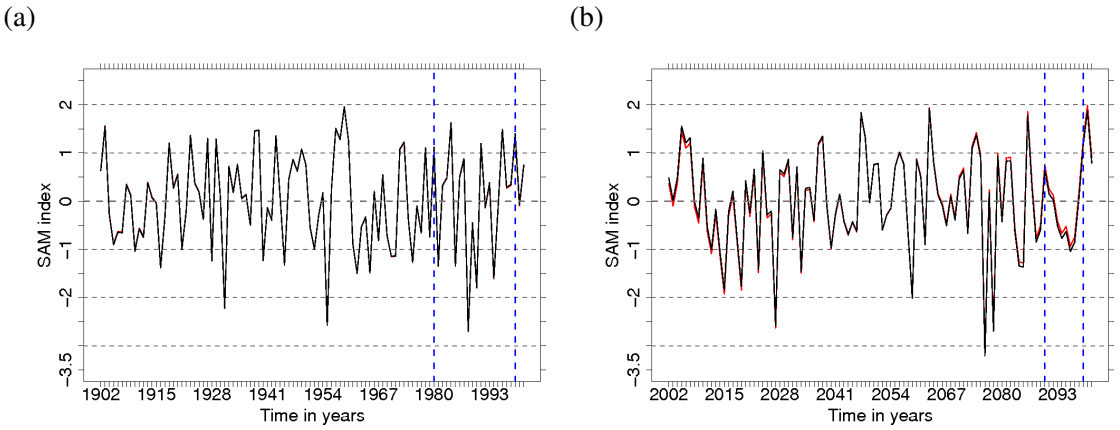

Figure 6.5— SAM time series computed from monthly means of (a) the 20C simulation and (b) the A1B scenario. The red line shows the original time series, while a linear trend is subtracted in the black line. The blue dashed lines denote the first and last year of the time slice taken for the trend analysis in chapter 4.

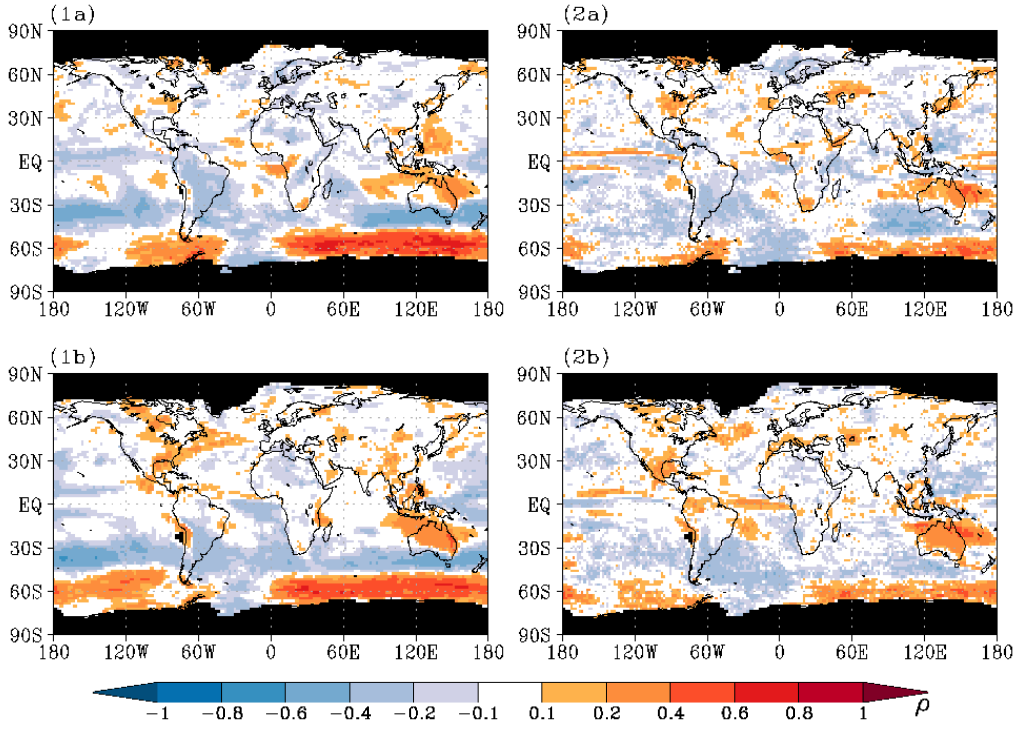

Figure 6.6— Correlations between SAM (1) and CAPE, and (2) CIN respectively. Correlation coefficients ρ computed from monthly means of (a) the 20C simulation and (b) the A1B scenario. Coloured shadings are significant at the 95 % level. The black shading marks those regions with CAPE > 0 Jkg^{-1} occurring less than 10 times during an average year.

6.4 Mean meridional circulation

The mean meridional circulation (MMC) reflects the large scale atmospheric circulations caused by the equator to pol temperature gradient and the Coriolis force (Fig. 6.7). Three cells on each hemisphere balance the temperature gradient. The ascending branches of these cells favour the development of CAPE and counteract CIN (e.g. Dudhia and Moncrieff, 1987; Emanuel et al., 1994 and Stevens et al., 1997). The descending branches of the cells operate vice versa.
In the tropics the influence of the Hadley Cell on the distribution of CAPE and CIN is clearly visible. However, the impact of the Ferrel and polar cell are small compared to those from synoptic disturbances on the development of CAPE and CIN. Note, that several studies argue that it is the convection and thus CAPE that fuel the Hadley circulation (e.g. Fierro et al., 2009). However, this thesis is not about discussing whether the hen or the egg was first, but to describe the variability in CAPE caused by large scale interactions. A change of the location or strength of the MMC leads to a change in distribution of CAPE and CIN. Ye et al. (1998) report about how a changing Hadley Cell due to climate change causes changes in CAPE. However, regional climate change influences should not be neglected.
The change of the Hadley and the Ferrel Cell in the A1B scenario relative the 20C simulation shows a shift in location southwards on both hemispheres (Fig. 6.7), with the exception of the Northern hemispheric Ferrel Cell which hardly changes. The southward shift of the Northern hemispheric Hadley Cell leads to more instability and thus favourable conditions for CAPE along $\sim 10°$N, while the shift of the sinking branch of the Hadley Cell leads to a decrease in CAPE around 30°N. The increase in CAPE is clearly visible in the trend pattern (Fig. 4.1). However, the decrease in CAPE is not. The shift of the Southern hemispheric cells leads to a decrease in CAPE between around 30°S as well as an increase along the equator. Both changes in CAPE are confirmed by the trend patterns, especially for higher percentiles. The expected increase in CIN magnitudes around 30-40°S due to the shift of the sinking branch of the Hadley and Ferrel Cells are also visible in the CIN trends (Fig. 4.1).

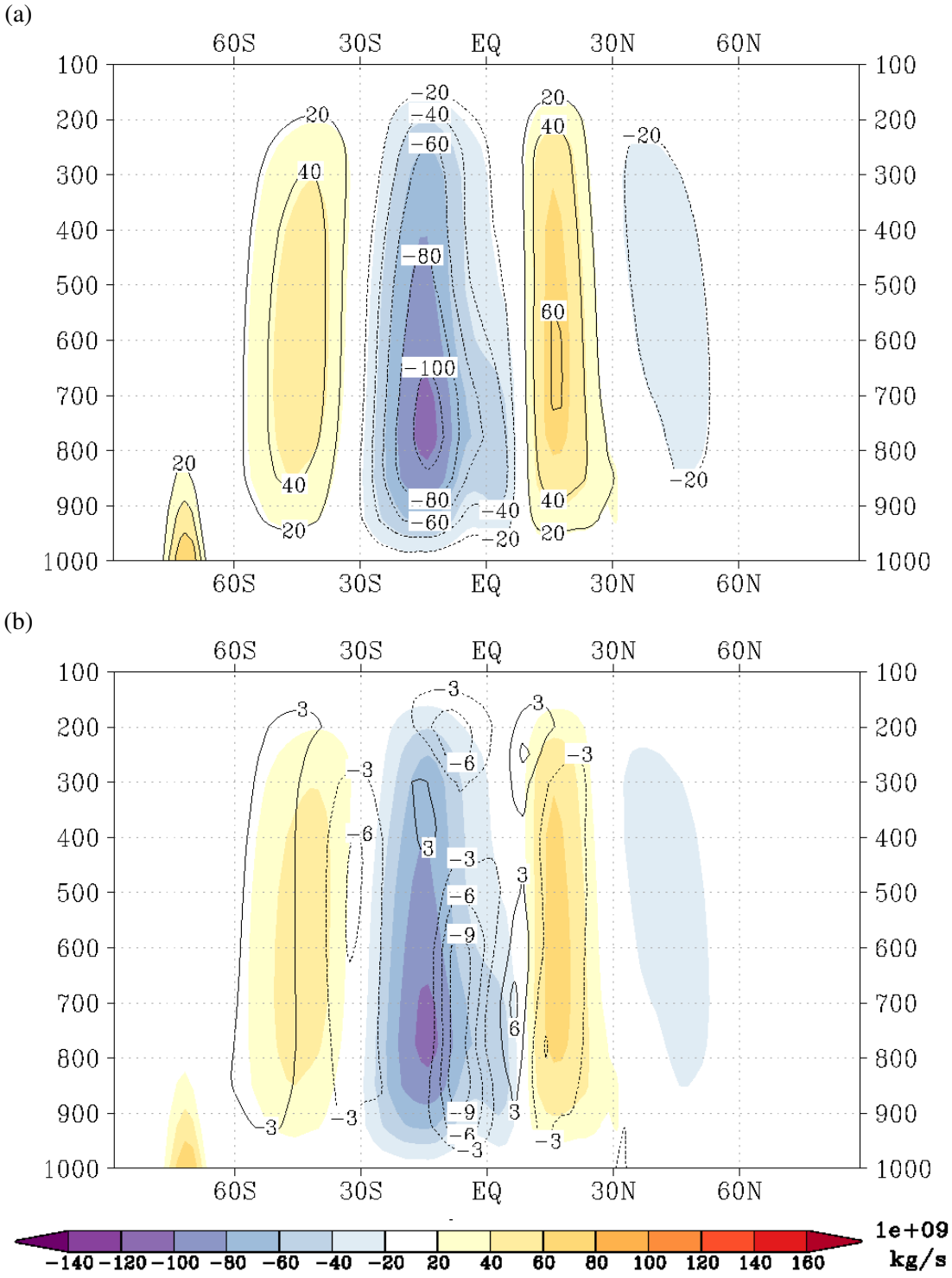

Figure 6.7— Mean Meridional Circulation in units 10^{+09} kg/s computed from the 20C simulation (1980-1999) and the A1B scenario (2090-2099): (a) 20C simulation in shaded colours and A1B scenario in black contours, (b) 20C simulation in shaded colours and difference between the MMC in A1B and 20C in black contours.

6.5 Summary and conclusions

The correlation analysis shows the influence of teleconnections on CAPE and CIN on a global scale. The interactions between CAPE and the Hadley Cell are confirmed and complemented by additional interactions with CIN. However, changes in the strength and location of the teleconnections and the MMC can only partially explain the trend patterns in CAPE and CIN. The strength of the individual large scale influences vary regionally and seasonally. Therefore, the combination of each with the trend patterns in temperature and humidity create the trend pattern in CAPE and CIN. The most prominent factor for the tropical trend patterns is the distribution of humidity along the equator and the adjacent regions. Very similar patterns are reflected in the distributions of q_{ML} and LPW as well as in the correlations of ENSO, NAO and SAM and thus in the trends of CAPE and CIN. The northern hemispheric trends especially over the continental regions seem to be mostly caused by the general increase in temperature and humidity. In contrast, the impact of the SAM and the MMC seem most pronounced in the ocean basins of the Southern Hemisphere.

Chapter 7

Variability of observed precipitation

For the reasons of comparison and assessment, the variability of observed precipitation is analysed from the combined HOAPS-3/GPCC data set kindly provided by Andersson et al. (2010). The Hamburg Ocean Atmosphere Parameters and Fluxes from Satellite Data (HOAPS, $www.hoaps.org$) supplies precipitation over ice free ocean. A detailed description of the methodology deriving precipitation from the satellite measurements is given in Andersson (2009). Continental precipitation is provided via rain gauge measurements by the data reanalysis product version 4 of the Global Precipitation Climatology Centre (GPCC) (Schneider et al., 2008). The two data sets are not adjusted. The combined data set covers most parts of the globe with an equidistant grid spacing of 0.5° with monthly mean values of total precipitation between 1988 and 2006. Caution must be taken by comparing the observed precipitation with the results shown in the previous chapters as the observations show total precipitation. The convective part cannot be analysed separately from large scale precipitation. Least caution is needed when comparing the results in the tropics. About 60 % of tropical rainfall is caused by convective systems. The amount of convective precipitation decreases with increasing latitude.

7.1 First moments of precipitation

The mean and residual standard deviations are compared to those of CAPE and CIN for the whole time series as well as for each season separately. The mean annual cycle is subtracted before calculating the standard deviation yielding the residual standard deviation. The pattern of mean CAPE in the tropics in the ERA-40 data set reflects a similar pattern to the mean precipitation (Fig. 7.1). One ITCZ north of the equator is clearly identifiable, which represents the main difference between the pattern in the tropical CAPE of the 20C simulation and those in the ERA-40 data set. Moreover, the CAPE pattern representing the ITCZ is wider in the tropical Pacific. However, the magnitudes of CIN are large in those regions too and probably prevent convection from developing. The regions with the large CIN overlay the wider CAPE regions leaving a similar pattern as in precipitation. A combination of too wide CAPE patterns which resemble those of precipitation if the large magnitudes of CIN are accounted for, occur over Central Africa, the western part of the Sahara and those regions with cold upwelling water at the west coasts of most continents. In addition, the pattern of the mean distributions resemble each other over North America.

The agreement of the pattern improves further during the winter and summer seasons (Fig. 7.1), especially over Asia during JJA.

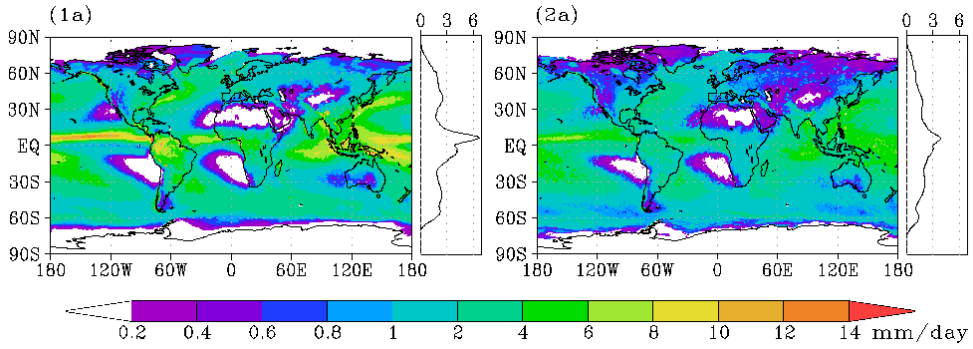

Figure 7.1— (1) Mean and (2) residual standard deviation of observed precipitation in mm/day.

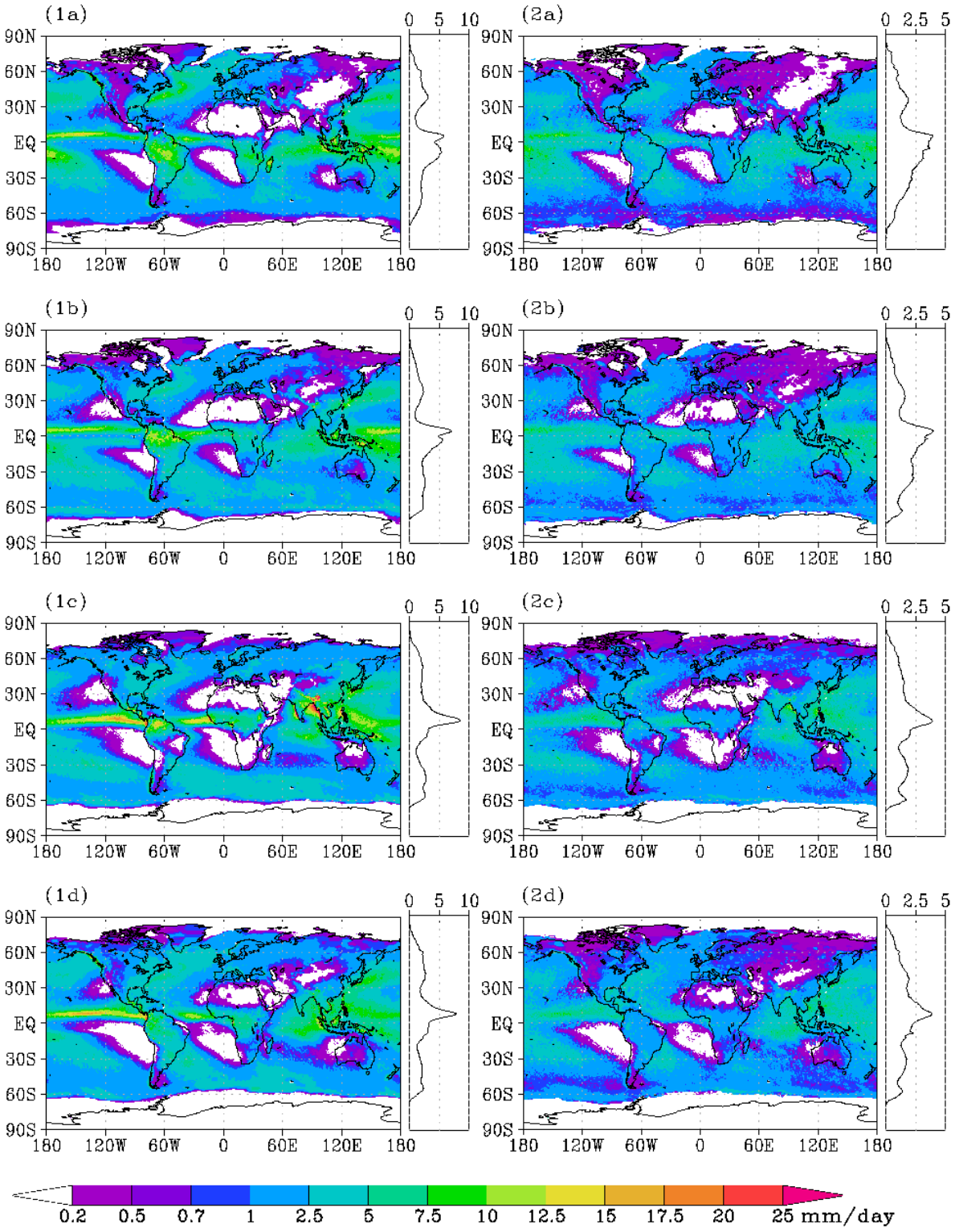

Figure 7.2— (1) Seasonal mean and (2) residual standard deviation of observed precipitation in mm/day: (a) DJF, (b) MAM, (c) JJA, (d) SON.

7.2 Memory in precipitation

The distribution and length of the memory in the observed precipitation is analysed globally (see section 5.1 for methodology). An additional regional analysis focus on the same regions as in chapter 5. The regional memory analysis shows a short memory of 3 days in the ACF and a long memory up to 9000 days in DFA2 and power spectra in CAPE over the North Atlantic (Fig. 5.4-5.6), south-east of Greenland ($\sim 41°$W, 59°N). Due to the monthly mean values in the precipitation time series, the lowest time range consisting memory is restricted to one month. Therefore, it is not surprising that the ACF does not reveal any memory in this region (Fig. 7.2). However, the power spectra and the DFA2 show memory up to 20 months. The memory in precipitation is not as long as in CAPE. Nevertheless, 20 months is surprisingly long for total precipitation, which is probably caused by the influence of the NAO (Andersson et al., 2010).
The memory in CAPE and precipitation is also compared in detail over the western equatorial Pacific, where the influence of ENSO is visible in CAPE ($\sim 161°$E, 0.5°N). The ACF in CAPE from the ERA-40 data set indicates long memory with scaling, which is confirmed in the power spectra and the DFA2 analyses ($\beta \sim 1$ up to 7000 days). The ACC in precipitation also indicates longer memory. Note, that the magnitude of the ACC is smaller at lag = 1 month compared to the ACC at lag = 2 months. The power spectra of precipitation also reveals large variability during the first ten months, before it follows a relatively smooth slope of $\beta \sim 1$ up to 100 months. Unfortunately, the precipitation data set is not long enough to reveal any clear signals of superimposed cycles. The power spectrum shows one peak between 6 and 7 months, which could indicate the Madden-Julian oscillation. However, the peak does not exceed the range of variability during the previous months. In addition, one could argue that a very wide cycle superimposes the periods of 20 to 100 months, which indicates ENSO. On the other hand, the slope might be steeper than $\beta \sim 1$ which reaches saturation around 200 months. The DFA2 in CAPE as well as in precipitation shows long memory until the end of the time series analysed (DFA2 is able to detect memory reliably up to a fourth of the length of the original time series.). CAPE computed from the ERA-40 data set does not indicate a clear influence of ENSO but indicates it by an increasing slope at low frequencies in DFA2. A similar increase is visible in DFA2 determined from the precipitation data.
The global distribution of memory in precipitation determined by the decay time scale τ_m does not represent the pattern in CAPE and vice versa. However, the pattern of the memory determined by DFA2 in CAPE and precipitation resemble each other well. The agreement of the spread and magnitude of α improves further if the memory of CIN is considered. Roughly speaking: $\alpha_{precipitation} \approx \alpha_{CAPE} - \alpha_{CIN}$.

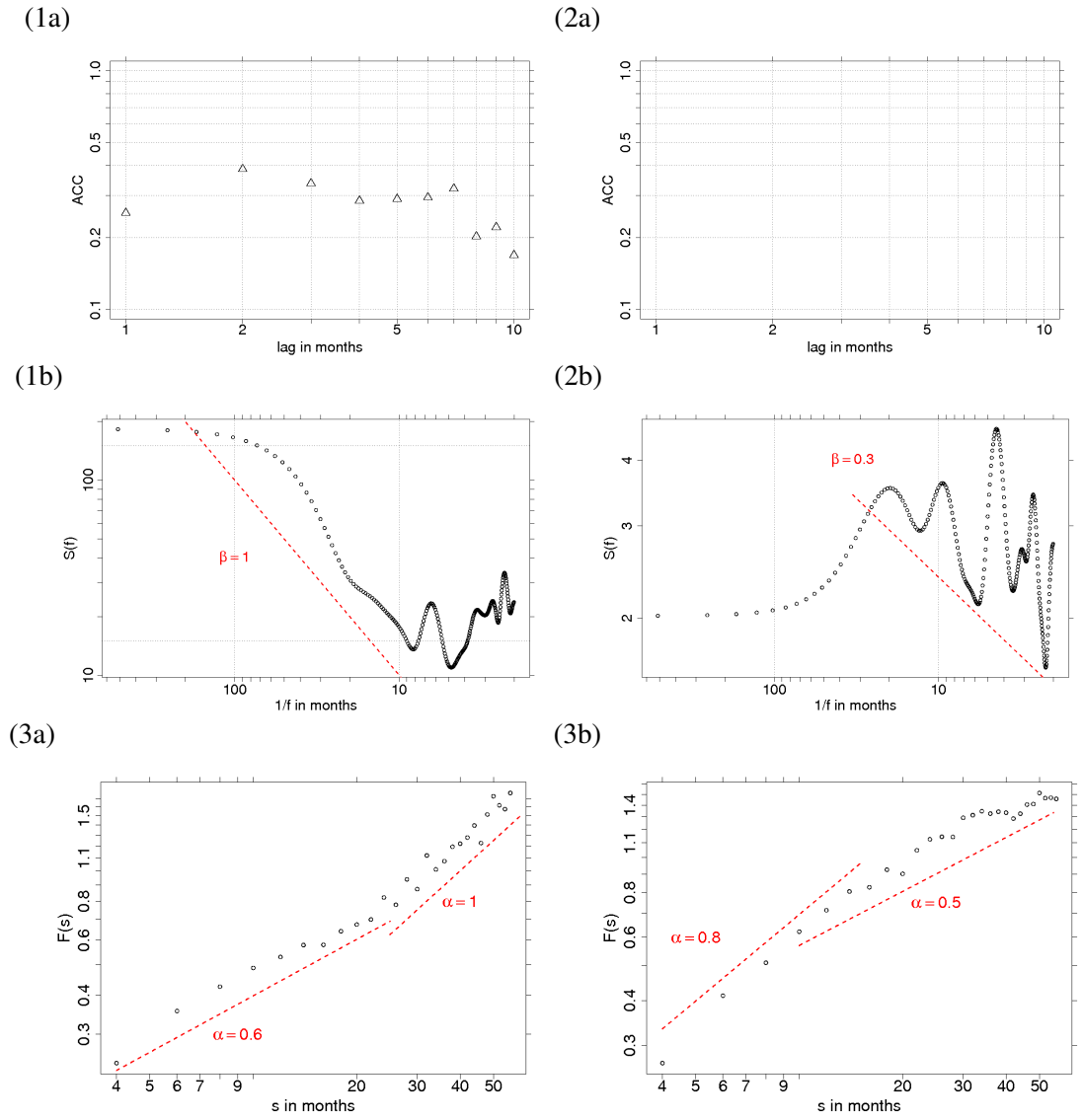

Figure 7.3— (1) ACF, (2) power density spectra and (3) fluctuation function (DFA2) of observed precipitation at (a) the equatorial Pacific and (b) south-east of Greenland.

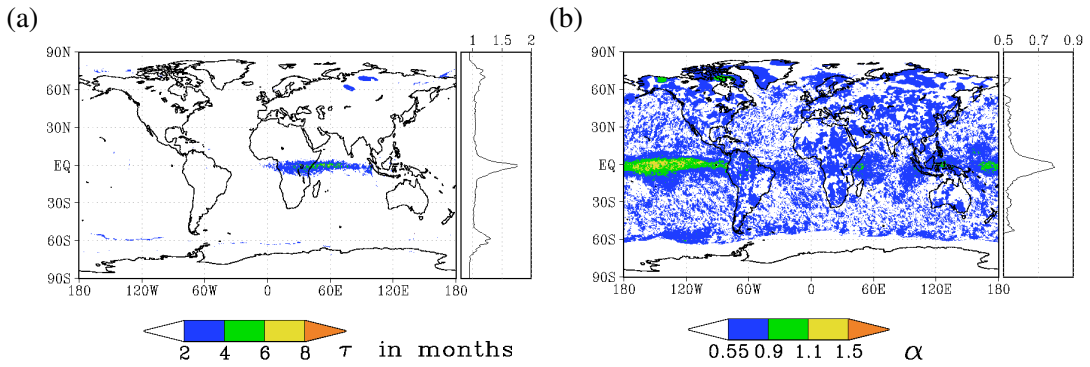

Figure 7.4— (a) Decay time scale in months and (b) DFA2 in the time interval 14 to 60 months of observed precipitation.

7.3 Summary and conclusions

A comparison is presented in this chapter between the variability of total precipitation and CAPE in combination with CIN. The comparison is restricted by the length of the precipitation data set and by the fact that convective precipitation cannot be considered on its own if precipitation is observed rather than simulated. Nevertheless, the variability of a combined CAPE and CIN distribution resembles those relatively well of total precipitation in the tropics. The memory shows similar spread and length. Although, all variables show interactions with the NAO and the mean distributions over North America agree reasonable well, the similarities in variability decrease outside the tropics considerably. Therefore, the combination of CAPE and CIN is able to express the variability of convective precipitation on a broad regional and time scale. However, the comparison fails to confirm this result for extra-tropical regions.

Chapter 8

Discussion and conclusions

This thesis addresses the question whether CAPE and CIN combined are able to reflect the variability in convective precipitation (CP) and thus can be used to determine CP variability in a warmer climate. The detour via CAPE and CIN is made due to the fact that CP cannot be measured independently from large scale precipitation (LSP). Moreover, general circulation models parameterise CP. CAPE determines the energy available to develop convection while CIN describes the stability of the lower atmosphere and thus determines whether convection is likely to be initiated. Many parametrisations of CP include CAPE. However, it is debated whether CIN is sufficient in estimating the initiation of convection. The advantage of the CAPE and CIN combination is their direct dependence on temperature and humidity which are easier measured and thus better assimilated in reanalysis data. Moreover, temperature and humidity variables are more realistically represented in simulations.
Trends and memory of CAPE and CIN are analysed globally on short and long time scales in present-day and a future warmer climate. To identify the cause of their variability, additional analyses are conducted for temperature and humidity in the mixed layer (ML, the lowest 100 hPa of the atmosphere) and above. Furthermore, correlations with teleconnections and the location and strength of the mean meridional circulation (MMC) are investigated. A comparison of the results, gained in this thesis, with the variability in observed total precipitation (TP, TP = CP + LSP) partially answers the question of the CP variability. Although, the TP data set consists of a high spatial resolution, the temporal resolution consists of monthly time steps only. Nevertheless, the variability of a combined CAPE and CIN distribution resembles those relatively well of total precipitation in the tropics, where the ratio of CP in TP lies at about 60 %. Although, all variables (CAPE, CIN and CP) show interactions with the NAO and their mean distributions over North America agree reasonably well, the similarities in variability decrease considerably outside the tropics.
From this comparison, the conclusion is drawn that the combination of CAPE and CIN is able to express the variability of CP on a broad regional and time scale. However, the comparison fails to confirm this result for extra-tropical regions. Within the tropics, the weather conditions leading to convection are determined by large scale flows of temperature and humidity like the Hadley circulation. These large scale flows in combination with the absence of synoptic disturbances yield the dominant type of CP. Thus the variability in CP is mainly caused by these large scale flows. However, the variability of the tropical oceans, especially the Pacific, is strongly influenced by ENSO.

The pattern of ENSO is visible in the correlations between CAPE, CIN and Enthalpy H, the trend pattern in CAPE and CIN, and the pattern of memory on inter-annual time scales. The influence of the Hadley cell is visible in the trend pattern in CAPE and CIN in the southern hemisphere tropics which are caused by the southward extension of the Hadley cell. In addition to ENSO, the distribution of humidity within the ML, q_{ML}, plays the strongest role in CAPE and CIN and thus CP variability.
Outside the tropics, the dominant form of precipitation is LSP. CP occurs mainly along cold fronts and in convective cells in the mid-latitudes, and is produced by polar lows in higher latitudes. The weather conditions leading to convection are caused by mesoscale phenomena. The smaller size of the synoptic conditions leading to convection as well as the fact that the extra-tropical northern hemisphere is largely covered by continents redistribute the order of the influences of CAPE and CIN variability. The correlation analysis shows that the distribution of q_{ML} has the strongest impact on CAPE and CIN over the continents. Over the continents, variability is also affected by orography which influences the availability of humidity and such the variability in CAPE and CIN. However, the NAO causes a negative trend over the North Atlantic and is also visible in the memory distributions.
Since the southern hemisphere, especially in the extra-tropics, is mainly covered by ocean, the influences of the MMC as well as of the SAM are less disturbed by orographic effects and thus seem to have the strongest effects on variability in CAPE and CIN. An additional explanation for the decreasing magnitudes in CAPE and CIN on the southern hemispheric extra-tropics yields the correlation between CAPE, CIN and Enthalpy H.
From the changing CAPE and CIN distributions in a warmer climate the following conclusions are drawn:

- The simultaneous increase in CAPE and CIN over most continents and northern hemisphere ocean areas lead to less often but more intense CP.
- Over the North Atlantic, CAPE decreases while CIN increases and thus CP is likely to occur less frequent and less intense.
- North Atlantic polar lows seem to shift their region of highest frequency and intensity from south-east of Greenland towards north of Norway where CAPE increases in magnitude but CIN decreases.
- Most regions over the southern hemisphere ocean show decreasing CAPE with simultaneously decreasing CIN which leads to more frequent but less intense CP.

The global analyses of the memory of the atmosphere reveal that almost all continents and ocean basins show memory in daily CAPE and CIN time series at long time scales. Knowledge of regions with memory shows potential in predictability and if, in addition, scaling exists, the probability of extreme event recurrence times can be anticipated. On the other hand it has to be noted, that memory, in general, is strongly linked to trends and their analyses which, however, are eliminated when employing detrended fluctuation analysis (DFA2). In a warmer climate the regions with higher fluctuation (Hurst) exponents expand in the tropics due to an intensification of ENSO with regard to spread and frequency. In contrast, SAM and NAO do not change in a warmer climate and thus the memory pattern does not change considerably in the extra-tropics. The additional analyses

of the ECHAM5 simulation with the climatological SST confirm not only the previous findings that the more realistic the ocean simulation, the longer the memory (Fraedrich and Blender, 2003), but that the ocean variability influences the mean CAPE distribution, while it does not impact the mean CIN distribution.

Chapter 9

Outlook

The advantage of any global analysis is the detection of the 'big picture'. In this thesis, the global correlation analysis identified that e.g. ENSO influences CAPE over the Southern Ocean. However, the disadvantage of global analysis is that there is not enough time for a detailed investigation of every region. For example, the pattern of the NAO correlation with CAPE indicates the presence of the PNA (Pacific/North American index), which is not further investigated in this study. Moreover, the theoretical distribution of CAPE ranges from near Gaussian within the tropics towards a Gamma-like shape in higher latitudes, which complicates the global analysis of a trend considerably.
If I had infinite time and computer resources, especially hard disc memory, I would like to analyse the following subtopics further:

- In the computation of CAPE the presence of ice particles in high altitude clouds is neglected. The freezing of the water droplets within a parcel (lifted reversibly) in high altitudes would release latent heat, which increases the buoyancy of the parcel. This effect is expected to play a non-negligible role outside the tropics.

- The Topeka sounding (Fig. 2.1) reveals that a low vertical resolution can miss the correct altitude of the tropopause by more than 50 hPa. Therefore, a higher vertical resolution of the data set analysed, especially at higher altitudes, would improve the global distributions of CAPE and might reveal underestimated large CAPE magnitudes which then might change the variability.

- The results gained in this thesis show that the variability in CP can only be obtained by a combination of CAPE and CIN. Therefore, creating one parameter might simplify the variability analysis, especially those of memory. The new parameter needs probably regional weights depending on the magnitude and frequency of CAPE, e.g.

$$KR = \frac{CAPE}{CIN}\omega$$

  where ω is the weighing factor.

- I would like to identify the influence of more teleconnections and cycles, such as the PNA, the Madden-Julian circulation, or the Walker circulation.

- The comparison of additional time slice differences between a control run and the A1B scenario could test how much change in variability is caused by global warming and how much change is caused by ENSO and other teleconnections.
- Regional simulations can supplement the 'big picture' in a specific region, e.g. Hamburg or Trentino (Italy). The higher horizontal resolution would include additional humidity sources like the Elbe river or the Adriatic Sea. Furthermore, more realistic orographic features like the Alps are expected to change the variability of temperature and lapse rates as well as the flow of moisture and thus instability.
- The combination of CAPE with other variables e.g. with wind shear reveals the distribution of severe storm potential (Brooks et al., 2003). On the other hand, the combination of CAPE with the ocean temperature and boundary layer temperature leads to the thermodynamic potential intensity of tropical cyclones (Bister and Emanuel, 2002). The focus of this thesis could be extended towards the analyses of thunderstorms or hurricanes.

Bibliography

Allan, R. P. and B. J. Soden, 2007: Large discrepancy between observed and simulated precipitation trends in the ascending and descending branches of the tropical circulation. *Geophysical Research Letters*, **34**, L18705.

Andersson, A., 2009: *The HOAPS climatology: Evaluation and applications*. PhD thesis, Universität Hamburg, Max-Planck-Institut für Meteorologie.

Andersson, A., S. Bakan, and H. Graßl, 2010: Satellite derived precipitation and freshwater flux variability and its dependence on the North Atlantic Oscillation. *Tellus*, **62A**, 453–468.

Arpe, K., S. Hagemann, D. Jacob, and E. Roeckner, 2005: The realism of the ECHAM5 models to simulate the hydrological cycle in the Arctic and North European area. *Nordic Hydrology*, **36**(4-5), 349–367.

Bengtsson, L., S. Hagemann, and K. I. Hodges, 2004: Can climate trends be calculated from reanalysis data? *Journal of Geophysical Research*, **109**, D11111.

Bernstein, L., P. Bosch, O. Canziani, Z. Chen, R. Christ, and et al., 2007: *Climate Change 2007: Synthesis Report. Contribution of Working Groups I, II and III to the Fourth Assessment Report of the Intergovernmental Panel on Climate Change*. IPCC, Geneva, Switzerland, 104.

Bister, M. and K. A. Emanuel, 2002: Low frequency variability of tropical cyclone potential intensity 1. Interannual to interdecadal variability. *Journal of Geophysical Research*, **107**, 4801.

Blechschmidt, A.-M., S. Bakan, and H. Graßl, 2009: Large-scale atmospheric circulation patterns during polar low events over the Nordic seas. *Journal of Geophysical Research*, **114**, D06115.

Blender, R. and K. Fraedrich, 2003: Long time memory in global warming simulations. *Geophysical Research Letters*, **30**, 1769–1772.

Bolton, D., 1980: The computation of equivalent potential temperature. *Monthly Weather Review*, **108**, 1046–1053.

Brooks, H. E., A. R. Anderson, K. Riemann, I. Ebbers, and H. Flachs, 2007: Climatological aspects of convective parameters from the NCAR/NCEP reanalysis. *Atmospheric Research*, **83**, 294–305.

Brooks, H. E., C. A. Doswell III, and M. P. Kay, 2003: Climatological estimates of local daily tornado probability for the United States. *Weather and Forecasting*, **18**, 626–640.

Brooks, H. E., J. W. Lee, and J. P. Craven, 2003: The spatial distribution of severe thunderstorm and tornado environments from global reanalysis data. *Atmospheric Research*, **67-68**, 73–94.

Cai, W., P. van Rensch, T. Cowan, and A. Sullivan, 2010: Asymmetry in ENSO teleconnection with regional rainfall, its multi-decadal variability, and impact. *Journal of Climate*, **in press**.

Carleton, A. M. and D. A. Carpenter, 1990: Satellite climatology of 'polar lows' and broadscale climatic associations for the Southern Hemisphere. *International Journal of Climatology*, **10**, 219–246.

Claud, C., A. Carleton, B. Duchiron, and P. Terray, 2009: Southern Hemisphere winter cold-air mesocyclones: Climatic environments and associations with teleconnections. *Climate Dynamics*, **33**, 383–408.

Claud, C., B. Duchiron, and P. Terray, 2007: Associations between large-scale atmospheric circulation and poplar low developments over the North Atlantic during winter. *Journal of Geophysical Research*, **112**, D12101.

Colby Jr., F. P., 1984: Convective inhibition as a predictor of convection during AVE-SESAME II. *Monthly Weather Review*, **112**, 2239–2252.

Craven, J. P., R. E. Jewell, and H. E. Brooks, 2002: Comparison between observed convective cloud-base heights and lifting condensation level for two different lifted parcels. *Weather and Forecasting*, **17**, 885–890.

DeMott, C. A. and D. A. Randall, 2004: Observed variations of tropical convective available potential energy. *Journal of Geophysical Research*, **109**, D02102.

Dima, I. M. and J. M. Wallace, 2003: On the seasonality of the Hadley Cell. *Journal of the Atmospheric Sciences*, **60**, 1522.

Doswell III, C. A. and J. S. Evans, 2003: Proximity sounding analysis for derechos and supercells: An assessment of similarities and differences. *Atmospheric Research*, **67-68**, 117–133.

Dudhia, J. and M. Moncrieff, 1987: A numerical simulation of quasi-stationary tropical convective bands. *Quarterly Journal of the Royal Meteorological Society*, **113**, 929–967.

Emanuel, K. A., 1994: *Atmospheric Convection*. Oxford University Press.

Emanuel, K. A., J. D. Neelin, and C. S. Bretherton, 1994: On large-scale circulations in convecting atmospheres. *Quarterly Journal of the Royal Meteorological Society*, **120**, 1111–1143.

Emori, S., A. Hasegawa, T. Suzuki, and K. Dairaku, 2005: Validation, parameterization dependence, and future projection of daily precipitation simulated with a high-resolution atmospheric GCM. *Geophysical Research Letters*, **32**, L06708.

Emori, S., T. Nozawa, A. Numaguti, and I. Uno, 2001: Importance of cumulus parameterization for precipitation simulation over East Asia in June. *Journal of the Meteorological Society Japan*, **79**, 939–946.

Fierro, A. O., J. Simpson, M. A. LeMone, J. M. Straka, and B. F. Smull, 2009: On how hot towers fuel the Hadley Cell: An observational and modeling study of line-organized convection in the equatorial trough from TOGA COARE. *Journal of the Atmospheric Sciences*, **66**, 2730–2746.

Fraedrich, K., 2002: Fickian diffusion and Newtonian cooling: A concept for noise induced climate variability with long-term memory? *Stochastics and Dynamics*, **2**, 403–412.

Fraedrich, K. and R. Blender, 2003: Scaling of atmosphere and ocean temperature correlations in observations and climate models. *Physical Review Letters*, **90**, 108501–(1–4).

Fraedrich, K. and C. Larnder, 1993: Scaling regimes of composite rainfall time series. *Tellus*, **45A**, 289–298.

Fraedrich, K., U. Luksch, and R. Blender, 2004: 1/f model for long-time memory of the ocean surface temperature. *Physical Review E*, **70**, 037301.

Gates, W. L., J. S. Boyle, C. Covey, C. G. Dease, C. M. Doutriaux, R. S. Drach, M. Fiorino, P. J. Gleckler, J. J. Hnilo, M. M. Marlais, T. J. Philips, G. L. Potter, B. D. Santer, K. R. Sperber, K. E. Taylor, and D. N. Williams, 1999: An overview of the results of the Atmospheric Model Intercomparison Project (AMIP I). *Bulletin of the American Meteorological Society*, **80**, 29–55.

Gettelmann, A., D. J. Seidel, M. C. Wheeler, and R. J. Ross, 2002: Multidecadal trends in tropical convective available potential energy. *Journal of Geophysical Research*, **107**, 4606.

Gregory, D., J.-J. Morcrette, C. Jakob, . C. M. Beljaars, A, and T. Stockdale, 2000: Revision of convection, radiation and cloud schemes in the ECMWF integrated forecasting system. *Quarterly Journal of the Royal Meteorological Society*, **126**, 1685–1710.

Hagemann, S., K. Arpe, and L. Bengtsson, 2005: Validation of the hydrological cycle of ERA-40. ERA-40 Project Report 24, ECMWF, http://www.ecmwf.int/publications/.

Hagemann, S., K. Arpe, and E. Roeckner, 2006: Evaluation of the hydrological cycle in the ECHAM5 model. *Journal of Climate*, **19**, 3810–3827.

Holloway, C. E. and J. D. Neelin, 2009: Moisture vertical structure, column water vapor, and tropical deep convection. *Journal of the Atmospheric Sciences*, **66**, 1665–1683.

Hurrell, J. W. and C. Deser, 2010: North Atlantic climate variability: The role of the North Atlantic Oscillation. *Journal of Marine Systems*, **79**, 231–244.

Jungclaus, J. H., M. Botzet, H. Haak, J. Marotzke, U. Mikolajewicz, E. Roeckner, N. Keenlyside, M. Latif, and J.-J. Luo, 2006: Ocean circulation and tropical variability in the coupled model ECHAM5/MPI-OM. *Journal of Climate*, **19**, 3952–3972.

Khodayar, S., N. Kalthoff, J. Wickert, U. Corsmeier, C. J. Morcrette, and C. Kottmeier, 2010: The increase of spatial data resolution for the detection of the initiation of convection. A case study from CSIP. *Meteorologische Zeitschrift*, **19**, 179–198.

Kuang, Z. and C. S. Bretherton, 2006: A mass-flux scheme view of a high-resolution simulation of a transition from shallow to deep cumulus convection. *Journal of the Atmospheric Sciences*, **63**, 1895–1909.

Maraun, D., H. Rust, and T. J., 2004: Tempting long-memory - On the interpretation of DFA results. *Nonlinear Processes in Geophysics*, **11**, 495–503.

Margules, M., 1905: *Über die Energie der Stürme*. Jahrbuch der K. K. Zentralanstalt f¨r Meteorologie, Wien.

Market, P., S. Allen, R. Scofield, R. Kuligowski, and A. Gruber, 2003: Precipitation efficiency of warm-season midwestern mesoscale convective systems. *Weather and Forecasting*, **18**, 1273–1285.

Markowski, P. M., J. M. Straka, and E. N. Rasmussen, 2002: Direct surface thermodynamic observations within the rear-flank downdrafts of nontornadic and tornadic supercells. *Monthly Weather Review*, **130**, 1692–1721.

Marsland, S., H. Haak, J. Jungclaus, M. Latif, and F. Rske, 2003: The Max-Planck-Institute global ocean/sea ice model with orthogonal curvilinear coordinates. *Ocean Modeling*, **5**, 91–127.

Mo, K. C., 2010: Interdecadal modulation of the impact of ENSO on precipitation and temperature over the United States. *Journal of Climate*, **in press**.

Moncrieff, M. W. and M. Miller, 1976: The dynamics and simulation of tropical cumulonimbus and squall lines. *Quarterly Journal of the Royal Meteorological Society*, **102**, 373–394.

Müller, W. A. and E. Roeckner, 2008: ENSO teleconnections in projections of future climate in ECHAM5/MPI-OM. *Climate Dynamics*, **31**, 533–549.

Nakicenovic, N., J. Alcamo, G. Davis, B. de Vries, J. Fenhann, and et al., 2000: *Emission scenarios*. Cambridge University Press.

Nordeng, T. E., 1994: Extended versions of the convective parameterization scheme at ECMWF and their impact on the mean transient activity of the model in the tropics. Technical report, ECMWF Research Department.

Norris, J., 2005: Trends in upper-level cloud cover and surface divergence over the tropical Indo-Pacific Ocean between 1952 and 1997. *Journal of Geophysical Research*, **110**, D21110.

Parker, D. J., 2002: The response of CAPE and CIN to tropospheric thermal variations. *Quarterly Journal of the Royal Meteorological Society*, **128**, 119–130.

Peng, C.-K., S. Havlin, S. H. E., and A. L. Goldberger, 1995: Quantification of scaling exponents and crossover phenomena in nonstationary heartbeat time series. *Physical Review E*, **5**, 82.

Rasmussen, E. N. and D. O. Blanchard, 1998: A baseline climatology of sounding -derived supercell and tornado forecast parameters. *Weather and Forecasting*, **13**, 1148–1164.

Riemann-Campe, K., R. Blender, and K. Fraedrich, 2010: Global memory analysis in observed and simulated CAPE and CIN. *International Journal of Climatology*, **in press**.

Riemann-Campe, K., K. Fraedrich, and F. Lunkeit, 2009: Global climatology of Convective Available Potential Energy (CAPE) and Convective Inhibition (CIN) in ERA-40 reanalysis. *Atmospheric Research*, **93**, 534–545.

Roeckner, E., R. Brokopf, M. Esch, M. Giorgetta, S. Hagemann, E. Kornblueh, L. Manzini, U. Sclese, and U. Schulzweida, 2006: Sensitivity of simulated climate to horizontal and vertical resolution in the ECHAM5 atmosphere model. *Journal of Climate*, **19**, 3771–3791.

Roeckner, E., G. Buml, L. Bonaventura, R. Brokopf, M. Esch, M. Giorgetta, S. Hagemann, I. Kirchner, L. Kornblueh, E. Manzini, A. Rhodin, U. Schlese, U. Schulzweida, and A. Tompkins, 2003: The atmospheric general circulation model ECHAM5 part1, model description. Report 349, Max-Planck-Institut für Meteorologie.

Schneider, U., T. Fuchs, A. Meyer-Christoffer, and B. Rudolf, 2008: Global Precipitation Analysis Products of the GPCC. Internet Publication, available at: http://www.dwd.de/bvbw/generator/DWDWWW/Content/Oeffentlichkeit/KU/KU4/KU42/en/Reports_Publications/GPCC_intro_products_2008,templateId=raw,property=publicationFile.pdf/GPCC_intro_products_2008.pdf.

Simmons, A. J., P. Jones, V. da Costa Bechtold, A. C. M. Beljaars, P. W. Kllberg, S. Saarinen, S. M. Uppala, P. Viterbo, and N. Wedi, 2004: Comparison of trends and low-frequency variability in CRU, ERA-40, and NCEP/NCAR analyses of surface air temperature. *Journal of Geophysical Research*, **109**, D24115.

Stevens, B., D. A. Rabdall, L. X., and M. Montgomery, 1997: Comments on 'On large-scale circulations in convecting atmospheres' by Kerry A. Emanuel, J. David Neelin and Christopher S. Bretherton (July B, 1994, 120, 1111-1143). *Quarterly Journal of the Royal Meteorological Society*, **123**, 1771–1778.

Tiedtke, M., 1989: A comprehensive mass flux scheme for cumulus parameterization in large-scale models. *Monthly Weather Review*, **117**, 1779–1800.

Trapp, R. J., N. S. Diffenbaugh, H. E. Brooks, M. E. Baldwin, E. D. Robinson, and J. S. Pal, 2007: Changes in severe thunderstorm environment frequency during the 21st century caused by anthropogenically enhanced global radiative forcing. *Proceedings of the National Acadamy of Science of the United States of America*, **104**, 19719–19723.

Trapp, R. J., N. S. Diffenbaugh, and A. Gluhovsky, 2009: Transient response of severe thunderstorm forcing to elevated greenhouse gas concentrations. *Geophysical Research Letters*, **36**, L01703.

Trenberth, K. E., 1997: The definition of El Niño. *Bulletin of the American Meteorological Society*, **78**, 2771–2777.

Uppala, S., P. Kallberg, A. Simmons, U. Andrae, V. da Costa Bechtold, M. Fiorino, and et al., 2005: The ERA-40 Reanalysis. *Quarterly Journal of the Royal Meteorological Society*, **131**, 2961 – 3012.

van Oldenborgh, G. J., S. Y. Philip, and M. Collins, 2005: El Niño in a changing climate: A multi-model study. *Ocean Science*, **1**(2), 81–95.

Vyushin, D. I. and P. J. Kushner, 2009: Power-law and long-memory characteristics of the atmospheric general circulation. *Journal of Climate*, **22**, 2890–2904.

Wang, W. and M. E. Schlesinger, 1999: The dependence of convection parameterizations of the tropical intraseasonal oscillation simulated by the UIUC 11-layer atmospheric GCM. *Journal of Climate*, **12**, 1423–1457.

Watterson, I. G., 2009: Components of precipitation and temperature anomalies and change associated with modes of the Southern Hemisphere. *International Journal of Climatology*, **29**, 809–826.

Yano, J.-I., K. Fraedrich, and R. Blender, 2001: Tropical convective variability as 1/f Noise. *Journal of Climate*, **14**, 3608–3616.

Ye, B., A. D. Del Genio, and K. K.-W. Lo, 1998: CAPE variations in the current climate and in a climate change. *Journal of Climate*, **11**, 1997–2015.

Zawadski, I., J. Morneau, and R. Laprise, 1994: Predictability of precipitation patterns: An operational approach. *Journal of Applied Meteorology*, **33**, 1562–1571.

Zhang, G. J., 2002: Convective quasi-equilibrium in midlatitude continental environment and its effect on convecctive parameterization. *Journal of Geophysical Research*, **107**, 4220.

Additional remarks

During my time as a PhD student I worked on several publications: The first publication is based on the earlier computed surface based CAPE. However, the results discussed in this thesis are based on mixed layer CAPE.

- Riemann-Campe, K. K. Fraedrich, and F. Lunkeit, 2009: Global climatology of Convective Available Potential Energy (CAPE) and Convective Inhibition (CIN) in ERA-40 reanalysis. *Atmospheric Research*, **93**, 534-545, DOI: 10.1016/j.atmosres.2008.09.037.

The second publication discusses the memory in present-day climate CAPE and CIN and their correlations with ENSO and NAO. The results published are also used in this thesis in chapter 5.

- Riemann-Campe, K., R. Blender, and K. Fraedrich, 2010: Global memory analysis in observed and simulated CAPE and CIN. *International Journal of Climatology*, **in press**, available online, DOI: 10.1002/joc.2148.

The relation between hail occurrence and CAPE, CIN, wind shear and other atmospheric variables is analysed in the region of Trentino, Italy in a cooperation with Emanuele Eccel, Piero Cau and Franco Biasioli from the IASMA Research and Innovation Centre - Fondazione Edmund Mach - Environment and Natural Resources Area. My Italian colleagues analyse hailpad data with regards to crop damage. They found an increase in extreme hail events during the last decades, which can be confirmed by my CAPE and CIN computation. CAPE decreases while CIN increases in the analysed region leading to less frequent but more intensive occurrences of convection which can lead to hail.

- Eccel, E., P. Cau, K. Riemann-Campe and F. Biasioli, 2010: Quantitative hail monitoring in an alpine area: 35-year climatology and links with atmospheric variables. *International Journal of Climatology*, **in press**, available online, DOI:10.1002/joc.2291.

In addition, a manuscript about the dependency of CAPE and CIN on their vertical resolution is in progress. This work is accomplished in a cooperation with Julia Sander from the Deutsches Zentrum für Luft- und Raumfahrt in Oberpfaffenhofen.

List of Figures

List of Tables

Appendix A

Additional figures

A.1 Seasonal mean and standard deviation of CAPE and CIN

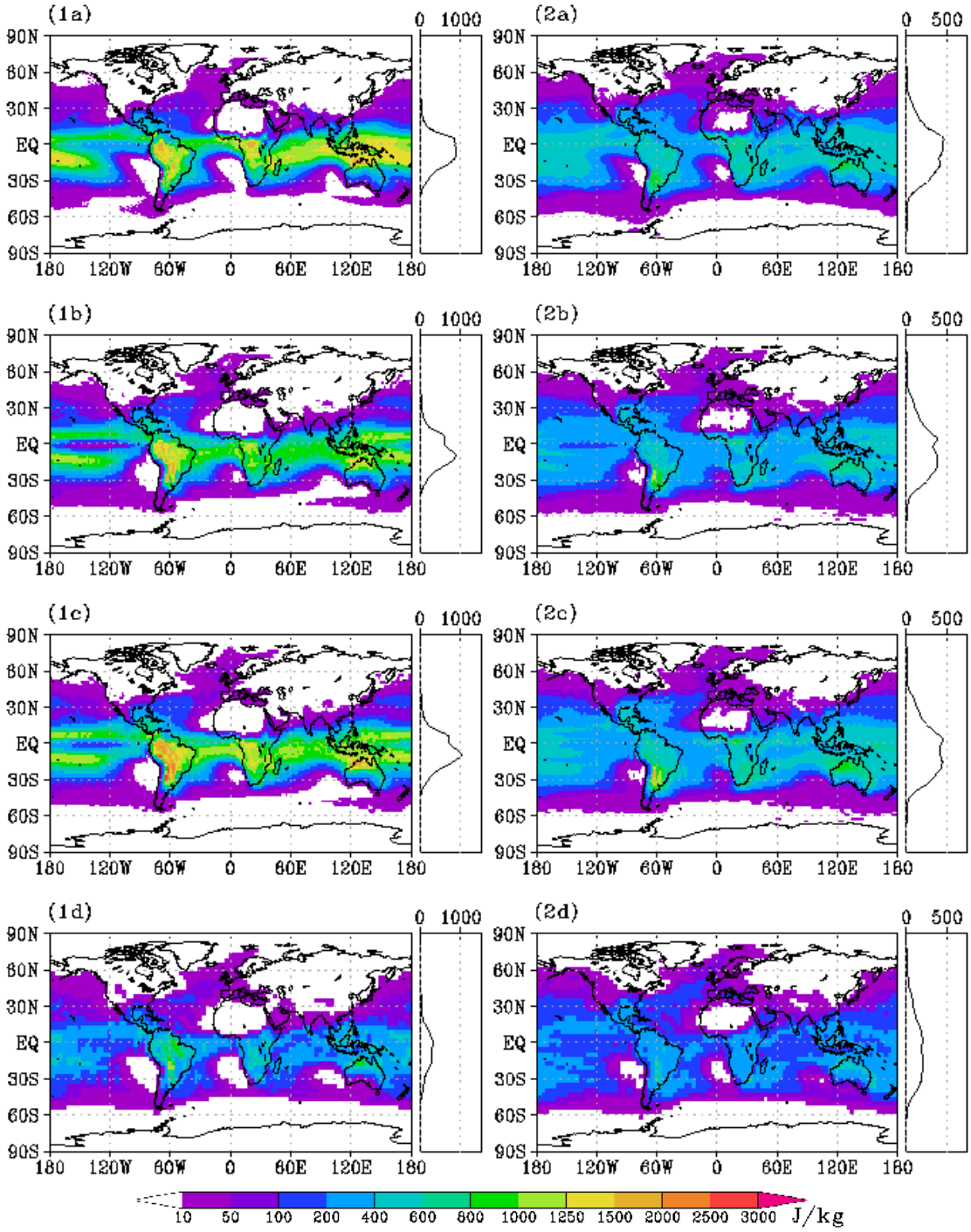

Figure A.1— (1) Mean and (2) residual standard deviation of CAPE in Jkg^{-1} during December, January and February computed from (a) ERA-40 data, (b) 20C simulation, (c) A1B scenario, and (d) UCM.

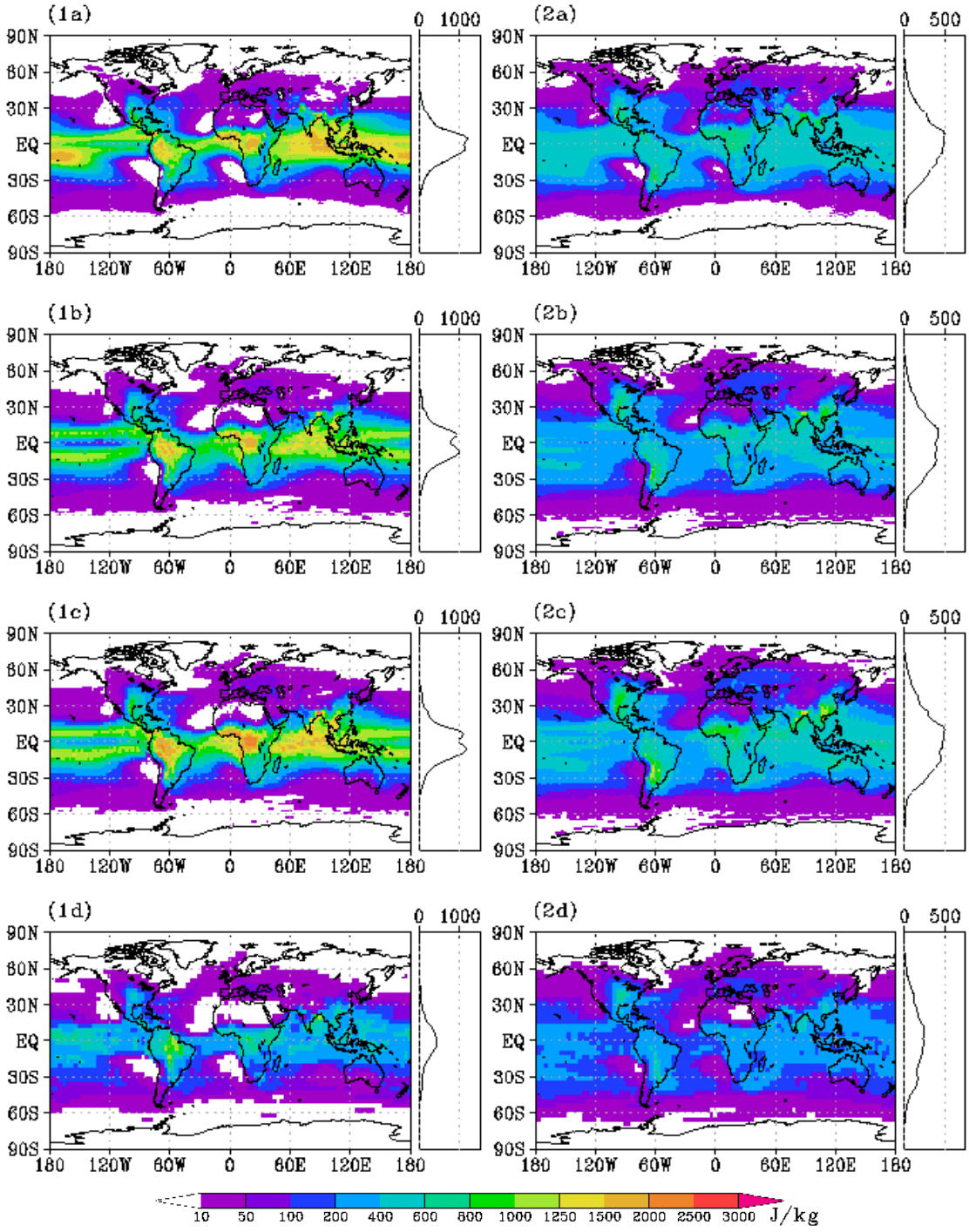

Figure A.2— (1) Mean and (2) residual standard deviation of CAPE in Jkg^{-1} during March, April and May computed from (a) ERA-40 data, (b) 20C simulation, (c) A1B scenario, and (d) UCM.

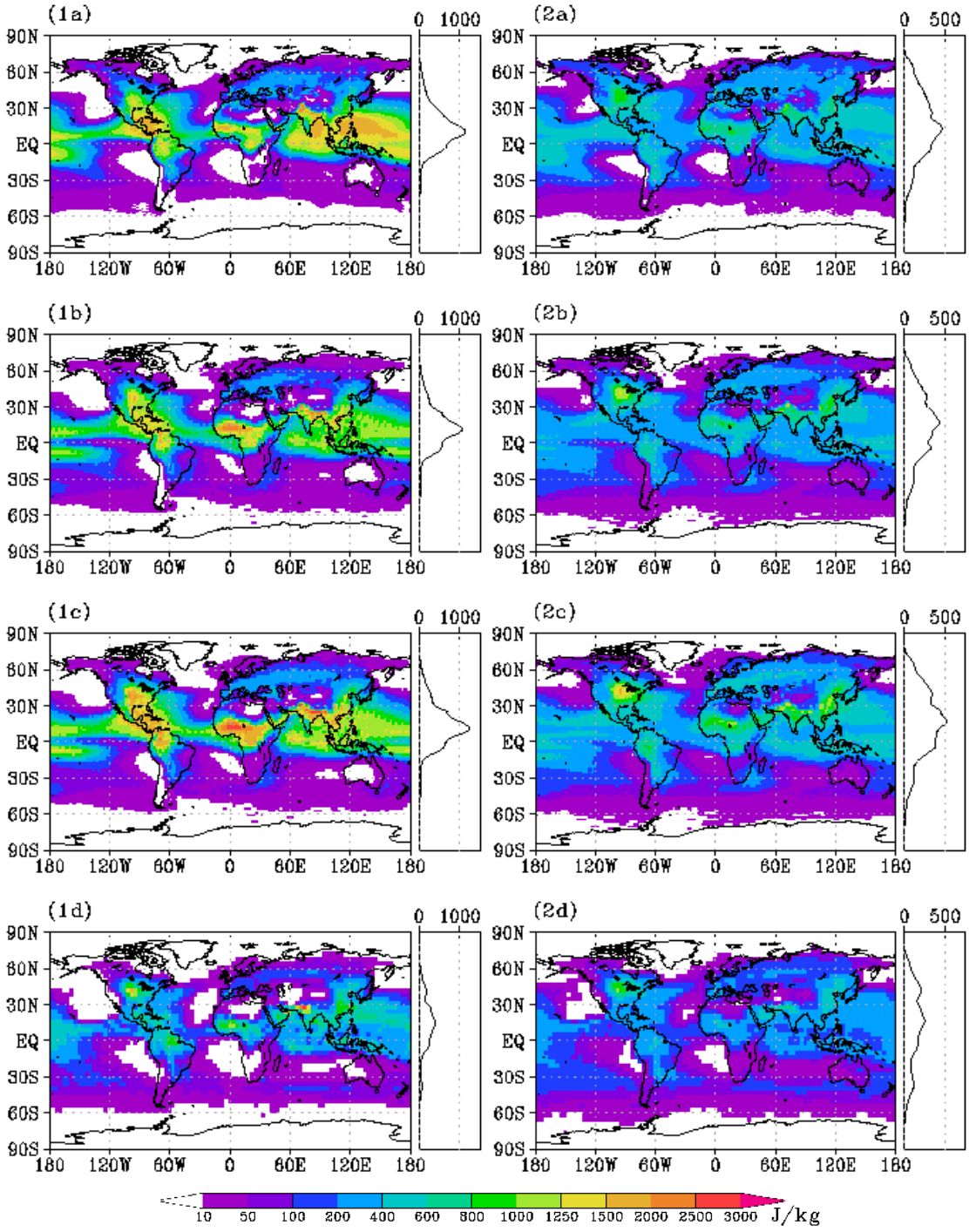

Figure A.3— (1) Mean and (2) residual standard deviation of CAPE in Jkg^{-1} during June, July and August computed from (a) ERA-40 data, (b) 20C simulation, (c) A1B scenario, and (d) UCM.

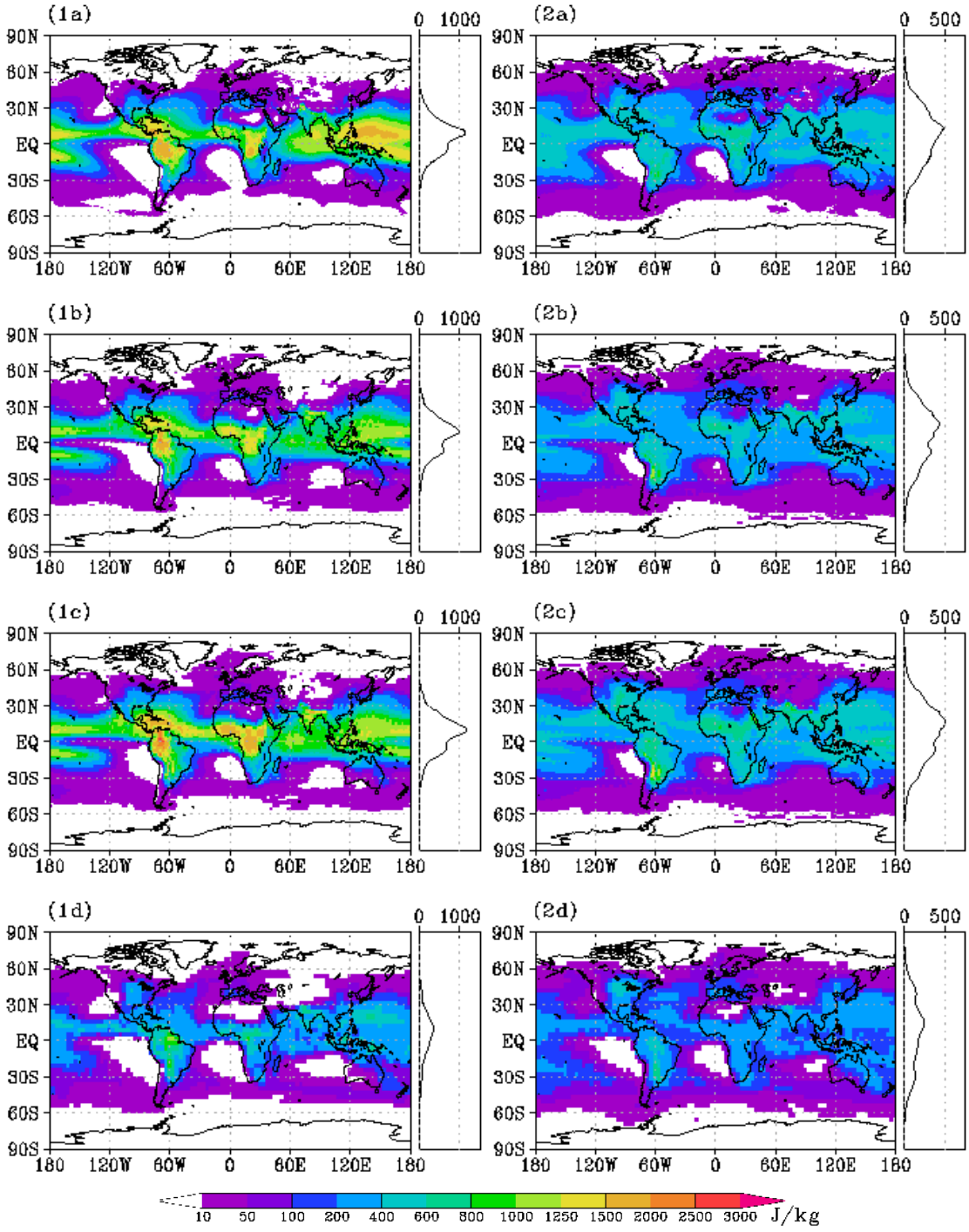

Figure A.4— (1) Mean and (2) residual standard deviation of CAPE in Jkg^{-1} during September, October and November computed from (a) ERA-40 data, (b) 20C simulation, (c) A1B scenario, and (d) UCM.

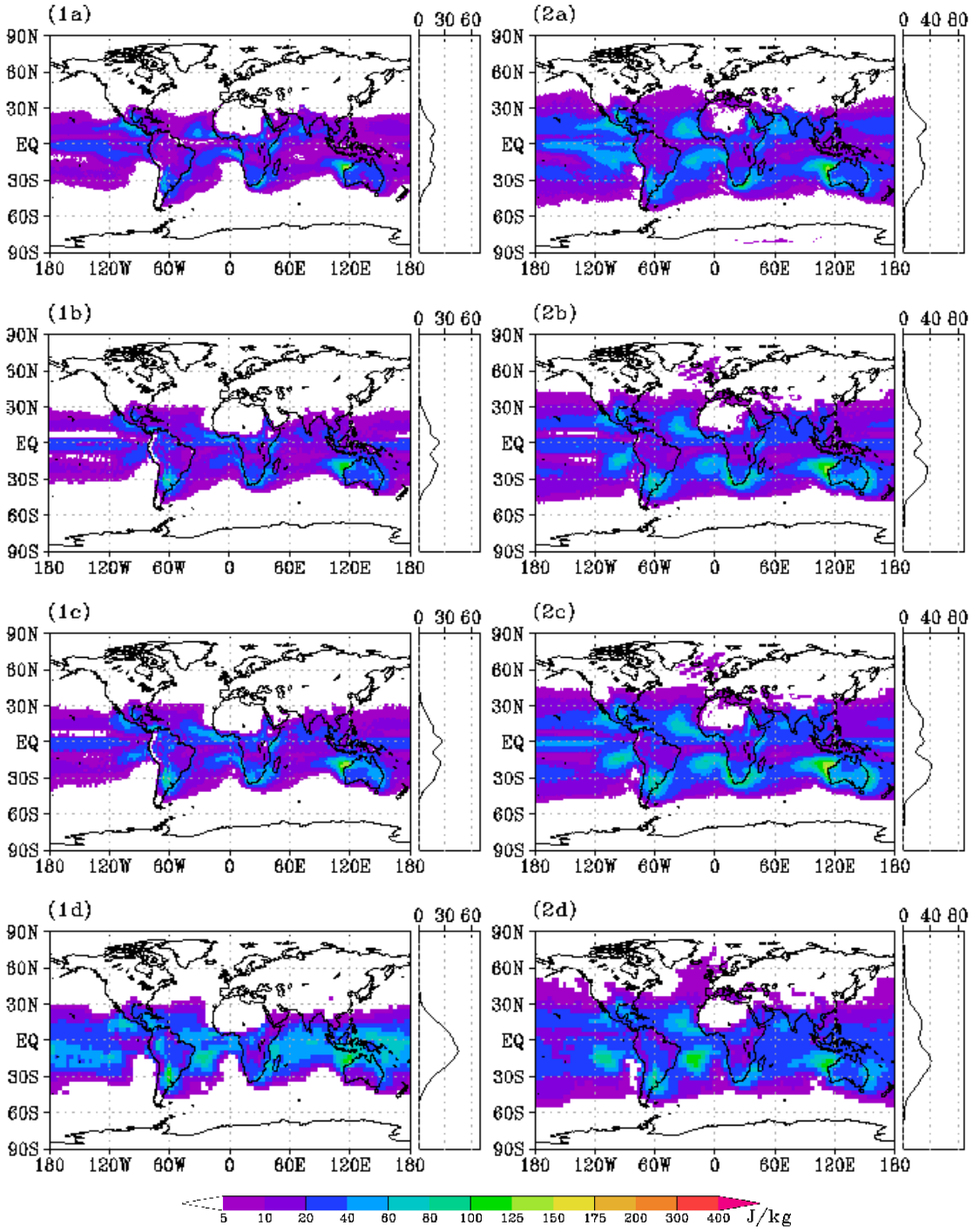

Figure A.5— (1) Mean and (2) residual standard deviation of CIN in Jkg^{-1} during December, January and February computed from (a) ERA-40 data, (b) 20C simulation, (c) A1B scenario, and (d) UCM.

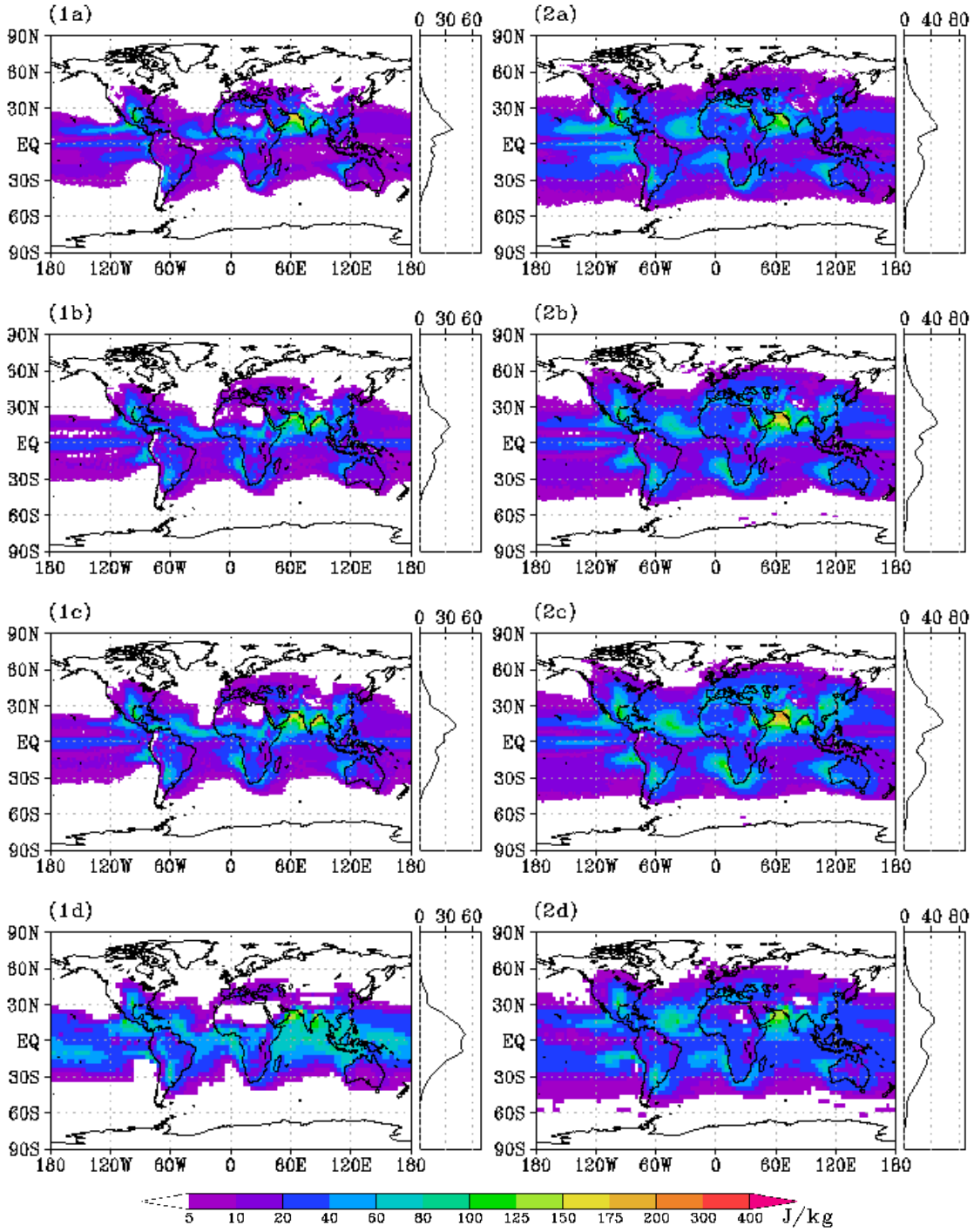

Figure A.6— (1) Mean and (2) residual standard deviation of CIN in Jkg^{-1} during March, April and May computed from (a) ERA-40 data, (b) 20C simulation, (c) A1B scenario, and (d) UCM.

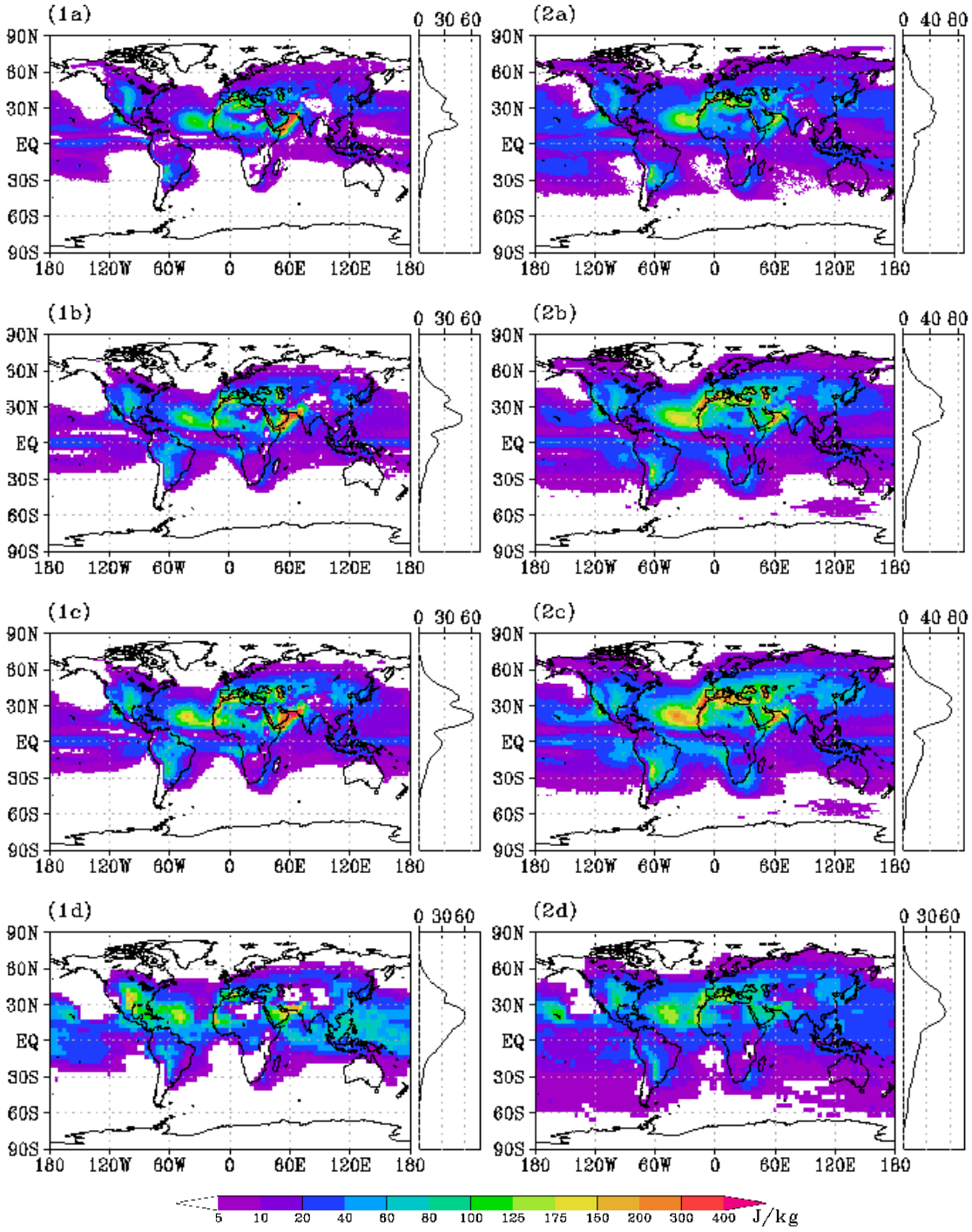

Figure A.7— (1) Mean and (2) residual standard deviation of CIN in Jkg^{-1} during June, July and August computed from (a) ERA-40 data, (b) 20C simulation, (c) A1B scenario, and (d) UCM.

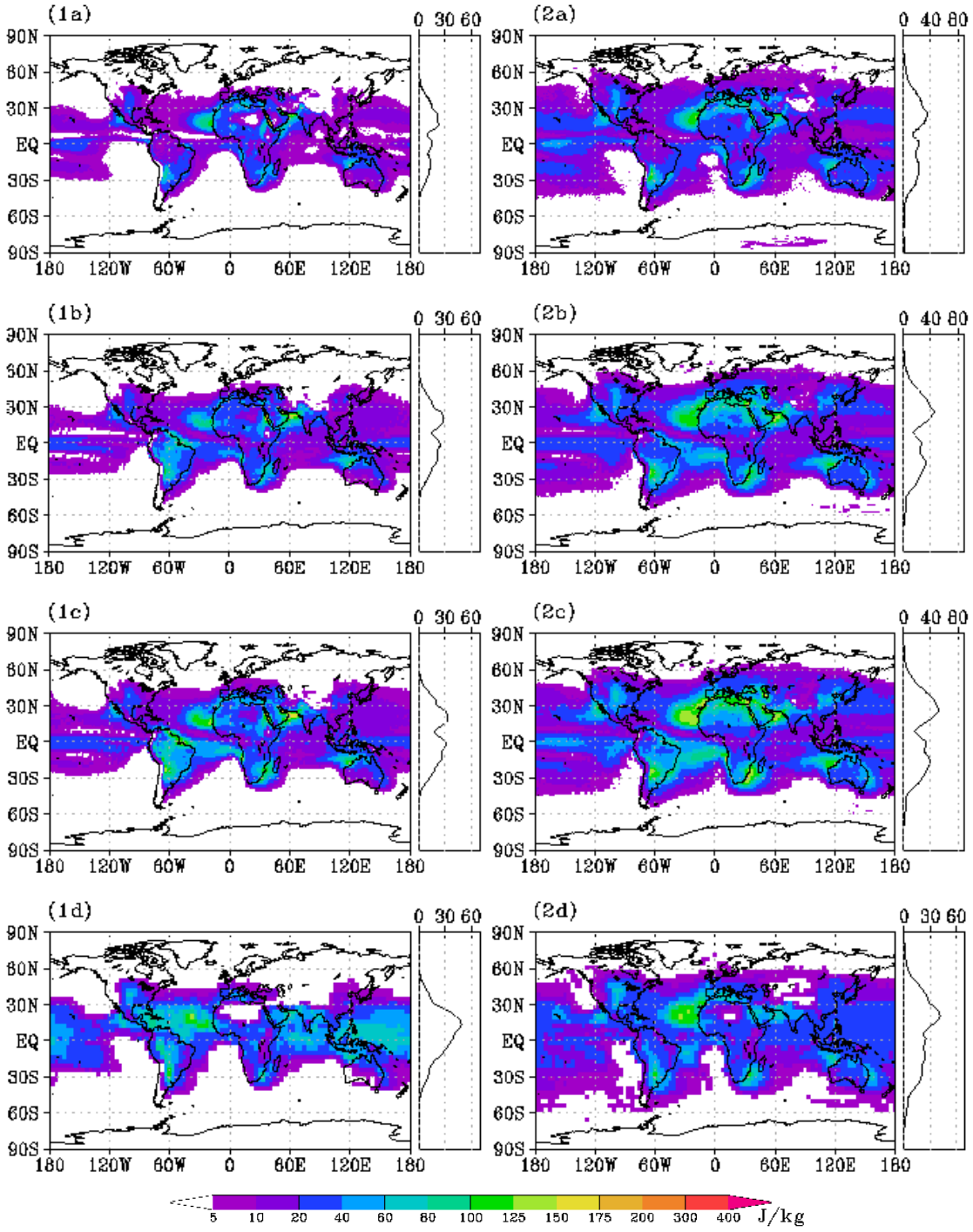

Figure A.8— (1) Mean and (2) residual standard deviation of CIN in Jkg^{-1} during September, October and November computed from (a) ERA-40 data, (b) 20C simulation, (c) A1B scenario, and (d) UCM.

A.2 Seasonal trends in CAPE and CIN

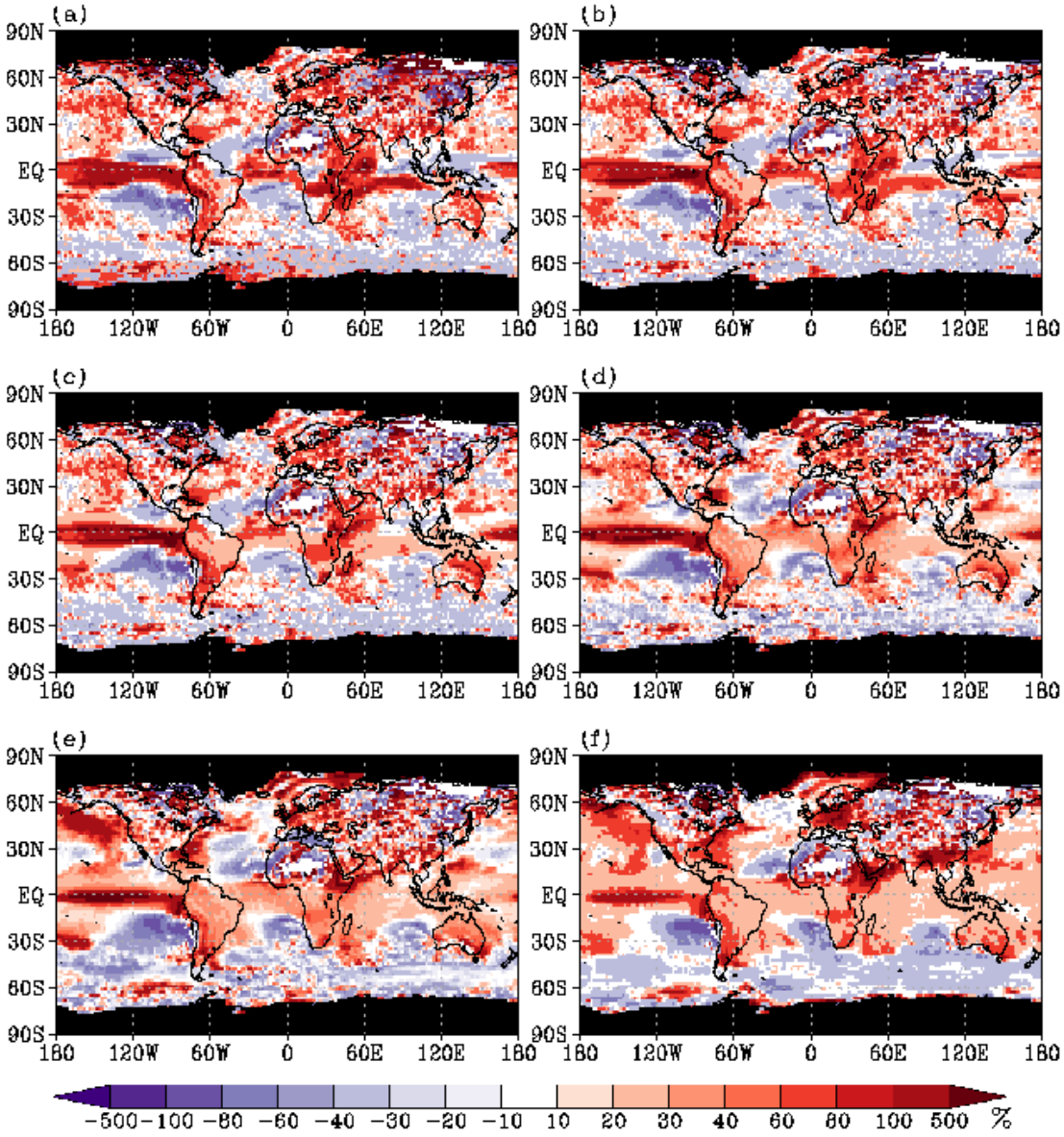

Figure A.9— Ratio of change in % in CAPE during DJF between the A1B scenario (2090-2099) and the 20C simulation (1980-1999) for different percentiles: (a) 5th, (b) 20th, (c) 40th, (d) 60th, (e) 80th, (f) 95th. The black shading marks those regions with CAPE $> 0\ Jkg^{-1}$ occurring less than 10 times during an average year.

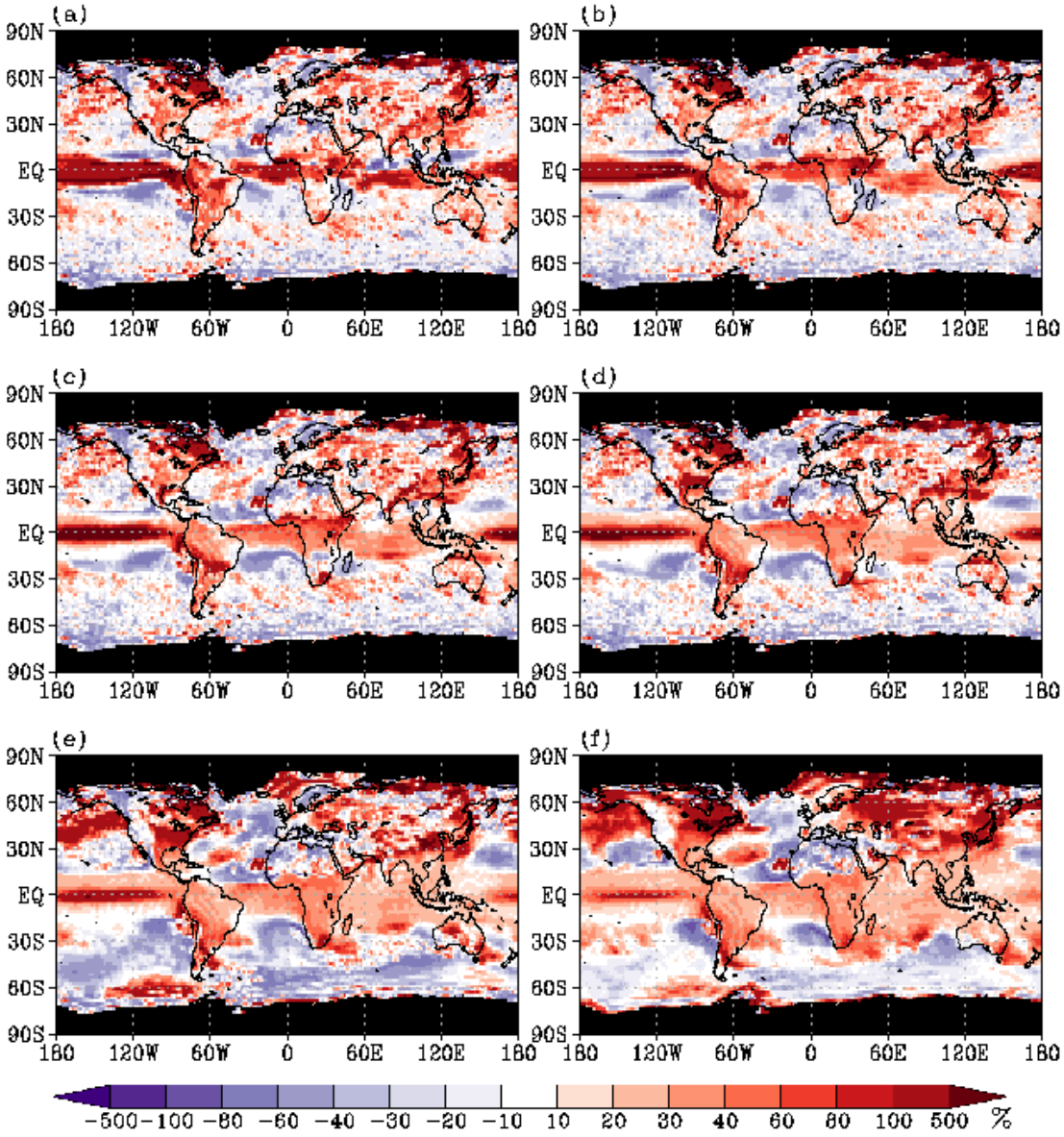

Figure A.10— Ratio of change in $\%$ in CAPE during MAM between the A1B scenario (2090-2099) and the 20C simulation (1980-1999) for different percentiles: (a) 5th, (b) 20th, (c) 40th, (d) 60th, (e) 80th, (f) 95th. The black shading marks those regions with CAPE $> 0\ Jkg^{-1}$ occurring less than 10 times during an average year.

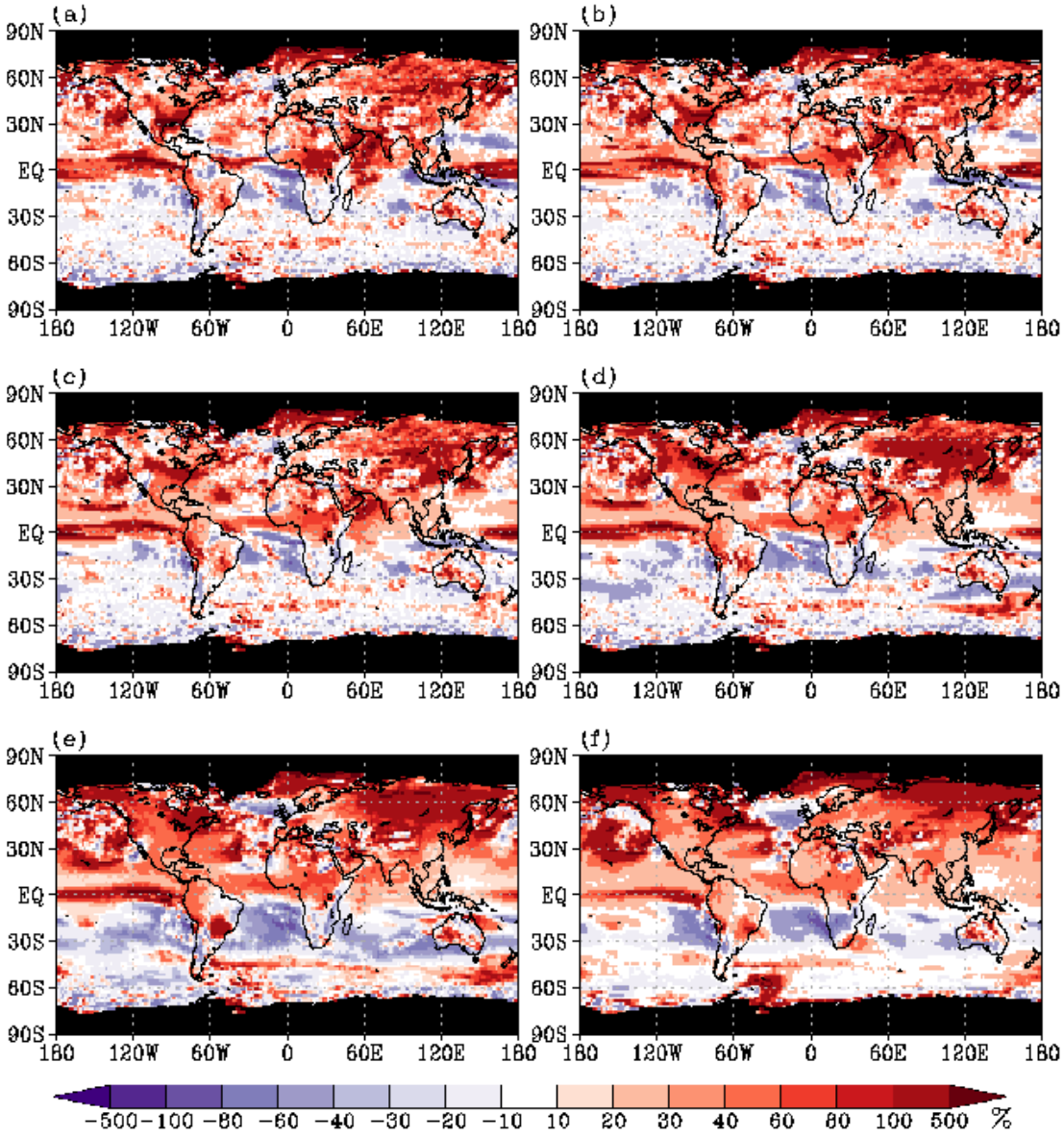

Figure A.11— Ratio of change in % in CAPE during JJA between the A1B scenario (2090-2099) and the 20C simulation (1980-1999) for different percentiles: (a) 5th, (b) 20th, (c) 40th, (d) 60th, (e) 80th, (f) 95th. The black shading marks those regions with CAPE > 0 Jkg^{-1} occurring less than 10 times during an average year.

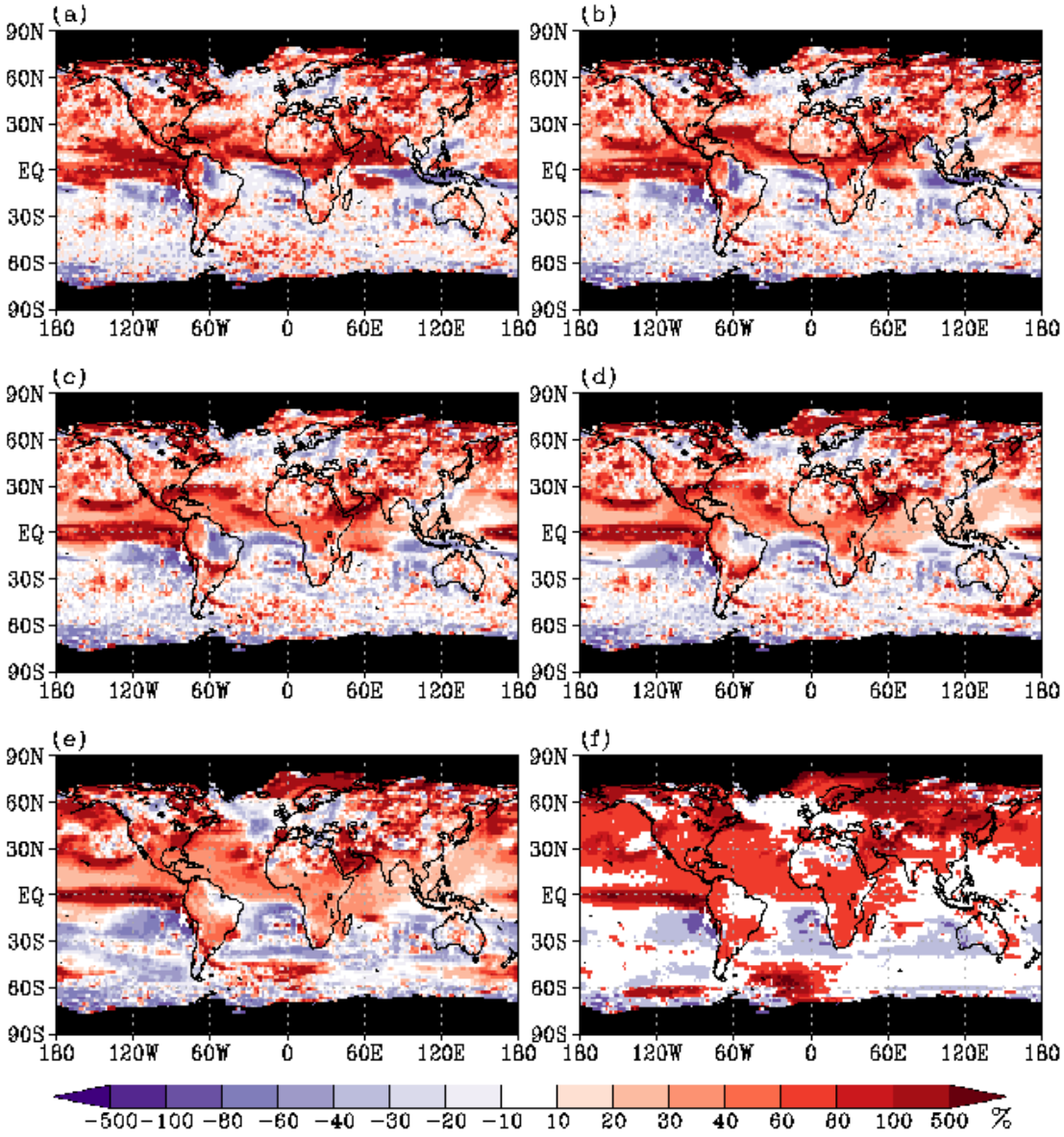

Figure A.12— Ratio of change in % in CAPE during SON between the A1B scenario (2090-2099) and the 20C simulation (1980-1999) for different percentiles: (a) 5th, (b) 20th, (c) 40th, (d) 60th, (e) 80th, (f) 95th. The black shading marks those regions with CAPE $> 0\ Jkg^{-1}$ occurring less than 10 times during an average year.

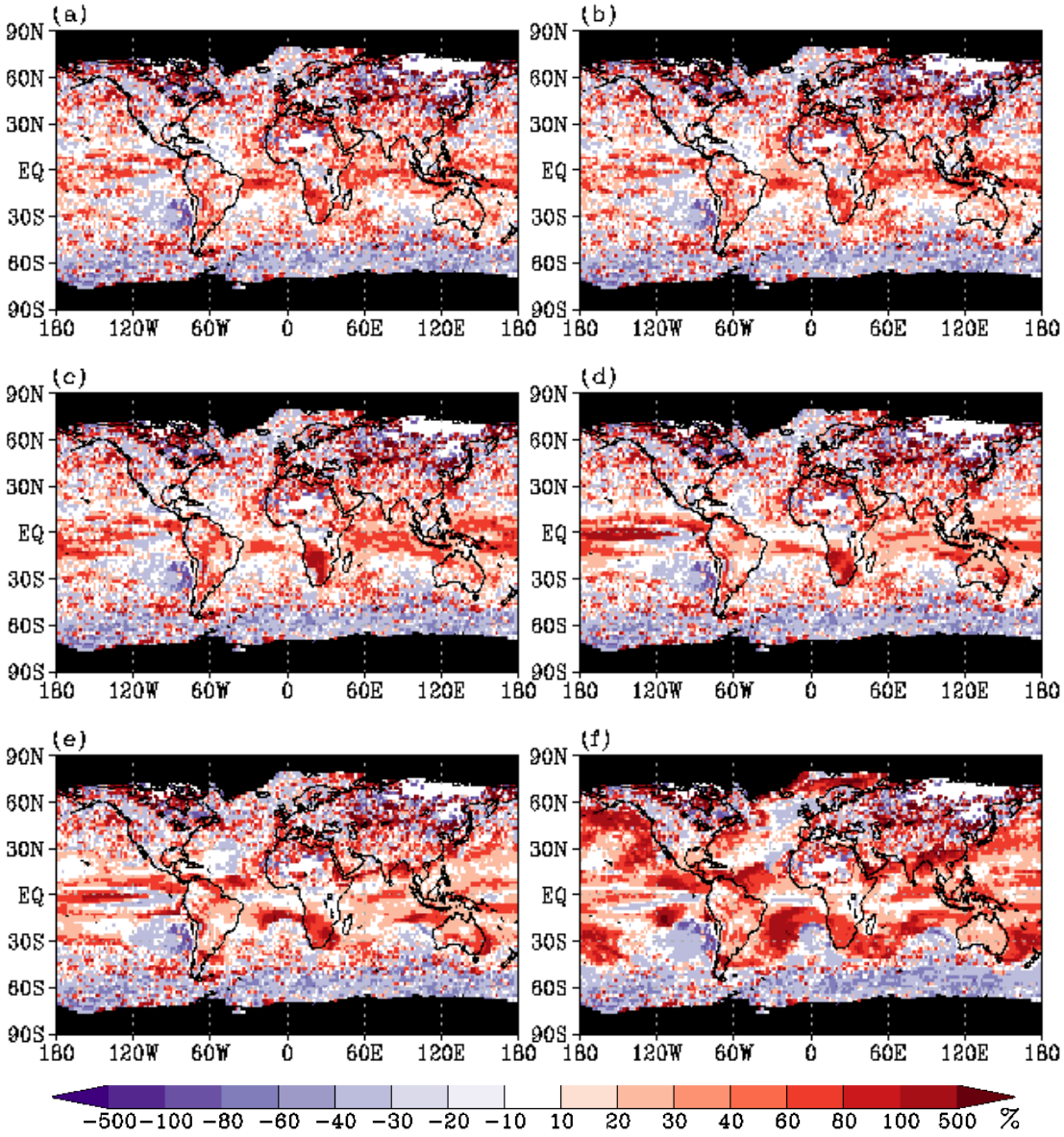

Figure A.13— Ratio of change in % in CIN during DJF between the A1B scenario (2090-2099) and the 20C simulation (1980-1999) for different percentiles: (a) 5th, (b) 20th, (c) 40th, (d) 60th, (e) 80th, (f) 95th. The black shading marks those regions with CAPE > 0 Jkg^{-1} occurring less than 10 times during an average year.

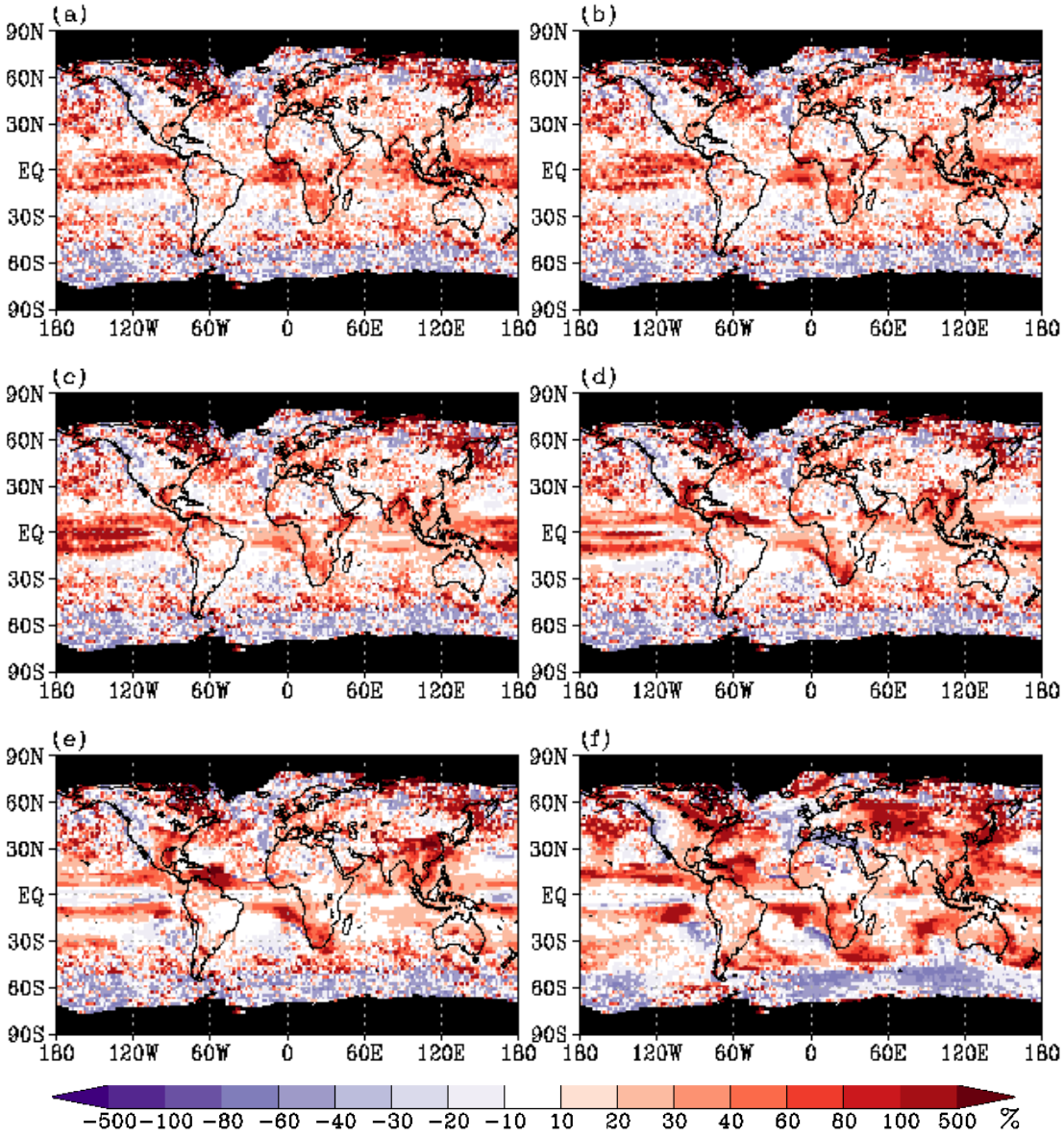

Figure A.14— Ratio of change in % in CIN during MAM between the A1B scenario (2090-2099) and the 20C simulation (1980-1999) for different percentiles: (a) 5th, (b) 20th, (c) 40th, (d) 60th, (e) 80th, (f) 95th. The black shading marks those regions with CAPE > 0 Jkg^{-1} occurring less than 10 times during an average year.

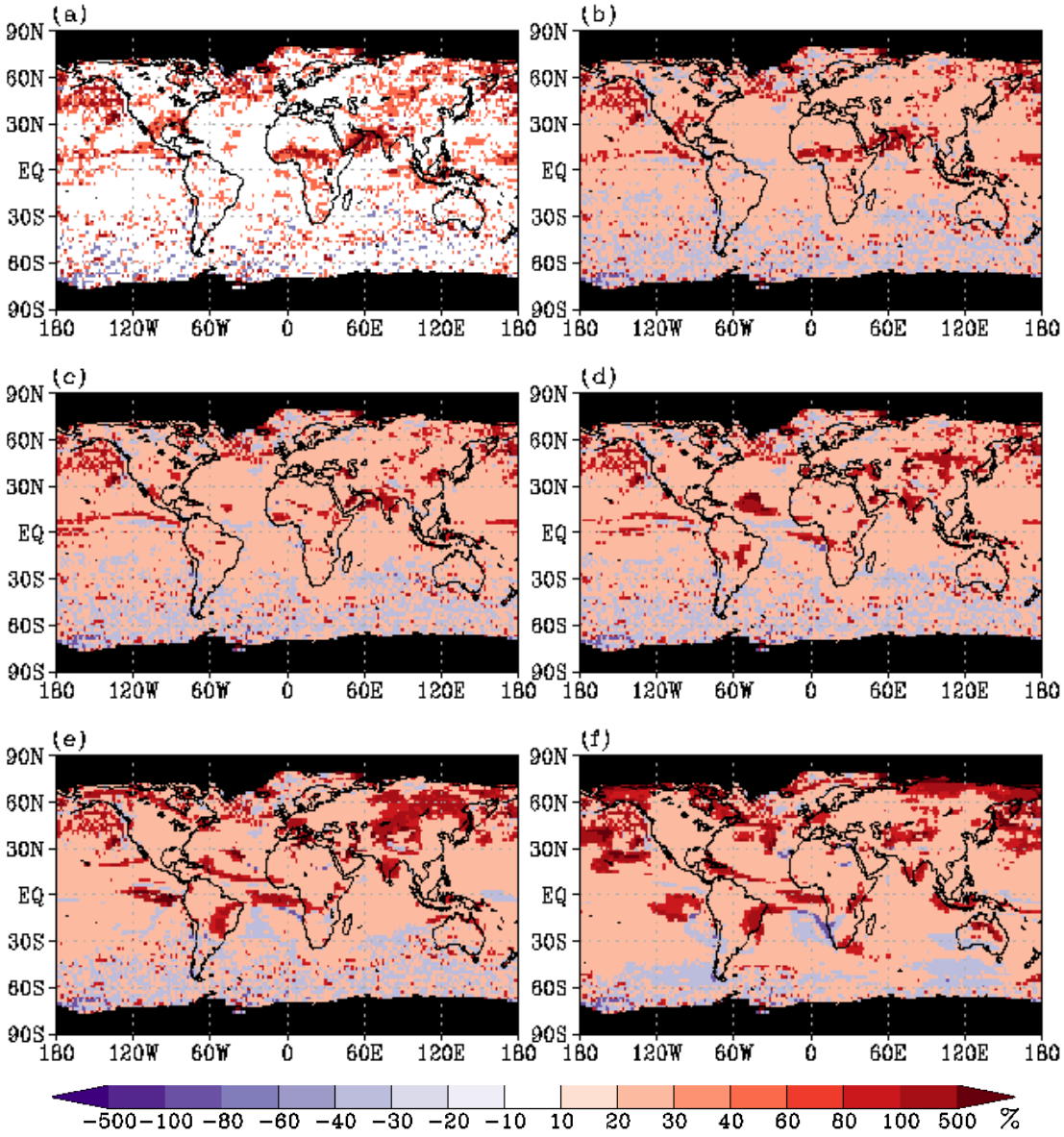

Figure A.15— Ratio of change in % in CIN during JJA between the A1B scenario (2090-2099) and the 20C simulation (1980-1999) for different percentiles: (a) 5th, (b) 20th, (c) 40th, (d) 60th, (e) 80th, (f) 95th. The black shading marks those regions with CAPE > 0 Jkg^{-1} occurring less than 10 times during an average year.

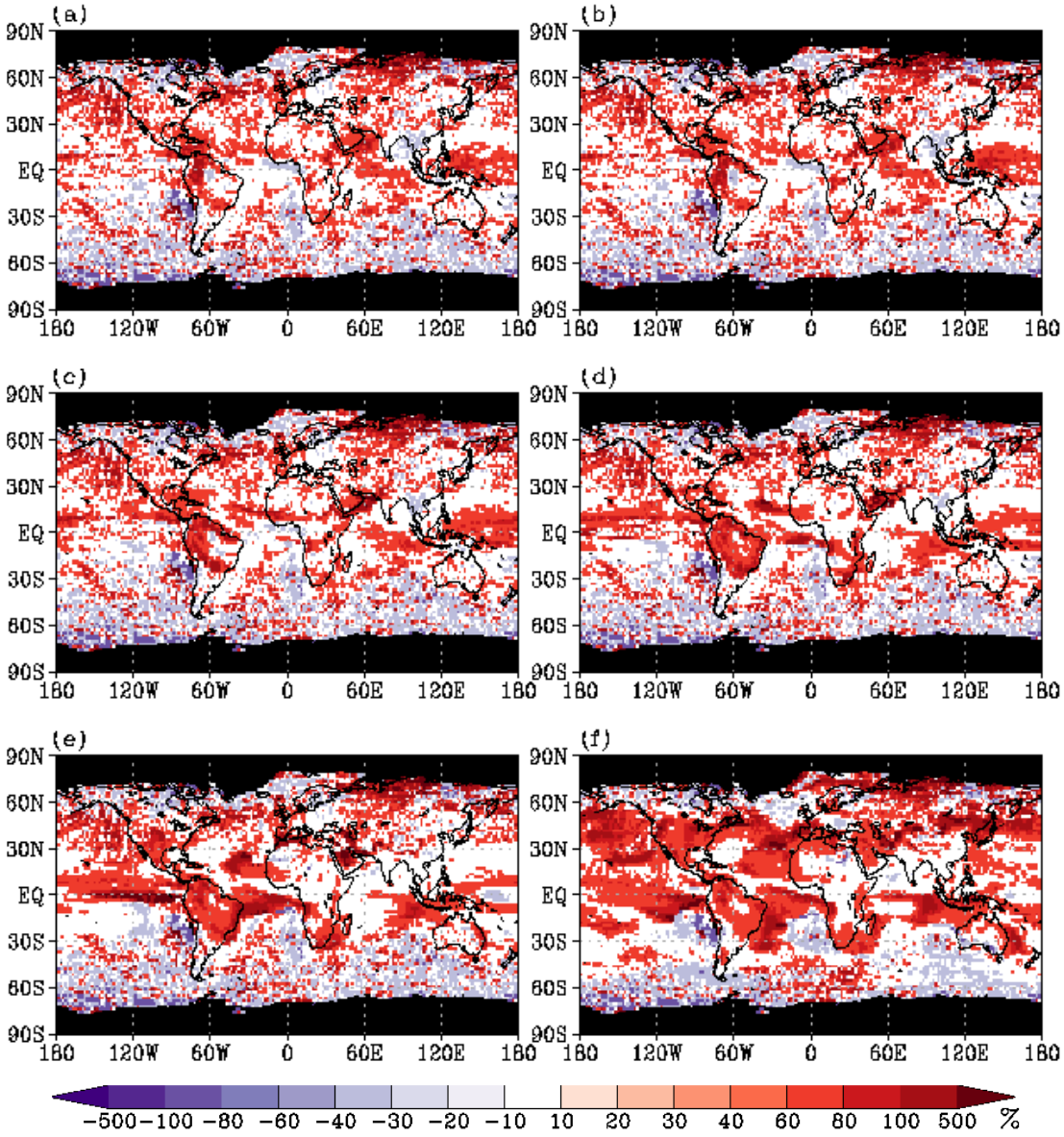

Figure A.16— Ratio of change in % in CIN during SON between the A1B scenario (2090-2099) and the 20C simulation (1980-1999) for different percentiles: (a) 5th, (b) 20th, (c) 40th, (d) 60th, (e) 80th, (f) 95th. The black shading marks those regions with CAPE > 0 Jkg^{-1} occurring less than 10 times during an average year.

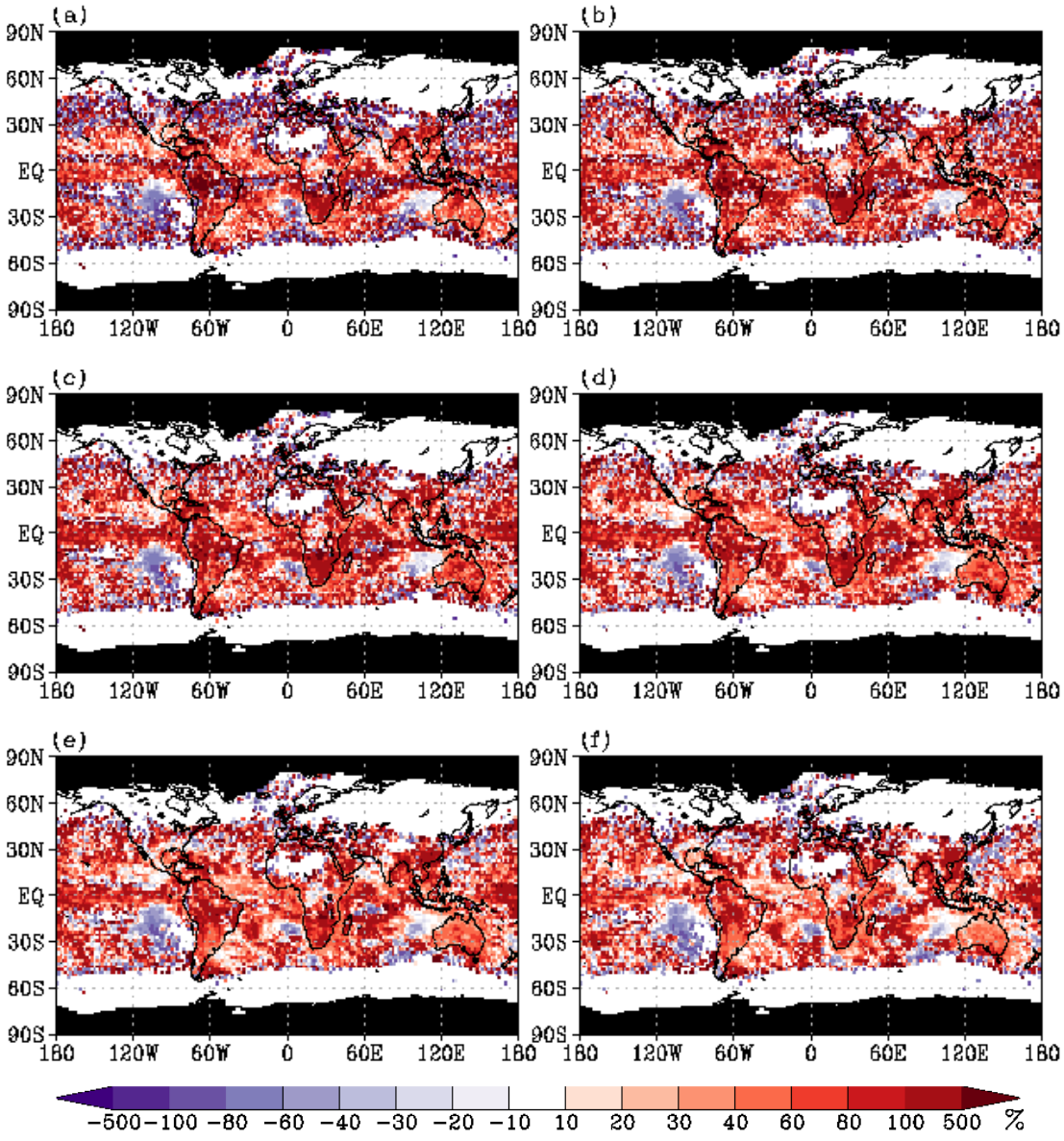

Figure A.17— Ratio of change in % in CAPE if CIN $\geq$ 100 Jkg^{-1} between the A1B scenario (2090-2099) and the 20C simulation (1980-1999) during DJF for different percentiles: (a) 5th, (b) 20th, (c) 40th, (d) 60th, (e) 80th, (f) 95th.

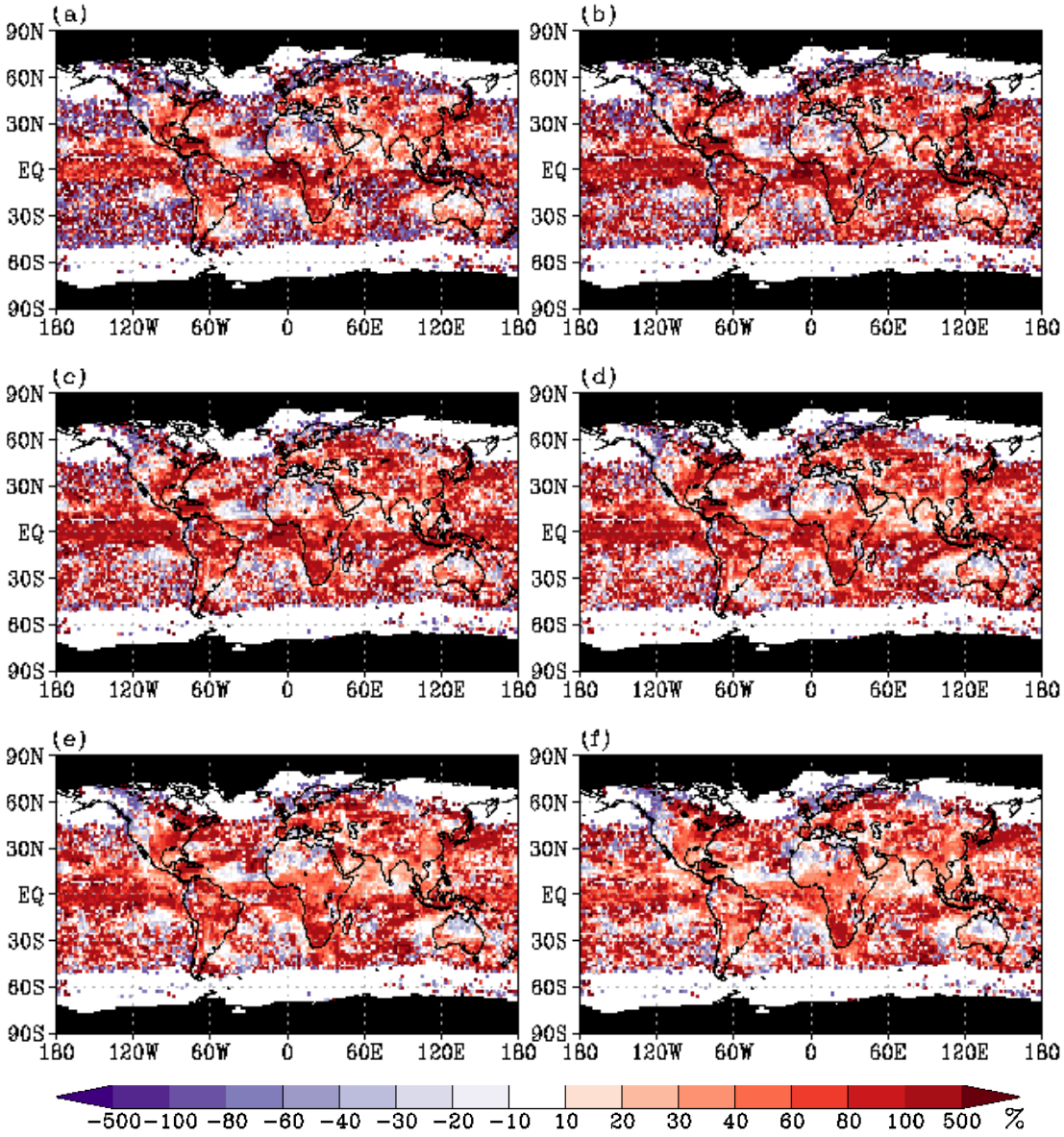

Figure A.18— Ratio of change in % in CAPE if CIN $\geq$ 100 Jkg^{-1} between the A1B scenario (2090-2099) and the 20C simulation (1980-1999) during MAM for different percentiles: (a) 5th, (b) 20th, (c) 40th, (d) 60th, (e) 80th, (f) 95th. The black shading marks those regions with CAPE $>$ 0 Jkg^{-1} occurring less than 10 times during an average year.

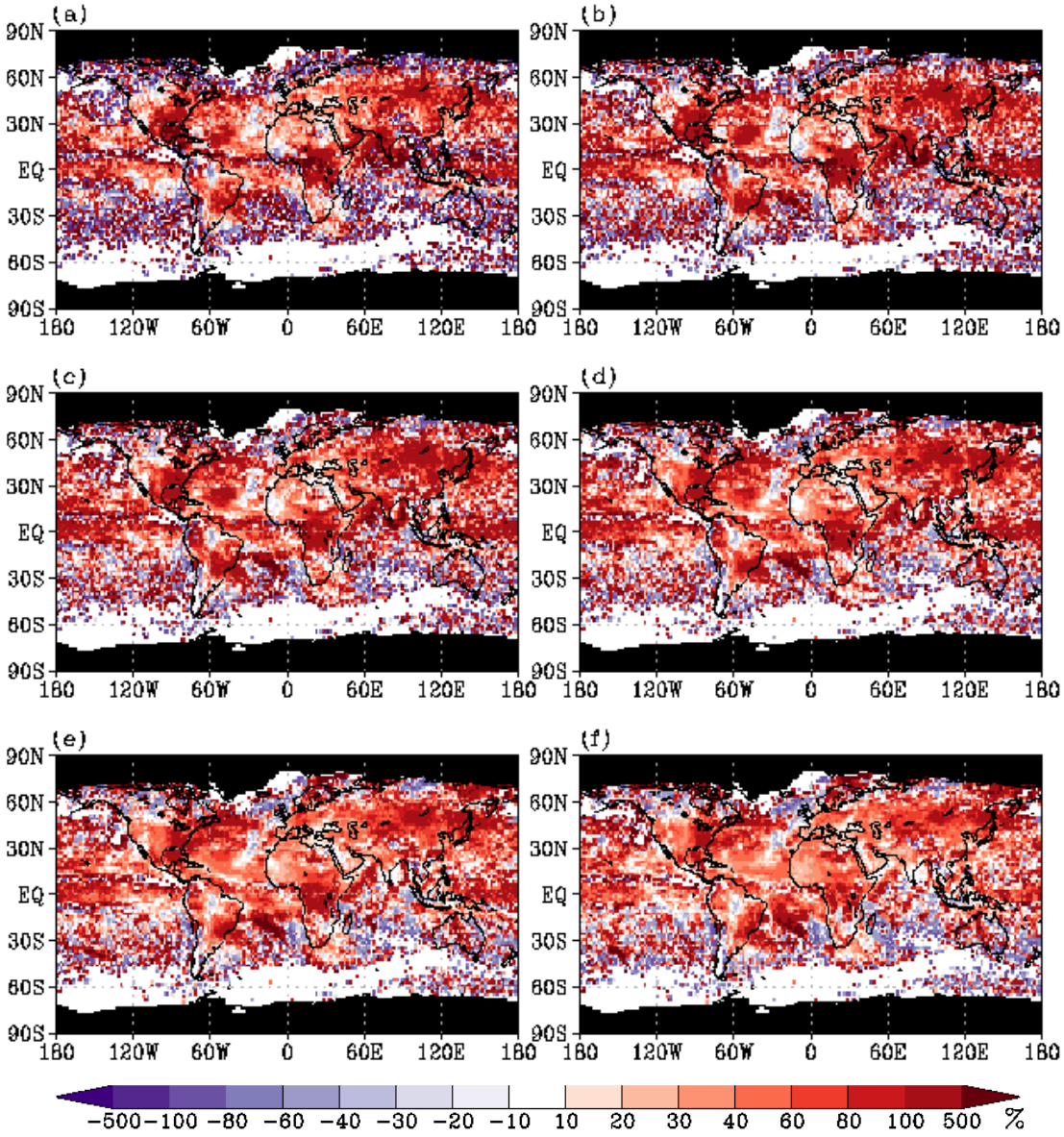

Figure A.19— Ratio of change in % in CAPE if CIN $\geq$ 100 Jkg^{-1} between the A1B scenario (2090-2099) and the 20C simulation (1980-1999) during JJA for different percentiles: (a) 5th, (b) 20th, (c) 40th, (d) 60th, (e) 80th, (f) 95th. The black shading marks those regions with CAPE $>$ 0 Jkg^{-1} occurring less than 10 times during an average year.

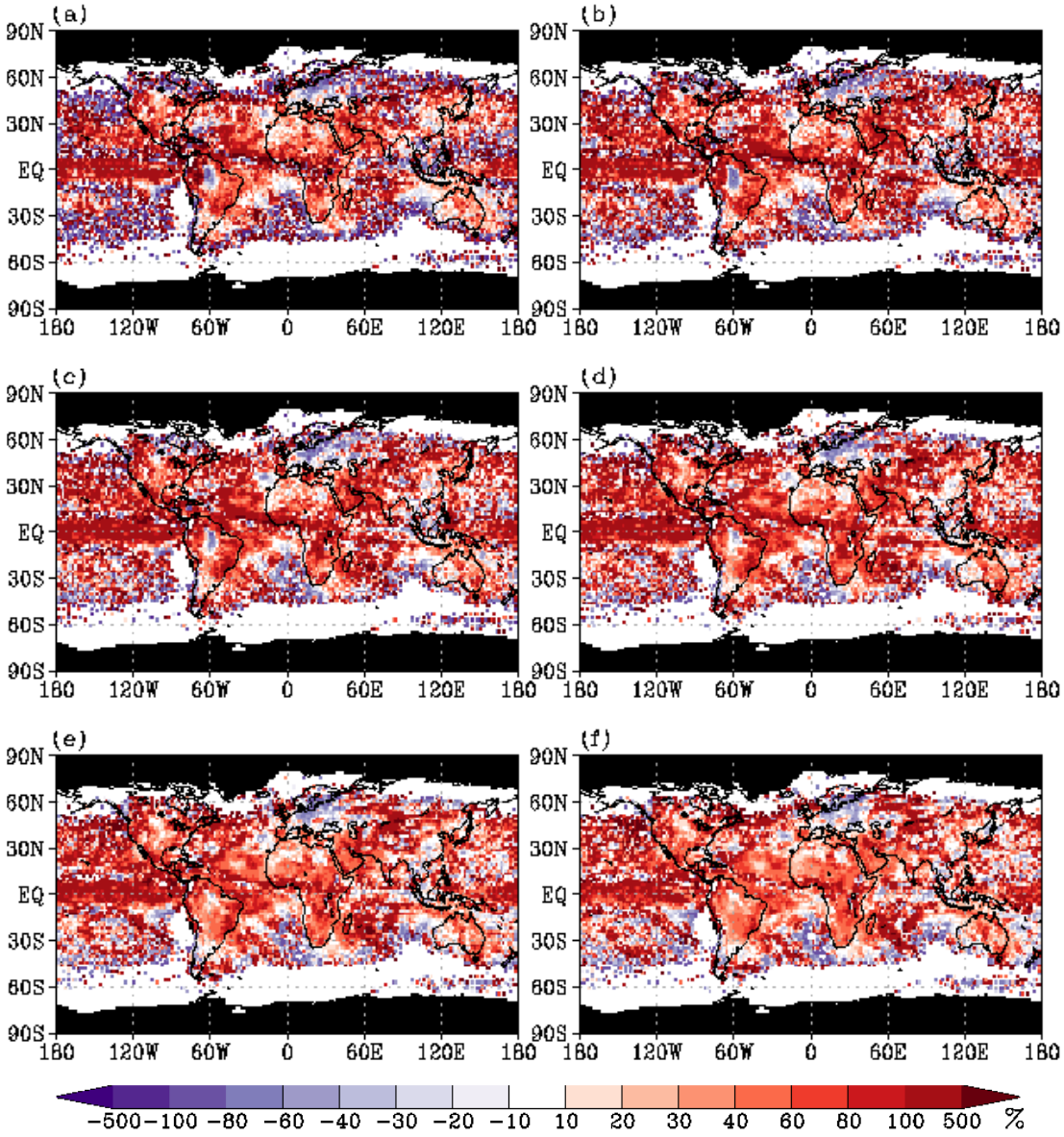

Figure A.20— Ratio of change in % in CAPE if CIN $\geq$ 100 Jkg^{-1} between the A1B scenario (2090-2099) and the 20C simulation (1980-1999) during SON for different percentiles: (a) 5th, (b) 20th, (c) 40th, (d) 60th, (e) 80th, (f) 95th. The black shading marks those regions with CAPE $>$ 0 Jkg^{-1} occurring less than 10 times during an average year.

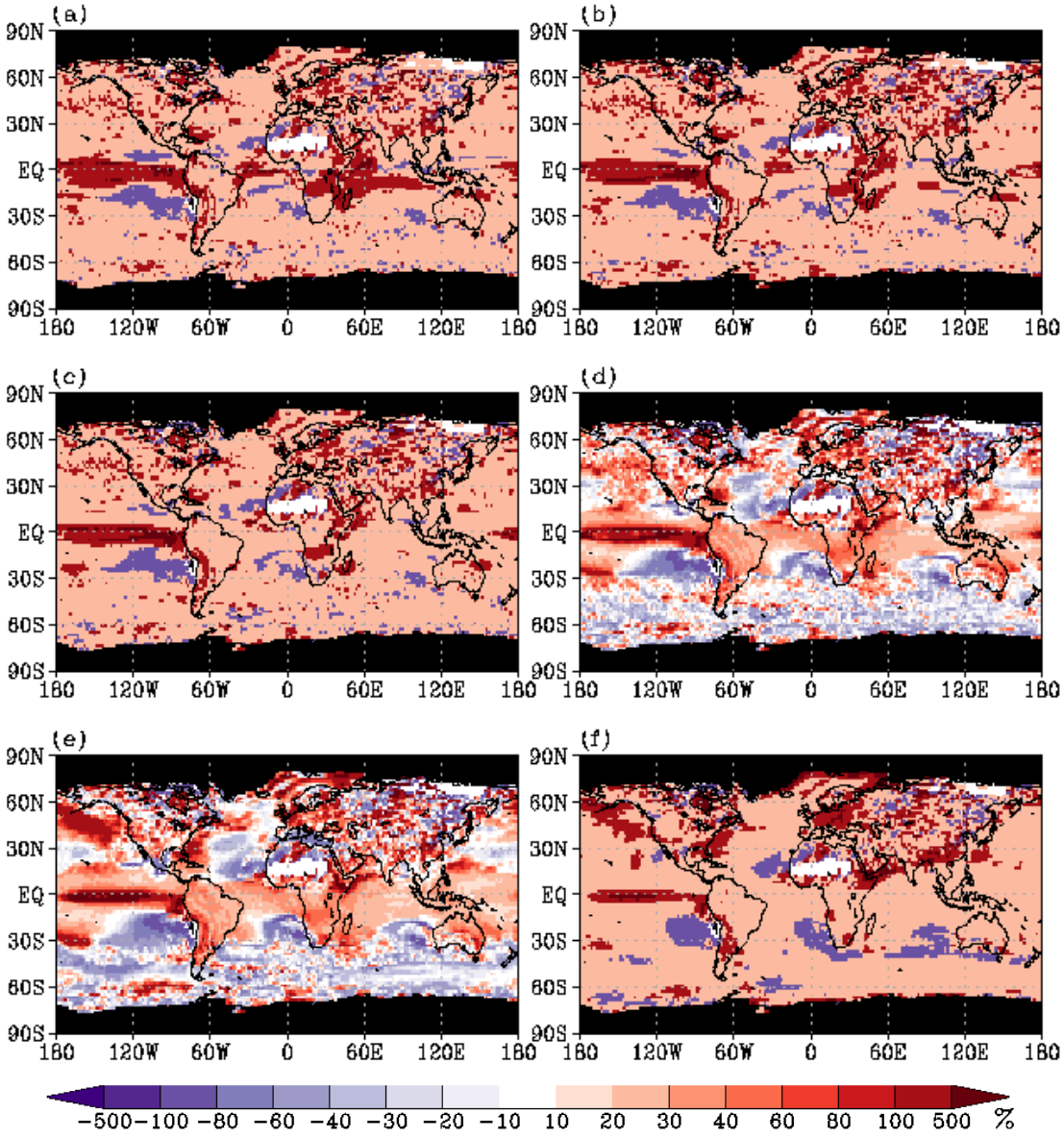

Figure A.21— Ratio of change in % in CAPE if CIN $< 20\ Jkg^{-1}$ between the A1B scenario (2090-2099) and the 20C simulation (1980-1999) during DJF for different percentiles: (a) 5th, (b) 20th, (c) 40th, (d) 60th, (e) 80th, (f) 95th. The black shading marks those regions with CAPE $> 0\ Jkg^{-1}$ occurring less than 10 times during an average year.

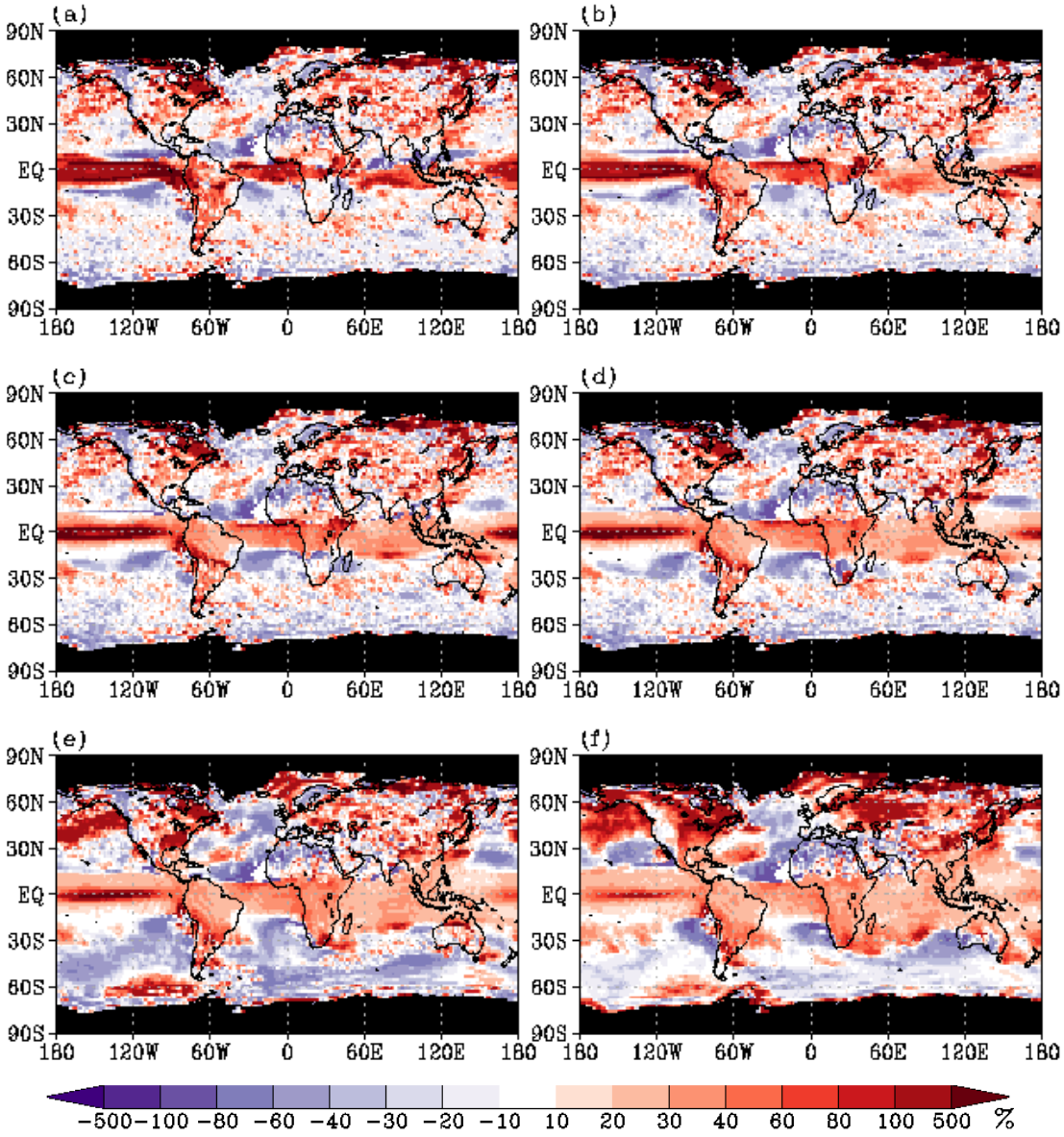

Figure A.22— Ratio of change in % in CAPE if CIN $< 20\ Jkg^{-1}$ between the A1B scenario (2090-2099) and the 20C simulation (1980-1999) during MAM for different percentiles: (a) 5th, (b) 20th, (c) 40th, (d) 60th, (e) 80th, (f) 95th. The black shading marks those regions with CAPE $> 0\ Jkg^{-1}$ occurring less than 10 times during an average year.

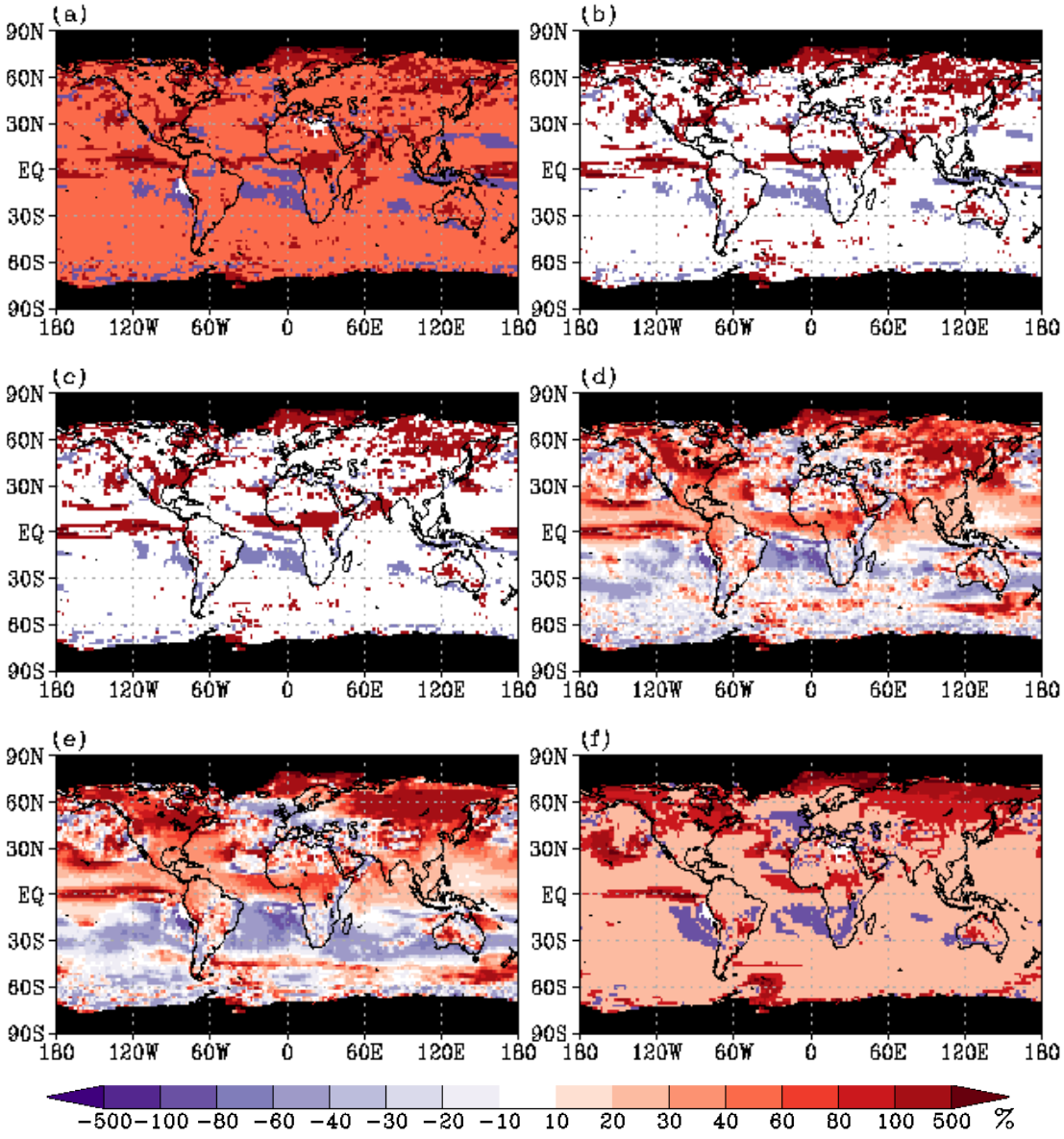

Figure A.23— Ratio of change in % in CAPE if CIN $< 20\ Jkg^{-1}$ between the A1B scenario (2090-2099) and the 20C simulation (1980-1999) during JJA for different percentiles: (a) 5th, (b) 20th, (c) 40th, (d) 60th, (e) 80th, (f) 95th. The black shading marks those regions with CAPE $> 0\ Jkg^{-1}$ occurring less than 10 times during an average year.

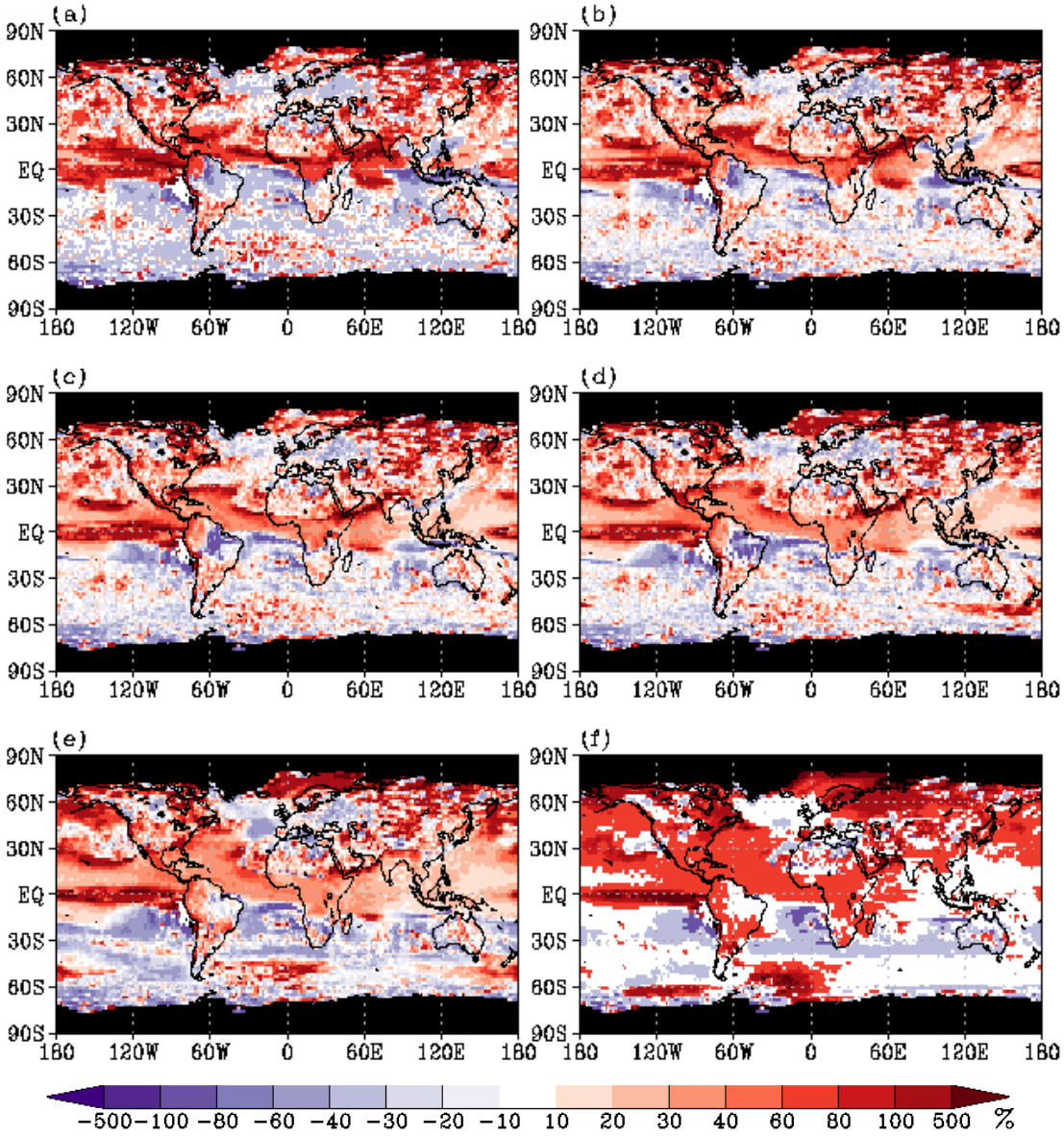

Figure A.24— Ratio of change in % in CAPE if CIN $< 20\ Jkg^{-1}$ between the A1B scenario (2090-2099) and the 20C simulation (1980-1999) during SON for different percentiles: (a) 5th, (b) 20th, (c) 40th, (d) 60th, (e) 80th, (f) 95th. The black shading marks those regions with CAPE $> 0\ Jkg^{-1}$ occurring less than 10 times during an average year.

A.3 Memory in temperature and humidity

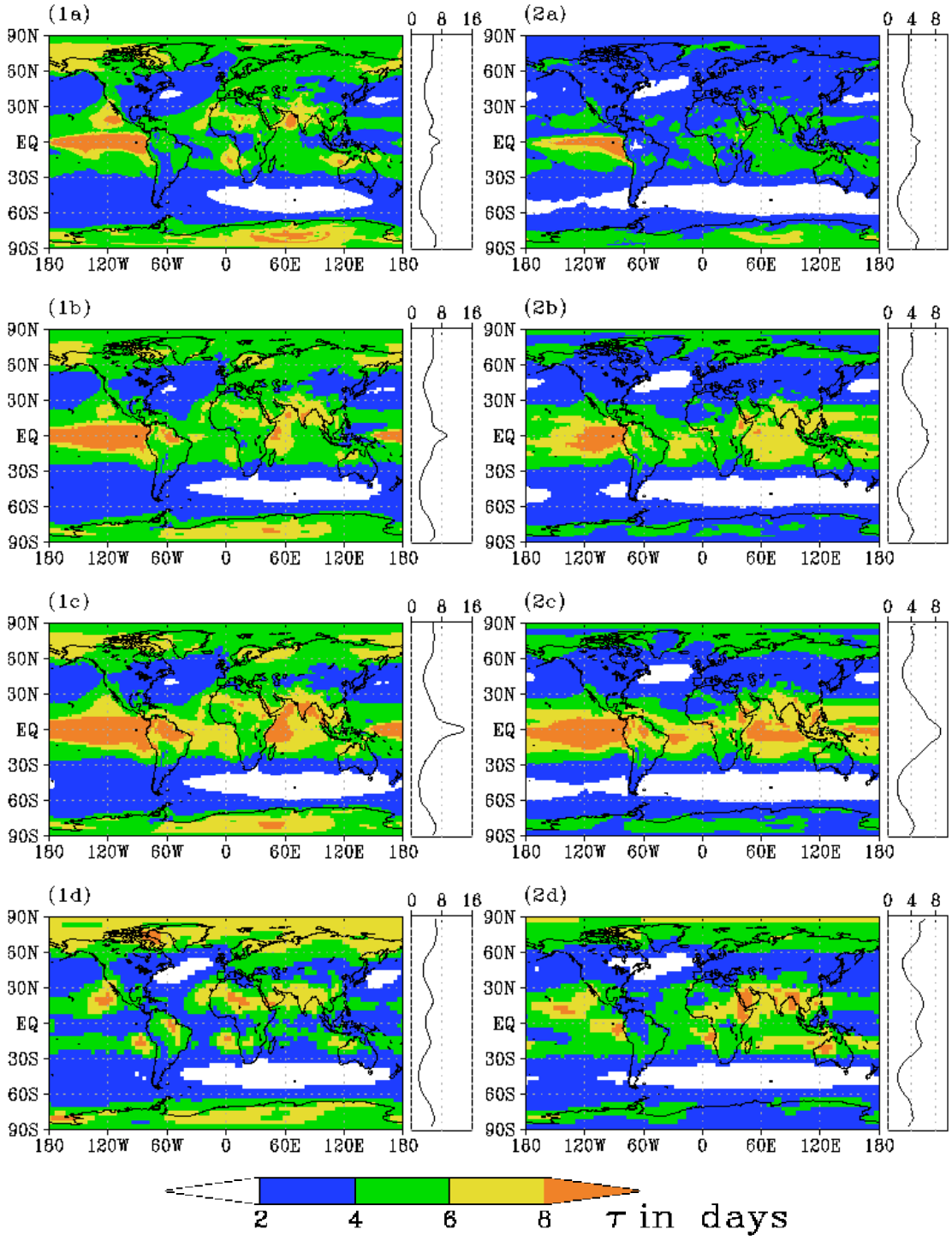

Figure A.25— Decay time scale τ_d in days of (1) T_{ML} and (2) q_{ML} computed from: (a) ERA-40 data, (b) 20C simulation, (c) A1B scenario, and (d) UCM. The black shading marks those regions with CAPE > 0 Jkg^{-1} occurring less than 10 times during an average year.

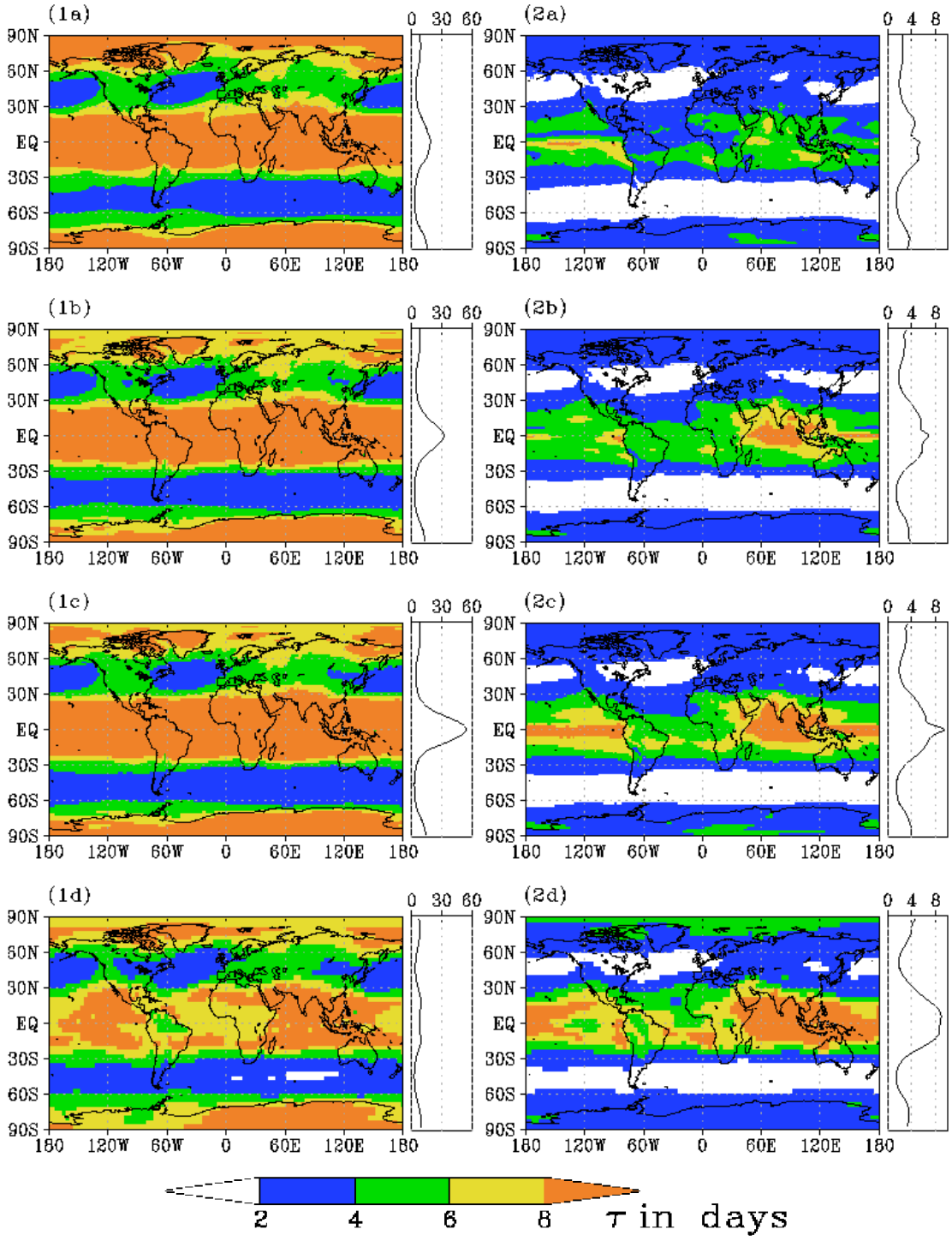

Figure A.26— Decay time scale τ_d in days of (1) H and (2) LPW computed from: (a) ERA-40 data, (b) 20C simulation, (c) A1B scenario, and (d) UCM. The black shading marks those regions with CAPE > 0 Jkg^{-1} occurring less than 10 times during an average year.

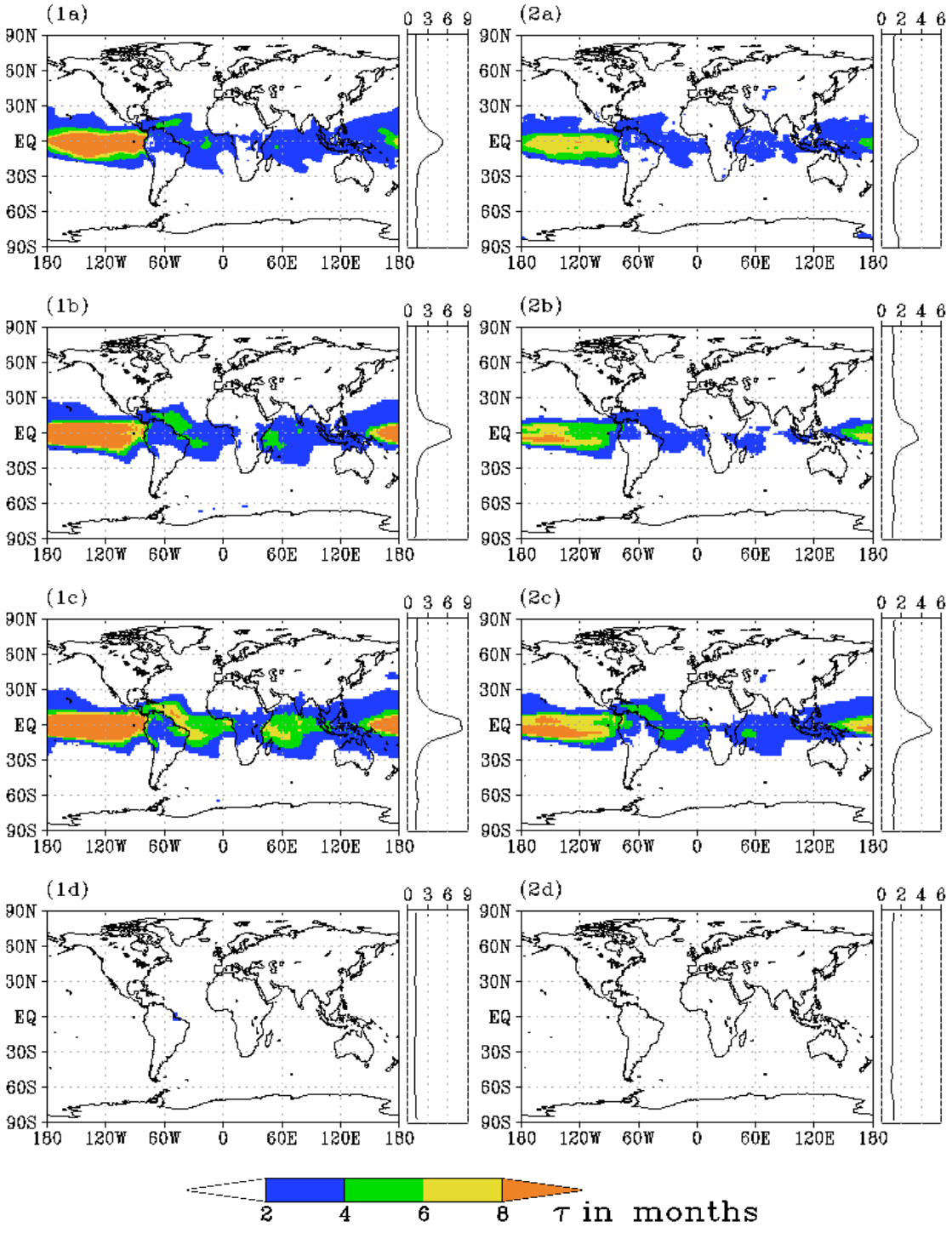

Figure A.27— Decay time scale τ_m in months of (1) T_{ML} and (2) q_{ML} computed from: (a) ERA-40 data, (b) 20C simulation, (c) A1B scenario, and (d) UCM. The black shading marks those regions with CAPE > 0 Jkg^{-1} occurring less than 10 times during an average year.

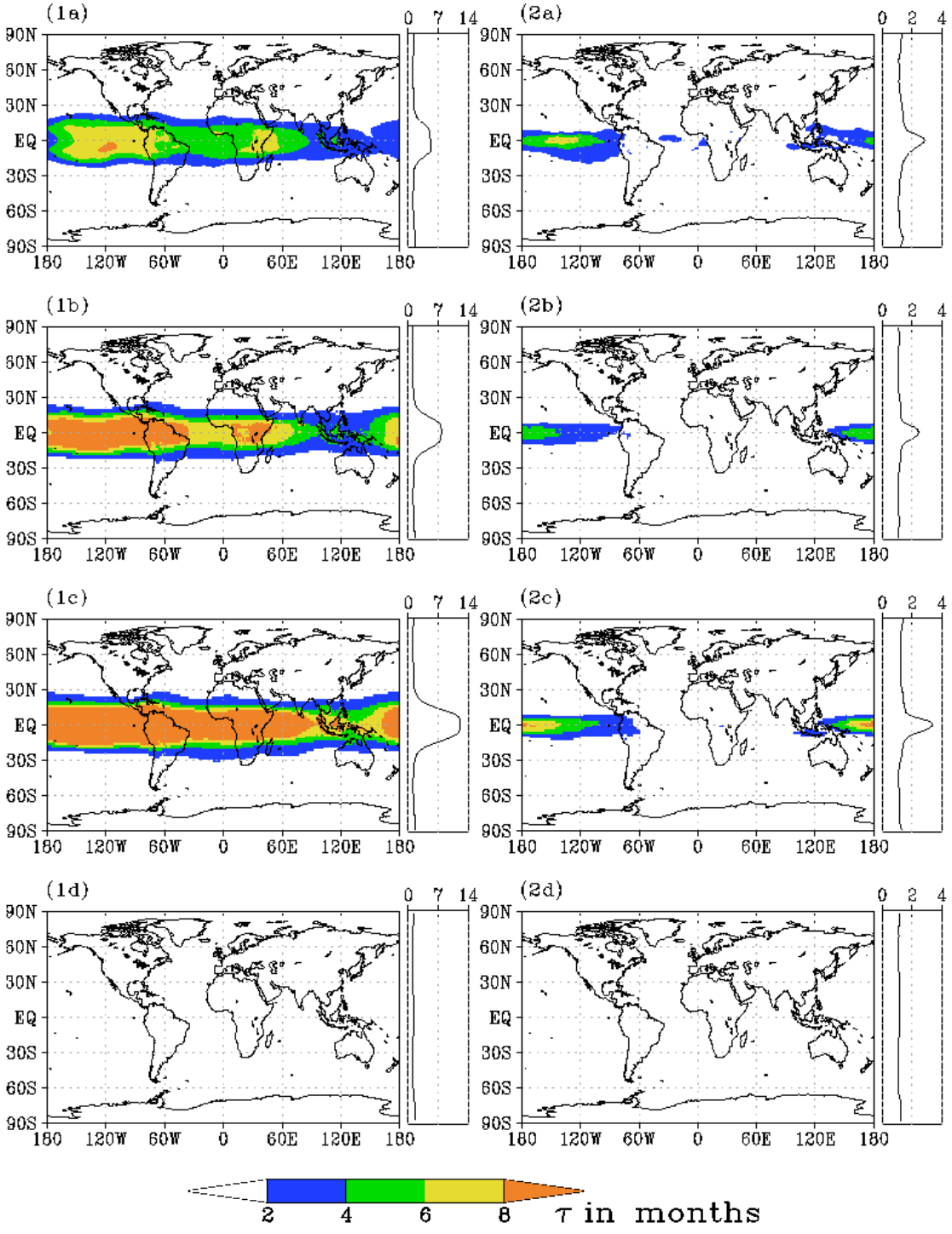

Figure A.28— Decay time scale τ_m in months of (1) H and (2) LPW computed from: (a) ERA-40 data, (b) 20C simulation, (c) A1B scenario, and (d) UCM. The black shading marks those regions with CAPE > 0 Jkg^{-1} occurring less than 10 times during an average year.

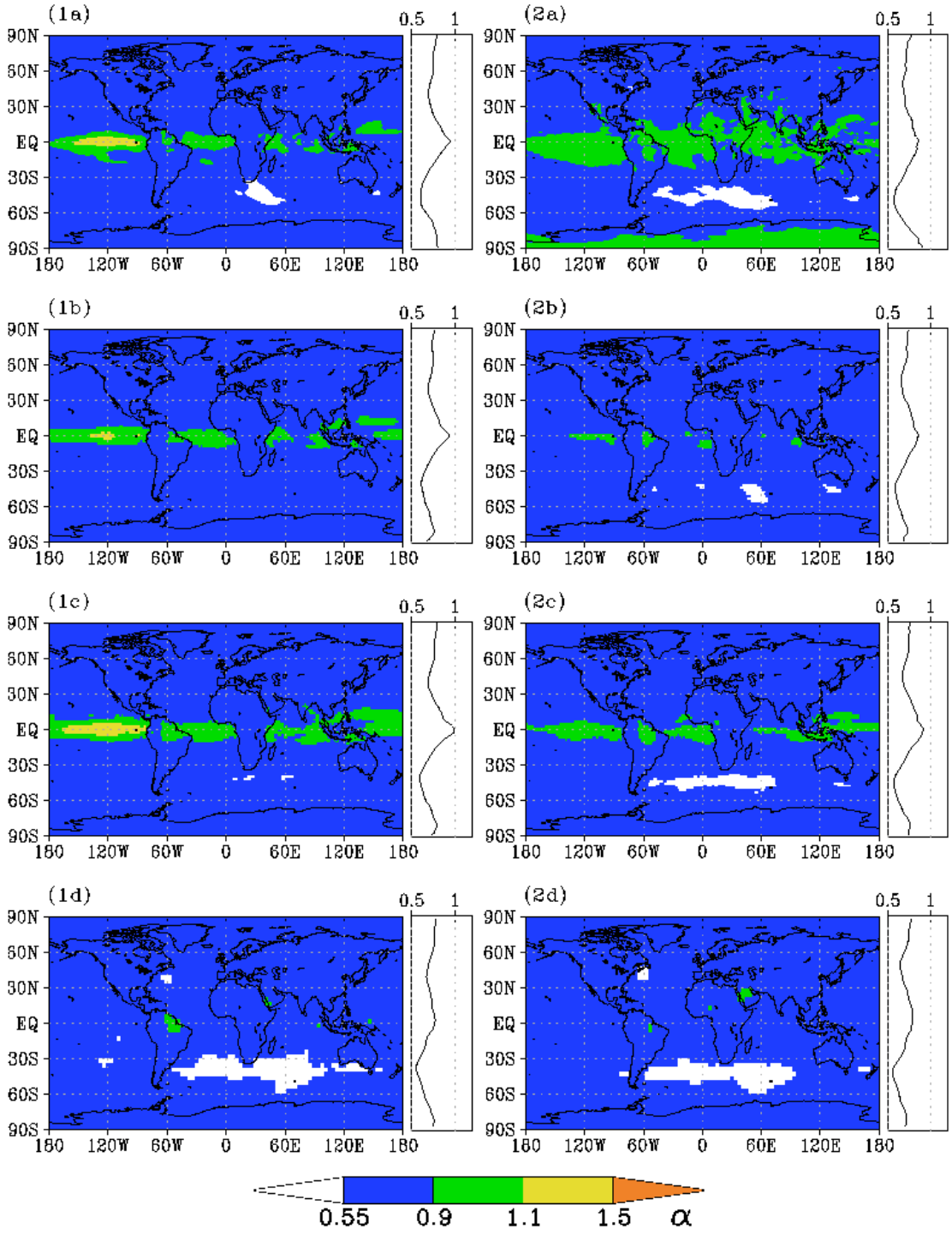

Figure A.29— Hurst exponent α in 30 days to 300 days of (1) T_{ML} and (2) q_{ML} computed from: (a) ERA-40 data, (b) 20C simulation, (c) A1B scenario, and (d) UCM. Hurst exponents exceeding 0.55 indicate memory. The black shading marks those regions with CAPE > 0 Jkg^{-1} occurring less than 10 times during an average year.

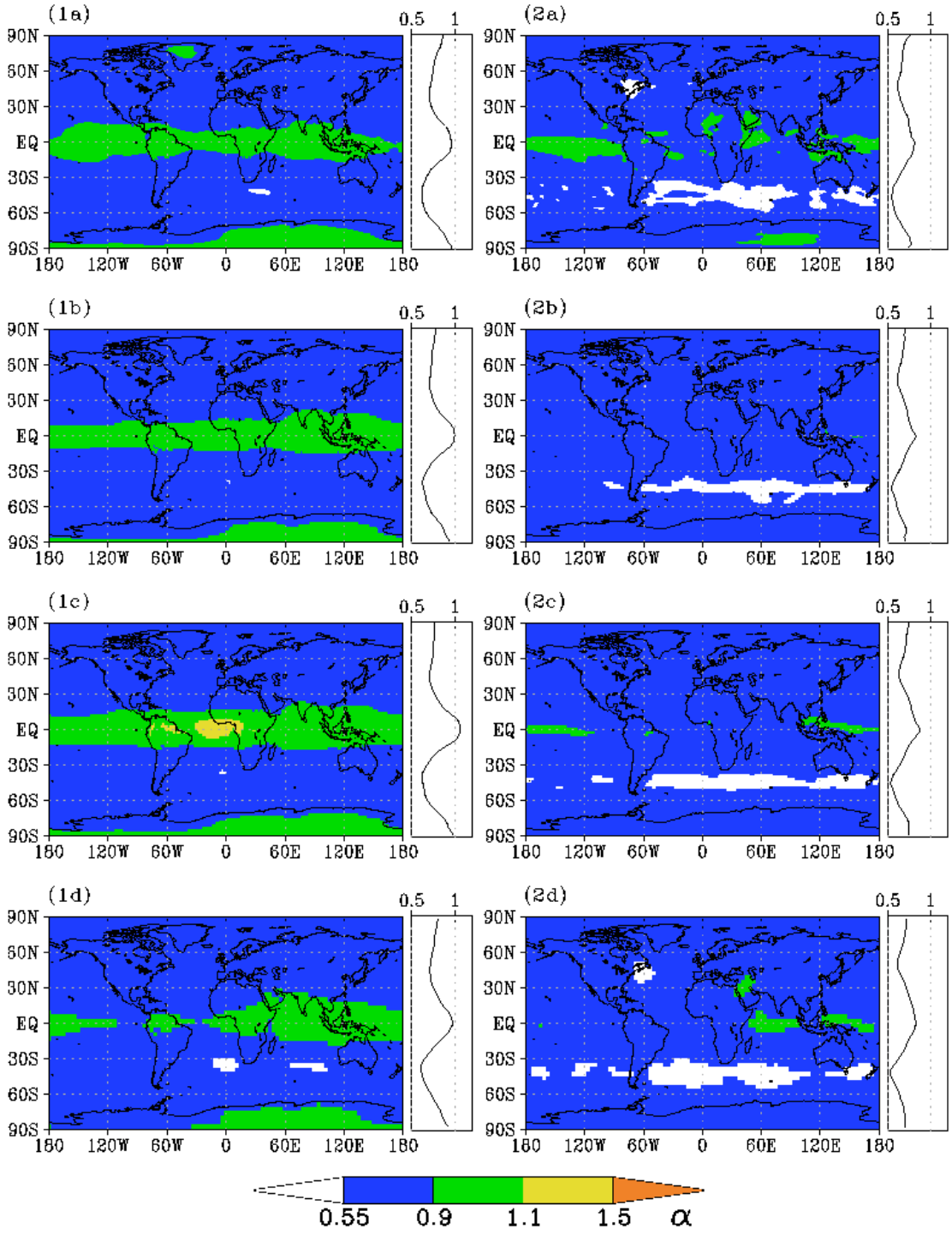

Figure A.30— Hurst exponent α in 30 days to 300 days of (1) H and (2) LPW computed from: (a) ERA-40 data, (b) 20C simulation, (c) A1B scenario, and (d) UCM. Hurst exponents exceeding 0.55 indicate memory. The black shading marks those regions with CAPE $> 0\ Jkg^{-1}$ occurring less than 10 times during an average year.

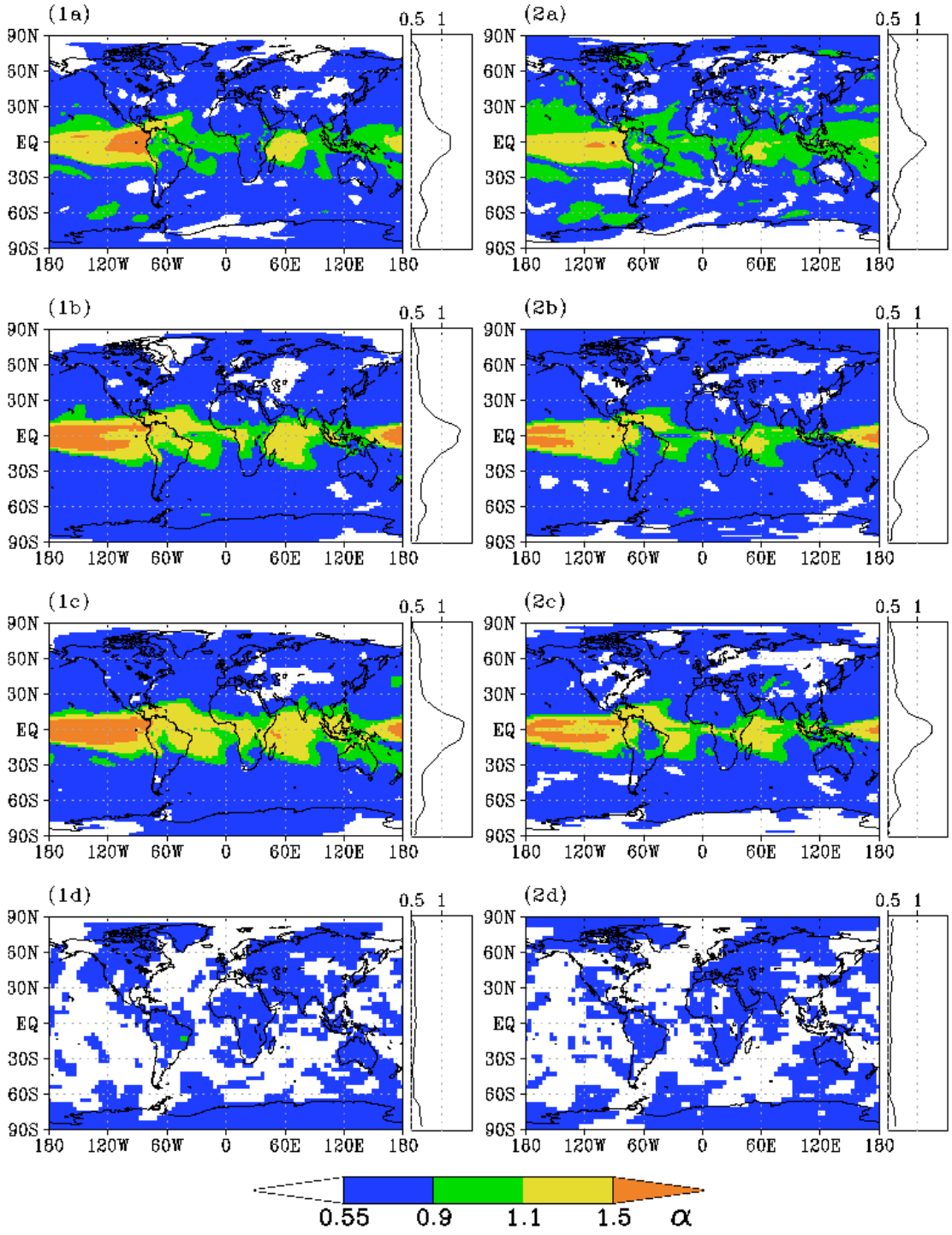

Figure A.31— Hurst exponent α in 400 days to 5 years of (1) T_{ML} and (2) q_{ML} computed from: (a) ERA-40 data, (b) 20C simulation, (c) A1B scenario, and (d) UCM. Hurst exponents exceeding 0.55 indicate memory. The black shading marks those regions with CAPE > 0 Jkg^{-1} occurring less than 10 times during an average year.

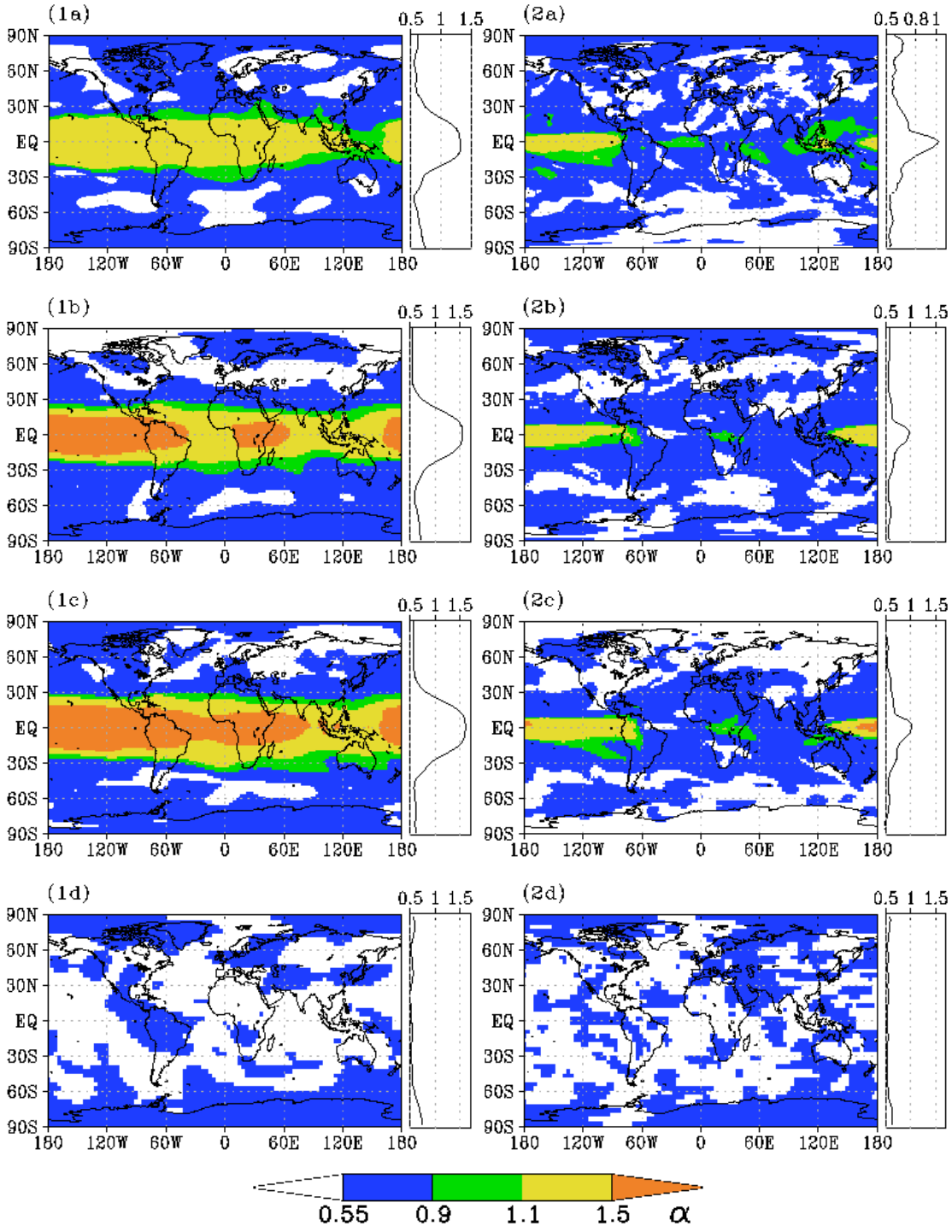

Figure A.32— Hurst exponent α in 400 days to 5 years of (1) H and (2) LPW computed from: (a) ERA-40 data, (b) 20C simulation, (c) A1B scenario, and (d) UCM. Hurst exponents exceeding 0.55 indicate memory. The black shading marks those regions with CAPE $> 0\ Jkg^{-1}$ occurring less than 10 times during an average year.

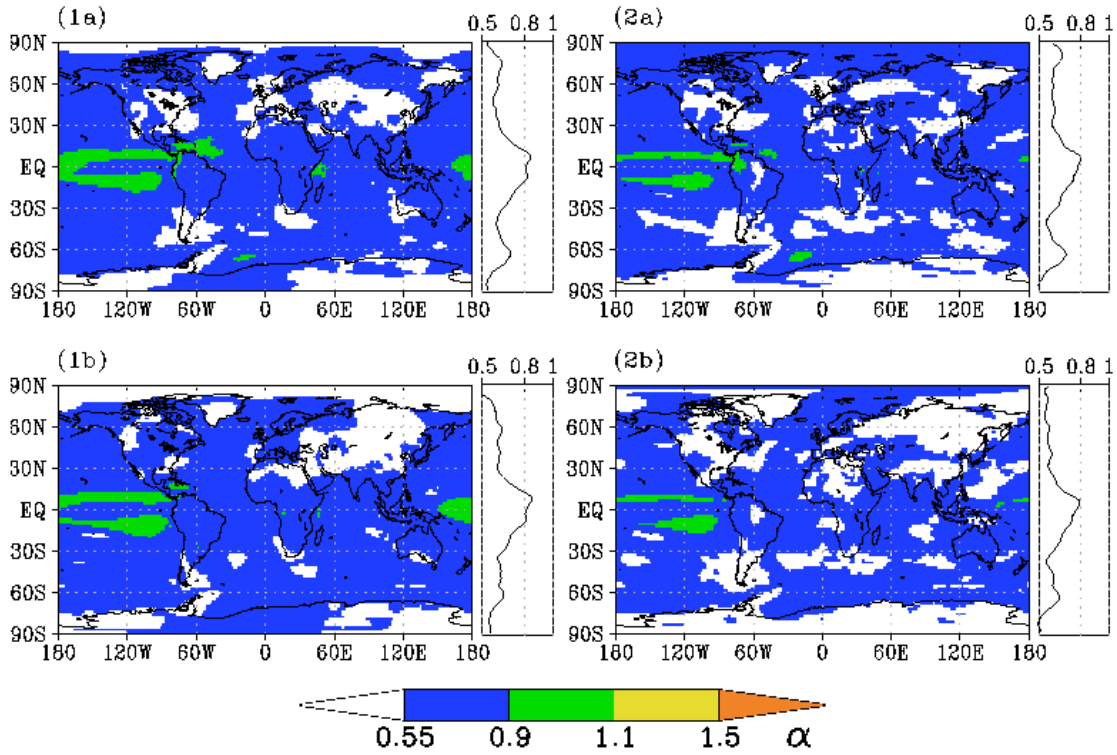

Figure A.33— Hurst exponent α in 2 years to 20 years of (1) T_{ML} and (2) q_{ML} computed from: (a) 20C simulation, (b) A1B scenario. Hurst exponents exceeding 0.55 indicate memory. The black shading marks those regions with CAPE > 0 Jkg^{-1} occurring less than 10 times during an average year.

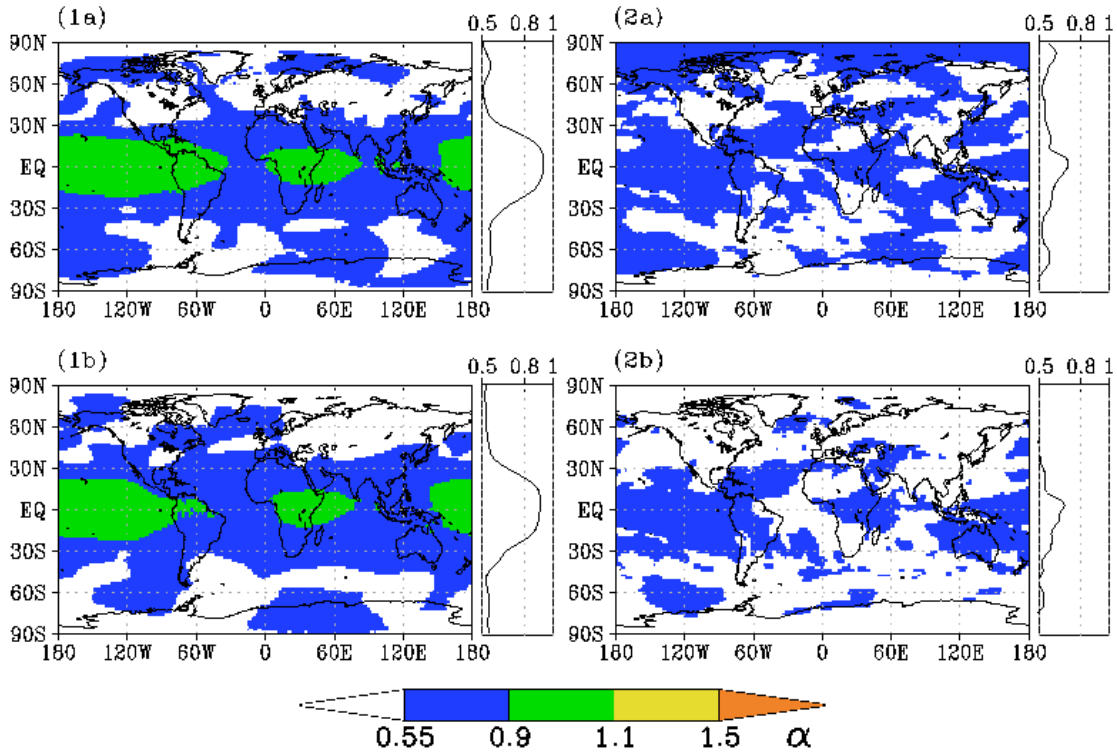

Figure A.34— Hurst exponent α in 2 years to 20 years of (1) H and (2) LPW computed from: (a) 20C simulation, (b) A1B scenario. Hurst exponents exceeding 0.55 indicate memory. The black shading marks those regions with CAPE > 0 Jkg^{-1} occurring less than 10 times during an average year.

Die gesamten Veröffentlichungen in der Publikationsreihe des MPI-M
„Berichte zur Erdsystemforschung“,
„Reports on Earth System Science“,
ISSN 1614-1199

sind über die Internetseiten des Max-Planck-Instituts für Meteorologie erhältlich:

http://www.mpimet.mpg.de/wissenschaft/publikationen.html



ISSN 1614-1199